

Università degli Studi di Salerno

.DIEM

Dipartimento di Ingegneria dell'Informazione ed Elettrica e Matematica Applicata

Dottorato di Ricerca in Ingegneria dell'Informazione
Ciclo 38

TESI DI DOTTORATO / PH.D. THESIS

Human-aware haptic teleoperation for safe and dexterous interactions

LORENZO Pagliara

SUPERVISORS: **PROF. PASQUALE CHIACCHIO**
PROF. GIOVANNI RUSSO

PHD PROGRAM DIRECTOR: **PROF. PASQUALE FOGGIA**

Anno 2026

Contents

Abstract **IX**

1 Introduction **1**
1.1 Context 1
1.2 Motivation and scope 4
1.3 Objectives 11
1.4 Outline 14

2 Haptic teleoperation under unreliable network conditions **17**
2.1 Haptic bilateral teleoperation architectures . . .19
2.1.1 Requirements of a haptic bilateral teleoperation system 20
2.1.1.1 Stability 20
2.1.1.2 Passivity 21
2.1.1.3 Transparency 23
2.1.1.4 Usability 24
2.1.2 State-of-the-art architectures 25
2.1.2.1 Position-position architecture .26
2.1.2.2 Position-force measured architecture 27

2.1.2.3 Position-force computed architecture 28
2.1.2.4 3-channel Architecture 29
2.1.2.5 4-channel Architecture 30
2.2 Control approaches for unreliable network conditions 31
2.2.1 Passivity-based approaches 32
2.2.1.1 Wave-variable approach 32
2.2.1.2 Time domain passivity approach33
2.2.2 Model-based approaches 35
2.2.2.1 Model-mediated teleoperation .36
2.2.2.2 Model-Augmented Haptic Telemanipulation 37
2.3 Assessment of haptic teleoperation under time delays 38
2.3.1 Background 39
2.3.2 Human-robot interface for haptic control in ISRU missions 43
2.3.2.1 System Design 43
2.3.2.2 Mission Operations Concept . .45
2.3.2.3 Haptic controller 47
2.3.2.4 Robot Visualization & Planning48
2.3.3 Results 49
2.3.3.1 Haptic control assessment . . .51
2.3.3.2 Analysis of the system in case of communication delays 52
2.3.3.3 Ease of training new operators53

3 Safe and natural haptic teleoperation 55
3.1 Haptic feedback 58
3.1.1 Haptic devices 59
3.1.1.1 Classes of haptic devices 60

3.1.1.2 Operation of a haptic device . .62
3.1.2 Haptic feedback rendering in a HBTS . .63
3.2 Interaction control 65
3.2.1 Dynamic model of manipulators 65
3.2.1.1 Dynamic model in free space .65
3.2.1.2 Dynamic model with environment interaction 66
3.2.2 Hybrid force/motion control 67
3.2.3 Impedance control 70
3.2.4 Admittance control 73
3.2.5 Including force references in the controller74
3.2.6 Variable impedance/admittance control .74
3.2.7 Interaction control for pHRI 76
3.3 Mapping and scaling techniques 77
3.3.1 Problem formulation 77
3.3.2 Control techniques 78
3.3.2.1 Position mapping techniques . .79
3.3.2.2 Rate control 82
3.3.2.3 Hybrid mapping techniques . .82
3.3.2.4 Force scaling 85
3.4 Design of a stable, usable, and safe HBTS for precision tasks 85
3.4.1 System design 87
3.4.1.1 Feedforward haptic controller .88
3.4.1.2 Robot interaction control . . .90
3.4.1.3 Force feedback rendering 92
3.4.2 Experiments 94
3.4.2.1 Force/torque measure-based force feedback 97
3.4.2.2 Virtualized force feedback without references saturation 98

3.4.2.3 Virtualized force feedback with references saturation 100
3.5 HBTS for free-hand dental procedures 100
3.5.1 Background 102
3.5.1.1 Related works 104
3.5.1.2 Contributions 108
3.5.2 Preliminaries 109
3.5.2.1 Notation 109
3.5.2.2 Haptic device and robot reference frames 110
3.5.3 Methodology 111
3.5.3.1 Eye-hand coordination controller112
3.5.3.1.1 Engagement phase . .114
3.5.3.1.2 Human tremors filtering115
3.5.3.1.3 Eye-hand coordination116
3.5.3.2 Robot interaction control . . .119
3.5.3.2.1 Admittance model . .120
3.5.3.2.2 Free-hand force limitation strategy 120
3.5.3.2.3 Safety mechanisms and emergency stop protocols122
3.5.3.3 Haptic feedback controller . . .123
3.5.3.4 Integrated mechanical end-effector124
3.5.4 Technical validation 127
3.5.4.1 Experimental setup 127
3.5.4.2 Controller parameterization . .128
3.5.4.2.1 Admittance controller parametrization 128
3.5.4.2.2 Eye-hand coordination controller parametrization 129

3.5.4.2.3 Virtual feedback parametrization 130
3.5.4.3 Force limitation assessment . .131
3.5.4.4 Eye-hand coordination assessment133
3.5.4.5 End-to-end experimental demonstration 134
3.6 Clinical evaluation of the HBTS for free-hand dental procedures 138
3.6.1 Study design 140
3.6.2 Participants 140
3.6.3 Equipments and materials 141
3.6.3.1 Robotic teleoperation system .141
3.6.3.2 Dental model 142
3.6.4 Experimental procedures 143
3.6.4.1 Training protocol 143
3.6.4.2 Clinical procedure 143
3.6.5 Outcomes measures 145
3.6.5.1 Efficacy measurements 145
3.6.5.2 System safety and efficiency measurements 146
3.6.5.3 System usability assessment . .146
3.6.6 Statistical analysis 147
3.6.6.1 System efficacy 147
3.6.6.2 Execution times 150
3.6.6.3 Interaction forces 150
3.6.6.4 Questionnaire 150
3.6.7 Results 153
3.6.8 Discussion 156

4 Human supervisory control **159**
4.1 Control paradigms 160
4.1.1 Shared control paradigm 162

4.1.2 Discussion on level of autonomy 163
4.2 Human supervisory control paradigm 165
4.2.1 Components of human supervisory control167
4.2.2 Human supervisory roles and hierarchy .168
4.2.3 Modeling human supervisory control operations 169
4.2.4 Interface design for supervisory control .171
4.2.4.1 Multimodal display and control172
4.3 Control framework for dependable robotized bolting operations 173
4.3.1 Background 174
4.3.2 Methodology 179
4.3.2.1 Multimodal human-robot interface183
4.3.2.2 Active compliance control . . .184
4.3.2.3 Driving torque control 186
4.3.2.4 Manual control 186
4.3.2.5 High-level supervision 187
4.3.2.5.1 Bolt tightening pipeline188
4.3.2.5.2 Supervisor 189
4.3.3 Experimental validation 190
4.3.3.1 Experimental setup 191
4.3.3.2 Prevention of interaction faults191
4.3.3.3 Handling of vision system failures193
4.3.3.4 Handling of bolt driver failures194

5 Conclusions 197
5.1 Haptic teleoperation under time delays 197
5.1.1 Discussion 199
5.2 Improvements and limitations of novel haptic bilateral teleoperation systems 200
5.2.1 Haptic bilateral teleoperation system for precision tasks 200

5.2.2 Haptic bilateral teleoperation system for free-hand dental procedures 201
5.2.3 Discussion 204
5.3 Towards autonomy: human supervisory control206

List of Figures **209**

List of Tables **213**

List of Algorithms **215**

Acronyms **217**

List of Symbols **221**

Bibliography **225**

Abstract

Advanced robotics is a key pillar of the ongoing fourth industrial revolution, with robots now required to perform complex tasks that often involve physical interaction with humans. An effective deployment of physical human-robot interaction requires the fulfillment of safety and dependability requirements, ensuring a safe and predictable behavior even in the presence of faults or unforeseen events, as well as fostering human acceptance, which critically relies on the robot displaying human-like and transparent behaviors.

In this context, haptic teleoperation has emerged as one of the most advanced modalities of physical human–robot interaction, capable of extending human cognitive and manipulative capabilities into remote environments, and combining them with the skills of robots. The bidirectional nature of haptic bilateral teleoperation systems enhances the human situational awareness and the safety of the interaction, but also introduces several challenges in terms of stability and usability, arising from the strong coupling of the different entities and by the presence of unreliable network conditions in the communication channel connecting them. In such a scenario, this dissertation contributes to three fundamental aspects in the design of human-aware haptic bilateral teleoperation systems: haptic feedback rendering,

interaction control, and mapping and scaling techniques, with an emphasis on their integration to ensure safe and effective task execution.

A first contribution is the formal assessment of haptic teleoperation under time delays, highlighting how haptic feedback improves the safety of the considered task, increases human awareness, allowing to compensate for communication delays, and improves the usability of the system. When applied to a planetary manipulation tasks, haptic teleoperation enables the execution of the latter, requiring a high degree of accuracy, with a success rate 2.25 times higher than that of unilateral teleoperation systems, relying solely on visual feedback, almost nullifying the probability of failure due to exceeding a safety threshold in the exerted forces.

Building on this analysis, two novel haptic bilateral teleoperation systems for precision tasks are proposed. The first leverages a novel virtualized force feedback that enables a natural perception of contact states, increasing human operator awareness and system stability. Furthermore, it integrates an interaction force limitation strategy, to enhance task safety according to the current certification process of applications with physical human-robot interaction. The second, conceived for free-hand dental procedures, integrates the virtualized force feedback with an eye–hand coordination mapping strategy, enabling the human operator to perceive the motion correspondence between their movements and those of the end-effector observed in the view of an eye-in-hand camera, preserving manual dexterity and expertise. Such system leverages a novel force limitation strategy, ensuring procedural safety also in highly unstructured environments. Experimental validation of both systems demonstrates improvements in accuracy, safety, and usability of the

system, compared to state-of-the-art approaches. Furthermore, the haptic bilateral teleoperation system for free-hand dental procedures was clinically evaluated with 19 participants with different levels of experience in the dental field, who performed four dental scaling procedures on a resin model using the system equipped with an active dental scaler. The study confirmed the feasibility of the system for free-hand dental procedures and showed consistent performance across all user groups. Participants effectively completed the tasks and reported high usability and comfort, highlighting the potential of this system as a reliable and intuitive platform for both clinical and educational applications.

Finally, on the topic of human supervisory control, this thesis presents a novel control framework and a robotic system for dependable robotized bolting operations, integrating state-of-the-art components with a multimodal human-robot interface and a high-level supervisor orchestrating them. An experimental evaluation on a representative bolting task confirms that this approach enables dependable execution, reliable fault detection, and effective operator intervention. Overall, the results demonstrate that integrating human supervision with direct control capabilities enhances system safety and dependability.

In conclusion, the results achieved in this dissertation show that designing human-aware haptic teleoperation systems, with novel strategies for haptic feedback rendering, interaction control, mapping and scaling, significantly improves both safety and usability in interaction tasks, and paves the way for new approaches to transferring human knowledge to the robot, bridging the gap between direct human control and autonomous robotic behavior.

Chapter 1

Introduction

1.1 Context

In the early decades of the 21st century, humanity is witnessing the most disruptive transformation ever experienced, commonly recognized as the Fourth industrial revolution (4IR). First conceptualized in 2016 [1], the 4IR defines a complex phase of convergence in which digitalization, automation, and intelligent technologies are reshaping not only industries but also the broader socio-economic structures upon which society is built, driven by the fundamental pillars: *efficiency*, *automation*, and *human–machine interaction* [2].

In this scenario, the concept of Industry 4.0 (I4.0), first introduced in Germany in 2011 [3], represents the industrial embodiment of this revolution. Industries worldwide are rapidly adapting to align with competitiveness fostered by digitalization, by changing their business models and evolving into the so-called *smart factories*. Underpinning this evolution, previously separate domains, such as advanced robotics, cloud computing,

data management and artificial intelligence are now converging, mutually enhancing each other, under the guiding principle of *inter-connectivity*.

The labor market directly reflects this transition. With the integration of digitalized and highly automated systems, occupational categories are undergoing substantial restructuring [4]. Large-scale employment roles coexist with highly specialized technical positions, essential for designing, implementing, and maintaining automated production environments. Industries are thus led to balance the demand for highly skilled talents with the productivity gains offered by automation.

Consequently, this transition also requires a critical rethink of workforce education and training. Schools and corporate academies are increasingly focusing on interdisciplinary studies that combine engineering, computer science, and cognitive science to prepare the workforce for highly automated and intelligent production systems. At the same time, research trends are shifting toward human-centered robotics, cooperative artificial intelligence, and adaptive automation, where the emphasis is on creating systems that can interact with humans safely and effectively, continuously learning from ever-changing environments.

Among the main actors of 4IR, robotics plays a crucial role. Initially introduced as a driver of automation, robots have evolved from rigid systems for repetitive tasks into intelligent and interconnected systems equipped with perceptual abilities and adaptability, capable of actively collaborating with humans. This enhancement has extended robotics well beyond production lines, enabling its use in flexible and dynamic human-centered contexts that integrate both industrial and social applications.

According to the *International Federation of Robotics* [5] (2021), between 2015 and 2020, industrial robots recorded a cumulative

growth rate of +51% in terms of annual installations, with collaborative robots (cobots) increasing by 6%. A steady growth of +11% is expected for the period 2024–2027 [6]. In addition, to highlight the growing interest in the robotics market, the previous analyses also show a rapid expansion, over the same period, into several application domains, such as logistics (+35%), surgery (+36%), rehabilitation and assistance (+30%), and agriculture (+21%).

Indeed, beyond the industrial domain, robotics is increasingly applied to address social challenges such as workforce shortages and population aging. In many countries, where the working-age population is expected to decline dramatically in the coming years, robotics is recognized as a necessary means to fill gaps in care and daily support. Robots capable of providing feeding assistance, mobility support, and monitoring can reduce the physical burden on caregivers while ensuring the continuity of essential services in societies undergoing demographic shifts.

Within healthcare, medical robotics has emerged as a transformative field. Surgical robots, rehabilitation systems, and teleoperated devices enable clinicians to perform procedures with extreme precision, reduce patient recovery times, and deliver specialized care to remote or underserved areas, thereby enhancing both the quality and accessibility of healthcare services.

Robotics has also found a critical role in scientific infrastructures, where precision, safety, and repeatability are essential. In large-scale laboratories or research facilities, robots are employed for tasks that would otherwise expose humans to hazardous environments or require levels of accuracy beyond human capabilities. From handling sophisticated instruments to support remote operations in high-radiation or high-risk environments, robots

contribute in advancing scientific progress while safeguarding human lives.

The aerospace sector represents another frontier for robotic applications. From orbital support to in-space manufacturing, planetary exploration, and potential forms of colonization, robotics enables missions that would otherwise be logistically or physically impractical for humans. In such scenarios, additional challenges arise, as efficiency and autonomy must be balanced with sustainability goals, particularly regarding energy consumption and the management of limited available resources.

1.2 Motivation and scope

What emerges from Section 1.1 is an extremely anthropocentric vision in which technological innovations from different domains converge to improve the quality of life of all individuals. The way in which this is taking place was unimaginable until a few years ago and involves not only the co-existence but also active collaboration and mutual assistance between humans and machines. This can be summarized by the word *human–machine interaction*, already mentioned in the discussion above as a pillar of the 4IR.

Human–machine interaction is a broad and multifaceted concept that takes on different modalities depending on the process in which it is required. It spans from the simple exchange of information through traditional user interfaces, such as keyboard, mouse, or touchscreen, to more sophisticated form of interaction between humans and robots in shared workplaces. Within this continuum lies one of the most advanced and challenging forms of human–machine interaction, i.e. *physical human-robot interaction (pHRI)*, characterized by direct physical contact,

entailing the exchange of forces and movements [7].

Typical examples include industrial processes where humans and robots share tasks and responsibilities, actively cooperating in the manipulation and transportation of shared objects. Beyond industrial settings, a key application is found in healthcare, where robots operate directly on patients or are physically connected to them, as in the case of rehabilitative robotics.

In general, regardless of the specific modality, pHRI relies on two fundamental requirements: *safety* and *dependability* [8]. Safety refers to the prevention of catastrophic consequences for the human, the environment, or the robot itself, even in the presence of failures, malfunctions or unexpected collisions. It is inherently related to principles of manipulator design, including mechanics, electronics, and control. Dependability is an integrated concept that encompasses a set of essential system attributes, including availability, reliability, safety, integrity, and maintainability. It reflects the degree to which the system continues to operate correctly even in the presence of faults or external disturbances. A dependable system is therefore one that, not only fulfills its intended functions in normal operation, but also maintains acceptable performance under degraded conditions, guaranteeing continuity and predictability of its behavior.

The relevance of these requirements becomes even more evident when considering fully autonomous robots. Indeed, despite the remarkable progress achieved by automation in recent years, current robotic systems are still far from reaching this level of autonomy, while fulfilling the requirements of dependability and safety, especially when operating in unstructured or unpredictable environments [9]. As a result, in most robotic applications, direct operation or supervision by a human operator remains, not only common, but often necessary. Humans provide

superior situational awareness, cognitive abilities, and problem-solving skills compared to the current capabilities of robots. In some cases, such supervision is strictly mandated by safety regulations or ethical considerations. A prominent example is surgical robotics, where the robot may enhance precision and dexterity, but the surgeon remains the ultimate decision-maker, fully responsible for the procedure.

Furthermore, the effective deployment of pHRI does not depend solely on technical robustness. Human acceptance represents a decisive factor, as several studies indicate that attitudes toward robots become more favorable when the latter exhibit limited autonomy [10]. Indeed, the more the robot appears independent in its decisions and actions, the greater the perceived risk and, consequently, the psychological resistance to physical contact. Conversely, when the robot is perceived as an equipment, operating under human decision-making and judgment, attitudes are significantly more positive [11]. This phenomenon represents a significant barrier to the widespread adoption of pHRI and makes the design of human-like and predictable behaviors even more crucial, as they facilitate understanding and foster acceptance on the part of humans [12].

In other words, even the most advanced robotic systems require a certain level of human control. This naturally leads to the concept of *telerobotics*, which refers to a *human-in-the-loop* approach for the supervision and control of a remote robotic system. It involves a continuous exchange of information between the human operator and the remote robot. The nature of this information depends on the level of control given to the operator, or analogously to the level of autonomy of the robot.

Starting from the 1940s, researchers are putting up methodologies with the goal of defining and establishing a framework

for remote-controlling a robot within its environment. Remote control is intrinsically linked to the existence of a barrier, which can take on different extents: the remote environment could be inaccessible to humans for multiple reasons, such as its distance, as in the case of planetary missions, its hazardousness, as in the case of nuclear plants and deep-sea exploration, or scales beyond human capabilities. At the time this thesis is written, many techniques exist to tackle this matter, each of them assuming certain hypotheses, addressing some trade-offs, and proposing various solutions dealing with this particular problem, which is generally defined as *teleoperation*.

Since the first telerobotic systems, the field of teleoperation was revolutionized by the development of robotics and information technologies. This introduced new modalities of interaction between humans and remote robots, and expanded the application domain to many other fields. In such fields teleoperation is not merely a way to overcome a barrier, but becomes a means to enhance human manipulative capabilities, combining them with the efficiency and precision of robots. Furthermore, it opened the way to another promising field, *learning from human demonstration* [13]. Indeed, humans naturally combine vision and touch to generate effective policies, encapsulating human-likeness of movement and interaction. How humans achieve such policies remains an open question, and it is widely accepted to be the result of learning from experience. Consequently, developing models that can inspire solutions for implementing these control strategies in robotic systems remains challenging. In this context, teleoperation provides an effective shortcut to transfer these human-conceived policies to robots.

Merging the two aforementioned concepts of pHRI and teleoperation, one of the most promising open fields in recent times is

haptic teleoperation. The latter represents a particular modality of pHRI in which the interaction between the human and the robot, operating in a remote environment, is achieved through the exchange of motion commands and haptic feedback, which is displayed to the human operator through dedicated hardware, typically *haptic devices (HDs)*. Such bidirectional exchange is a double-edged sword. On the one hand, it allows the operator to perceive the remote interaction, thus enhancing situational awareness. This, in turn, provides substantial benefits in terms of both safety and dependability, by allowing immediate human reaction in the event of unforeseen contingencies. On the other hand, haptic teleoperation poses considerable challenges in terms of stability and control. As depicted in Figure 1.1, such systems, named *haptic bilateral teleoperation systems (HBTSs)*, involve multiple entities, i.e. controllers and actors. The former entail the remote robot controller and the teleoperation controller, while the latter involve the human operator, the HD, the communication channel, the remote robot, and the environment, whose dynamics are often unknown or uncertain. Such entities continuously influence each other through multiple feedback loops, resulting in a complex and highly coupled system. Indeed, although different solutions exist for unilateral remote control of robotic systems, no consolidated methodology has yet been established to adequately handle all these interactions, while simultaneously guaranteeing dependability, safety, and other requirements.

The focus of this dissertation is on the topic of *haptic teleoperation* for the execution of interaction tasks, which involve both physical interaction with other humans and with highly unstructured or not fully known environments. This dissertation assumes that delays, jitter, and packet losses in the communication channel are negligible, as is typical in healthcare and

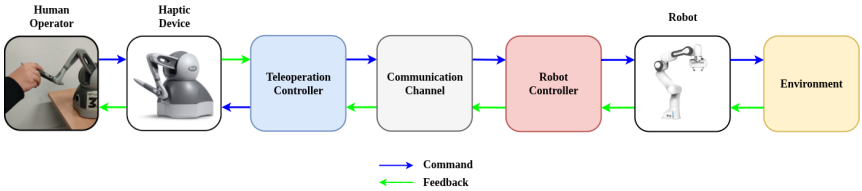


Figure 1.1: High-level scheme of a haptic bilateral teleoperation system.

scientific facilities, and that any system instabilities, resulting from such unreliable network conditions, are properly compensated by appropriate control methodologies. Such methodologies do not fall directly within the application domain of this thesis, which instead focuses on analyzing the impact of time delays on the task effectiveness.

In fact, when dealing with teleoperation, an essential factor that must inevitably be taken into account is the unreliable conditions of the communication channel linking the human operator with the remote robot. The hypothesis of a stable teleoperation system under adverse network conditions frequently holds. This is supported by the fact that numerous methodologies addressing this challenge exist in contemporary literature and have been extensively validated in realistic scenarios. A prominent example is provided by several space missions conducted by agencies worldwide, where robots on the Earth's surface have been teleoperated by astronauts in orbit.

Alongside network-related challenges, another critical factor must be considered. The bidirectional nature of a HBTS can potentially enable leveraging human expertise in the interaction with the surroundings, by recreating haptic cues they are used to from past experiences with the environment. However, this

depends on the accuracy, naturalness, and modality in which haptic feedback is rendered, a topic to which this dissertation devotes particular attention. Indeed, *haptic feedback rendering* (handled by the "teleoperation controller" in Figure 1.1) significantly affects the perception of the human operator, who acts not only as the system operator but also as the evaluator. Furthermore, haptic feedback is the primary source of system instability, with a dynamics strongly influenced by the remote robot-environment interaction.

For this reason, rendering an accurate and natural haptic feedback is not sufficient to ensure the fulfillment of all requirements. There is a strong need to control task execution with properly designed controllers, i.e. *interaction controllers* ("robot controller" in Figure 1.1), another topic of interest in this dissertation. Such controllers, in their standard design, can adjust commands sent to the robot to ensure compliant behavior during interaction with the environment. Advanced versions of interaction controllers introduce greater adaptive capabilities to satisfy more stringent performance indices.

In some cases, haptic feedback and control are not sufficient to make the system effective: it is necessary to appropriately convert human intentions into actual commands for the robot, ensuring that the observed behavior aligns with the operator's expectations, and that the action exerted is proportional to the task being performed. This transfer involves *scaling and mapping techniques* (also handled by the "teleoperation controller" in Figure 1.1), which must take into account not only the kinematic and mechanical aspects of the controlled robot, but also external factors, such as the presence of visual feedback provided by a camera.

Finally, although haptic teleoperation represents a form of direct

robot control by the human operator, it should not necessarily be regarded as an alternative to autonomy. In particular, for highly repetitive tasks, and with the aim of reducing the operator's cognitive load, it can be integrated into a higher-level paradigm, e.g. *human supervisory control*, in which the human acts as a supervisor of a robotic system, endowed with a certain level of autonomy. In such a configuration, system failures or unforeseen contingencies can be addressed manually by the human operator. This combination of autonomous execution and human supervision provides a higher level of robustness and dependability to the overall system.

This thesis contributes to the problem of the teleoperation of robotic manipulators, with a focus on haptic teleoperation, particularly through the investigation of haptic feedback rendering, interaction and human supervisory control methodologies, and the effect of time delays on system's performance. The main improvements on this field are briefly introduced in the following sections, and discussed in detail in the next chapters.

1.3 Objectives

Whether applied to industrial, medical, and space applications, haptic teleoperation deals with extending the cognitive and manipulative capabilities of humans into remote environments, combining them with the precision and efficiency of robots. Following the discussion done in Section 1.2, the control of a HBTS can be compared to that of a *complex system*. The emergent behavior of this system arises from the interactions of different entities, whose dynamics are strongly coupled and uncertain.

Within the application domain of haptic teleoperation, the

management of each entity, e.g. the HD, the remote robot, and the communication channel, has mostly been treated as an independent control problem. Unfortunately, in the attempt to maximize the performance of each, solving independent problems does not guarantee the achievement of the overall system's performance and requirements. More recently, the different problems have been combined and solved together, although, because of the problem's complexity, several trade-offs have been made. Providing a unified solution to the problem of haptic teleoperation, guided by the principles of stability, dependability, safety, and usability in real-world scenarios, is the objective of this dissertation. In order to address this issue, several gaps have been identified and addressed.

For instance, haptic feedback plays a key role in shaping the operator's perception and situational awareness, facilitating the exploitation of prior expertise in task completion. At the same time, it represents one of the main sources of instability due to the coupled dynamics of the system. The development of human-aware *haptic feedback rendering* methodologies has received particular attention in recent years, with the goal of making the sensory experience for the human operator as natural as possible. However, contemporary techniques still present several methodological and technical limitations, particularly in balancing naturalness with overall system stability.

On the other hand, *interaction controllers*, e.g. admittance controller and impedance controller, can regulate the robot motion in a compliant manner. The development of variable impedance controllers has recently emerged as a significant advancement in this field, with the aim of enhancing the performance of these controllers in terms of transient, overshoot, and steady-state force-tracking. Nevertheless, state-of-the-art controllers gener-

ally do not provide guarantees in terms of limiting interaction forces, which are necessary in the certification processes for pHRI applications.

Moreover, an effective teleoperation depends not only on feedback and control but also on the correct mapping of human intentions into robot actions. The literature offers numerous *mapping and scaling strategies* to address this problem, considering the kinematic constraints and mechanical structure of the robot. However, state-of-the-art strategies disregard how external factors, such as the presence of a camera providing visual feedback, may influence the consistency between the operator's expectations and the actual behavior of the robot.

Given the identified gaps, the specific objectives and contributions of this thesis lie in the proposal of novel techniques across all these areas, with particular attention to their integration, in order to achieve satisfactory overall system performance. In particular, this dissertation, after analyzing the impact of time delays on task effectiveness, puts forward two novel HBTS for the execution of precision tasks. These systems leverage novel haptic rendering, interaction control, and mapping strategies to fulfill the aforementioned requirements.

Furthermore, evaluating the impact of the integration of such systems, both in terms of robustness and dependability, within higher-level architectures where the controlled robot exhibits increased autonomy, is another objective of this dissertation.

A more thorough examination of the thesis contents can be found in the subsequent section.

1.4 Outline

The content of this dissertation is organized in chapters addressing the problems described in Section 1.3. The chapters share a common structure. Each of them introduces the particular topic under study, discusses the state-of-the-art methodologies tackling the related research issues, and presents elements of novelty in the area, supported by experiments conducted on real robotic platforms. The remainder of the thesis is summarized as follows:

- Chapter 2 presents an overview of teleoperation architectures, with a particular focus on control approaches to manage unreliable network conditions. These serve as a fundamental ingredient to compensate for the instabilities induced by the communication channel.
  - The contribution presented in this subject is the assessment of task execution in a teleoperation scenario, in which time delays are not compensated by the aforementioned control approaches.
- Chapter 3 elaborates on the topics of interaction control, haptic feedback rendering, and mapping and scaling techniques, to be implemented with the aim of developing teleoperation systems that ensure safety, effectiveness, and naturalness for the human operator. The novelties introduced in this subject are as follows:
  - A haptic bilateral teleoperation system, exploiting virtualized force feedback and interaction force limitation strategies to enhance task safety and operator comfort.
  - A haptic bilateral teleoperation system for free-hand dental procedures, combining an eye-hand coordina-

tion mapping strategy that provides motion correspondence between the operator's movements and those of the robot, as observed in the camera view, and a novel force limitation strategy, to ensure a natural teleoperation experience and procedural safety.

  - A clinical evaluation of the previous system in a scaling and root planing procedure with an active dental scaler, conducted by dentists on a realistic dental phantom.

- Chapter 4 discusses the topic of human supervisory control, i.e., the high-level teleoperation paradigm to supervise and command a semi-autonomous robotic system, aimed at reducing the human operator's cognitive load.
  - The contribution presented in this subject is a control framework enabling dependable robotized bolting operations, integrating state-of-the-art components responding to specific requirements of autonomy, flexibility and fault tolerance, and a supervisor to orchestrate them.
- Chapter 5 concludes the thesis, summarizing the main achievements, describing the limitations of the proposed methodologies, and outlining possible improvements to be addressed in future research.

Chapter 2

Haptic teleoperation under unreliable network conditions

HBTSs rely on a bidirectional communication channel that couples the human operator with the remote robot. While this channel enables an effective pHRI, it also can compromise both stability and usability of the system, due to unreliable network conditions, i.e. time delays, jitter, and packet losses, it is subjected to.

A fundamental requirement for the success of any teleoperation task is the capability to manage such unreliable network conditions. To that aim, several control approaches are used, ranging from *passivity-based* to *model-based control approaches*. They mainly differ in that the former do not compensate for any communication delay, but rather enforce stability in the presence of such delays; the latter virtually eliminate time delays by shifting the interaction to the local site by virtual modeling the remote

environment. Alongside these, contemporary literature offers numerous innovative solutions that combine the advantages of both approaches. The majority of these approaches have proved effective in real-world teleoperation contexts, e.g. space experiments conducted by agencies worldwide, better described in Section 2.3.1.

Within this context, it becomes relevant to evaluate how adverse network conditions, if not properly handled, affect the teleoperation experience. Of particular significance is the assessment of how the presence of haptic feedback, as opposed to unilateral teleoperation systems, may influence the human operator's ability to compensate for delays and the overall effectiveness of control.

The remainder of this chapter is structured as follows:

- Section 2.1 presents the design requirements of a HBTS, highlighting their conflicting nature through the analysis of the main state-of-the-art architectures.
- Section 2.2 illustrates the main control approaches for handling unreliable network conditions, emphasizing their advantages and limitations.
- Section 2.3 elaborates on the effects of time delays on the teleoperated task effectiveness. This section introduces an original contribution [14], which proposes a formal assessment of the haptic teleoperation for planetary manipulation tasks.

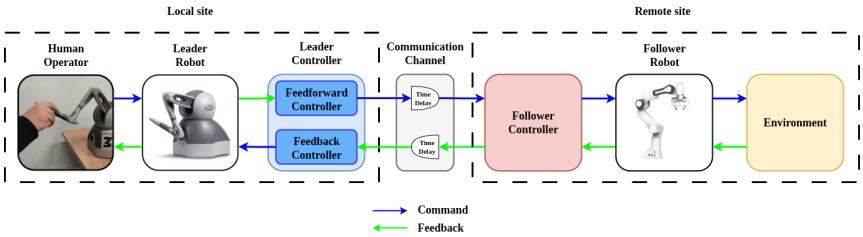


Figure 2.1: Low-level scheme of a haptic bilateral teleoperation system.

2.1 Haptic bilateral teleoperation architectures

A HBTS is a typology of teleoperation system, in which the human operator directly controls the remote robot while perceiving haptic feedback, representative of the remote robot–environment interaction. As mentioned in Section 1.2, it is always possible to identify a barrier between the human operator and the remote robot that needs to be overcome by the system.

On one end of this barrier is the *local site*, which encompasses the human operator and all the sensory and command interfaces which connect them to the remote robot. The human-machine interface that the human operator interacts with, e.g. a HD, is referred to as the *leader robot (LR)*. On the other side is the *remote site*, which includes the robot to be controlled, the supporting sensors and control elements, as well as the environment it interacts with. In literature, the remote robot is usually referred to as the *follower robot (FR)*.

As shown in Figure 2.1, the design space of the leader controller of a HBTS lies in the definition of two control laws, that couple the LR and FR dynamics, while complying to a given set of

control requirements.

2.1.1 Requirements of a haptic bilateral teleoperation system

The ultimate goal of a HBTS is enabling the human operator to experience *telepresence*, defined not only as *the ability to manipulate the remote environment*, but also *to perceive it as if directly encountered* [15]. This is only achievable if the human operator is provided with enough sensory information, displayed in a natural way to feel sense of immersion in the remote environment, and the system meets certain performance indices and requirements [16].

Among these, three are rooted in control theory, namely *stability*, *passivity* and *transparency*, while a third one focuses on practical aspects, namely *usability*. The latter is not formally recognized as a requirement of a HBTS in the literature. However, in order to evaluate the effectiveness of a HBTS, it is introduced and formally defined in this dissertation. These requirements will be discussed in the following sections.

2.1.1.1 Stability

While HBTSs represent the greatest promise for telepresence, they pose some of the biggest *stability* problems. As mentioned in the previous sections, one key intuition for understanding the sources of these instability issues is that the interconnection of the human operator, the LR, the FR and the environment is a complex dynamic system with multiple feedback loops.

In particular, the closure of the leader-follower loop via haptic feedback is the primary source of instability. This holds particularly for specific feedback modalities, which are discussed

in detail in Chapter 3. A second loop is closed in the interaction between the human operator and the LR at the local site. However, while the dynamics of the LR are typically well characterized, those of the human operator remain unknown and can exhibit considerable complexity. In fact, the human operator is an active system which can cause instabilities in the HBTS. A third loop is closed in the interaction between the FR and the environment at the remote site. The dynamics of this loop are usually unknown, as teleoperation systems are often deployed to interact with unknown environments. In order to guarantee the stability of this control loop under different operating conditions, impedance control strategies are often used to control the interaction between the FR and the environment [17].

Furthermore, a well-known source of instability in HBTSs is the presence of a time delay in the communication channel. The stability analysis is even more complicated when considering a communication channel which presents non-deterministic effects such as jitter and packet losses. In light of these factors, a typical tool to solve this limitation is the concept of *passivity*, which examines the energy flows in a system and makes stability assertions if energy is dissipated instead of generated, that is, if the system is passive.

2.1.1.2 Passivity

Passivity is an input–output property of dynamic systems which originated in network theory [18]. A dynamic system with input vector $\mathbf{u} \in \mathbb{R}^m$, output vector $\mathbf{v} \in \mathbb{R}^m$ and state vector $\mathbf{x} \in \mathbb{R}^n$ is passive if there exists a *storage function* $S(x) : \mathbb{R}^n \mapsto \mathbb{R}$ such

that:

$$\int_0^T \mathbf{u}(t)^T \mathbf{y}(t)\, dt \geq S(\mathbf{x}(T)) - S(\mathbf{x}(0)), \quad \forall \mathbf{u}, T \geq 0. \tag{2.1}$$

Equation (2.1) has an intuitive physical interpretation: the system is passive if its absorbed energy is greater or equal than its stored energy from a given time $t = 0$. In other words, a passive system is a system which cannot generate energy on its own. Considering the system energy $E(t)$ as the storage function $S(x)$, the following passivity inequality can be obtained:

$$E(t) = E(0) + \int_0^t \mathbf{u}(\tau)^T \mathbf{y}(\tau)\, d\tau \geq 0, \quad \forall t \geq 0. \tag{2.2}$$

A relationship between passivity and Lyapunov stability can be established by employing the storage $S(x)$ as a Lyapunov function, hence passivity is a sufficient condition for stability.

The usefulness of passivity theory lies in the fact that interactions between physical systems can be effectively modeled with energy interchanges. Hence, the natural way for the control of interacting physical systems is using energy-aware control strategies [19]: passivity theory is the bridge between the stability of a system and its energetic properties. A common counter-argument to the use of passivity-based techniques for achieving the stability of a system is that they are too restrictive. Indeed, a passive system is a system that cannot generate energy, which is a very strong assumption. It should be noted that passivity gives only a sufficient condition for stability: a system can be stable without being passive. However, an important result of systems theory is that in the interaction between a system and an environment, stability with respect to an arbitrary passive environment is guaranteed if and only if the system is passive

[20]. As a passive system is stable with respect to any passive environment, passivity allows handling uncertainty in a very effective way, which is particularly useful in the context of the teleoperation, in which the environment is often unknown and unpredictable.

2.1.1.3 Transparency

Transparency is a measure of how well the system is able to convey to the user the perception of direct interaction with the environment [21]. In other words, a perfectly transparent system should make the impedance perceived by the human operator $Z_{to}(s)$ perfectly match the environment impedance Z_e(s):

$$Z_{to}(s) \equiv Z_e(s), \tag{2.3}$$

where the impedance Z_e(s) is a quantity relating the wrenches exerted by the FR on the environment $\mathbf{H}_e(s)$ to its twists $\mathbf{V}_f(s)$ in the Laplace domain:

$$\mathbf{H}_e(s) = Z_e(s)\mathbf{V}_f(s). \tag{2.4}$$

In the time domain, the exerted wrenches are formally defined as follows:

$$\mathbf{h}_e = \begin{bmatrix} \mathbf{f}_e \\ \mathbf{m}_e \end{bmatrix} \in \mathbb{R}^{6\times 1}, \tag{2.5}$$

where $\mathbf{f}_e \in \mathbb{R}^{3\times 1}$ and $\mathbf{m}_e \in \mathbb{R}^{3\times 1}$ represent the forces and moments exerted by the FR on the environment, respectively.

On the other hand, the twist is defined as follows:

$$\mathbf{v} = \begin{bmatrix} \dot{\mathbf{p}} \\ \boldsymbol{\omega} \end{bmatrix}, \in \mathbb{R}^{6\times 1}, \tag{2.6}$$

where $\dot{\mathbf{p}} \in \mathbb{R}^{3\times 1}$ and $\boldsymbol{\omega} \in \mathbb{R}^{3\times 1}$ represent the linear and angular velocities, respectively.

The condition in (2.3) is not trivial to guarantee in practice, especially in the presence of time delays and other adverse network conditions, which give rise to a discrepancy between the interaction perceived at the local site and the one effectively occurring at the remote site. Indeed, it is well-known that transparency and stability are conflicting requirements in HBTS, similarly to the balance between transient response and stability in a control system [22].

Building on this premise, transparency is usually treated as a secondary requirement with respect to stability: occasional losses of transparency are often deemed acceptable to keep the system stable.

2.1.1.4 Usability

Although transparency and stability represent fundamental requirements for the proper operation of a HBTS, they are not, by themselves, sufficient to guarantee an overall positive experience for the operator. Stability ensures that the interaction remains safe and free of uncontrolled behaviors, while transparency enables a faithful perception of the interactions with the remote environment. However, a stable and transparent system may not necessarily be comfortable for the human operator, for example due to the modality and dynamics through which the haptic feedback is rendered.

For this reason, a HBTS must also be evaluated in terms of *usability*, defined, according to ISO 9241-210 [23], as *the extent to which a system can be used by specified users to achieve specified goals with effectiveness, efficiency, and satisfaction in a specified context of use*.

Applied to HBTSs, usability can be broken down into the fol-

lowing requirements:

- *effectiveness*: the system's capability to ensure that the operator can accomplish the task with success;
- *efficiency*: the degree to which tasks can be completed with minimal deployment of temporal, physical, and cognitive resources;
- *ease of use*: the degree to which the system can be readily understood and used by a human operator, reducing the need for extensive training;
- *naturalness*: the degree to which interaction with the system accurately mirrors human perceptual and motor modalities, thereby allowing prior manual task experience to be exploited.

Only by integrating these requirements is it possible to ensure that the system is truly usable in complex real-world scenarios.

All the experiments described in this thesis, including those in this and other chapters, foresee the evaluation of the proposed systems using these quality criteria, appropriately translated into quantitative and/or qualitative performance metrics.

2.1.2 State-of-the-art architectures

In this section, the main haptic bilateral teleoperation architectures, representative of the state-of-the-art are presented. Each subsection is dedicated to a specific architecture, analyzed in terms of its operation, advantages, and disadvantages.

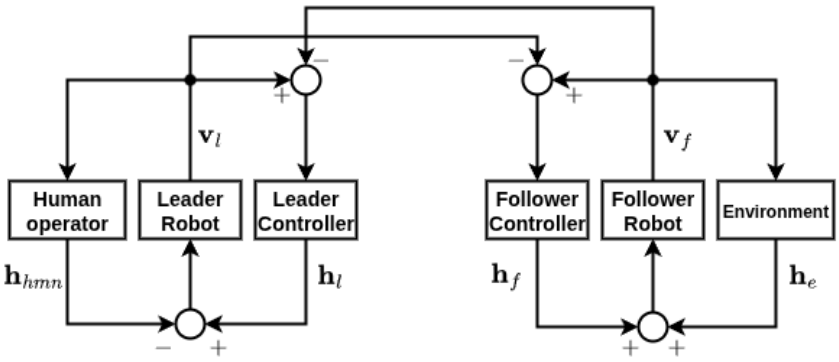


Figure 2.2: Position-position architecture.

2.1.2.1 Position-position architecture

In the simplest case, both the leader and follower robots are controlled to track each other. This architecture is known as the *Position-position (P-P) architecture*, shown in Figure 2.2, and can be described by the following PI control laws:

$$\begin{aligned} \mathbf{h}_l &= -\mathbf{K}_l(\mathbf{x}_l - \mathbf{x}_{ld}) - \mathbf{D}_l(\mathbf{v}_l - \mathbf{v}_{ld}), \\ \mathbf{h}_f &= -\mathbf{K}_f(\mathbf{x}_f - \mathbf{x}_{fd}) - \mathbf{D}_f(\mathbf{v}_f - \mathbf{v}_{fd}), \end{aligned} \tag{2.7}$$

where the subscripts l and f denote the LR and the FR, respectively, $\mathbf{h}_*$ is the control wrench, $\mathbf{x}_*$ and $\mathbf{x}_{*d}$ are the actual and desired robot poses, $\mathbf{v}_*$ and $\mathbf{v}_{*d}$ are the actual and desired robot twists, and $\mathbf{K}_*$ and $\mathbf{D}_*$ are the diagonal matrices, containing the proportional and derivative gains.

The pose $\mathbf{x}$ is defined as follows:

$$\mathbf{x} = \begin{bmatrix} \mathbf{p} \\ \mathbf{\hbar} \end{bmatrix}, \tag{2.8}$$

where $\mathbf{\hbar} \in \mathbb{H}_1$ is the quaternion representing the orientation and $\mathbf{p} \in \mathbb{R}^{3\times 1}$ is the position.

This architecture is simple to implement and requires no force/torque (F/T) sensors. An intuitive physical interpretation of the P-P architecture can be given by considering the LR and FR as two masses connected by a spring-damper system, regulated by the PI control laws. This interpretation has two immediate consequences. First, the P-P architecture is inherently stable, as the dynamics of the coupling between the two robots is intrinsically passive. Second, the P-P architecture is not transparent, as the control law in (2.7) defines a virtual impedance on the leader side $Z_{to}(s)$ which is not equal to the environment impedance Z_e(s). In particular, the wrenches displayed to the human operator depend on the tracking error between the LR and FR, which is influenced not only by the environment wrenches $\mathbf{h}_e$, but also by the controlled robot dynamics. In other words, with the P-P architecture, the human operator feels the wrenches associated with the spring-damper system connecting the LR and FR, which are not null even when the FR is not interacting with the environment. The displayed wrenches also depend on the particular choice of the control gains $\mathbf{K}_l$ and $\mathbf{D}_l$.

2.1.2.2 Position-force measured architecture

In the *Position-force measured (P-Fm) architecture*, shown in Figure 2.3, the FR is controlled to track the position of the LR, while the LR is controlled to directly render $\mathbf{h}_e$. Such architecture is described by the following control laws:

$$\begin{aligned} \mathbf{h}_l &= \mathbf{h}_e, \\ \mathbf{h}_f &= -\mathbf{K}_f(\mathbf{x}_f - \mathbf{x}_{fd}) - \mathbf{D}_f(\mathbf{v}_f - \mathbf{v}_{fd}). \end{aligned} \tag{2.9}$$

It is one of the most common architectures in HBTSs, as it allows achieving better transparency than the P-P architecture,

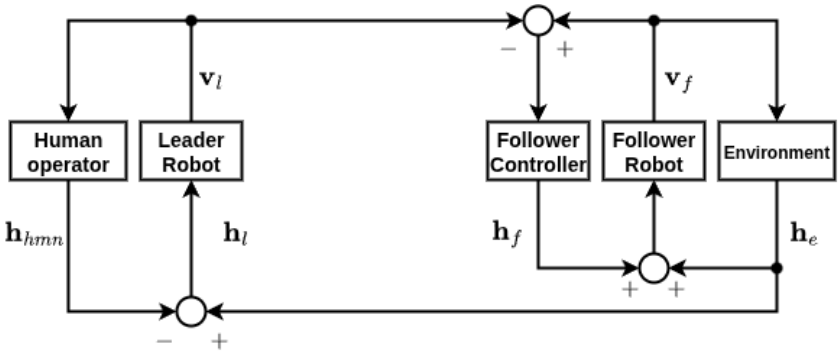


Figure 2.3: Position-force measured architecture.

as the human operator feels only $\mathbf{h}_e$. One drawback is that it requires the measurement of the wrench via a F/T sensor mounted at the FR's end-effector. On the other hand, the P-Fm architecture is not passive, which does not allow guaranteeing the stability of the system. A common approach to stabilize the P-Fm architecture is to passivize the teleoperation system using passivity-based control approaches. The comparison between the P-P architecture and the P-Fm architecture clearly highlights the trade-off between transparency and stability in HBTS.

All the HBTSs described in this thesis, including the ones in this and other chapters, build upon both the P-P and P-Fm architectures.

2.1.2.3 Position-force computed architecture

In the *Position-force computed (P-Fc)* architecture, shown in Figure 2.4, the FR is controlled to track the pose of the LR, while the latter is controlled to render the opposite of the wrenches computed by the leader controller. This architecture is thus

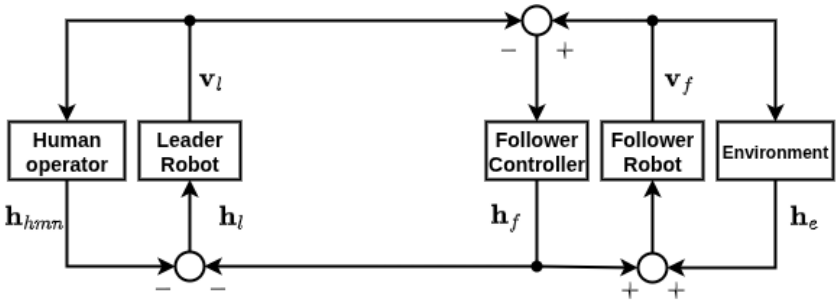


Figure 2.4: Position-force computed architecture.

described by the following control laws:

$$\begin{aligned} \mathbf{h}_l &= -\mathbf{h}_f, \\ \mathbf{h}_f &= -\mathbf{K}_f(\mathbf{x}_f - \mathbf{x}_{fd}) - \mathbf{D}_f(\mathbf{v}_f - \mathbf{v}_{fd}). \end{aligned} \tag{2.10}$$

P-Fc architecture is very popular in literature as it is intrinsically stable like the P-P architecture, and does not require the measurement of $\mathbf{h}_e$, i.e. it does not require a F/T sensor mounted at the FR's end-effector. On the other hand, such architecture achieves a better transparency than the P-P architecture, as the human operator feels $\mathbf{h}_e$ as part of the opposite control wrench $-\mathbf{h}_f$. However, transparency is worse than the P-Fm architecture, as $\mathbf{h}_f$ also include the follower inertia and damping wrenches. Note that if the control gains $\mathbf{K}_*$ and $\mathbf{D}_*$ are chosen equal for both the LR and the FR, and neglecting time delays, the P-P and P-Fc architectures are equivalent.

2.1.2.4 3-channel Architecture

The P-Fm and P-Fc architectures can be merged in a *3-channel architecture* with hybrid force feedback, as shown in Figure 2.5. Such architecture is described by the following control laws:

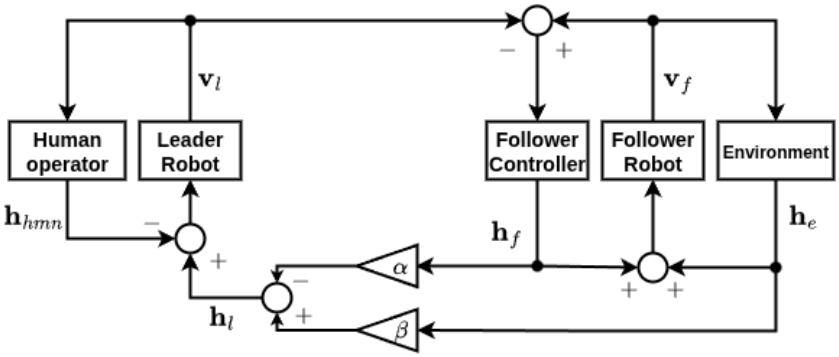


Figure 2.5: 3-channel architecture.

$$\begin{aligned} \mathbf{h}_l &= -\alpha \mathbf{h}_f + \beta \mathbf{h}_e, \\ \mathbf{h}_f &= -\mathbf{K}_f(\mathbf{x}_f - \mathbf{x}_{fd}) - \mathbf{D}_f(\mathbf{v}_f - \mathbf{v}_{fd}), \end{aligned} \tag{2.11}$$

where α and β are the gains of the linear combination of computed and exerted wrenches, respectively. Such combination can provide a high-fidelity haptic feedback, compared to previous discussed architectures [24], [25]. Furthermore, as the P-Fm architecture, this architecture requires the measurement of $\mathbf{h}_e$, and it is not inherently stable. Therefore, stability must be guaranteed via an appropriate control design.

2.1.2.5 4-channel Architecture

The *4-channel architecture* [21], shown in Figure 2.6 is a generalization of the previous architectures in which both pose and wrench signals are exchanged in both directions. With respect to the 3-channel architecture, the 4-channel also requires the measurement of the wrench exerted by the human operator on the LR $\mathbf{h}_{hmn}$, which acts as a feedforward term in the FR control

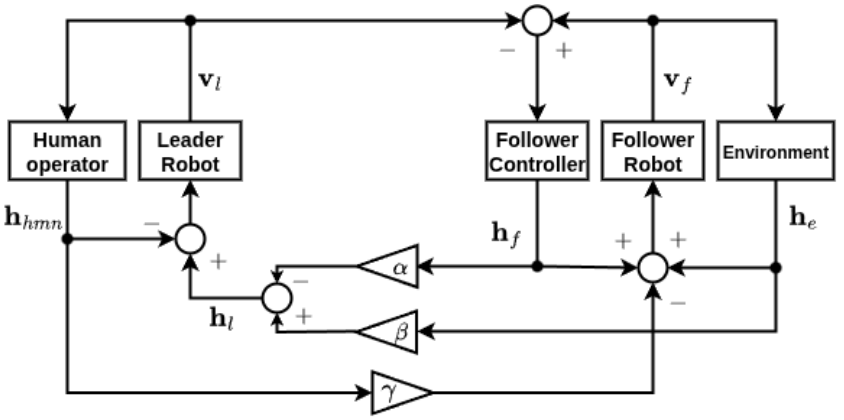


Figure 2.6: 4-channel architecture.

law:

$$\begin{aligned} \mathbf{h}_l &= -\alpha \mathbf{h}_f + \beta \mathbf{h}_e, \\ \mathbf{h}_f &= -\mathbf{K}_f(\mathbf{x}_f - \mathbf{x}_{fd}) - \mathbf{D}_f(\mathbf{v}_f - \mathbf{v}_{fd}) - \gamma \mathbf{f}_{hmn}, \end{aligned} \tag{2.12}$$

where γ is the gain of $\mathbf{h}_{hmn}$. Perfect transparency can be achieved in this architecture [26].

2.2 Control approaches for unreliable network conditions

At the beginning of Chapter 2, we discussed how several control approaches have been developed to compensate for the detrimental effects of unreliable network conditions. In this section, we analyze the main state-of-the-art approaches, ranging from passivity-based to model-based ones. It is important to note that these methods should not be regarded as specific implementations of either the leader controller or the follower controller.

Rather, they are conceived as parallel approaches, integrated as functional blocks at the ends of the communication channel, shown in Figure 2.1.

2.2.1 Passivity-based approaches

Given the importance of passivity in a HBTS, discussed in Section 2.1.1.2, this section analyzes the main passivity-based techniques operating in the time-domain, such as the *Time domain passivity approach (TDPA)* and the *wave-variables approach*, which are adaptive over time and thus less conservative than frequency domain approaches.

2.2.1.1 Wave-variable approach

Prior to 1989, the main challenge hindering progress in bilateral teleoperation was the instability caused by time delays. The pioneering work in [27] applies the notion of scattering variables, which is well-known in transmission line theory, to the problem of bilateral teleoperation. Two years later, [28] extends this work with the more general formulation of wave variables, applying a linear transformation to the wrench and twist variables to make the two-port communication lossless for arbitrarily large constant-time delays.

For instance, in P-Fc and P-Fm architectures, in which $\langle \mathbf{h}_l, \mathbf{v}_l \rangle$ represent the leader-side power port of the communication channel and $\langle \mathbf{h}_f, \mathbf{v}_f \rangle$ represent the follower-side power port, the wave variables are defined as:

$$\begin{aligned} \mu_l &= \frac{1}{\sqrt{2b}} \left(\mathbf{h}_l + b\mathbf{v}_l \right), \quad \mu_f = \frac{1}{\sqrt{2b}} \left(\mathbf{h}_f + b\mathbf{v}_f \right), \\ \nu_l &= \frac{1}{\sqrt{2b}} \left(\mathbf{h}_l - b\mathbf{v}_l \right), \quad \nu_f = \frac{1}{\sqrt{2b}} \left(\mathbf{h}_f - b\mathbf{v}_f \right), \end{aligned} \tag{2.13}$$

where b is the characteristic impedance of the communication channel. Transmitting the wave variables μ_l in the LR-to-FR direction and ν_f in the FR-to-LR direction, rather than the power variables, makes the communication channel lossless. When applying this transformation, the communication channel is physically equivalent to a distributed mass–spring system [17]. This has the advantage of making the exchange of information equivalent to physical dynamics and, therefore, passive and stable. However, this deteriorates the transparency of the overall system, because of this very same dynamics. Therefore, a modification of the approach is proposed in [17], in which the simple idea of exploiting the wave variables for storing the energy exchanged between the leader and the follower, while modulating the incoming power, is employed for reproducing a desired transparent behavior. To mitigate the distortion of transmitted waves caused by time-varying communication delays, [29] introduces a corrective wave, determined by the difference between the desired and the fictitious poses, obtained by integrating the variables of the undistorted wave. A common issue with the wave-variable approach is the phenomenon of wave reflection: an input wave variable is reflected and returned as an output wave variable. To overcome this issue, a 4-channel architecture is proposed in [30], [31], in which position, velocity, and external wrenches are transmitted separately through two modified wave transform schemes.

2.2.1.2 Time domain passivity approach

The TDPA is widely recognized as one of the most effective passivity-based techniques for HBTSs. The pioneering work in [32] introduces for the first time the *Time domain passivity control (TDPC)* technique, with the idea of passivizing any

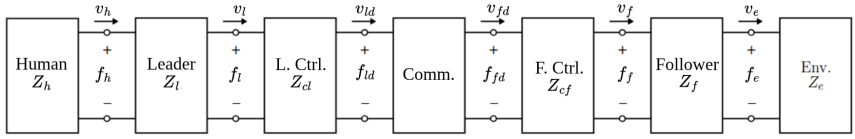


Figure 2.7: Network representation of a teleoperation system [33].

system by monitoring energy flows with a *passivity observer (PO)* and dissipating excess energy through a time-varying resistive element, the *passivity controller (PC)*.

Let consider the HBTS as a chain of two-port networks, as shown in Figure 2.7. In circuit theory, *two-port networks* are a special case of four terminal networks where the port condition is met in both pair of terminals. The PO can be defined as a discrete-time integrator of the power absorbed by the network:

$$E^{obs}(n) = T_s \sum_{k=0}^{n} (\mathbf{h}(k)\mathbf{v}(k)), \tag{2.14}$$

where n is the discrete time step, and T_s the sampling time. For each two-port network, if $E^{obs}(n) \geq 0, \forall n \geq 0$, the network is passive, according to (2.2). Whenever $E^{obs}(n) < 0$, the required amount of energy must be dissipated by a PC. Ensuring the passivity of the communication channel in a HBTS is therefore equivalent to guaranteeing that the energy of the corresponding two-port network satisfies $E^{obs}(n) \geq 0$.

The first application of the TDPA framework to bilateral teleoperation is proposed in [34], and later extended to time-delayed scenarios in [35]. After several iterations led by Ryu and Artigas, they converge to the algorithm proposed by both authors, that is widely known as TDPA [36]. Such algorithm resolves one key problem that arises when trying to apply the original TDPC ap-

proach to time-delayed systems: the fact that the energy flowing in and out of the communication channel can not be measured at the same time on both sides of the channel. The solution proposed [36] is to split the energy flow into two components: LR-to-FR and FR-to-LR, and to ensure that both flows are passive by employing communicating POs and a PCs on both sides of the channel. One of the major drawbacks of this approach is the position drifting that occurs when a commanded velocity is modified by a PC. To mitigate this effects, [37] introduces a technique to actively injecting energy into the system while preserving passivity. Moreover, in [38] is proposed the *Time domain passivity networks (TDPN)* framework to simplify the modeling of complex teleoperation architectures and extend TDPA to time-delayed systems. To reduce the conservatism of TDPA, [39] links TDPA with the energy tank framework and proposes a unified approach where both the channel and the follower controller are passivized with a single energy tank. This reduces position drifting, although its applicability is mainly restricted to P-Fc and P-P architectures. Building on these developments, [40] introduces the *Time domain passivity approach with high delay (TDPA-HD)* for the P-Fm architecture, employing two PCs to passivize the communication channel, by enforcing passivity only on the upper network branch. Such approach improves both position tracking accuracy and transparency in presence of high time delays, while reducing execution time and unintended impacts.

2.2.2 Model-based approaches

Passivity-based approaches discussed in the previous section, allow handling uncertain environments with time delays of up to 3 s [41]. However, teleoperation with such a significant delay

is still demanding for the human operator, as they are required to adapt to the delayed feedback. To overcome this limitation and make teleoperation possible also with higher time delays, model-based techniques for the design of HBTSs have been proposed in literature. The following sections are dedicated to the most relevant state-of-the-art approaches.

2.2.2.1 Model-mediated teleoperation

The *Model-mediated teleoperation (MMT)* is introduced in [42] as an alternative strategy to passivity-based approaches to deal with high communication delays. In MMT, a virtual model of the remote environment is estimated at the remote site, based on the data collected in the interaction between the FR and the surrounding environment. Instead of directly exchanging haptic cues, the estimated model, consisting of both the object geometry and the estimated physical properties, is transmitted back to the local site. On such site, a copy of the virtual model is reconstructed accordingly. Therefore, the human operator can haptically interact with the local model without any perceived delay. For these reasons, MMT is also known in literature as *virtual-reality-based* [43]. The main challenge of this approach lies in environment modeling and continuous model updates, which are required to avoid mismatches. Instabilities can arise during model transitions or when interacting with non-homogeneous environments, as the haptic feedback is only indirectly related to the actual remote interaction [44]. To address these issues, both parametric and non-parametric identification techniques have been proposed in literature, often combined with advanced haptic rendering algorithms [45], [46]. Despite these efforts, model jumps and rendering instabilities remain the major drawbacks, motivating the design of

passivity-preserving update strategies [47].

2.2.2.2 Model-Augmented Haptic Telemanipulation

Model-augmented haptic telemanipulation (MATM) is a novel approach for HBTSs proposed in [48] which aims to combine the convenience of traditional bilateral teleoperation schemes with the advantages of MMT and the shared autonomy paradigm, discussed more in detail in Chapter 4. Instead of splitting the HBTS in two decoupled loops as in MMT, this approach builds on a traditional teleoperation architecture, as the ones proposed in Section 2.1.2. The HBTS is made robust to time delays and packet losses with any of the techniques discussed in Section 2.2.1, and augmented with both a local model of the remote environment to generate augmented haptic feedback and a remote model to enable shared autonomy. Therefore, the feedback that is rendered on the HD is a combination of both the interaction with the remote environment and the local model. For this reason, this architecture can be seen as a generalization of the MMT architecture in which the FR has a higher level of autonomy. A concrete application of the MATM to overcome some of the limitations of the TDPA-HD is proposed in [49], where a local model of the remote environment is used to generate a virtual force feedback for the operator, which is then combined with the interaction forces measured at the remote site.

2.3 Assessment of haptic teleoperation under time delays

As mentioned at the beginning of Chapter 2, handling unreliable network conditions is critical for the correct operation of a HBTS.

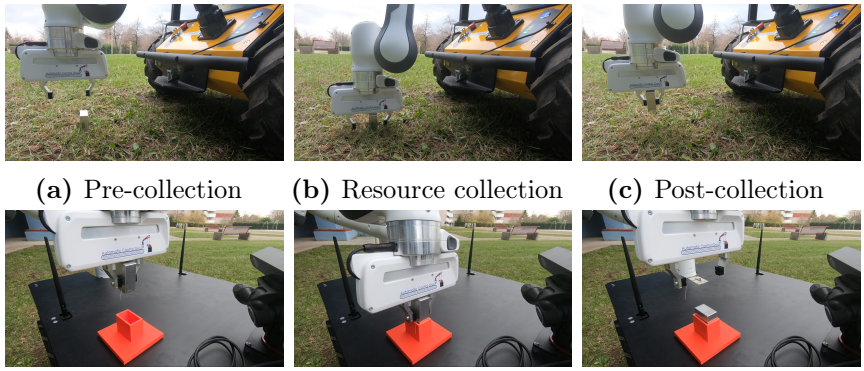
In Section 2.1.1, we have seen the fundamental requirements of a HBTS, namely *stability*, *passivity* and *transparency*, emphasizing how unreliable network conditions may hinder their fulfillment. In Section 2.1.2, we highlighted their conflicting nature by analyzing the main state-of-the-art haptic bilateral teleoperation architectures. Furthermore, in Section 2.1.1, we introduced an additional requirement, *usability*, recalling that the fulfillment of the former does not guarantee that the system can be effectively employed in complex real-world scenarios. Finally, in Section 2.2, we analyzed the advantages and limitations of the main state-of-the-art control approaches for handling unreliable network conditions. The discussion has revealed that the primary focus of such approaches lies in ensuring stability and/or transparency, whereas usability aspects are frequently neglected.

Therefore, in [14] we perform a formal assessment of haptic teleoperation under time delays in a manipulation task. The work proposes a new concept of operations and associated human-robot interface to assist human operators in the control of remote robotized systems for planetary missions. Through the rehearsal across multiple trials of a peg-in-hole manipulation task, we assess how the haptic feedback influences the usability of the system, in terms of task effectiveness, even in the presence of time delays, and in terms of ease of use. The results of the execution of the aforementioned task are reported in Section 2.3.3.

2.3.1 Background

Many space agencies and organizations around the world have a long-term objective of sending humans into deep space to explore destinations like Mars and beyond. Such a challenging goal requires intensive study in terms of evaluating possible scenarios, strategies, architectures, and mission elements [50], as well as solid international cooperation and collaboration. An innovative effort in this direction is National Aeronautics and Space Administration (NASA)'s Artemis program [51], which by 2024 plans to land the first woman and the next man on the lunar South Pole, establishing a sustainable infrastructure on the surface [52] and in the lunar orbit [53], [54]. This will enable the crew to spend more time and explore more of the Moon than ever before, gaining invaluable knowledge and experience for future human missions.

One key aspect of space exploration and colonization is the use of resources that are available on other celestial bodies, a practice defined as *in-situ resources utilization (ISRU)*, an example of which is shown in Figure 2.8. The use of in-situ resources can significantly reduce the cost of logistical challenges of space exploration and colonization by allowing for local production of rocket fuel, extraction of water, and mining of minerals and other materials for use in construction and manufacturing. Accessing, extracting, and using such resources can be particularly dangerous for humans because of the hostile environments on the surface of extraterrestrial planets. For this reason, a common solution for achieving such goals is the use of telerobots. They have been used since the earliest space missions and allowed performing a range of works to increase the productivity of space exploration. Because of communication delays, space agencies have been working to develop robots that can be re-



(a) Pre-collection **(b)** Resource collection **(c)** Post-collection

(d) Pre-utilization **(e)** Resource utilization **(f)** Post-utilization

Figure 2.8: Example of ISRU mission operations pipeline [55].

motely controlled on the surface of planets by astronauts in orbiting spacecrafts rather than ground stations on Earth.

First, NASA and European Space Agency (ESA), with the Human exploration telerobotics (HET) and Multi-purpose end-to-end robotic operation network (METERON) projects, respectively, conducted teleoperation experiments of robots on Earth by astronauts orbiting in the International Space Station (ISS) [56]. The METERON Haptics experiments investigated the effects of microgravity on haptic feedback perception using a 1-degree of freedom (DoF) force-feedback joystick to teleoperate a robot on Earth from the ISS [57]. The experiments demonstrated the absence of significant alterations in flight when compared to ground data, hence the feasibility of bilateral control with force feedback, with time delays in the order of 820 ms [58]. Using the same experimental setup, the METERON Interact experiment employed force-feedback teleoperation to complete a sub-millimeter peg-in-hole task [59]. During the experiment, the astronaut was supported by visual markers and predictive

video information of pending commands.

During the experiments of the KONTUR-2 mission [60]–[62], astronauts used a 2-DoF force-feedback joystick to control surface robots and feel the forces of interaction with the environment, using an Earth-ISS communication link characterized by a latency of 20–30 ms. The bilateral control, based on the TDPC, used during the experiments, enabled stability and performance even in the presence of jitter and data losses, demonstrating the effectiveness of haptic teleoperation with force feedback for deploying robots in prior unknown situations, even with delays up to 1 s.

More recently, during the Analog-1 experiments, a mobile manipulator was commanded on Earth, via a 6-DoF force-feedback HD, to complete a rock-collecting task [40]. The experiment demonstrated the effectiveness of haptic telemanipulation even with a constant communication delay of about 850 ms.

Parallel to the investigation of haptic teleoperation, METERON SUPVIS-E and METERON SUPVIS-M experiments explored supervised autonomy as a modality of telerobotic control. In this context, the operational concept was based on the employment of intuitive graphical user interface (GUI)s to perform teleoperation with task-level commands [63], [64]. This concept offers two main advantages: it ensures the reliability of teleoperations even in the presence of extreme delays in the communication link, and reduces the physical and mental workload of astronauts during teleoperation phases, significantly facilitating the training of new inexperienced operators [65]. More recent developments of this operational concept integrated haptic teleoperation as a modality of robot commanding, allowing astronauts to complete complex tasks where human cognitive capabilities and operational flexibility and dexterity are crucial [66].

Carrying out such activities effectively requires expertise and long training sessions for astronauts [67]. In particular, missions with robotic co-workers often require additional training of astronauts, often supported by hardware-in-the-loop virtual reality (VR) simulation systems [68]. Motivated by this, in the present work, we specifically target those elements of typical teleoperation systems that negatively affect the ease of learning and use. Then, we propose a new operational concept and associated human-robot interface to overcome such limitations.

In haptic teleoperation, usability is mainly affected by command mapping between the HD and the FR. In position mapping, 1:1 (or lower) scaling is paramount for accurate operations, but the FR's task space is confined to be not larger than the HD's, which limits the manipulator's reachability. On the other hand, mapping the HD's velocity, or adopting a workspace-extending position scaling would negatively affect accuracy and ease of use, both for precision and large movements. In this work, we tackle this trade-off by designing a set of software tools, supporting an operational concept where the FR task space, subject to 1:1 position mapping (*kinematic mapping* in Section 3.3.2.1), is extended through offline-planned point-to-point trajectories. Therefore, through the alternation of haptic teleoperation and autonomously planned collision-aware trajectories, we aim at facilitating the accomplishment of mission goals, simplifying training procedures, and reducing the learning time for new operators without previous experience with robotic teleoperation. Supported by quasi-real-time visual and force feedback, as well as suitable planning tools integrated into an all-encompassing human-robot interface, the operator can complete our validation objectives with ease, which consist in fetching a resource from the planetary soil and assembling it on board.

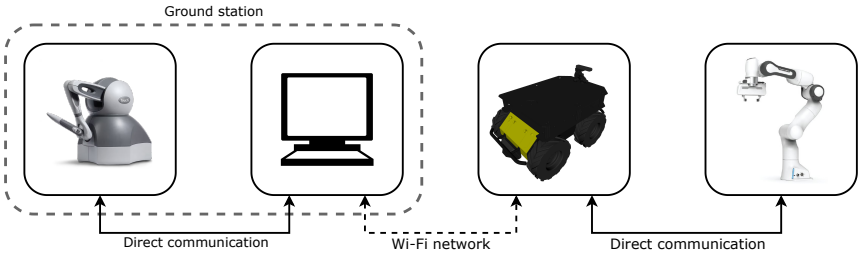


Figure 2.9: High-level overview of the system architecture.

2.3.2 Human-robot interface for haptic control in ISRU missions

2.3.2.1 System Design

We assume a typical system setup as in Figure 2.9, including a control station and two robots, which we term exploration robot (ER) and manipulation robot (MR), with the latter mounted on the former. Our MR is a Panda arm by Franka Emika [69] equipped with a two-finger gripper: it is the entity that physically interacts with the resource, actually performing the sample collection and assembly tasks. Our ER is a customized version of Husky by Clearpath Robotics [70]. It is a wheeled unmanned ground vehicle (UGV): it serves as an exploration agent that drives toward the resource to manipulate. It is provided with cameras framing the points in which fetching and assembly operations are performed.

The MR is subject to Cartesian impedance control. First, it guarantees stability, even in case of communication loss since, in case of missing references, the controller keeps tracking the last position received. Second, it prevents damage to the arm structure or the manipulated sample, as it adapts the received references to ensure safe interaction with the surroundings [71].

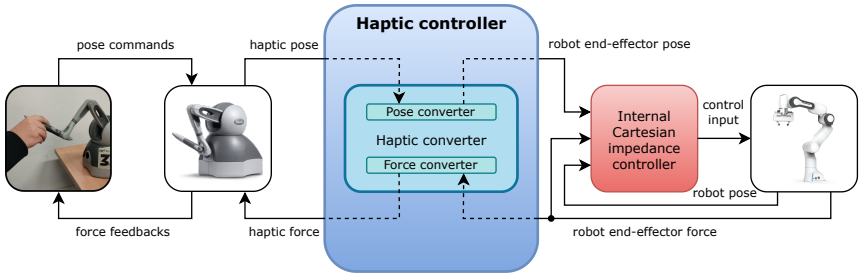


Figure 2.10: Haptic control system block scheme.

The control station features a workstation and a HD [72], with a stylus at its tip, installed in a laboratory, with the robots located outdoors. The control station communicates over a Wi-Fi network with the ER, which accounts for forwarding the commands to the MR through its onboard computer.

The proposed human-robot interface is made of two components, namely Haptic controller (HC) and Robot visualization & planning (RVP), whose name is inspired by [73]. HC establishes the mapping between the HD stylus' and robot end-effector's poses and renders at the stylus the force feedback perceived at the MR's flange so that they can be felt by the human operator. Its logic is illustrated in Figure 2.10, where arrows indicate the data flow between the human, the robot, and the HD. RVP supports autonomous planning and validation of trajectories and manages transitions from autonomous mode to haptic teleoperation. Their goals and functions are explained in Section 2.3.2.3 and Section 2.3.2.4, respectively, after introducing our mission operations concept in Section 2.3.2.2.

2.3.2.2 Mission Operations Concept

Our ISRU mission includes a peg-in-hole teleoperated task, in which the MR collects a metal parallelepipedon and places it in a 3D-printed slot, provided with a hole of the same size as the sample (tolerance: 0.002 m). During the whole experiment, the robot is placed outdoors and communicates remotely with the indoor ground station, hence the human operator can control the arm only via quasi-real-time visualization and teleoperation, monitoring the actual state of the mission through visual feedback consisting of the cameras' streams and 3D reconstruction of the robot state, both displayed in RVP.

The proposed mission operations concept consists of the following phases, illustrated in Figure 2.8:

1. *Pre-collection*: the MR moves in the proximity of the sample to collect. In our concept, it suffices that the sample is framed in the rear cameras, without a precise knowledge of its pose. Haptic teleoperation compensates for inaccuracies at the next step thanks to the visual feedback from the rear camera (an example is shown in Figure 2.11a). At the control station, this phase is supported by RVP, which assists the operator in planning collision-free trajectories.
2. *Collection*: the MR precisely moves to the actual sample location. This step is performed via HC: the human operator drives the robot towards a configuration where the gripper's fingers can safely close to collect the resource. Kinematic mapping allows for natural and accurate placement in a neighborhood of the resource, while the force feedback allows the user to feel the actual contact with the resource, thus inherently yielding a more reliable grasp and a safer motion. This phase ends when the MR closes



(a) Rear camera framing the sample in the collection phase



(b) Front camera framing the slot in the utilization phase

Figure 2.11: Onboard camera images during teleoperation.

the gripper's fingers, actually grasping the sample.

3. *Post-collection*: the MR retracts from the soil (or fetching location). In real scenarios, this phase possibly requires the ER to navigate toward a different location for resource exploitation.
4. *Pre-utilization*: the MR moves in the proximity of the location where resource utilization can happen, which possibly is in a different region of the MR's workspace. Thus, workspace extension is necessary, while human expertise is not required. The desired workspace extension is obtained by means of autonomous collision-aware planning through RVP.
5. *Utilization*: the MR inserts the resource in its assembly slot. Here, human expertise is crucial for safe and accurate assembly. Kinematic mapping, implemented by HC, with arm visualization from both cameras and the 3D model, implemented by RVP, help the operator guide the robot near the hole (as in Figure 2.11b). Then, by sensing the force feedback on the HD, they can have a natural and comfortable feeling of the hole's walls, which allows for

completing insertion with ease.

6. *Post-utilization*: the MR opens the gripper's fingers, releasing the sample inside its assembly slot and achieving the mission goal.

2.3.2.3 Haptic controller

In teleoperation through HDs, various scaling and mapping techniques have been proposed in the literature [74], such as position control and rate control. In rate control, the displacement of the HD is interpreted as a velocity command, while position control consists of some linear position mapping from the HD's tip to the robot's end-effector.

In our design for ISRU, we connect the LR and FR with kinematic mapping: this particular choice is especially important for the peg-in-hole task, as it yields the most direct, simple, and accurate transfer from human commands to robot motion. The linear mapping undergoes transformations to provide the user with the feeling of operating the MR from the ER cameras. Therefore, all displacements in the HD's workspace are relatively mapped in either rear or front camera frames (depending on the mission phase), so as to increase the naturalness of teleoperated control. In our design, the drawbacks of kinematic mapping, i.e. a limited workspace and slow motions, are compensated by the execution of autonomous trajectories.

Concerning forces, we adopt linear mapping to transfer the force sensed at the robot's end-effector, in the order of tens of Newtons, to the HD, so as to be in the order of units. This is crucial to naturally and successfully perform a contact-rich manipulation task.

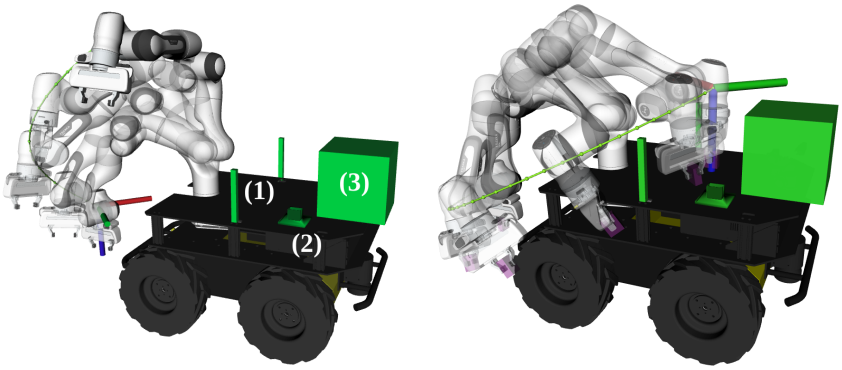
HC also features gravity compensation of the robot's payload,

as well as filtering of human tremors to generate stable poses for the robot and increase accuracy.

2.3.2.4 Robot Visualization & Planning

RVP is designed to accomplish three goals:

1. Visualize and assess the robot state, i.e. its joint configuration, in real-time. If the robot state is continuously updated and replayed in a 3D scene, the operator can assess the results of the commands, remotely sent from the control station. For complete awareness, cross-verification with camera streams is also possible through the RVP GUI.
2. Plan, rehearse, and validate point-to-point collision-aware trajectories during pre-collection (see Section 2.3.2.2, step 1) and pre-utilization phases (see Section 2.3.2.2, step 4). Eventually, the planned trajectories (depicted in Figure 2.12) are uplinked to the robot. This is the feature that allows extending the teleoperated robot's workspace: indeed, differently from [66], our human-robot interface, together with assisting the operator by providing visual feedback, allows combining accurate teleoperation positioning with a large workspace.
3. Manage the transitions between autonomous trajectories and teleoperation, i.e. support the operator in engaging the MR with the HD when its stylus' and the robot's end-effector's orientations match, as visible in Figure 2.13. This component is crucial to activating teleoperation at different workspace locations with ease; indeed, without a visual assistive tool, the engagement would be practically unfeasible.



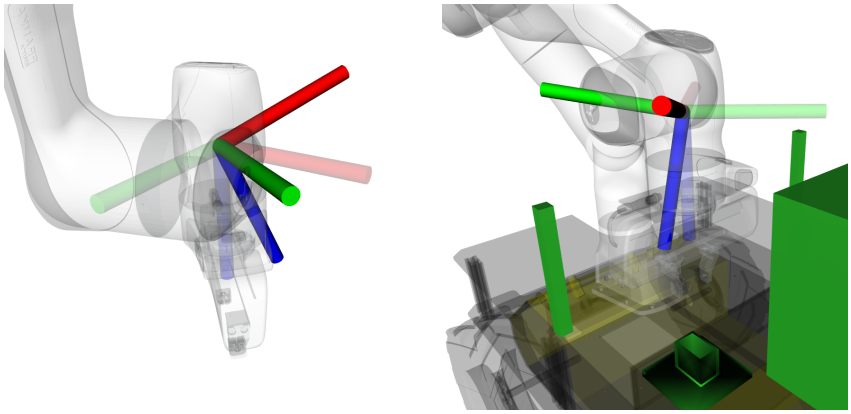
(a) Plan from initial configuration to fetching location

(b) Plan from fetching location to assembly location

Figure 2.12: Point-to-point trajectory planning in RVP. Together with ER and MR meshes, additional collision objects (in light green) are added to replicate (1) the ER's antennas, (2) the hole in which the sample is assembled, and (3) the front camera, modeled as a box to account for all possible orientations (being the front camera pair mounted on a passive pan-tilt unit, without encoders).

2.3.3 Results

This section reports the results of rehearsing the operations of Section 2.3.2 with the proposed human-robot interface. The end-to-end system is shown deployed in a remote ISRU mission in [55], while this section's focus is on performing a formal assessment of different aspects of the system. With the aim to confirm the impact of haptic control on mission operations, in Section 2.3.3.1 we compare trials with force and visual feedback with trials with visual feedback only. In Section 2.3.3.2, we



(a) Engagement at the fetching location

(b) Engagement at the assembly location

Figure 2.13: Engagement procedure in RVP. The HD moving frame is shown with solid colors, while the fixed robot's end-effector frame is displayed as shaded.

assess the end-to-end system in case of communication delays. Such trials are performed by the same experienced operator on the same day. The operator has previous experience with haptic teleoperation for robotic interaction tasks and interaction control in general and a deep knowledge of how to operate the MR.

Finally, in Section 2.3.3.3, we assess the ease of learning to use the system to achieve the intended goal. These trials are therefore performed by operators with some knowledge of robotics, yet without any expertise in either the specific task or haptic teleoperation in general.

All the trials are conducted in a controlled environment, i.e. a laboratory room (yet with the robot not in the view of the operator), with the workstation connected to the ER's wireless

Table 2.1: Success rate of the mission operations out of 20 trials in different scenarios.

Scenario	Force feedback	Delay d	Fetching	Assembly
A	✗	0 s	85%	40%
B	✓	0 s	95%	90%
C	✓	0.5 s	95%	90%
D	✓	1.0 s	95%	65%

network. For each trial, the parallelepipedon to collect (see Figure 2.11a) is approximately placed in front of the camera, with little variations of the samples' pose across the trials.

2.3.3.1 Haptic control assessment

The task to perform is composed of two human-driven sub-tasks (i.e., *Fetching* and *Assembly*), both requiring haptic teleoperation. With reference to the pipeline presented in Section 2.3.2.2, *Fetching* includes steps 2–3, while *Assembly* corresponds to steps 5–6. *Fetching* is considered successful if the object is stably grasped, and the arm is lifted with the sample firmly held by the fingers. *Assembly* is considered successful if the sample is assembled in its slot, and the fingers are open. If, in any sub-task, the measured forces exceed a safety threshold (above which the sample is considered as damaged), the MR controller stops and the *Task* is counted as failed.

We exercise the whole operational procedure 20 times excluding the haptic feedback (Scenario A), and 20 times including the haptic feedback (Scenario B); in the former case, the user can solely rely on visual feedback. The overall results are reported in Table 2.1 in terms of the success rate of the *Fetching* and *Assembly* sub-tasks.

The results show that considerable improvements are achieved when perceiving the forces: indeed, the *Assembly* success rate is increased by a factor of 2.25, while sensible improvements (the success rate is 1.06 times higher) are observed for *Fetching* too, hence almost nullifying the probability of a failure, highlighting how the implicit compliance delivered by the human-in-the-loop is fundamental for the sample integrity.

2.3.3.2 Analysis of the system in case of communication delays

Since we aim at replicating a planetary manipulation task, we test the robustness of our system by introducing, via software, a delay in the communication link between the MR and the workstation. Given a delay d, if an operator forwards a command by moving the HD at time t, the MR receives the reference at time $t + d$, and the resulting forces produced by the motion are fed back to the operator at approximately $t + 2d$.

We perform 20 experiments with $d = 0.5\,\mathrm{s}$ (Scenario C), and 20 experiments with $d = 1.0\,\mathrm{s}$ (Scenario D), exercising, in both scenarios, the procedure detailed in Section 2.3.2.2, as before. We assume no inherent delay in the communication, besides the one introduced via software. The operator can rely on both visual and haptic feedback to perform the task, with the state of the robot displayed by RVP.

The results of the trials in Scenarios C and D are reported in Table 2.1. Although a round-trip delay of $2d = 1.0\,\mathrm{s}$, the performance of Scenario A are preserved. On the other hand, a remarkable decrease in performance is registered in Scenario D. In particular, because of the round-trip delay $2d = 2.0\,\mathrm{s}$, the success rate of the *Assembly* phase drops from 90% to 65%, as the user's comfort during the peg-in-hole operation is degraded

Table 2.2: Training time of 3 different operators.

Operator	Number of attempts	Total training time
1	9	1 h 38 min
2	5	35 min
3	10	1 h 20 min

by the delayed perception of the contact forces between the sample and the assembly slot.

Although successful trials in Scenario D are twice more frequent than failures, a success rate of 65% is not enough to consider the system's performance acceptable in the case of $d = 1.0\,\mathrm{s}$. Therefore, we consider $d = 0.5\,\mathrm{s}$ as the limit case, confirming the results of [40], [59].

2.3.3.3 Ease of training new operators

In order to assess the proposed human-robot interface's ease of use in view of training new operators, we select three subjects with no experience with haptic teleoperation. Each participant is first explained procedures and tools, then they exercise the entire operational procedure several times. We consider the training to be complete when the operator is able to perform 5 consecutive successful trials.

The experiments foresee haptic feedback and no communication delays. We consider two metrics for the evaluation of ease of training, i.e. the total training time and the number of attempts. The results are shown in Table 2.2.

Although the number of involved subjects is not enough to draw general conclusions, our preliminary results suggest that combining haptic teleoperation with suitable human-robot interface

and operational procedures might greatly simplify the training process for completely inexperienced operators. Therefore, we aim at extending our trials to a larger audience, possibly made of subjects with heterogeneous backgrounds.

Chapter 3

Safe and natural haptic teleoperation

Haptic teleoperation plays a crucial role in extending human capabilities to remote environments. Whether in industrial, medical, or space applications, it combines the cognitive and manipulative skills of humans with the precision and efficiency of robotic systems. However, this synergy introduces a range of control challenges that must be addressed to ensure the fulfillment of stringent requirements.

Among these, the *haptic feedback rendering* is one of the key aspects for successful teleoperation. Haptic feedback is central in shaping the operator's perception, yet it also represents one of the main sources of instability. Moreover, it is strongly affected by the remote robot–environment interaction. With the aim of making the sensory experience for the human operator as natural as possible, without compromising system stability, several rendering methodologies are used. These differ in the way haptic feedback is delivered to the human operator, both in

terms of sensory modality and interaction, as well as in the type of information used for its computation. Another fundamental requirement for the success of any interaction task, is the capability to manage the physical contact between the robot and the environment. To that aim, *interaction controllers* are used, as pure motion control turns out to be inadequate because of unavoidable modeling and planning errors. For this reason, it becomes necessary to devise alternative control strategies that explicitly account for the presence of physical contacts. Since the 1980s, various interaction control approaches have been proposed, which can broadly be classified into two categories: *direct force control* and *indirect force control*. The distinction lies primarily in their treatment of interaction: in the former, an explicit model of the interaction task is required, with the user specifying both motion and force trajectories in accordance with task requirements, which are often dictated by the geometry of the environment. In the latter, contact forces are regulated through a mechanical impedance/admittance, resulting in deviations from the desired motion as a response to external forces. This latter feature makes them particularly suitable for operation in uncertain or unknown environments. Finally, successful teleoperation cannot be achieved without the capability to translate human intentions into robot commands, while accounting for kinematic compatibility, actuation limits, and motion constraints. To this end, several *mapping and scaling strategies* have been proposed, differing in how human intention is captured and in the type of commands generated for the robot.

Historically, within the domain of haptic teleoperation, each of these challenges has been treated as an independent control problem, which has not ensured overall system performance. For this reason, there comes the need for a unified approach aimed at maximizing system performance by optimizing not

only the individual components but also their integration. A review of the contemporary literature reveals the existence of several solutions addressing this need, albeit inevitably involving trade-offs between conflicting requirements.

The remainder of this chapter is structured as follows:

- Section 3.1 presents the different modalities of the haptic feedback rendering, highlighting its central role not only in determining the performance of the HBTS, but also in shaping operator perception.
- Section 3.2 introduces the concept of indirect force control, elaborating on impedance and admittance control schemes. It discusses also about variable impedance control, highlighting the differences compared to the aforementioned standard control schemes.
- Section 3.3 discusses about the main mapping and scaling techniques for translating human intentions, captured by an HD, into actual robot commands.
- Section 3.4 elaborates on how improving the usability, the stability and the safety of HBTSs, presenting a novel HBTS [75], integrating a virtualized force feedback with an interaction force limitation strategy, embedded in the admittance controller.
- Section 3.5 elaborates on how improving free-hand dental procedures, introducing a HBTS [76] specifically designed for these. It integrates, the virtualized force feedback, with a novel force limitation strategy, designed to operate in unstructured environments, and with a eye-hand coordination mapping strategy, providing force and motion correspondence.
- Section 3.6 investigates the feasibility of employing the

HBTS for free-hand dental procedures introduced in [76], focusing on a scaling and root planing procedure performed by dentists on a realistic dental phantom **[TBD]**.

3.1 Haptic feedback

Haptics describes the sense of touch, the movement and the mechanical interactions involving these. It is easy to understand that touch always requires interaction: no perception of touch can exist without something being touched. This implies that haptics always has an impact on the objects involved in the interaction and that the latter is strictly dependent on the physical properties of objects and bodies.

Human haptics is the study of how human beings sense and manipulate the world through touch. The human sense of touch, differently from the other senses, is not localized to a specific region, but is distributed throughout the body via the skin, joints, muscles and tendons. Such sense is typically divided into two modalities: *kinesthetic* and *tactile* [77]. Kinesthetic sensations, such as forces and torques, are perceived by muscles, tendons and joints and enable a perception of the body's position in space, relative to other objects. Tactile sensations are perceived by specialized sensory organs in the skin, called mechanoreceptors, and enable the perception of shape, temperature, vibration, stiffness, and texture. It's worth specifying that humans have asymmetric input/output capabilities [78]: human movements, particularly of the hand, can respond at frequencies as high as $5 - 10Hz$; in contrast, tactile receptors are able to respond at frequencies as high as $10kHz$ [79]. In Figure 3.1 is shown a comprehensive analysis of the bandwidth with which humans can react to haptic kinaesthetic and tactile interactions.

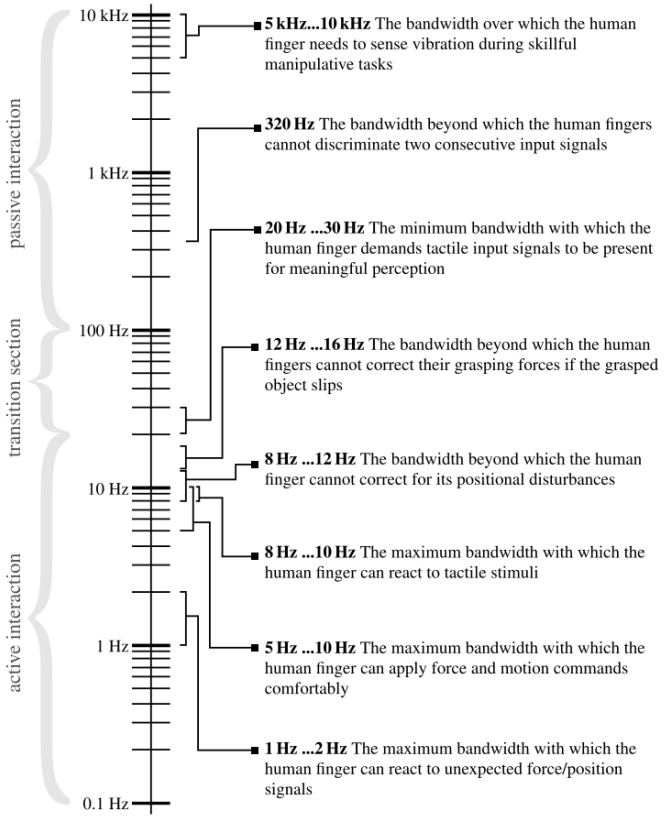


Figure 3.1: Kinaesthetic and tactile haptic interaction [80].

HDs attempt to replicate or improve the haptic experience for a human operator manipulating a remote or virtual environment through electromechanical devices and computer control.

3.1.1 Haptic devices

A HD consist of a mechanical input-output system, analogous to a robotic manipulator with sensors and actuators, requiring

a control software relating human operators inputs to haptic information display [81]. They can be categorized according to different classes, which are described in the following sections

3.1.1.1 Classes of haptic devices

There are two classes of HDs based on input/output configuration: *impedance* and *admittance* devices [82]. The *impedance devices* measure the motion input of the human operator and apply a haptic feedback according to the behavior of the remote system (or the virtual environment). The typologies of haptic feedback provided by this class of devices are based on the two complementary modalities of the human sense of touch described in Section 3.1. Impedance devices are the most widely used ones, due in part to the inexpensiveness of the required sensors. In all the experiments presented in this dissertation, a HD of this class have been used. On the other hand, *admittance devices* sense the wrench applied by the human operator and constrain their pose to match the appropriate deflection of the remote (virtual) environment.

Another classification of HDs can be obtained using the two-level approach [83]. The first level identifies how the device is positioned relative to the user, whether it is fixed to a structure, held in the hand, or worn on the body. The second level further defines the interaction type, such as direct actuation, tactile feedback, or kinesthetic feedback.

Such approach divides the HDs in the following classes:

1. **grounded devices**: physically attached to a fixed structure, which enables them to generate an accurate kinesthetic feedback. These systems are particularly effective when high fidelity and stability in haptic feedback render-

ing are required, such as in medical applications.

- *graspable*: designed to be grasped by the user, allowing interaction through the hand;
- *touchable*: designed to interact with the user, without grasping them. This category includes force-feedback joysticks and control levers used in robotic control stations and industrial setups. The touch interaction is usually limited to a surface or handle, but still provides meaningful haptic cues;

2. **hand-held devices**: portable HDs that are manipulated freely by the user without being fixed to any external structure. They are often used in immersive environments like virtual or augmented reality.
   - *directly actuated*: designed to provide kinesthetic feedback directly to the user's hand. Examples include specialized surgical tools equipped with actuators that simulate tissue resistance.
   - *indirectly actuated*: designed to provide a tactile feedback, through vibrations or dynamically modulated cues generated by the movement itself;
3. **wearable devices**: worn directly on the body, allowing for continuous or location-specific tactile stimulation. These devices provide flexibility in usage and are particularly valuable in applications where full mobility is required.
   - *exoskeletons*: typically worn over the limbs, applying mechanical resistance to joints;
   - *finger-worn*: worn directly on the fingers, providing either kinesthetic or tactile feedback;
   - *arm-worn*: typically vibro-tactile bands worn on the

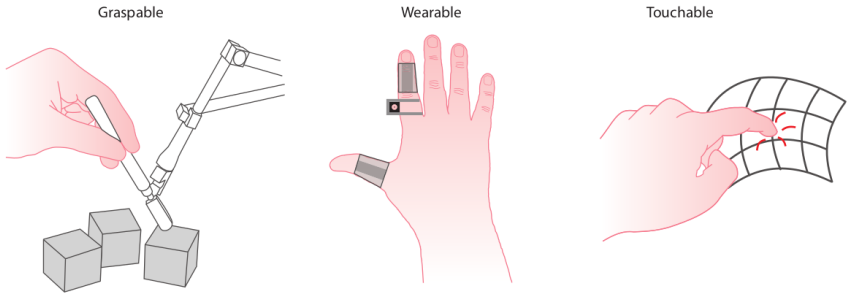


Figure 3.2: Examples of graspable, wearable, and touchable haptic devices [84].

forearm or upper arm, providing navigational cues.

Some examples of HDs are shown in Figure 3.2.

3.1.1.2 Operation of a haptic device

Regardless the HD class, its operation follows what is commonly known as the *haptic loop*, which involves the following steps:

1. *sensing*: the input provided by the human operator is captured by means of the internal sensors with which the device is equipped.
2. *command*: the sensed input is applied to the virtual environment or sent to the remote site, after being suitably mapped into a robot command;
3. *haptic feedback rendering*: this step requires a distinction between applications in virtual environments and teleoperation scenarios. In the former case, rendering consists in computing the haptic feedback, through dedicated algorithms, based on the response of the virtual environment model to the user's input. In the latter case, rendering is

understood as the computation of the control input of the LR, according to a control law such as those discussed in Section 2.1, or their variants.

4. *actuation*: the haptic feedback is displayed to the human operator via the actuators of the HD.

The actuation of the haptic feedback leads to a modification of the input, either due to the human response or solely to the device dynamics, thus closing the loop.

Although *haptic feedback rendering* and *actuation* are presented as two distinct steps, in this dissertation we use the term *haptic feedback rendering* to denote both the computation of the control input of the LR and its actuation.

3.1.2 Haptic feedback rendering in a HBTS

As previously noted, the typologies of haptic feedback provided in a HBTS are based on the two complementary modalities of the human sense of touch: *kinesthetic* and *tactile*.

Kinesthetic feedback can potentially affect the stability of the system, by introducing oscillations into the control loop. Despite this, it has historically been the focus of haptic feedback research, as it increases the *transparency* of teleoperation, and provides the most natural transfer of the remote interaction to the human operator. On the other hand, the tactile feedback does not affect the *stability*, but greatly reduces the transparency, as it does not allow a natural and transfer of the sensed forces and the impedance of the remote environment to the human operator. In parallel with these two modalities, efforts have been made to identify a suitable trade-off between stability and transparency in a HBTS, replacing haptic feedback with different sensory modalities. Such a strategy is known as *sensory*

substitution and involves the use of auditory stimuli or visual displays [85], [86]. The da Vinci Surgical System™, for instance, exploits the visual force feedback to avoid tissue damage during surgical procedures [87]. These solutions promote stability at the cost of reduced transparency. The alternative approach, is to combine the different feedback modalities into a single multimodal platform, so as to offer an experience as close as possible to the actual human sense of touch [88]. Although some of the research on these approaches provide some promising solutions based on platforms that combine different feedback modalities, the main interest is in force feedback, as it provides the most natural transfer of the remote interaction to the human operator. Indeed, in order to let the human operator perceive contact wrenches, most works in the literature focus on P-Fm architectures [40], [89], [90], providing F/T measurement-based force feedback.

As discussed in [91] humans are able to perceive both *interaction events*, i.e. contact state transitions, collisions, and sliding, and *interaction effects*, i.e. contact forces, reaction forces, and friction. The lack of perception of any of these aspects may compromise the *usability* of the HBTS. F/T measurement-based force feedback does not allow a clear distinction of interaction events, which causes the human operator to be pushed back strongly due to the wrenches exerted by the LR being greater than expected. To address this issue, [91] introduces a haptic feedback pipeline capable of rendering interaction forces distinctly for each contact state. To mitigate sudden changes in the forces and improve the usability of the system, [36] introduces a virtual mass-spring system acting as a low-pass filter. Each of these approaches leverages the advantages of kinesthetic feedback while ensuring system stability, at the cost of the transparency.

3.2 Interaction control

This section introduces the main interaction control schemes, with particular emphasis on impedance and admittance control, following a brief introduction to the dynamic model of a manipulator.

3.2.1 Dynamic model of manipulators

The relationships between actuation and contact forces acting on robot mechanisms and the motion trajectories that result is provided by the *dynamic equations of motion*. Dynamics is fundamental for diverse aspects in the broad robotics spectrum, including mechanical design, control, and simulation.

3.2.1.1 Dynamic model in free space

The manipulator dynamics in free-space can be modeled with the following equations of motion [92]:

$$\mathbf{B}(\mathbf{q})\ddot{\mathbf{q}} + \mathbf{C}(\mathbf{q}, \dot{\mathbf{q}})\dot{\mathbf{q}} + \tau_f(\dot{\mathbf{q}}) + \mathbf{g}(\mathbf{q}) = \boldsymbol{\tau}, \tag{3.1}$$

where $\mathbf{B}(\mathbf{q}) \in \mathbb{R}^{n\times n}$ is the symmetric positive-definite inertia matrix, $\mathbf{C}(\mathbf{q}, \dot{\mathbf{q}}) \in \mathbb{R}^{n\times n}$ is the matrix accounting for Coriolis and centrifugal effects, $\boldsymbol{\tau}_f(\dot{\mathbf{q}}) \in \mathbb{R}^{n\times 1}$ is the joint friction vector, $\mathbf{g}(\mathbf{q}) \in \mathbb{R}^{n\times 1}$ expresses the gravitational torques, $\boldsymbol{\tau} \in \mathbb{R}^{n\times 1}$ is the joint torque vector, and $\mathbf{q}, \dot{\mathbf{q}}, \ddot{\mathbf{q}} \in \mathbb{R}^{n\times 1}$ are the joint kinematic variables, namely positions, velocities and accelerations, with $n \in \mathbb{N}$ indicating the numbers of DoF.

3.2.1.2 Dynamic model with interaction with the environment

The free-space dynamic model presented in Section 3.2.1.1 holds when the robot is not in contact with the environment. When this happens, the two systems exchange *interaction wrenches* $\mathbf{h}_e$ depending on the task the robot is executing. In this case, (3.1) becomes:

$$\mathbf{B}(\mathbf{q})\ddot{\mathbf{q}} + \mathbf{C}(\mathbf{q}, \dot{\mathbf{q}})\dot{\mathbf{q}} + \tau_f(\dot{\mathbf{q}}) + \mathbf{g}(\mathbf{q}) = \boldsymbol{\tau} - \mathbf{J}^\top(\mathbf{q})\mathbf{h}_e, \tag{3.2}$$

where $m \leq 6 \leq n$ is the number of variables needed to describe the task and $\mathbf{J}(\mathbf{q})$ is the geometric Jacobian.

To simplify the notation in devising model-based control laws, it is often useful to define the so-called *bias*, defined as:

$$\mathbf{n}(\mathbf{q}, \dot{\mathbf{q}}) = \mathbf{C}(\mathbf{q}, \dot{\mathbf{q}})\dot{\mathbf{q}} + \tau_f(\dot{\mathbf{q}}) + \mathbf{g}(\mathbf{q}). \tag{3.3}$$

In virtue of (3.3), (3.1) becomes:

$$\mathbf{B}(\mathbf{q})\ddot{\mathbf{q}} + \mathbf{n}(\mathbf{q}, \dot{\mathbf{q}}) = \boldsymbol{\tau} - \mathbf{J}^\top(\mathbf{q})\mathbf{h}_e. \tag{3.4}$$

The wrenches $\mathbf{h}_e$ are typically considered to be unknown a priori, as they depend on the geometrical and physical characteristics of the environment itself, usually hard to devise in advance. As regards the linear forces, it is common to assume the environment to behave like a linear spring [93]–[100]:

$$\mathbf{f}_e = \mathbf{K}_e \left(\mathbf{p} - \mathbf{p}_e\right), \tag{3.5}$$

where $\mathbf{K}_e \in \mathbb{R}^{m \times m}$ is the environment stiffness diagonal matrix, $\mathbf{p}_e \in \mathbb{R}^{m \times 1}$ is the environment rest position, and $\mathbf{p} \in \mathbb{R}^{m \times 1}$ is the position of the robot's end-effector interacting with it. Clearly, if no contact happens, $\mathbf{f}_e$ does not follow (3.5) but simply $\mathbf{f}_e = \mathbf{0}$ holds.

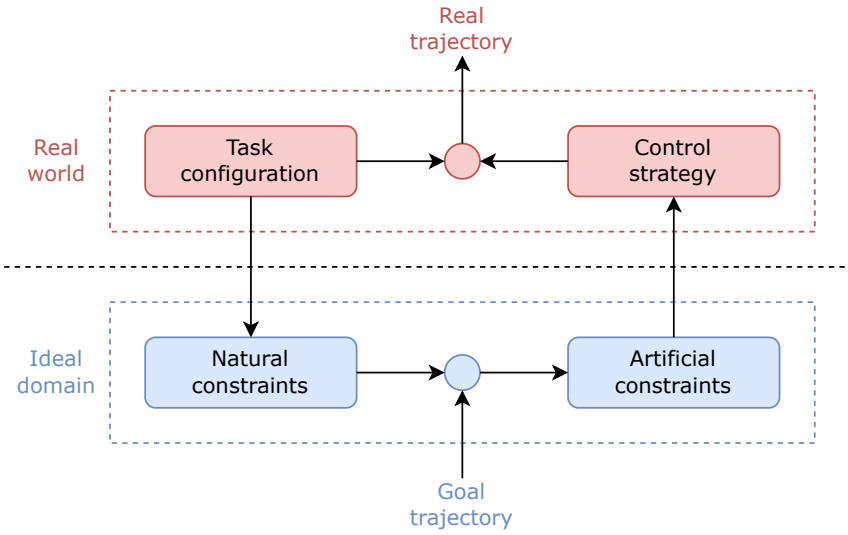


Figure 3.3: Overview of control strategy synthesis in the interaction control framework based on natural and artificial constraints.

Alternatively, the robot-environment interaction can be modeled, in general, with a spring-damper dynamics [71], [101]–[104]

$$\mathbf{f}_e = \mathbf{K}_e(\mathbf{p} - \mathbf{p}_e) + \mathbf{D}_e\dot{\mathbf{p}}, \tag{3.6}$$

where $\mathbf{D}_e \in \mathbb{R}^{m\times m}$ is the environment damping diagonal matrix and $\dot{\mathbf{p}} \in \mathbb{R}^{m\times 1}$ is the linear velocity of the robot's end-effector.

3.2.2 Hybrid force/motion control

When the robot is operated in free space, its joint values can be set to any desired value, as the resulting end-effector pose would not produce any effect on the surrounding environment. In this case, the manipulator is subject to an *unconstrained* motion. In

case of an interaction task, the motion is inevitably *constrained* by the task geometry, as the manipulator is no longer free to move in its whole workspace, forced to avoid high impact forces on the environment [105].

The solution is imposing a *compliant motion* on the robot, the crucial characteristic that distinguishes between interaction- and motion-controlled manipulators. Indeed, compliance is definitely the fundamental feature for executing an interaction task safely. Producing compliant motion is possible through two primary methods: a *passive* mechanical compliance built into the manipulator, or an *active* compliance implemented in the software control loop [106].

Although passive compliance can yield performance improvements, as it does make the robot less rigid towards the environment, interaction controllers offer the advantage of programmability, allowing the user to customize the control law imposing the desired interaction dynamics, which usually translates to tune the parameters of the controller.

One of the first steps that set the breakthrough of interaction control was done in [71], which explicitly adopts the concept of compliance to set up a general framework with the aim to properly configure any interaction task. The main idea is planning for a goal trajectory which, once actually performed on the robot, will be turned in a real trajectory as a reaction to the contact forces arisen during the execution. Figure 3.3 represents the framework with a simple diagram, whose components will be detailed next.

Given a task in the real world, the planning phase consists in defining a set of *natural constraints*, which depend on the mechanical and geometrical characteristics of the task configuration. Additional constraints, called *artificial constraints*, are

introduced to specify desired motions or force trajectories in task space. The axes for which a motion pattern is imposed are called non-compliant axes, as no forces are expected along them. On the other hand, compliant axes are the ones along which contacts may happen: for them, a force reference must be set.

While planning happens in the ideal domain, as the constraints and the goal trajectory result from how the task is modeled (and, as already stated, this modeling is inevitably inaccurate), the execution takes place in the actual environment. Hence, the role of the control strategy is producing and commanding the trajectory to the manipulator, by imposing the artificial constraints and reacting more or less compliantly to the interaction forces at the same time.

Given the natural separation of compliant and non-compliant axes, the most immediate solution is designing a *hybrid force/position controller*, first proposed by [101]. The idea is adopting a motion control law on the non-compliant axes (which compensates the position error), and a force control law on the compliant ones (which compensates the force error). This logic is implemented with the following law:

$$\mathbf{x}_f = \mathbf{\Gamma}\left(\mathbf{K}_p\tilde{\mathbf{h}} + \mathbf{K}_i\int_t \tilde{\mathbf{h}}\,dt\right) + (\mathbf{I}-\mathbf{\Gamma})\mathbf{x}_d, \tag{3.7}$$

where $\tilde{\mathbf{h}} = \mathbf{h}_d - \mathbf{h}_e \in \mathbb{R}^{m\times 1}$ is the wrench error between the desired wrench $\mathbf{h}_d \in \mathbb{R}^{m\times 1}$ and the actual wrench $\mathbf{h}_e$, and $\mathbf{K}_p, \mathbf{K}_i \in \mathbb{R}^{m\times m}$ are PI control gains. As regards the pose reference $\mathbf{x}_d$, it is followed only along the *unconstrained* directions, while the wrench reference is tracked along the *constrained* axes. This choice is performed via the selection matrix $\mathbf{\Gamma} \in \mathbb{R}^{m\times m}$, a diagonal matrix in which the coefficients are evaluated to 1 if the corresponding axis is constrained, 0 otherwise. Alternatively the

parallel force/position controller can be implemented as [107]

$$\mathbf{x}_f = \mathbf{x}_d + \mathbf{\Gamma}\left(\mathbf{K_p}\tilde{\mathbf{h}} + \mathbf{K}_i \int_t \tilde{\mathbf{h}}\, dt\right), \tag{3.8}$$

where now $\mathbf{x}_d$ is treated as a disturbance, compensated by the integral action.

This type of control strategy is suitable for tasks when there is a rough model for the environment, and the force and motion trajectory can somehow be divided among the directions of the Cartesian space. For more general tasks, indirect force controllers are preferable, but still the framework proposed in these seminal works can provide a basic concept to understand the problem of interaction control in general.

3.2.3 Impedance control

Impedance control is a control law introduced in [102] that allows to control the dynamic behavior of the manipulator in addition to commanding its motion. It is based on the concept that the robot and the environment it is in contact with are considered as a mechanical physical system, in which both velocities and forces flow along each degree of freedom.

The peculiarity of this controller is the ability to accept a motion trajectory as reference, but the interaction forces are seen as disturbances to the manipulator. Modulating the response to such disturbances permits control of dynamic interactions.

This means that the impedance controller can be used in the free space without changing control strategy, instead it implements a dynamic relation between the manipulator's motion variables (e.g. end-effector position and velocity or force) rather than just control these variables alone [108], as the latter approach is, in general, inadequate.

The impedance control law is based on inverse dynamics control. Given the robot's dynamic model (3.4):

$$\mathbf{B}(\mathbf{q})\ddot{\mathbf{q}} + \mathbf{n}(\mathbf{q}, \dot{\mathbf{q}}) = \mathbf{u} - \mathbf{J}^{\top}(\mathbf{q})\mathbf{h}_e, \tag{3.9}$$

let $\mathbf{u} := \boldsymbol{\tau}$ be the control input, computed with the following control law:

$$\mathbf{u} = \mathbf{B}(\mathbf{q})\mathbf{y} + \mathbf{n}(\mathbf{q}, \dot{\mathbf{q}}) + \mathbf{J}^{\top}(\mathbf{q})\mathbf{h}_e, \tag{3.10}$$

with:

$$\mathbf{y} = \mathbf{J}_A^{-1}(\mathbf{q}){\mathbf{M}_d}^{-1}\left(\mathbf{M}_d\ddot{\mathbf{x}}_d + \mathbf{K}_D\dot{\tilde{\mathbf{x}}} + \mathbf{K}_P\tilde{\mathbf{x}} - \mathbf{M}_d\dot{\mathbf{J}}_A(\mathbf{q}, \dot{\mathbf{q}})\,\dot{\mathbf{q}} - \mathbf{h}_A\right), \tag{3.11}$$

where $\mathbf{M}_d, \mathbf{K}_D, \mathbf{K}_P$ are the mass, damping, and stiffness diagonal matrices, respectively, of proper size, which are used to impose specific second-order mass-spring-damper dynamics, $\tilde{\mathbf{x}} = \mathbf{x}_d - \mathbf{x}$ is the pose error and $\dot{\tilde{\mathbf{x}}}$ its time derivative and:

$$\mathbf{J}_A(\mathbf{q}) = \begin{bmatrix} \mathbf{I} & \mathbf{0} \\ \mathbf{0} & \boldsymbol{T}_A \end{bmatrix} \mathbf{J}(\mathbf{q}) \tag{3.12}$$

is the analytical Jacobian, and:

$$\mathbf{h}_A = \begin{bmatrix} \mathbf{I} & \mathbf{0} \\ \mathbf{0} & \boldsymbol{T}_A \end{bmatrix} \mathbf{h}_e. \tag{3.13}$$

In (3.12)–(3.13), the matrix $\boldsymbol{T}_A$ is a function of the end-effector's orientation, whose formulation depends on the convention adopted to represent the orientation angles.

Equation (3.10) implements an *inverse dynamic controller*, compensating all the terms of the manipulator's dynamic model, and accounting for the actual impedance control law (3.11). By substituting (3.11) in (3.10) and then in (3.9), the impedance

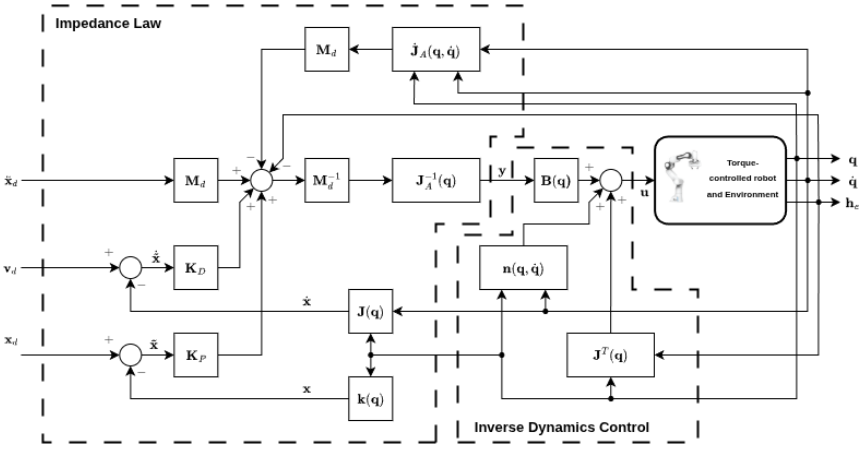


Figure 3.4: Impedance controller's block scheme.

controller imposes a *mass-spring-damper* dynamics at the end-effector:

$$\mathbf{M}_d\ddot{\tilde{\mathbf{x}}} + \mathbf{K}_D\dot{\tilde{\mathbf{x}}} + \mathbf{K}_P\tilde{\mathbf{x}} = \mathbf{h}_e, \tag{3.14}$$

where $\ddot{\tilde{\mathbf{x}}} = \ddot{\mathbf{x}}_d - \ddot{\mathbf{x}}$ is the acceleration error. Figure 3.4 represents the controller with a block scheme [109]. A similar formulation can be done for direct force controllers based on dynamics compensation [107].

This controller can be used as is even without exerting interaction wrenches, whose presence cause deviations from the desired motion, but compliance is achieved using the same control logic. In that sense, impedance control can be seen as an augmentation of typical motion control. The main challenge is tuning its parameters so as to achieve a desired behavior: a suitable choice would be to reach a trade-off between deviation from the reference path and exertion of wrenches [110].

3.2.4 Admittance control

Impedance control is not always suitable for industrial robots, since the laws (3.10)–(3.11) output a torque command, while usually a position interface is exposed by the manipulators' manufacturer. Besides, it is not immediate to tune the parameters in (3.14) for controlling both the interaction dynamics and position tracking. For example, high stiffness $\mathbf{K}_P$ is required to follow the reference trajectory, but introduces elevated forces during contact.

For this reasons, *admittance control* can be used instead. First introduced in [111] with the name *position-based impedance controller*, it outputs a *compliant pose* $\mathbf{x}_c$ to a motion control loop, consisting in a properly tuned motion-in torque-out controller, such that it can be assumed that $\mathbf{x}_c \equiv \mathbf{x}$. As regards the admittance controller, it interfaces with a system composed of motion controller, robot, and environment, which is seen as an impedance. Usually, manufacturers embed the motion controller in the robot itself, exposing to the user a position port.

Performance and stability of impedance and admittance controllers are complementary [112]: as also pointed out in [113], the stability bounds worsen when time delays are introduced by the digital implementation. Although they can be considered two implementations of the same control goal, impedance control has stable dynamic interaction with stiff environments, while admittance control can result in instability, but is more accurate in controlling the position with a smooth dynamics for soft environments [97].

As shown in Figure 3.5, the control law is similar to (3.14), imposing a mass-spring-damper dynamics on $\tilde{\mathbf{z}} := \mathbf{x}_d - \mathbf{x}_c$,

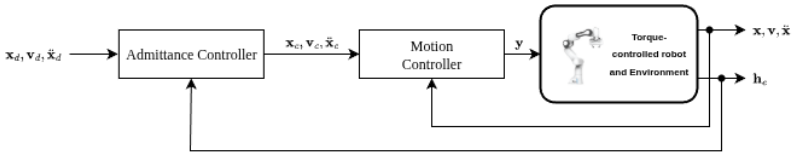


Figure 3.5: Admittance controller's block scheme

issuing $\mathbf{x}_c$ as reference to the motion controller:

$$\mathbf{M}_d\ddot{\tilde{\mathbf{z}}} + \mathbf{K_D}\dot{\tilde{\mathbf{z}}} + \mathbf{K_P}\tilde{\mathbf{z}} = \mathbf{h_e}. \tag{3.15}$$

3.2.5 Including force references in the controller

According to the dynamics imposed by the impedance (3.14) and the admittance (3.15) controllers, the position command depends on $\mathbf{h}_e$ only.

If it is desired to modify the motion depending on a desired wrench reference $\mathbf{h}_d$ too, then (3.14) becomes:

$$\mathbf{M}_d\ddot{\tilde{\mathbf{x}}} + \mathbf{K}_D\dot{\tilde{\mathbf{x}}} + \mathbf{K}_P\tilde{\mathbf{x}} = -\tilde{\mathbf{h}},$$

and (3.15) becomes:

$$\mathbf{M}_d\ddot{\tilde{\mathbf{z}}} + \mathbf{K_D}\dot{\tilde{\mathbf{z}}} + \mathbf{K_P}\tilde{\mathbf{z}} = -\tilde{\mathbf{h}}, \tag{3.16}$$

where $\tilde{\mathbf{h}} := \mathbf{h}_d - \mathbf{h}_e$.

3.2.6 Variable impedance/admittance control

In addition to the considerations in Section 3.2.4, indirect controllers suffer from two major drawbacks: *stability* issues, as the environment can significantly alter the system dynamics,

especially in the presence of stiff contacts or sensor noise, filtering delays, and contact discontinuities, potentially leading to instability [113], [114]; limited *force tracking* capabilities, since indirect force control, although provides robustness to uncertainties and disturbances, does not guarantee accurate tracking of a desired force reference, which may be essential in certain applications [93], [95], [96].

A well-established strategy to overcome these issues is *variable* (or *adaptive*) *impedance/admittance control*, where the control law is adapted online to improve force tracking performance and robustness against model imperfections. The pioneering work in [93] introduces two main approaches: *direct adaptive impedance control*, which computes the reference trajectory as a function of the force error, and *indirect adaptive impedance control*, which estimates environment parameters and uses them to compute a suitable reference. Both approaches proved effective in simulations and experiments [94], showing robustness to abrupt stiffness variations, geometric inaccuracies, and noise. However, direct methods require tuning a larger number of parameters, while indirect ones depend on initial estimates and may converge slowly. Alternative methods modify the impedance parameters directly. The null-stiffness strategy [95], [98] sets $\mathbf{K}_P = \mathbf{0}$, thus ensuring zero steady-state force error regardless of $\mathbf{K}_e$. While simple to tune, this approach suffers from large overshoots and oscillations at impact. Enhancements have been proposed to address these issues, such as adding derivative terms and decay coefficients in the adaptation law [100], although differentiation of noisy force signals remains a critical limitation. A related direction is variable stiffness control [96], in which the proportional gain is adapted online according to the measured force error and its derivative. This method achieves accurate force tracking with reduced overshoot and rise time, but still faces challenges

due to the need to compute force derivatives reliably. A specific yet crucial problem is impact management, as switching from free motion to contact typically generates high transient forces [115]. Several strategies aim to mitigate this effect, such as optimizing the reference generation through online estimation of environment stiffness and damping with Extended Kalman Filters [103], [104], or using variable-damping impedance control combined with PI controllers. Such approaches feature anti-windup and adaptive saturation to regulate both steady-state force tracking and transient overshoot [116], [117]. Overall, variable impedance control provides a versatile framework to achieve accurate and robust force regulation, with different methodologies offering specific trade-offs between performance, robustness, and implementation complexity.

3.2.7 Interaction control for pHRI

Although the control approaches presented earlier offer notable benefits in terms of stability and force-tracking performance, they still fall short of satisfying the more stringent safety requirements necessary for the certification of pHRI applications [118]. In particular, ISO/TS 15066 defines limit values for contact forces with different parts of a human operator's body.

Building on the certification process of pHRI applications, [119], [120] propose an energy-based control approach, where the robot's energy is kept below a prescribed safety budget to ensure safe interaction. Following the same line as variable impedance control, several advanced solutions specifically tailored for pHRI have been introduced in the literature. A combined active–passive variable admittance control is presented in [121], aiming to mitigate the negative impact of accidental collisions by minimizing contact time. This ensures safe robot

motion while guaranteeing the application of a consistent desired force. Variable admittance control-based methods are also explored in [122], where variable damping is applied to adjust the robot's velocity according to external torques. Additionally, a variable reference angle is introduced, adapting to different interaction scenarios to facilitate motion. With the goal of adapting robot impedance to dynamic environments and human collaborators in torque-controlled systems, [123] propose a human-like learning controller. In a more recent work, [124] introduce a motion-reshaping strategy that combines a projection filter with a Lie group setpoint controller. This method constrains the robot's motion within predefined geometric boundaries, preventing excessive contact forces and avoiding catastrophic failures. Finally, [125] present an algorithm that shapes task impedance as a function of the robot's time-varying inertial properties. These properties are expressed as virtually constrained masses and inertias, which adaptively counteract the task in order to comply with given constraints.

3.3 Mapping and scaling techniques

Establishing an effective mapping between the LR and FR is a critical aspect of a HBTS design. This process determines how operator inputs, whether captured via a HD, motion tracking system, or joystick, are translated into commands for the FR.

3.3.1 Problem formulation

Let $\mathcal{W}_l$ denote the workspace of the LR and of the FR and $\mathcal{C}_f$ the control space of the FR. A mapping function M defines the relationship between the two spaces and can be defined as

follows:

$$M : \mathcal{W}_l \mapsto \mathcal{C}_f. \tag{3.17}$$

Such function must account for kinematic compatibility, discrepancy in the DoF, actuation limits, and motion constraints of both LR and FR. These factors are crucial to ensure that the commands generated by the LR are physically feasible and consistent with the capabilities of the FR [126]. Indeed, even the LR and the FR share the same DoF, discrepancies in their kinematic structures, joint arrangements, can prevent the implementation of a direct 1:1 correspondence. For instance, a human arm and an anthropomorphic manipulator may both exhibit the same DoF, but due to differences in joint limits and kinematic configuration, their motions cannot be directly transferred without additional processing or interpretation [127], [128].

Let $\mathbf{s}_l(t) \in \mathcal{W}_l$ be the state of the LR at time t and $\mathbf{u}_f(t)$ the FR's command at the same time. An effective mapping strategy is such that:

$$\mathbf{u}_f(t) = M(\mathbf{s}_l(t)) \in \mathcal{C}_f, \forall \mathbf{s}_l(t) \in \mathcal{W}_l, t \geq 0. \tag{3.18}$$

3.3.2 Control techniques

Several control techniques can be used to establish the mapping in (3.18), depending on the task to be accomplished as well as the kinematic similarity between the LR and FR:

1. *position control* establishes a mapping between the pose of the LR and the pose of the FR; This is the most common technique used in telemanipulation systems and can be enforced in both joint and task spaces;
2. *rate control* establishes a mapping between the pose of the LR and the velocity of the FR. This is the most

common technique used in telenavigation systems, e.g. remote controlled rovers;

3. *hybrid control techniques* have been used to exploit the advantages of both position and rate control. The combination of rate control and position control can be very useful in cases where each, separately, does not guarantee the successful execution of teleoperated tasks.

3.3.2.1 Position mapping techniques

In HBTSs one common approach to mapping the motion of the LR to the FR is through position-based strategies. In this paradigm, the position and orientation of the LR are directly related, through various transformations or scaling laws, to the desired position and orientation of the FR. In this section we present the main state-of-the-art position mapping techniques.

Kinematic mapping If the LR and the FR are kinematically similar, a direct mapping can be imposed, named *kinematic mapping* or *1:1 position mapping* [74], between their joint positions:

$$\begin{aligned} \mathbf{q}_{fd} &= \mathbf{q}_{l} + \mathbf{q}_{\text{offset}}, \\ \mathbf{q}_{ld} &= \mathbf{q}_{f} - \mathbf{q}_{\text{offset}}, \end{aligned} \tag{3.19}$$

in which $\mathbf{q}_{*d} \in \mathbb{R}^{n\times 1}$, where n are the DoF of both robots, are the desired joint positions and $\mathbf{q}_{\text{offset}} \in \mathbb{R}^{n\times 1}$ is a constant offset between the two joint spaces.

If the leader and the follower are kinematically different, a direct mapping between the poses of the LR and of the FR can be imposed:

$$\begin{aligned} \mathbf{p}_{fd} &= \mathbf{p}_{l} + \mathbf{p}_{\text{offset}}, \\ \mathbf{p}_{ld} &= \mathbf{p}_{f} - \mathbf{p}_{\text{offset}}, \end{aligned} \tag{3.20}$$

where $\mathbf{p}_{*d} \in \mathbb{R}^{3\times1}$ and $\mathbf{p}_{*} \in \mathbb{R}^{3\times1}$ are the desired and actual robot positions, respectively, and $\mathbf{p}_{\text{offset}} \in \mathbb{R}^{3\times1}$ is the offset between the two robot position. As for the orientation the mapping is as follows:

$$\begin{aligned} \mathbf{R}_{fd} &= \mathbf{R}_{l}\mathbf{R}_{\text{offset}}, \\ \mathbf{R}_{ld} &= \mathbf{R}_{f}\mathbf{R}_{\text{offset}}, \end{aligned} \tag{3.21}$$

where $\mathbf{R}_{*d} \in SO(3)$ and $\mathbf{R}_{*} \in SO(3)$ are the desired and actual robot rotation matrices, respectively, representing the orientation, and $\mathbf{R}_{\text{offset}} \in SO(3)$ is the offset between the two orientation.

Position control Usually, the workspace of the LR is smaller than the workspace of the FR. To overcome this issue and increase the space covered by the FR, it is be possible to rely on scaling techniques. *Position control* it is the simplest and most commonly used technique to this purpose. This is achieved by scaling the displacement of the LR, with a suitable scaling factor, and mapping it to the workspace of the FR:

$$\begin{aligned} \mathbf{p}_{fd} &= \lambda_{p}\mathbf{p}_{l} + \mathbf{p}_{\text{offset}}, \\ \mathbf{p}_{ld} &= \frac{\mathbf{p}_{f} - \mathbf{p}_{\text{offset}}}{\lambda_{p}}, \end{aligned} \tag{3.22}$$

where $\lambda_{p} \in \mathbb{R}$ is the scaling factor.

Position control with linear scaling factor The scaling factor plays a pivotal role in balancing movement speed with workspace size. Its effect can be intuitively described as follows: a smaller scaling factor enhances accuracy, making it advantageous for tasks that require fine manipulation, but at the expense of reducing the workspace of the FR. Conversely, a

larger scaling factor expands the FR's workspace, since motions of the LR are amplified, but this comes with a loss of precision, which may hinder the operator's ability to accurately guide the FR. *Position control with a linear scaling factor* addresses this trade-off by enabling the scaling factor to be increased or decreased according to a linear function during teleoperation. This adjustment can be performed through buttons or switches available on the LR [129].

Ballistic control *Ballistic control* introduces a dynamic scaling mechanism aimed at improving the usability of the system in response to varying human operator's dynamics. Rather than employing a static scale factor, this technique adapts the scaling factor in real-time based on the velocity of the LR. The relative mapping between the motion of the LR and that of the FR can be expressed as follows [130]:

$$\mathbf{p}_f(t) = \mathbf{p}_f(t-1) + K(\dot{\mathbf{p}}_l(t))(\mathbf{p}_l(t) - \mathbf{p}_l(t-1)), \qquad (3.23)$$

where $K(\dot{\mathbf{p}}_l(t))$ is a velocity-dependent dynamic scaling factor. When the LR moves rapidly, the system increases the scaling factor to extend the workspace. Conversely, when the LR slows down, the scaling factor is decreased to enhance precision.

Position control with indexing Another effective method for fully exploiting the FR's workspace is the reuse of the LR's limited workspace through a technique known as *position control with indexing* [131], [132]. It consists of temporarily interrupting communication between the LR and the FR once the operator reaches the boundaries of the LR's workspace. The LR can then be repositioned to a more convenient location, after which communication is resumed. In practice, this operation is typically

performed using switches or buttons integrated into modern LRs.

3.3.2.2 Rate control

When teleoperating a mobile robot, the FR's workspace can be considered infinite, whereas the LR is inherently limited. Although it entails a loss of positioning accuracy, *rate control*, also referred to as position-velocity control [133], offers an effective means to cope with these issues, as it facilitates the management of very large workspaces.

In this control approach, the commands sent to the FR are proportional to the displacement of the LR handle from its neutral position [134]. Consequently, the operator can hold the LR in a fixed pose, different from neutral one, while the FR continues moving at a constant velocity determined by that displacement. The desired linear velocity of the FR $\dot{\mathbf{p}}_{fd}$ is computed as follows:

$$\dot{\mathbf{p}}_{fd} = \gamma_v \left(\mathbf{p}_l - \mathbf{p}_l(0) \right), \tag{3.24}$$

where $\gamma_v \in \mathbb{R}$ is the linear velocity scaling factor and $\mathbf{p}_l(0)$ is the neutral position of the LR. The desired angular velocity $\boldsymbol{\omega}_{fd}$ is computed as follows:

$$\boldsymbol{\omega}_{fd} = \gamma_\omega \mathbf{r} \vartheta, \tag{3.25}$$

where $\gamma_\omega \in \mathbb{R}$ is the angular velocity scaling factor, and $\mathbf{r}$ and ϑ are the axis and the angle representing the relative rotation between the actual LR's orientation and the neutral one.

3.3.2.3 Hybrid mapping techniques

Hybrid control strategies combine position and velocity control, enabling dynamic switching between the two modes and thereby

providing the operator with greater flexibility. This adaptability allows the system to balance speed and precision according to task demands. Rate control, for instance, is particularly advantageous for long-range motions, as it supports rapid movement and straightforward stopping, though at the cost of reduced positional accuracy [135], [136]. Conversely, position control ensures higher precision but is inherently constrained by the physical limits of the LR's workspace [137], which can limit its effectiveness in tasks requiring extended motion.

To achieve such flexibility, several studies have proposed multimodal control schemes in which the active mode is selected based on contextual cues [138]–[140]. Among the most straightforward of these are manual methods, where the operator explicitly chooses the control mode via a switch or interface on the LR. While simple in concept, this approach requires additional hardware, may lack responsiveness in dynamic or time-critical tasks, and increases the overall complexity of the control architecture.

To mitigate these limitations, automatic switching based on human intention estimation has been introduced. In this paradigm, the system infers the operator's intent and transitions between modes accordingly. Various methods have been explored in the literature. For instance, [141] proposes estimating the operator's intention to accelerate or decelerate using measured velocity together with the derivatives of the applied forces. The two principal approaches to intention-based human control are discussed in the following sections.

Single zone with intention-based mode selection The main idea behind the *single zone with intention-based mode selection* is that the system autonomously determines the most suitable control mode based on real-time parameters such as the

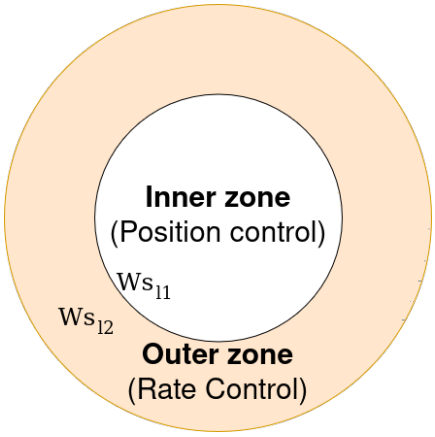


Figure 3.6: Leader workspace-based partitioning for double zone with intention-based scaling factor technique [74].

velocity of the operator's input or proximity to environmental obstacles. These methods increase autonomy and responsiveness but may require sophisticated sensing and prediction algorithms.

Double zone with intention-based scaling factor *Double zone with intention-based scaling factor*, is triggered by a predefined mapping of the working environment. For instance, the system may automatically transition to position control when the robot enters specific task-related areas. Formally, let W_s denote the LR workspace. This workspace can be partitioned into two regions: an inner zone $W_{s_{l1}}$, associated with position control, and an outer zone $W_{s_{l2}}$, associated with rate control, as illustrated in Figure 3.6. The approach can be formally expressed as follows:

$$\mathbf{p}_{fd} = \lambda_p \mathbf{p}_l + \dot{\mathbf{p}}, \tag{3.26}$$

where:

$$\dot{\mathbf{p}} = \begin{cases} \gamma_v \mathbf{p}_l & \text{if } \mathbf{p}_l \in W_{s_{l2}} \\ 0 & \text{if } \mathbf{p}_l \in W_{s_{l1}} \end{cases}. \tag{3.27}$$

3.3.2.4 Force scaling

Alongside mapping and scaling techniques for converting human inputs into robot commands, force scaling methods are also required. In fact, HDs can typically render forces in the range of $0 - 20\,\mathrm{N}$, whereas the interaction forces $\mathbf{f}_e$ can be much higher. Multiple force scaling techniques have been proposed in literature, the simplest of which is scaling the force by a constant factor λ_f:

$$\mathbf{f}_h = \frac{1}{\lambda_f} \mathbf{f}_e, \tag{3.28}$$

where $\mathbf{f}_h$ is the force rendered on the HD. This technique requires an accurate modeling of the interaction task, particularly the estimation of the maximum interaction force $\mathbf{f}_e$, in order to ensure that the range of the HD is always respected. Alternatively, haptic force saturation techniques are employed to guarantee proper operation. These methods ensure that the rendered force complies with the physical limits of the device, without altering its direction.

3.4 Design of a stable, usable, and safe HBTS for precision tasks

As introduced at the beginning of this chapter, haptic teleoperation plays a pivotal role in extending human capabilities to remote environments, by combining the cognitive and manipulative skills of humans with the precision and efficiency

of robotic systems. This synergy, however, also raises several control challenges that must be addressed while meeting stringent requirements. Beyond those outlined in Section 2.1.1, the intrinsic link between HBTSs and the broader domain of pHRI implies that their design must also comply with the *safety* and *dependability* requirements discussed in Section 1.2.

In Section 3.2, we emphasized the central role of interaction control in managing physical contact between the robot and its environment to ensure successful task execution, focusing on the two main strategies, namely *admittance control* and *impedance control*. In Section 3.2.6, we analyzed their limitations and introduced state-of-the-art solutions based on the concept of *variable impedance/admittance*. While these approaches offer notable benefits in terms of stability and force-tracking performance, they still fall short of satisfying the more stringent safety requirements necessary for the certification of pHRI applications, which call for tailored solutions, as discussed in Section 3.2.7. In Section 3.3, we reviewed the principal control strategies for mapping human intentions, captured by a HD, into effective robot commands. From this analysis, a major limitation emerges in handling complex scenarios, where external factors can significantly affect the required mapping. Finally, in Section 3.1, we analyzed different modalities for haptic feedback rendering, underscoring its central role not only in influencing the performance of HBTSs, but also in modeling operator perception, teleoperation experience, and overall system usability. This is corroborated by the results in [14], presented in Section 2.3.3, which demonstrate that haptic feedback enhances both safety and task performance, improves operator awareness, and mitigates the impact of communication delays.

Nevertheless, the system in [14], based on P-Fm architecture (see

Section 2.1.2.2), also revealed certain drawbacks. Specifically, the step dynamics of the measured forces used for generating force feedback occasionally induced instabilities and oscillations in the control loop, compelling the human operator to cope with sudden force variations that did not match their prior experience of interacting with the environment.

To address the gaps identified in this chapter, and build upon the experimental evidence discussed above, in [75] we propose a novel HBTS based on a P-P architecture, which, as discussed in Section 2.1.2.1, is inherently stable. Such system integrates a virtualized force feedback with a motion reference saturation strategy, embedded within the admittance control, enhancing the overall system stability, usability, and safety. The system design is detailed in Section 3.4.1, while the experimental validation on a blackboard writing task, comparing different architectures, is presented in Section 3.4.2.

3.4.1 System design

We propose and validate a HBTS architecture, shown in Figure 3.7, including a leader control station and a FR. The FR is a UR10 robotic arm by Universal Robots [142], equipped with a FT150 6-axis F/T sensor by Robotiq [143]: it is responsible for measuring the contact forces and supporting the tool that physically interacts with the environment. The FR is subject to admittance control to ensure stability and safety of teleoperation during the interaction phases, preventing damage to the arm or to the remote environment. Such a controller features the saturation of the motion references, as well as gravity compensation of the tool's payload. The objective of saturation and its operation are explained in Section 3.4.1.2.

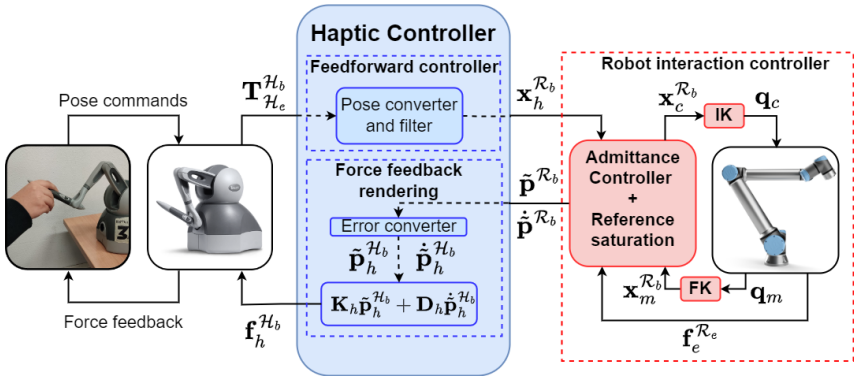


Figure 3.7: Haptic bilateral teleoperation system scheme.

The leader control station features a 6-DoF force-feedback HD [72] and a HC: it is responsible for generating the FR's motion references, starting from the HD's stylus motion, and rendering the haptic feedback to let the human operator perceive the remote interaction forces. In addition, to generate stable references for the FR, the HC features the filtering of human tremors. The generation of motion references and their filtering are explained in Section 3.4.1.1. The haptic feedback rendering methodology is explained in Section 3.4.1.3.

3.4.1.1 Feedforward haptic controller

One of the main features of the HC is capturing the HD stylus poses with respect to the HD base frame $\mathcal{H}_b$, and transforming them into robot end-effector poses with respect to the base reference frame $\mathcal{R}_b$, so that the robot follows the movements of the HD stylus. This type of linear mapping, in which poses are simply transferred from HD space to robot space, is defined kinematic mapping (see Section 3.3.2.1), and is particularly suitable for the considered task, as it provides the right trade-off

between the speed of movements and the workspace size.

We denote with $\mathbf{T}_b^a \in SE(3)$ the homogeneous transformation matrix from frame a to frame b, in the form

$$\mathbf{T}_b^a = \begin{pmatrix} \mathbf{R}_b^a & \mathbf{p}_b^a \\ 0 & 1 \end{pmatrix}, \tag{3.29}$$

where $\mathbf{R}_b^a \in SO(3)$ is the rotation matrix from frame a to frame b, and $\mathbf{p}_b^a \in \mathbb{R}^{3\times 1}$ represents b's origin in frame a.

At each control cycle, the stylus pose $\mathbf{T}_{\mathcal{H}_e}^{\mathcal{H}_b}$ is read by the HD driver, and converted in the robot end-effector pose $\mathbf{T}_{\mathcal{R}_e}^{\mathcal{R}_b}$ with the following kinematic equations:

$$\mathbf{R}_{\mathcal{R}_e}^{\mathcal{R}_b} = \mathbf{R}_{\mathcal{H}_b}^{\mathcal{R}_b}\mathbf{R}_{\mathcal{H}_e}^{\mathcal{H}_b}\mathbf{R}_{\mathcal{R}_e}^{\mathcal{H}_e}, \tag{3.30}$$

$$\mathbf{p}_{\mathcal{R}_e}^{\mathcal{R}_b} = \mathbf{p}_{\mathcal{R}_e}^{\mathcal{R}_b}(0) + \mathbf{R}_{\mathcal{H}_b}^{\mathcal{R}_b}\big(\mathbf{p}_{\mathcal{H}_e}^{\mathcal{H}_b} - \mathbf{p}_{\mathcal{H}_e}^{\mathcal{H}_b}(0)\big), \tag{3.31}$$

where $\mathcal{H}_e$ is the haptic stylus frame, $\mathcal{R}_e$ is the robot end-effector frame, and $\mathbf{p}_{\mathcal{R}_e}^{\mathcal{R}_b}(0)$ and $\mathbf{p}_{\mathcal{H}_e}^{\mathcal{H}_b}(0)$ are the starting positions of the robot end-effector and of the HD stylus, respectively. From $\mathbf{T}_{\mathcal{R}_e}^{\mathcal{R}_b}$, the corresponding robot end-effector pose is obtained as:

$$\mathbf{x}_{\mathcal{R}_e}^{\mathcal{R}_b} = \begin{bmatrix} \mathbf{p}_{\mathcal{R}_e}^{\mathcal{R}_b} \\ \mathbf{\hbar}_{\mathcal{R}_e}^{\mathcal{R}_b} \end{bmatrix}, \tag{3.32}$$

where $\mathbf{\hbar}_{\mathcal{R}_e}^{\mathcal{R}_b} \in \mathbb{H}_1$ is the quaternion associated with $\mathbf{R}_{\mathcal{R}_e}^{\mathcal{R}_b}$.

Commanding the robot with $\mathbf{x}_{\mathcal{R}_e}^{\mathcal{R}_b}$ would imply transferring the inevitable tremors of human motion, further emphasized by the control frequency, which is much higher than the typical bandwidth of hand tremors. Therefore, $\mathbf{x}_{\mathcal{R}_e}^{\mathcal{R}_b}$ is filtered online by a moving average filter. The desired position $\mathbf{p}_h^{\mathcal{R}_b}(i)$, at the i-th control cycle, is obtained by averaging samples from a recent past within a window of fixed size n. To achieve $\mathcal{O}(1)$

computational complexity, we keep a cumulative sum $\mathbf{c}(i)$, which is updated at each control cycle:

$$\mathbf{c}(i) = \begin{cases} \mathbf{c}(i-1) + \mathbf{p}_{\mathcal{R}_e}^{\mathcal{R}_b}(i), & \text{if } i < n; \\ \mathbf{c}(i-1) + \mathbf{p}_{\mathcal{R}_e}^{\mathcal{R}_b}(i) - \mathbf{p}_{\mathcal{R}_e}^{\mathcal{R}_b}(i-n), & \text{otherwise.} \end{cases} \tag{3.33}$$

The desired end-effector position $\mathbf{p}_h^{\mathcal{R}_b}(i)$ is obtained as:

$$\mathbf{p}_h^{\mathcal{R}_b}(i) = \frac{\mathbf{c}(i)}{m}, \tag{3.34}$$

where $m \leq n$ is the number of samples in the moving average window at the i-th control cycle. The desired orientation $\hbar_h^{\mathcal{R}_b}(i)$ is obtained by filtering $\hbar_{\mathcal{R}_e}^{\mathcal{R}_b}(i)$ as done in [144].

3.4.1.2 Robot interaction control

In this subsection, we first formalize the contact model between the environment and the robot (Section 3.4.1.2), then we present the forces limitation strategy (Section 3.4.1.2).

Admittance model Let $\mathbf{x}_d^{\mathcal{R}_b} = \mathbf{x}_h^{\mathcal{R}_b} = \left[\left(\mathbf{p}_h^{\mathcal{R}_b} \right)^\top \left(\hbar_h^{\mathcal{R}_b} \right)^\top \right]^\top$ be the desired task and $\mathbf{x}_c^{\mathcal{R}_e} = \left[\left(\mathbf{p}_c^{\mathcal{R}_e} \right)^\top \left(\hbar_c^{\mathcal{R}_e} \right)^\top \right]^\top$ be the robot-commanded pose in end-effector frame. For the sake of simplicity we take $\hbar_c^{\mathcal{R}_e} = \hbar_d^{\mathcal{R}_e}$. When the robot interacts with the environment, the relation between the contact forces $\mathbf{f}^{\mathcal{R}_e} \in \mathbb{R}^{3\times 1}$ and the position error $\tilde{\mathbf{p}} = \mathbf{p}_d^{\mathcal{R}_e} - \mathbf{p}_c^{\mathcal{R}_e}$ is established by a generalized mechanical impedance, represented by the second-order mass-spring-damper system in (3.16):

$$\mathbf{M}_d \ddot{\tilde{\mathbf{p}}}^{\mathcal{R}_e} + \mathbf{K}_D \tilde{\mathbf{p}}^{\mathcal{R}_e} + \mathbf{K}_P \tilde{\mathbf{p}}^{\mathcal{R}_e} = -\tilde{\mathbf{f}}^{\mathcal{R}_e}. \tag{3.35}$$

The force tracking error $\tilde{\mathbf{f}}^{\mathcal{R}_e} = \mathbf{f}_d^{\mathcal{R}_e} - \mathbf{f}_e^{\mathcal{R}_e}$ is the difference between the desired force $\mathbf{f}_d^{\mathcal{R}_e}$ and the exerted force $\mathbf{f}_e^{\mathcal{R}_e}$, which is equal and opposite to the measured force.

Computing $\mathbf{p}_c^{\mathcal{R}_e}$ from (3.35), the compliant position reference to be commanded to the robot is obtained as:

$$\mathbf{p}_c^{\mathcal{R}_b} = \mathbf{p}_d^{\mathcal{R}_b} + \mathbf{R}_{\mathcal{R}_e}^{\mathcal{R}_b} \mathbf{p}_c^{\mathcal{R}_e}. \tag{3.36}$$

Interaction force limitation strategy Let $\mathbf{f}_d^{\mathcal{R}_e} = \mathbf{0}$ to make the robot compliant with the environment and assume that the latter can be approximated by a linear spring model. The exerted force at the steady state [121] is:

$$\mathbf{f}_e^{\mathcal{R}_e} = \mathbf{K}_{eq}(\mathbf{p}_e^{\mathcal{R}_e} - \mathbf{p}_d^{\mathcal{R}_e}), \tag{3.37}$$

where $\mathbf{K}_{eq} = (\mathbf{K}_P \mathbf{K}_e)(\mathbf{K}_P + \mathbf{K}_e)^{-1}$ is the equivalent stiffness of the admittance stiffness $\mathbf{K}_P$ and environmental stiffness $\mathbf{K}_e$ [145], $\mathbf{p}_e^{\mathcal{R}_e}$ is the environment rest position. From (3.37), it follows that contact forces can be bounded through a suitable reference $\mathbf{p}_d^{\mathcal{R}_e}$ provided to the admittance controller. Accurate limitation requires perfect knowledge of the environment.

In the proposed strategy, the j-th component of the position reference is saturated when the corresponding component of the contact force exceeds a limit, i.e.,

$$p_{d,j}^{\mathcal{R}_b} = \begin{cases} p_{h,j}^{\mathcal{R}_b}, & \text{if } |f_{e,j}^{\mathcal{R}_b}| < f_{th,j} \\ \overline{p}_{d,j}^{\mathcal{R}_b}, & \text{if } |f_{e,j}^{\mathcal{R}_b}| > f_{th,j} \end{cases}, \tag{3.38}$$

where $f_{th,j} \in \mathbb{R}^+$ and $\overline{p}_{d,j}^{\mathcal{R}_b}$, $\forall j \in \{x, y, z\}$, are the saturation activation threshold and the reference saturation value along each axis of the base reference frame, respectively. From (3.37), we set

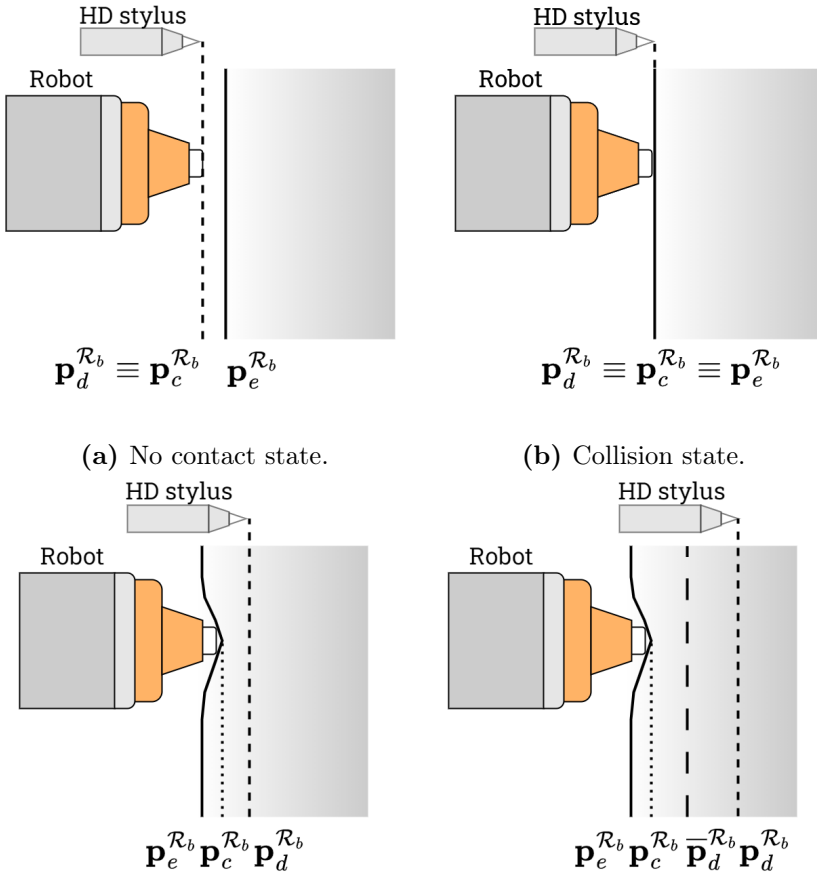
$$\overline{p}_{d,j}^{\mathcal{R}_b} = p_{e,j}^{\mathcal{R}_b} + \frac{f_{th,j}}{K_{eq,j}}, \tag{3.39}$$

where $\mathbf{p}_e^{\mathcal{R}_b}$ can be obtained through sensor sampling. In our design, assuming a stiff environment with uniform geometry, we approximate it by considering the last compliant position commanded to the robot $\mathbf{p}_c^{\mathcal{R}_b}$ at the saturation activation. With regard to the environment stiffness, we assume that $\mathbf{K}_e$ has been previously estimated, e.g., as in [146], and it does not change over time. We envisage the possibility of not having an accurate estimate, but rather a conservative one that allows for an effective forces limitation. Likewise, we note that $f_{th,j}$ does not represent an accurate force limit, as it is always exceeded before the saturation mechanism can take place. However, the strategy in (3.38) prevents that contact forces can grow indefinitely. The force threshold can be devised from the task requirements, or, if available, from observations/measurements of human operators manually performing the same task.

A pictorial view of the robot-environment contact phases is provided in Figure 3.8, with an indication of the symbols used in this paper.

3.4.1.3 Force feedback rendering

In impedance systems, such as the mass-spring-damper in (3.35), interactions are captured by both $\mathbf{f}_e^{\mathcal{R}_e}$ and $\tilde{\mathbf{p}}^{\mathcal{R}_e}$. The former exhibits step dynamics, while the latter, being the result of a second-order system, is characterized by slower transients. Displaying $\mathbf{f}_e^{\mathcal{R}_e}$ directly would make the transient of the interaction event unperceivable for the human operator, who would have to cope with sudden force changes they are not used to from their previous experience of interacting with the environment. Therefore, in our rendering strategy, we replace the direct measurements $\mathbf{f}_e^{\mathcal{R}_e}$ with $\tilde{\mathbf{p}}^{\mathcal{R}_e}$, and define a second impedance model



(a) No contact state. **(b)** Collision state.

(c) Penetration state. **(d)** Saturation state.

Figure 3.8: Operation of the robot interaction control in the different contact states with the environment.

generating the haptic forces:

$$\mathbf{f}_h^{\mathcal{H}_b} = \mathbf{K}_h \tilde{\mathbf{p}}_h^{\mathcal{H}_b} + \mathbf{D}_h \tilde{\mathbf{p}}_h^{\mathcal{H}_b}, \tag{3.40}$$

where $\mathbf{K}_h$ and $\mathbf{D}_h$ respectively are stiffness and damping diagonal matrices of the proper size,

$$\tilde{\mathbf{p}}_h^{\mathcal{H}_b} = \mathbf{R}_{\mathcal{R}_b}^{\mathcal{H}_b} \tilde{\mathbf{p}}^{\mathcal{R}_b} = \mathbf{R}_{\mathcal{R}_b}^{\mathcal{H}_b} \left(\mathbf{p}_h^{\mathcal{R}_b} - \mathbf{p}_c^{\mathcal{R}_b} \right) \tag{3.41}$$

is the unsaturated position error, and:

$$\tilde{\mathbf{p}}_h^{\mathcal{H}_b} = \mathbf{R}_{\mathcal{R}_b}^{\mathcal{H}_b} \mathbf{R}_{\mathcal{R}_e}^{\mathcal{R}_b} \tilde{\mathbf{p}}^{\mathcal{R}_e} \tag{3.42}$$

its time derivative. The choice of using the unsaturated position error is motivated by the interest of not limiting the haptic feedback and exploring the full range of forces that can be exerted by the HD.

Indeed, the system in (3.40) takes the role of virtualizing the contact force and decoupling it from the admittance control dynamics. The parameters $\mathbf{K}_h$ and $\mathbf{D}_h$ are tuned to provide a sense of naturalness while the FR interacts with the environment, regardless of the actual degree of compliance of the onboard admittance controller. In particular, $\mathbf{K}_h$ can be tuned to ensure a desired transient response, while $\mathbf{D}_h$ can be tuned to reduce the vibrations that occur especially when the robot slips along the tangential directions.

3.4.2 Experiments

To validate the performance of the proposed HBTS and perform a quantitative assessment of different aspects of the system, we conduct blackboard writing experiments with chalk, using three different architectures. The chosen task is as simple as it is significative, since it requires a naturally-rendered force feedback to achieve accurate handwriting, as well as a precise control of interaction to ensure the integrity of the chalk, both of which are crucial requirements for, e.g. medical procedures.

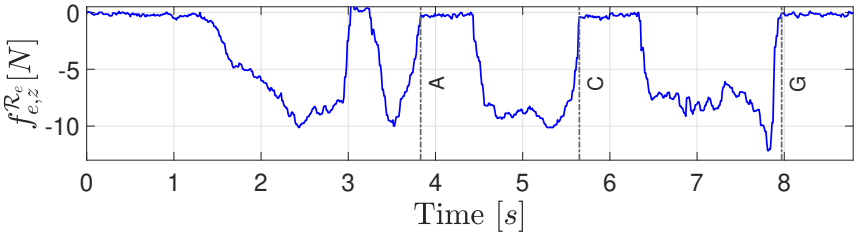


Figure 3.9: Human force profile representative of freehand writing for the sequence *A-C-G*.

With the aim of confirming the impact of the proposed HBTS on the naturalness of teleoperation and the safety of interaction, we compare the teleoperation experiments with manual handwriting, in terms of attained force profiles. Figure 3.9 shows a typical force profile of a freehand writing task, corresponding to the sequence of letters *A-C-G* (*Automatic Control Group*), recorded on a small force-sensed surface, oriented like a blackboard on the wall, as shown in Figure 3.10.

In order to compare the different architectures, we define three evaluation metrics: accuracy/continuity of the handwriting (qualitatively assessed) and similarity with human force profiles, in terms of the mean difference (MD) of the forces exerted by the human and robot, and of the absolute difference between their maximum values $\Delta\overline{f}_{e,z}^{\mathcal{R}_e}$:

$$MD = \left| \frac{1}{N} \sum_{i=1}^{N} {}^{hum} f_{e,z}^{\mathcal{R}_e}(i) - \frac{1}{M} \sum_{i=1}^{M} {}^{rob} f_{e,z}^{\mathcal{R}_e}(i) \right|, \tag{3.43}$$

$$\Delta\overline{f}_{e,z}^{\mathcal{R}_e} = \left| {}^{hum}\overline{f}_{e,z}^{\mathcal{R}_e} - {}^{rob}\overline{f}_{e,z}^{\mathcal{R}_e} \right|, \tag{3.44}$$

where M and N are the number of samples collected in the human and robot executions, respectively. The first term in

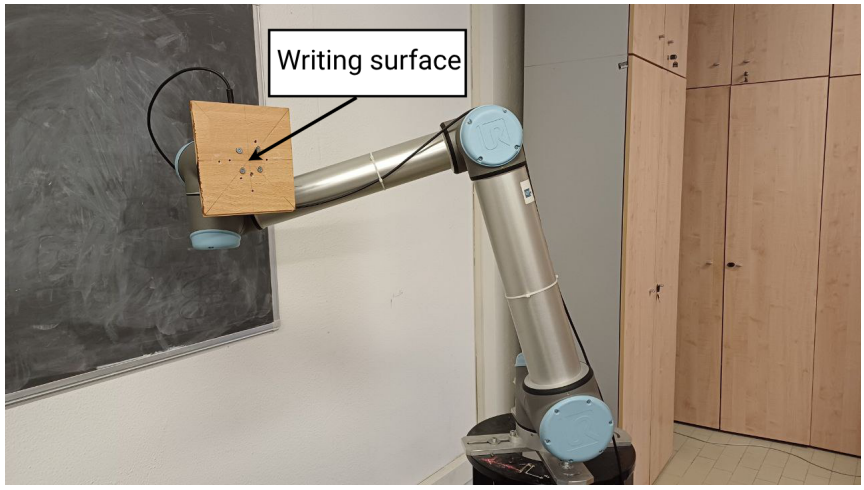


Figure 3.10: Experimental setup to record human force profiles.

(3.43) is $\mu_{hum} = -7.25\,N$, while ${}^{hum}\overline{f}_{e,z}^{\mathcal{R}_e} = -12.1600\,N$.

In Section 3.4.2.1, we report the results of the task execution through a HBTS, based on a P-Fm architecture, featuring a measurement-based force feedback (Scenario A). In such architecture the saturation of the admittance controller's motion references is disabled, therefore references beyond the maximum penetration are accepted and commanded. In Section 3.4.2.2, we report the results of the task execution through a HBTS, featuring the motion-error-based force feedback (Scenario B). As in the previous case, the references saturation is disabled. Finally, in Section 3.4.2.3, we report the results of the task execution through the HBTS proposed in this paper (Scenario C).

For all the scenarios, we set $\mathbf{M}_d = \text{diag}(50.0, 50.0, 50.0)$, $\mathbf{K}_D = \text{diag}(2500.0, 2500.0, 5000.0)$, $\mathbf{K}_P = \text{diag}(50000.0, 50000.0, 2500.0)$. Indeed, the task requires large compliance and modest damping



(a) Scenario A. **(b)** Scenario B. **(c)** Scenario C.

Figure 3.11: Outcomes of the blackboard writing task execution in the three scenarios.

along the normal axis, and greater positional accuracy along tangential axes.

Regarding the virtualization of the force feedback, employed in the last two scenarios, the impedance matrices of the HC are tuned to ensure a sense of naturalness for the human operator, both in terms of transient response and vibrations reduction. Thus, we set $\mathbf{K}_h = \text{diag}(100.0, 100.0, 100.0)$ and $\mathbf{D}_h = \text{diag}(0.1, 0.1, 0.1)$.

3.4.2.1 Force/torque measure-based force feedback

In order to assess the improved naturalness of the proposed virtualized force feedback, we execute the task with the typical rendering strategy directly from the force sensed at the robot's end-effector (P-Fm architecture). We adopt a non-linear mapping, based on hyperbolic cosine, to map such forces, in the order of tens of Newton, to the HD, so that they are in the order of units, and have a slower growth rate than linear mapping.

The chosen mapping is:

$$f_{h,j}^{\mathcal{H}_b} = \cosh\left(\frac{1}{\overline{f}_{e,j}^{\mathcal{H}_b}} \ln\left(4+\sqrt{15}\right) f_{e,j}^{\mathcal{H}_b}\right), \tag{3.45}$$

where

$$\mathbf{f}_e^{\mathcal{H}_b} = \mathbf{R}_{\mathcal{R}_b}^{\mathcal{H}_b}\mathbf{R}_{\mathcal{R}_e}^{\mathcal{R}_b}\mathbf{f}_e^{\mathcal{R}_e}, \tag{3.46}$$

$$\overline{\mathbf{f}}_e^{\mathcal{H}_b} = \mathbf{R}_{\mathcal{R}_b}^{\mathcal{H}_b}\mathbf{R}_{\mathcal{R}_e}^{\mathcal{R}_b}\overline{\mathbf{f}}_e^{\mathcal{R}_e}, \tag{3.47}$$

with $\overline{\mathbf{f}}_e^{\mathcal{R}_e}$ being the maximum expected contact force along each axis of the end-effector frame. For the task execution, we set the value of each component to $12\,N$.

We execute the task 3 times before obtaining a successful execution. The first 2 failures are due to the forces exerted exceeding the safety threshold, beyond which the robot stops and the chalk breaks or shatters.

The outcome of the successful execution is shown in Figure 3.11a. Visual inspection of the result showcases poor handwriting accuracy, with evident stroke discontinuities. This is due to the sudden changes in the force feedback causing strong backward pushes of the HD, resulting in a deterioration of writing performance. Regarding the interaction forces, Figure 3.12 highlights a highly oscillatory behavior, with $MD = 48.32\,N$ and $\Delta\overline{f}_{e,z}^{\mathcal{R}_e} = 80.40\,N$.

3.4.2.2 Virtualized force feedback without references saturation

Since we aim to overcome the limitations of measurement-based force feedback, we execute the task with the proposed virtualized force feedback. As for scenario A, the saturation of the admittance reference is disabled.

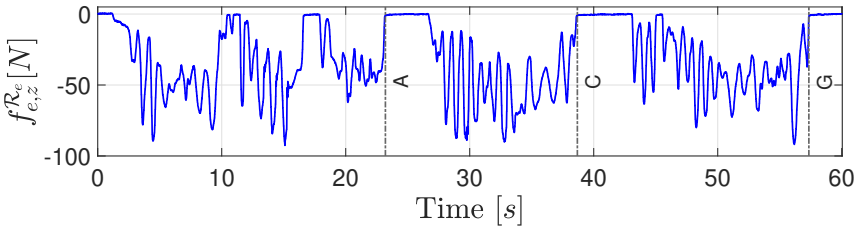


Figure 3.12: Interaction forces along the axis perpendicular to the blackboard plane in Scenario A.

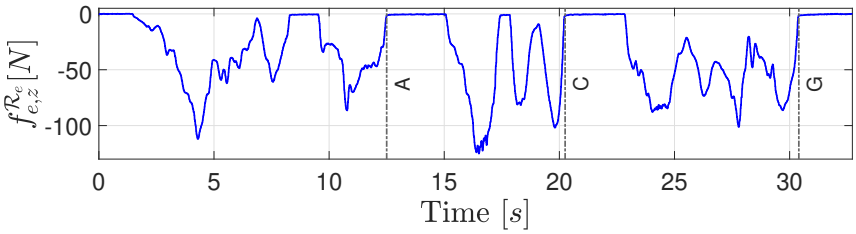


Figure 3.13: Interaction forces along the axis perpendicular to the blackboard plane in Scenario B.

We execute the task 2 times before obtaining a successful execution. Again, the first failure is due to the forces exerted exceeding the safety threshold.

The outcome of the successful task execution is shown in Figure 3.11b. Visual inspection of the result showcases a significant improvement in writing accuracy: indeed, the letters show an ideal height-to-width ratio [147], with significantly improved stroke continuity. Regarding the interaction forces, the overall results, shown in Figure 3.13, do not guarantee an improvement over Scenario A; on the contrary, $MD = 54.88\,N$ and $\Delta\overline{f}_{e,z}^{\mathcal{R}_e} = 137.21\,N$.

3.4.2.3 Virtualized force feedback with references saturation

In the last scenario, we execute the task by foreseeing both the virtualized force feedback rendering methodology and the saturation of the motion references provided to the admittance controller. For the execution of the procedure we define the saturation activation threshold along the axis perpendicular to the interaction plane to be $f_{th,x} = 12\,N$, corresponding to the maximum force exerted by the human operator in the freehand execution.

The task is successful on the first trial, whose outcome is shown in Figure 3.11c. As expected, the results are consistent with what was seen in the previous scenario. However, from Figure 3.14, we observe a significant reduction in contact forces, with $MD = 1.40\,N$ and $\Delta\overline{f}_{e,z}^{\mathcal{R}_e} = 14.22\,N$.

The impact of the architecture on the naturalness of execution can be captured from Figure 3.15, where the forces rendered on the HD in Scenario C are shown. Visual inspection of the result showcases a high similarity to the force profiles obtained from freehand writing, as well as slower dynamics than contact forces. This aspect improves both naturalness and comfort for the human operator.

3.5 Design of a HBTS for free-hand dental procedures

Building on the work presented in [75], in this section we introduce a novel HBTS [76], specifically conceived for free-hand dental procedures. The system integrates a new force-limitation strategy that, unlike the previous approach, is designed to op-

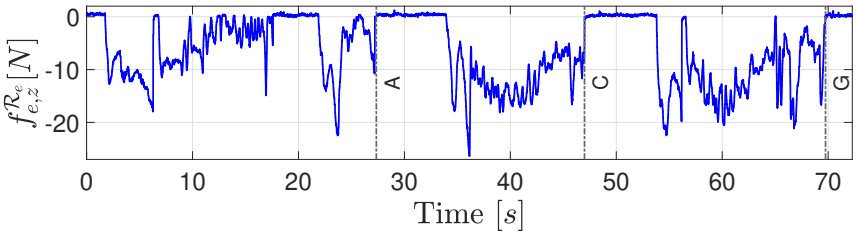


Figure 3.14: Interaction forces along the axis perpendicular to the blackboard plane in Scenario C.

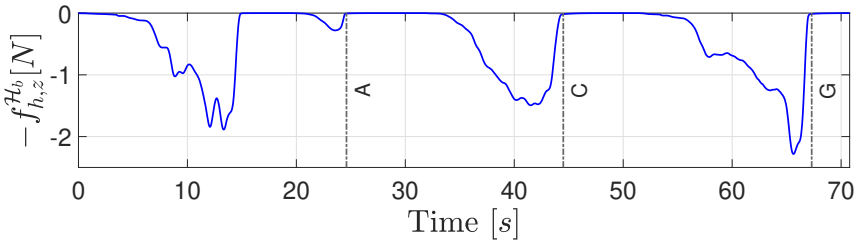


Figure 3.15: Forces rendered on the HD in Scenario C.

erate in unstructured environments without relying on prior knowledge of the environment. To improve visibility of the intervention site, the system features a dedicated mechanical end-effector that accommodates an eye-in-hand endoscopic camera, providing the visual feedback. The introduction of the latter required the design of an eye–hand coordination mapping strategy, which enables the human operator to perceive the motion correspondence between their movements and those of the end-effector observed in the camera view, thereby preserving manual dexterity and expertise.

3.5.1 Background

World Health Organization estimates that oral diseases affect nearly 3.5 billion people worldwide. However, access to primary oral health services is limited due to the high costs of procedures, the unequal distribution of oral health professionals, and the lack of adequate healthcare facilities [148].

Traditionally, routine, prosthetic, periodontal, and some surgical dental procedures are performed free-hand. Routine procedures include the treatment of dental caries and endodontic therapy, while prosthetic procedures focus on the replacement of teeth through the use of prostheses. These procedures involve the preparation of the tooth, which entails the removal of hard tissue using rotary instruments mounted on dental handpieces [149]. Periodontal procedures include scaling and root planing (SRP), i.e., the removal of plaque and calculus from the teeth and the smoothing of root surfaces, typically employing hand instruments and inserts mounted on sonic or ultrasonic handpieces [150]. Finally, although robotic computer-assisted implant surgery (r-CAIS) have shown a significant increase in the accuracy of dental implant placement, many operators still prefer the free-hand method for dental implantology [151]. Each of these procedures requires accuracy, extensively trained manual skills, and dexterity.

Remark 1 *The oral cavity is a highly unstructured environment, which is full of natural obstacles that occlude the view of the surgical site and reduce the space for maneuvering, requiring constant changes in the orientation of the clinical tool and the operator's posture.*

Therefore, the successful outcome of a procedure, as well as the comfort for the patient, depend on both human factors, i.e., the experience and skills of the human operator [152], the



Figure 3.16: Manual (left) vs teleoperated (right) dental procedures (pictorial views).

adequacy of the instrumentation used and the duration of the treatments [153], and environmental factors [154], as highlighted in Remark 1. In particular, the latter factors can significantly affect the operator's comfort. In [155] a high prevalence of musculoskeletal disorders among dentists is reported. The main causes of these disorders can be traced back to an incorrect application of ergonomics, such as awkward postures, repetitive and prolonged movements, use of small or narrow tool handles, exertion of forces on hard or sharp objects, and exposure to vibrations [156]. Hence, when training new operators, much emphasis is placed on learning skills related to space utilization and positioning of surgical and non-surgical instruments, e.g., mirrors, to overcome occlusions, while maintaining healthy and

comfortable postures [157]. In addition, to ensure the safety and effectiveness of the procedure, new operators must acquire skills related to the correct amount of pressure to apply to the site of interest, depending on the type of tool used.
Remark 2 *The sense of touch plays a key role in achieving successful and efficient procedures.*

This is also apparent from emerging trends in teaching, which make use of virtual environments and HDs for training new operators [158], [159].

In this context, the role of robots is to improve dental procedures, in terms of both patient satisfaction, i.e., broader access to care, reduced treatment time, and fast recovery, and operator comfort, i.e., reduced workload intensity, increased visibility of the surgical field, and improved ergonomics [160], as shown in Figure 3.16.

3.5.1.1 Related works

Haptic teleoperations are an enabling technology for the remote execution of complex tasks, employing a robotic system.
Remark 3 *Haptic teleoperations combine the robot skills with the flexibility, dexterity, and cognitive capabilities of humans, while overcoming barriers in terms of distance, hazardous environments, and scales beyond human reach.*

By providing multiple types of sensory information, i.e. visual and haptic feedback, HBTSs enable the human operator to experience *telepresence* [15]. Furthermore, by integrating different haptic feedback and guidance modalities [161], [162], and shared control approaches [163], they contribute to reducing errors and enhance the efficiency, accuracy and safety of procedures, while also improving operator comfort and confidence. For these

reasons, such technology is consolidated in, e.g., telesurgery, space exploration, and the handling of hazardous materials in nuclear or underwater environments. However, in the context of dentistry, its adoption is still very limited.

The majority of research in robotics for dentistry is focused on oral implantology [164], mainly because robotic implant surgery offers significant benefits in terms of implant accuracy in partially [165] or totally edentulous patients. Such technology also enables flapless implant placement, accelerating recovery time, reducing postoperative pain, and enhancing patient comfort [166]. [167] shows that a telerobotic-assisted drill can enhance accuracy while preserving awareness through an effective transmission of cutting forces and vibrations.

On the other hand, the state-of-the-art shows considerably less research effort in other free-hand procedures, a trend also highlighted in existing reviews of dental robotics [181], which report a strong imbalance in favor of implantology. Despite this imbalance, the literature reports evidence of the potential benefits of robotic technologies in free-hand dental procedures. Such evidence is analyzed in the following and summarized in Table 3.1. The analysis focuses on robotic systems explicitly developed for dental procedures and directly interacting with the oral environment, aiming at supporting or automating clinical free-hand procedures, while excluding works specifically addressing oral implantology. Only approaches supported by experimental, in vitro, or preliminary validation are considered, whereas purely virtual studies or robotic solutions not specifically tailored to dental procedures are not included.

In the context of prosthetic procedures, robotics can enhance the precision of manual grinding using a turbine drill during tooth preparation [168] and can compensate for hand tremors

Reference	Robotic system	Findings
	Prosthodontics	
[168]	Augmented reality-based tooth preparation-assisted robot	Improved accuracy in full crown adjacent surface preparation.
[169], [170]	Miniature robot for laser-based tooth crown preparation	Reduced hand tremor effects and improved accuracy through robotic laser control.
[171]	Miniature robotic end-effector for laser-based tooth preparation	Improved accuracy of laser dental preparation through trajectory tracking control
[172]	Robot-controlled ultrashort pulse laser system for tooth preparation	Increased efficiency and accuracy in tooth preparation.
[173]	Robotic tooth arrangement system for complete dentures	Improved precision in tooth arrangement.
[174]	Autonomous robotic system for veneer preparation	Improved accuracy in veneer preparation.
[175]	Automatic tooth preparation robotic device	Reliable automated crown preparation with controlled tool–tooth interaction.
	Endodontics	
[176], [177]	Autonomous endodontic microrobot	Automated and precise root canal access and manipulation.
[178]	Catalytic antimicrobial microrobots	Effective biofilm eradication addressing reinfection and biofilm recalcitrance.
[179]	Vision-guided robotic system for endodontic therapy	Accurate tool navigation enabled by visual guidance.
	Periodontology and oral hygiene assistance	
[180]	Force-regulated robotic system for tooth brushing	Safe physical interaction ensured by force–impedance control.

Table 3.1: Summary of robotic systems for free-hand dental procedures.

and the lack of tactile feedback in laser ablation [169], [170]. This can improve accuracy [171] and efficiency [172], and can enable automated tooth arrangement [173] and preparation for veneers and full crowns [174], [175]. In endodontics, robotics can automate and enhance precision and efficiency in root canal treatments [176], [177], outperforming current approaches also in effectively addressing biological and mechanical traits associated with biofilm recalcitrance and reinfection [178], and can support

visual-guided tool navigation [179]. In periodontal procedures, robots have the potential to increase accuracy, reducing the risk of errors and trauma to tissues by optimizing applied forces, as with other free-hand procedures. They can also improve the ergonomics for the operator, and comfort for the patient by reducing recovery time. However, for such procedures, robotic technologies are still lacking [182], and there is no empirical evidence of such advantages. Existing systems addressing force-regulated interaction with teeth are limited to adjacent tasks, such as tooth-brushing assistance [180], and are not designed for direct periodontal procedures.

Thus, although robotics shows promise in dental practice, several limitations remain. First, the quality of research is still insufficient in terms of clinical validation and technology readiness level (technology readiness level (TRL)) [183]. This is heavily influenced by the high costs of these systems and the need to ensure their compatibility with existing clinical tools [184]. Second, the most widespread robots are autonomous, which require the development of advanced capabilities in perception, recognition, and exception handling [184]. In this context, the presence of a human is still necessary not only as a supervisor but also as an operator. In light of Remark 2 and Remark 3, and considering the impact on the operator acceptance [185], haptic teleoperations represent a viable solution. Moreover, HBTSs would allow the acquisition of human control strategies directly exercised in the robot state space, simplifying the process of transferring the knowledge from the human to the robot [186] and enabling the effective and objective evaluation of operator skills during training [187]. However, as emerges from the literature analysis above, no robotic solutions based on haptic bilateral teleoperation have been reported for free-hand tasks. Finally, research tends to prioritize oral implantology over other

dental procedures, despite the high number of daily free-hand routine procedures and the less invasiveness, entailing better patient acceptance [188]. Considering these limitations, [181] recommends to shift the focus from oral implantology towards less invasive procedures, which are better suited as forerunners in the field, and also to invest in educational robotics research as a valuable tool to overcome the barrier of acceptance of robotic systems among future dentists.

3.5.1.2 Contributions

Motivated by the limitations or complete absence of robotic solutions for the most repetitive free-hand dental procedures, and in light of the advantages introduced by haptic teleoperations, as in Remark 3, we propose a HBTS for free-hand dental procedures (haptic bilateral teleoperation system for free-hand dental procedures (FH-HBTS)). The proposed system features a custom designed end-effector, compatible with existing clinical tools, and a dedicated haptic control system that ensures procedural safety, improves accuracy, and preserves manual dexterity. Therein, key contributions are: (1) an eye-hand coordination controller providing both motion and force correspondence between the HD's workspace and the video stream coming from the eye-in-hand camera; with respect to existing HBTSs, such mapping is bilateral and drift-free, even after prolonged teleoperation sessions; (2) a force limitation strategy effectively reducing interaction forces; with respect to existing HBTSs, this strategy needs no previous assumption or online estimation of the environment geometry, therefore accounting for the challenges outlined in Remark 1; notably, this strategy is part of the onboard robot controller and is therefore compatible with passivity-based teleoperations; (3) an integrated TRL-5 system

for free-hand dental procedures, validated on SRP, demonstrating technical feasibility and clinical suitability.

In light of the inclusion and exclusion criteria defined in Section 3.5.1.1, to the best of the authors' knowledge, this is the first HBTS specifically complying with the special requirements of safety, accuracy, and dexterity characterizing free-hand dental procedures.

3.5.2 Preliminaries

3.5.2.1 Notation

We denote by $\mathbf{T}_b^a \in SE(3)$ the homogeneous transformation matrix from frame a to frame b, in the form:

$$\mathbf{T}_b^a = \begin{pmatrix} \mathbf{R}_b^a & \mathbf{p}_b^a \\ \mathbf{0}^\top & 1 \end{pmatrix}, \tag{3.48}$$

where $\mathbf{R}_b^a \in SO(3)$ is the rotation matrix from frame a to frame b, with $\mathbf{R}_a^b = (\mathbf{R}_b^a)^{-1} \equiv (\mathbf{R}_b^a)^\top$, and $\mathbf{p}_b^a \in \mathbb{R}^{3\times 1}$ represents b's origin in frame a.

We let $\mathbf{x}_b^a = \left[(\mathbf{p}_b^a)^\top, (\hbar_b^a)^\top\right]^\top$ be the pose of the frame b with respect to the frame a, corresponding to $\mathbf{T}_b^a$, where $\hbar_b^a \in \mathbb{H}_1$ is the quaternion associated with $\mathbf{R}_b^a$.

We denote by $\mathbf{R}_{\mathbf{a}}^{\mathcal{F}}(\alpha) \in SO(3)$ the elementary rotation of an angle α about a generic axis $\mathbf{a}$ of a frame $\mathcal{F}$.

We denote by $\mathbf{v}_b^a = \left[(\dot{\mathbf{p}}_b^a)^\top, (\boldsymbol{\omega}_b^a)^\top\right]^\top \in \mathbb{R}^{6\times 1}$ the twist of the frame b with respect to the frame a, where $\dot{\mathbf{p}}_b^a, \boldsymbol{\omega}_b^a \in \mathbb{R}^{3\times 1}$ are the linear and angular velocities, respectively.

We let $\mathbf{h}^a = \left[(\mathbf{f}^a)^\top, (\mathbf{m}^a)^\top\right]^\top \in \mathbb{R}^{6\times 1}$ be the wrench with respect to the frame a, where $\mathbf{f}^a, \mathbf{m}^a \in \mathbb{R}^{3\times 1}$ are the forces and momenta, respectively.

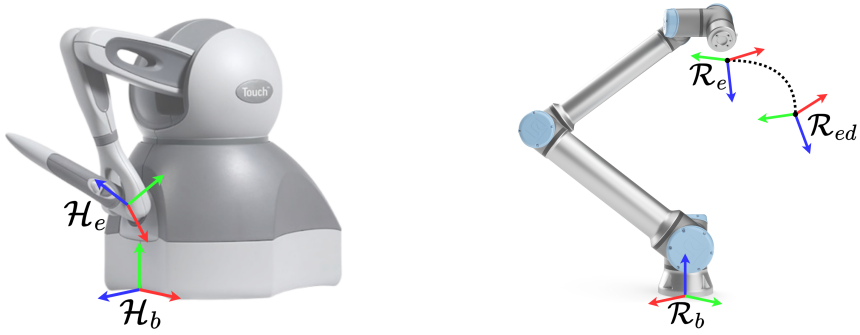


Figure 3.17: Haptic device and robot reference frames.

$\mathbf{I}_n$ indicates the $n \times n$ identity matrix.

3.5.2.2 Haptic device and robot reference frames

The frames used by the HD and the robot are reported in Figure 3.17. With regard to the HD, two frames are introduced: $\mathcal{H}_b$ is the base reference frame, in which the HD's stylus poses and the feedback forces are expressed; $\mathcal{H}_e$ is the HD's stylus frame. Regarding the robot, four frames are defined: $\mathcal{R}_b$ is the base reference frame, in which motion references are expressed; $\mathcal{R}_e$ is the robot's end-effector frame (computed from forward kinematics of joint measurements), corresponding to the tool center point (TCP); $\mathcal{R}_{ed}$ is the desired robot's end-effector frame, input to admittance control; $\mathcal{R}_c$ is the compliant frame, output by the admittance control law.

We note that, after admittance control, motion control guarantees that $\mathcal{R}_e$ tracks $\mathcal{R}_c$, as discussed next.

3.5.3 Methodology

The FH-HBTS we propose, shown in Figure 3.18, is based on a position-position architecture [189], coupling the LR and FR by means of a spring–damper, which is a passive element. Therefore, in the absence of communication delays, this architecture has the advantage of being intrinsically stable [190], [191]. A formal proof of absolute stability can be found in [192]. In the proposed design, we assume negligible time delays and packet losses and, accordingly, do not integrate passivity-based control approaches [40]. This choice is motivated both by the validity of this assumption in healthcare facilities and by the conservative nature of passivity-based methods, which are known to worsen transparency and system usability in order to ensure stability under adverse network conditions [193]. Indeed, in precision free-hand dental procedures, this trade-off is generally undesirable, as it may impair fine force discrimination and the naturalness of the interaction. Nevertheless, the management of communication delays and packet losses represents an orthogonal direction to the one investigated in this work. Indeed, under non-ideal network conditions, the proposed architecture can be readily extended to enforce time-domain passivity of the communication channel, for instance by adopting a TDPA-based approach [38], as demonstrated in Section 3.5.4.3.

The LR is an impedance HD, sensing the pose of the operator and rendering haptic feedback according to the remote interaction between the FR and the environment. The HD is controlled by a leader controller, featuring an eye-hand coordination controller (EHCC) and a haptic feedback controller (HFC). The former is responsible for capturing the HD's stylus poses, filtering human tremors, and generating the corresponding robot end-effector poses, so that the robot follows the stylus

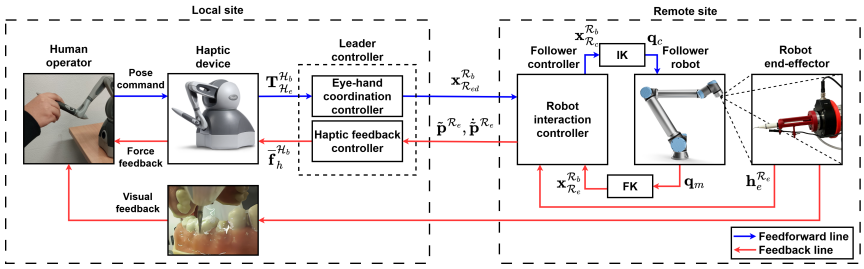


Figure 3.18: Haptic bilateral teleoperation system scheme.

motion in coordination with the visual feedback. The latter is responsible for rendering the force feedback on the HD to let the human operator perceive the remote environment. Both controllers record data throughout the entire procedure. The FR is a position-controlled robot, instructed to track the HD through an admittance controller, which provides a configurable degree of compliance on its target pose with respect to the environment and improves safety through dedicated mechanisms and emergency protocols.

With reference to Figure 3.18, depicting the complete system, the following sections examine its individual subcomponents in detail. Section 3.5.3.1 and Section 3.5.3.3 provide a detailed description of the objectives and operation of the EHCC and HFC controllers. Section 3.5.3.2 describes the robot interaction control. Finally, Section 3.5.3.4 presents the design of the mechanical end-effector for the FR.

3.5.3.1 Eye-hand coordination controller

In a HBTS, visual feedback plays a crucial role in overcoming the limitations caused by distance. In teleoperated free-hand dental procedures, using an eye-in-hand camera is the most effective

solution [194]. This approach enables the operator to maintain a consistently centered view of the operative field, offering a significant advantage over eye-to-hand camera configurations, where the view may be off-center with respect to the area of interest or obstructed by physical obstacles. In this context, the human operator relies on the video of the camera to command the FR via the HD. However, in the eye-in-hand configuration, a rotation of the tool (unavoidable, to preserve dexterity) causes a rotation of the viewing angle, whose lack of compensation results in a loss of both motion and force correspondence between the movements and perceived interaction expected by the operator and those actually executed by the robot in the camera view. This highlights the importance of an appropriate coupling.

The literature shows that this coupling can be achieved through simple kinematic transformations and scaling strategies [74]. Common mapping strategies include position control, workspace drift control [130], and rate control [195] which define how the operator's motions are translated into robot commands, complemented by force scaling [74] to map the interaction forces into the range of forces that the HD can exert. However, these methods generally neglect viewing angle effects, relying on display-level compensation and thus compromising force correspondence. Indeed, the da Vinci Surgical System^{TM}, which requires the insertion of multiple tools to implement an eye-to-hand strategy, thereby increasing bulk and cost of the equipment, provides the motion correspondence by projecting the endoscope image above the surgeon's hands by means of mirrored overlay optics [196]. In a similar manner, in eye-in-hand cases, motion correspondence is typically achieved by aligning the visual feedback with the operator's control frame through online compensation of camera–control frame misalignment in the displayed view [197].

To overcome this limitation, we introduce an eye–hand coordination mapping preserving both motion and force correspondence. Within the proposed EHCC, this mapping is implemented through a view-consistent transfer of the HD twist to the FR and incorporates dynamic scaling factors to improve control accuracy according to task requirements. To enhance the naturalness of the teleoperation, a rotational coupling is also established between the HD's stylus and the FR's TCP. This includes defining the desired relative rotation $\mathbf{R}_{\mathcal{R}_e}^{\mathcal{H}_e}$, and aligning manually. This is done by the human operator during what we indicate as the *engagement phase*.

The latter is presented in Section 3.5.3.1.1, while the human tremors filtering and the eye-hand coordination mapping, implementing the motion correspondence, are discussed in Section 3.5.3.1.2 and Section 3.5.3.1.3, respectively. The eye-hand coordination implementing the force correspondence is described in Section 3.5.3.3.

3.5.3.1.1 Engagement phase During the engagement phase, the EHCC retrieves the homogeneous transformation matrix of the HD's stylus $\mathbf{T}_{\mathcal{H}_e}^{\mathcal{H}_b}(k)$, and converts it into a robot's end-effector homogeneous transformation matrix with the following kinematic equations:

$$\mathbf{R}_{\mathcal{R}_{ed}}^{\mathcal{R}_b}(k) = \mathbf{R}_{\mathcal{H}_b}^{\mathcal{R}_b}\mathbf{R}_{\mathcal{H}_e}^{\mathcal{H}_b}(k)\mathbf{R}_{\mathcal{R}_e}^{\mathcal{H}_e}, \tag{3.49}$$

$$\mathbf{p}_{\mathcal{R}_{ed}}^{\mathcal{R}_b}(k) = \mathbf{p}_{\mathcal{R}_e}^{\mathcal{R}_b}(k), \tag{3.50}$$

where $\mathbf{R}_{\mathcal{H}_b}^{\mathcal{R}_b}$ is the fixed rotation between $\mathcal{H}_b$ and $\mathcal{R}_b$. We note that the position of the HD's stylus is not relevant for coupling, so it is converted to the current position of the robot's TCP. The obtained frame $\mathcal{R}_{ed}$ is real-time displayed in a visualization tool, together with the actual robot end-effector one $\mathcal{R}_e$, as shown in

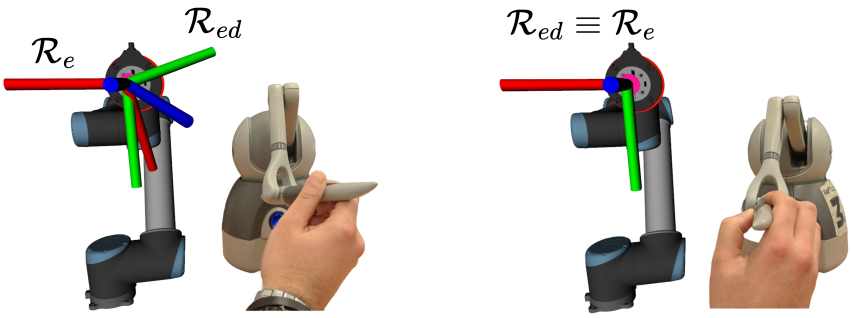


Figure 3.19: Engagement phase supported by the visualization tool.

Figure 3.19, so that the human operator, by acting on $\mathcal{H}_e$, can align the frame $\mathcal{R}_{ed}$ with the frame $\mathcal{R}_e$. Once the alignment is accomplished, i.e., $\mathbf{R}_{\mathcal{R}_b}^{\mathcal{R}_e}(k)\mathbf{R}_{\mathcal{R}_{ed}}^{\mathcal{R}_b}(k) = \mathbf{I}_3$, the engagement phase ends, i.e., HD and FR are aligned, and the human operator can begin teleoperation.

3.5.3.1.2 Human tremors filtering At each control cycle, the EHCC retrieves the actual pose $\mathbf{x}_{\mathcal{H}_e}^{\mathcal{H}_b}(k)$ of the HD's stylus, corresponding to $\mathbf{T}_{\mathcal{H}_e}^{\mathcal{H}_b}(k)$. Exploiting such a pose to generate a command for the robot would result in transferring the human hand tremors, further accentuated by the control frequency. Therefore, $\mathbf{x}_{\mathcal{H}_e}^{\mathcal{H}_b}(k)$ is filtered online by a moving average filter for poses. At the k-th control cycle, the filtered position is obtained as $\overline{\mathbf{p}}_{\mathcal{H}_e}^{\mathcal{H}_b}(k) = \mathbf{s}(k)/m$, where $m \leq n$ is the number of collected samples at the k-th control cycle in the moving average window of size n, and $\mathbf{s}(k)$ is their cumulative sum:

$$\mathbf{s}(k) = \mathbf{s}(k-1) + \mathbf{p}_{\mathcal{H}_e}^{\mathcal{H}_b}(k) - \begin{cases} 0, & \text{if } k < n; \\ \mathbf{p}_{\mathcal{H}_e}^{\mathcal{H}_b}(k-n), & \text{otherwise.} \end{cases} \tag{3.51}$$

The filtered quaternion $\overline{\mathbf{h}}_{\mathcal{H}_e}^{\mathcal{H}_b}(k)$ is the eigenvector associated with

the maximum eigenvalue of $\mathbf{M}(k) = \mathbf{C}(k)/m$ [144], where $\mathbf{C}(k)$ is the cumulative sum of samples within the window, updated at each control cycle:

$$\mathbf{C}(k) = \begin{cases} \mathbf{C}(k-1) + \hbar_{\mathcal{H}_e}^{\mathcal{H}_b}(k)\big[\hbar_{\mathcal{H}_e}^{\mathcal{H}_b}(k)\big]^\top, & \text{if } k < n; \\ \mathbf{C}(k-1) + \hbar_{\mathcal{H}_e}^{\mathcal{H}_b}(k)\big[\hbar_{\mathcal{H}_e}^{\mathcal{H}_b}(k)\big]^\top + & \\ \quad -\hbar_{\mathcal{H}_e}^{\mathcal{H}_b}(k-n)\big[\hbar_{\mathcal{H}_e}^{\mathcal{H}_b}(k-n)\big]^\top, & \text{otherwise.} \end{cases} \tag{3.52}$$

Keeping the cumulative sums $\mathbf{s}(k)$ and $\mathbf{C}(k)$ enables achieving $\mathcal{O}(1)$ computational complexity.

3.5.3.1.3 Eye-hand coordination Let $\Delta\overline{\mathbf{p}}_{\mathcal{H}_e}^{\mathcal{H}_b}(k)$ be the HD's displacement:

$$\Delta\overline{\mathbf{p}}_{\mathcal{H}_e}^{\mathcal{H}_b}(k) = \overline{\mathbf{p}}_{\mathcal{H}_e}^{\mathcal{H}_b}(k) - \overline{\mathbf{p}}_{\mathcal{H}_e}^{\mathcal{H}_b}(k-1), \tag{3.53}$$

and $\overline{\mathbf{R}}_{\mathcal{H}_e(k)}^{\mathcal{H}_e(k-1)}$ the relative rotation obtained from

$$\overline{\hbar}_{\mathcal{H}_e(k)}^{\mathcal{H}_e(k-1)} = \big[\overline{\hbar}_{\mathcal{H}_e}^{\mathcal{H}_b}(k-1)\big]^\top \overline{\hbar}_{\mathcal{H}_e}^{\mathcal{H}_b}(k). \tag{3.54}$$

At each control cycle, the EHCC computes the HD's stylus twist:

$$\mathbf{v}_{\mathcal{H}_e}^{\mathcal{H}_b}(k) = T_s^{-1}\left[\Delta\overline{\mathbf{p}}_{\mathcal{H}_e}^{\mathcal{H}_b}(k)^\top, \;\; \vartheta\mathbf{r}^\top\right]^\top, \tag{3.55}$$

where $T_s \in \mathbb{R}_+$ is the control period, and $\mathbf{r} \in \mathbb{R}^{3\times 1}$ and $\vartheta \in \mathbb{R}$ are the axis-angle representation corresponding to $\overline{\mathbf{R}}_{\mathcal{H}_e(k)}^{\mathcal{H}_e(k-1)}$, respectively.

From (3.55), the corresponding desired FR's end-effector twist is obtained as:

$$\begin{aligned} \mathbf{v}_{\mathcal{R}_{ed}}^{\mathcal{R}_b}(k) = &\big(\mathbf{I}_2 \otimes \mathbf{R}_{\mathcal{R}_e}^{\mathcal{R}_b}(k)\big)\Big\{\mathbf{\Lambda}\Big[\big(\mathbf{I}_2 \otimes \mathbf{R}_{\mathcal{H}_e}^{\mathcal{R}_e}(k)\big) \\ &\cdot\big(\mathbf{I}_2 \otimes \mathbf{R}_{\mathcal{H}_b}^{\mathcal{H}_e}(k)\big)\mathbf{v}_{\mathcal{H}_e}^{\mathcal{H}_b}(k)\Big]\Big\}. \end{aligned} \tag{3.56}$$

where $\otimes$ denotes the Kronecker product, $\mathbf{\Lambda} \in \mathbb{R}^{6\times6}$ is the scaling diagonal matrix with $\mathbf{\Lambda}_{4:6,4:6} = \mathbf{I}_3$, and

$$\mathbf{R}_{\mathcal{H}_e}^{\mathcal{R}_e}(k) = \mathbf{R}_{\mathbf{z}}^{\mathcal{R}_e}\big(\varphi(k)\big)\mathbf{R}_{\mathcal{H}_e}^{\mathcal{R}_e}. \tag{3.57}$$

We note that $\mathbf{R}_{\mathcal{H}_e}^{\mathcal{R}_e}$ is the fixed rotation defining the mapping between quantities in $\mathcal{H}_e$ and $\mathcal{R}_e$, and $\mathbf{z}$ is the axis of $\mathcal{R}_e$, which we assume to coincide with the optical axis of the camera $\mathbf{o}$ in $\mathcal{R}_e$ for negligible values of the camera tilt angle. Therefore, a rotation of $\varphi(k)$ about the $\mathbf{z}$ axis of $\mathcal{R}_e$ results in a viewing angle of $\varphi(k)$. The $\mathbf{z}$ axis of $\mathcal{R}_e$ is mapped to the $\mathbf{z}$ axis of $\mathcal{H}_e$, according to $\mathbf{R}_{\mathcal{H}_e}^{\mathcal{R}_e}$. Hence, in the absence of compliance along rotational axes, the same behavior is achieved by rotating of $\varphi(k)$ about the $\mathbf{z}$ axis of $\mathcal{H}_e$, as shown in Figure 3.20, and (3.57) can be equivalently written as:

$$\mathbf{R}_{\mathcal{H}_e}^{\mathcal{R}_e}(k) = \mathbf{R}_{\mathcal{H}_e}^{\mathcal{R}_e}\mathbf{R}_{\mathbf{z}}^{\mathcal{H}_e}\big(\varphi(k)\big). \tag{3.58}$$

The rotation $\mathbf{R}_{\mathbf{z}}^{\mathcal{R}_e}\big(\varphi(k)\big)$, or equivalently $\mathbf{R}_{\mathbf{z}}^{\mathcal{H}_e}\big(\varphi(k)\big)$, ensures the motion correspondence between the operator's movements and those of the FR's TCP in the camera view, by appropriately rotating the desired velocities according to the viewing angle. By setting $\mathbf{R}_{\mathbf{z}}^{\mathcal{R}_e}(\varphi(k)) = \mathbf{I}_3$ (or equivalently $\mathbf{R}_{\mathbf{z}}^{\mathcal{H}_e}(\varphi(k)) = \mathbf{I}_3$) the mapping between twists becomes viewing angle independent:

$$\mathbf{R}_{\mathcal{H}_e}^{\mathcal{R}_e}(k) = \mathbf{R}_{\mathcal{H}_e}^{\mathcal{R}_e}, \quad \forall k \in \mathbb{N}_0. \tag{3.59}$$

We note that the angle $\varphi(k)$ is obtained from the exact measurements provided by the FR's forward kinematics (or equivalently by the HD's). For this reason, even during prolonged procedures, no orientation drift is accumulated, and motion correspondence is consistently preserved.

The desired FR's TCP homogeneous transformation $\mathbf{T}_{\mathcal{R}_{ed}}^{\mathcal{R}_b}(k)$ is obtained by numerically integrating the desired twist in (3.56).

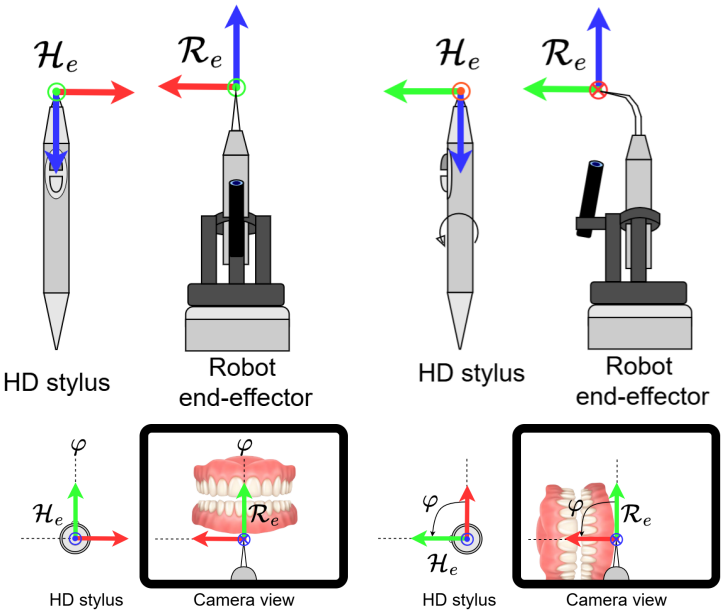


Figure 3.20: Visualization of the rotational coupling between $\mathcal{H}_e$ and $\mathcal{R}_e$: (top) top view; (bottom) user view; (left) $\varphi = 0$; (right) $\varphi = \pi/2$.

As for the desired rotation $\mathbf{R}^{\mathcal{R}_b}_{\mathcal{R}_{ed}}(k)$, it is

$$\mathbf{R}^{\mathcal{R}_b}_{\mathcal{R}_{ed}}(k) = \mathbf{R}^{\mathcal{R}_b}_{\mathcal{R}_e}(k-1)\mathbf{R}^{\mathcal{R}_e(k-1)}_{\mathcal{R}_{ed}(k)}, \tag{3.60}$$

where $\mathbf{R}^{\mathcal{R}_e(k-1)}_{\mathcal{R}_{ed}(k)}$ is the rotation matrix corresponding to the axis $\frac{\mathbf{r}}{\|\mathbf{r}\|}$ and angle ϑ:

$$\mathbf{r} = \mathbf{R}^{\mathcal{R}_e}_{\mathcal{R}_b}(k-1)\big(\boldsymbol{\omega}^{\mathcal{R}_b}_{\mathcal{R}_{ed}}(k)T_s\big), \quad \vartheta = \|\mathbf{r}\|\,. \tag{3.61}$$

As for the desired position $\mathbf{p}^{\mathcal{R}_b}_{\mathcal{R}_{ed}}(k)$, it is obtained as:

$$\mathbf{p}^{\mathcal{R}_b}_{\mathcal{R}_{ed}}(k) = \mathbf{p}^{\mathcal{R}_b}_{\mathcal{R}_{ed}}(k-1) + \dot{\mathbf{p}}^{\mathcal{R}_b}_{\mathcal{R}_{ed}}(k)T_s. \tag{3.62}$$

From $\mathbf{T}^{\mathcal{R}_b}_{\mathcal{R}_{ed}}(k)$ the desired FR's TCP pose is obtained as:

$$\mathbf{x}^{\mathcal{R}_b}_{\mathcal{R}_{ed}}(k) = \left[\mathbf{p}^{\mathcal{R}_b}_{\mathcal{R}_{ed}}(k)^\top, \quad \hbar^{\mathcal{R}_b}_{\mathcal{R}_{ed}}(k)^\top\right]^\top. \tag{3.63}$$

The eye-hand coordination mapping and scaling can be turned into an algorithmic procedure as described in Algorithm 1.

Algorithm 1 Eye-hand coordination mapping and scaling

Input: The HD's actual $\overline{\mathbf{x}}^{\mathcal{H}_b}_{\mathcal{H}_e}(k)$ and previous $\overline{\mathbf{x}}^{\mathcal{H}_b}_{\mathcal{H}_e}(k-1)$ filtered poses, and the previous desired pose $\mathbf{x}^{\mathcal{R}_b}_{\mathcal{R}_{ed}}(k-1)$

Output: The desired FR's TCP pose $\mathbf{x}^{\mathcal{R}_b}_{\mathcal{R}_{ed}}(k)$

1: Compute $\mathbf{v}^{\mathcal{H}_b}_{\mathcal{H}_e}(k)$ using (3.55)

2: Compute $\mathbf{v}^{\mathcal{R}_b}_{\mathcal{R}_{ed}}(k)$ using (3.56):

1. Convert $\mathbf{v}^{\mathcal{H}_b}_{\mathcal{H}_e}(k)$ into $\mathbf{v}^{\mathcal{R}_e}_{\mathcal{R}_{ed}}(k)$ and rotate it according to the viewing angle using (3.57):

$$\mathbf{v}^{\mathcal{R}_e}_{\mathcal{R}_{ed}}(k) := \left(\mathbf{I}_2 \otimes \mathbf{R}^{\mathcal{R}_e}_{\mathcal{H}_e}(k)\right)\left(\mathbf{I}_2 \otimes \mathbf{R}^{\mathcal{H}_e}_{\mathcal{H}_b}(k)\right)\mathbf{v}^{\mathcal{H}_b}_{\mathcal{H}_e}(k)$$

2.Scale $\mathbf{v}^{\mathcal{R}_e}_{\mathcal{R}_{ed}}(k)$ using $\mathbf{\Lambda}$ and convert it into $\mathbf{v}^{\mathcal{R}_b}_{\mathcal{R}_{ed}}(k)$:

$$\mathbf{v}^{\mathcal{R}_b}_{\mathcal{R}_{ed}}(k) = \left(\mathbf{I}_2 \otimes \mathbf{R}^{\mathcal{R}_b}_{\mathcal{R}_e}(k)\right)\left(\mathbf{\Lambda}\mathbf{v}^{\mathcal{R}_e}_{\mathcal{R}_{ed}}(k)\right)$$

3: Compute $\mathbf{T}^{\mathcal{R}_b}_{\mathcal{R}_{ed}}(k)$ from $\mathbf{v}^{\mathcal{R}_b}_{\mathcal{R}_{ed}}(k)$ using (3.60) and (3.62)

4: Extract $\mathbf{x}^{\mathcal{R}_b}_{\mathcal{R}_{ed}}(k)$ from $\mathbf{T}^{\mathcal{R}_b}_{\mathcal{R}_{ed}}(k)$

3.5.3.2 Robot interaction control

In this section, we first formalize the contact model between the robot and the environment (Section 3.5.3.2.1), and subsequently, we present the free-hand strategy for limiting the interaction forces (Section 3.5.3.2.2) and the other safety mechanisms embedded in the controller (Section 3.5.3.2.3).

3.5.3.2.1 Admittance model Let $\mathbf{x}_{\mathcal{R}_{ed}}^{\mathcal{R}_b}(k)$ be the desired pose and $\mathcal{R}_c$ the compliant frame specified by the quantities $\mathbf{p}_{\mathcal{R}_c}^{\mathcal{R}_{ed}}(k)$, $\mathbf{\hbar}_{\mathcal{R}_c}^{\mathcal{R}_{ed}}(k)$, $\mathbf{v}_{\mathcal{R}_c}^{\mathcal{R}_{ed}}(k)$, $\dot{\mathbf{v}}_{\mathcal{R}_c}^{\mathcal{R}_{ed}}(k)$. When the FR interacts with the environment, $\mathcal{R}_c$ can be completely defined in $\mathcal{R}_{ed}$ by integrating the mechanical impedance equation:

$$\mathbf{M}_d\dot{\mathbf{v}}_{\mathcal{R}_c}^{\mathcal{R}_{ed}}(k) + \mathbf{K}_D\mathbf{v}_{\mathcal{R}_c}^{\mathcal{R}_{ed}}(k) + \mathbf{K}_P\mathbf{x}_{\mathcal{R}_c}^{\mathcal{R}_{ed}}(k) = -\tilde{\mathbf{h}}^{\mathcal{R}_{ed}}(k), \quad (3.64)$$

where $\mathbf{M}_d, \mathbf{K}_D, \mathbf{K}_P \in \mathbb{R}^{6\times6}$ are the mass, damping, and stiffness diagonal matrices, respectively, which are used to impose specific second-order mass-spring-damper dynamics; $\tilde{\mathbf{h}}^{\mathcal{R}_{ed}}(k) = \mathbf{h}_d^{\mathcal{R}_{ed}}(k) - \mathbf{h}_e^{\mathcal{R}_{ed}}(k)$ is the wrench tracking error, defined as the difference between the desired wrench $\mathbf{h}_d^{\mathcal{R}_{ed}}(k)$ and the exerted one $\mathbf{h}_e^{\mathcal{R}_{ed}}(k)$, which is equal and opposite to the measured wrench. We take $\mathbf{h}_d^{\mathcal{R}_{ed}}(k) = \mathbf{0}, \forall k \in \mathbb{N}_0$ to make the robot behave compliantly with the environment.

3.5.3.2.2 Free-hand force limitation strategy In an admittance-controlled system, the interaction wrenches emerge from the combination of the admittance parameters, the mechanical properties of the environment, and the reference provided to the controller [121]. It follows that interaction forces can be limited through a suitable reference $\mathbf{x}_{\mathcal{R}_{ed}}^{\mathcal{R}_e}$. Accurate limitation requires perfect knowledge of the environment that is particularly challenging to achieve, especially in a medical environment, in which the FR interacts with surfaces of varying stiffness and non-uniform geometry. Therefore, in the proposed strategy, the position reference

$$\mathbf{p}_{\mathcal{R}_{ed}}^{\mathcal{R}_e}(k) = \mathbf{R}_{\mathcal{R}_b}^{\mathcal{R}_e}(k)\mathbf{p}_{\mathcal{R}_{ed}}^{\mathcal{R}_b}(k) - \mathbf{R}_{\mathcal{R}_b}^{\mathcal{R}_e}(k)\mathbf{p}_{\mathcal{R}_e}^{\mathcal{R}_b}(k), \quad (3.65)$$

is dynamically scaled based solely on the contact forces:

$$\underline{\mathbf{p}}_{\mathcal{R}_{ed}}^{\mathcal{R}_e}(k) = \frac{1}{1 + K_s\|\mathbf{f}_e^{\mathcal{R}_e}(k)\|}\mathbf{p}_{\mathcal{R}_{ed}}^{\mathcal{R}_e}(k), \quad (3.66)$$

where $K_s \in \mathbb{R}_+$ is a proportional gain representing a trade-off between smoothness and responsiveness of the scaling action. Indeed, K_s close to 0 reduces sudden variations of $\underline{\mathbf{p}}^{\mathcal{R}_e}_{\mathcal{R}_{ed}}(k)$, even in presence of noisy force measures, but provides less force-limiting action. On the other hand, K_s significantly greater than 0 makes the scaling action more responsive, but may yield oscillations in the presence of noisy measurements. Therefore, to increase the system's robustness to noisy forces, exhibiting high-frequency variations, $\mathbf{f}_e^{\mathcal{R}_e}$ is filtered online as done for positions in (3.51). We note that the strategy in (3.66) does not allow forces to be bounded below a predefined limit. However, it prevents contact forces from growing indefinitely, ensuring a limitation even in the transients of the interaction and for any orientation of the end-effector, without relying on the knowledge of the dental environment's complex geometry.

From a control theory perspective, it is appropriate to draw an analogy between the proposed strategy and passivity-based methods, such as TDPA [38], as both rely on modulating the reference provided to the downstream controller through an adaptive damping mechanism. However, a substantial difference exists in terms of control objectives. While passivity-based approaches provide an event-triggered modulation of the reference in response to violations of the energy balance, with the explicit goal of guaranteeing system passivity, the proposed strategy implements a continuous, non-energizing, force-driven reference modulation aimed at reducing interaction forces, without relying on explicit energy estimation. As a consequence, its attenuative and smoothly varying action on the reference, resulting from an appropriate choice of the gain K_s and of the force filtering window, does not inject energy into the system, nor does it alter the underlying dynamics, in contrast to state-of-the-art variable admittance–based approaches [121], [122], which explicitly

modify the controller dynamics and typically rely on explicit knowledge of the environment [146]. As a result, the stability properties of the admittance-controlled interaction remain unaffected. Moreover, as discussed above, passivity-based control addresses an orthogonal objective to the proposed approach, and can therefore be combined with the eye–hand coordination and force limitation strategies to guarantee stability even in the presence of considerable communication delays. We consider this scenario in Section 3.5.4.3.

3.5.3.2.3 Safety mechanisms and emergency stop protocols From (3.64) and (3.66), the compliant pose $\mathbf{x}_{\mathcal{R}_c}^{\mathcal{R}_b}(k)$ to be commanded to the robot is obtained. Specifically,

$$\mathbf{p}_{\mathcal{R}_c}^{\mathcal{R}_b}(k) = \underline{\mathbf{p}}_{\mathcal{R}_{ed}}^{\mathcal{R}_b}(k) + \mathbf{R}_{\mathcal{R}_{ed}}^{\mathcal{R}_b}(k)\mathbf{p}_{\mathcal{R}_c}^{\mathcal{R}_{ed}}(k), \tag{3.67}$$

$$\mathbf{\hbar}_{\mathcal{R}_c}^{\mathcal{R}_b}(k) = \mathbf{\hbar}_{\mathcal{R}_{ed}}^{\mathcal{R}_b}(k)\mathbf{\hbar}_{\mathcal{R}_c}^{\mathcal{R}_{ed}}(k), \tag{3.68}$$

where $\mathbf{x}_{\mathcal{R}_c}^{\mathcal{R}_{ed}}$, taking the semantics of a pose error, is obtained by time-integrating $\dot{\mathbf{v}}_{\mathcal{R}_c}^{\mathcal{R}_{ed}}$ from (3.64) twice. In addition to its compliant interaction properties and the embedded force limitation strategy, the controller incorporates two safety mechanisms and implements an emergency stop protocol. Regarding the safety mechanisms, the first ensures the stability of the FR in the absence of updated references from the EHCC $\mathbf{x}_{\mathcal{R}_{ed}}^{\mathcal{R}_b}(k)$, such as in the event of a communication loss, by continuing to track the last valid one $\mathbf{x}_{\mathcal{R}_{ed}}^{\mathcal{R}_b}(k-1)$. The second mechanism prevents abrupt motions of the FR by commanding $\mathbf{x}_{\mathcal{R}_e}^{\mathcal{R}_b}(k)$ whenever the generated command $\mathbf{x}_{\mathcal{R}_c}^{\mathcal{R}_b}(k)$ deviates excessively, either in translation or orientation, based on translational and rotational safety thresholds that can be configured by the operator according to the task requirements. With regard to the emergency stop, it focuses on the monitoring of the interaction forces. Whenever

$\|\mathbf{f}^{\mathcal{R}_e}\|(k)$ exceeds a predefined safety threshold f_{th}, the controller forwards $\mathbf{x}_{\mathcal{R}_e}^{\mathcal{R}_b}(k)$ as the new reference while continuing to compute the admittance control law. In this way, abrupt stopping is avoided, while still allowing the interaction forces to decrease progressively.

3.5.3.3 Haptic feedback controller

In performing medical procedures, the operator relies heavily on the sense of touch. Therefore, in a HBTS providing realistic haptic sensations, it becomes critical to the success of the procedures. In impedance systems, the interaction is captured by both the contact force $\mathbf{f}_e^{\mathcal{R}_e}$ and the position error $\tilde{\mathbf{p}}^{\mathcal{R}_e}$, the latter being characterized by slower transients than the former, which exhibits a step dynamics. As proposed in [75], replacing $\mathbf{f}_e^{\mathcal{R}_e}$ with $\tilde{\mathbf{p}}^{\mathcal{R}_e} = \mathbf{p}_{\mathcal{R}_{ed}}^{\mathcal{R}_e} - \mathbf{p}_{\mathcal{R}_c}^{\mathcal{R}_e}$ to generate the force feedback makes each contact state transparent to the operator, preventing them from having to deal with sudden force changes they are not used to from previous training and fieldworks. Therefore, the proposed HFC defines a second (virtual) impedance model, generating the force feedback from the motion error of the admittance controller:

$$\mathbf{f}_h^{\mathcal{H}_b}(k) = \mathbf{K}_h \tilde{\mathbf{p}}^{\mathcal{H}_b}(k) + \mathbf{D}_h \dot{\tilde{\mathbf{p}}}^{\mathcal{H}_b}(k), \tag{3.69}$$

where $\mathbf{K}_h \in \mathbb{R}^{3\times3}$ and $\mathbf{D}_h \in \mathbb{R}^{3\times3}$ respectively are virtual stiffness and damping diagonal matrices, where

$$\begin{bmatrix} \tilde{\mathbf{p}}^{\mathcal{H}_b}(k) \\ \dot{\tilde{\mathbf{p}}}^{\mathcal{H}_b}(k) \end{bmatrix} = \left(\mathbf{I}_2 \otimes \left(\mathbf{R}_{\mathcal{H}_e}^{\mathcal{H}_b}(k) \mathbf{R}_{\mathcal{R}_e}^{\mathcal{H}_e}(k) \right) \right) \begin{bmatrix} \tilde{\mathbf{p}}^{\mathcal{R}_e}(k) \\ \dot{\tilde{\mathbf{p}}}^{\mathcal{R}_e}(k) \end{bmatrix}. \tag{3.70}$$

We note that, as in (3.56), the rotation matrix $\mathbf{R}_{\mathbf{z}}^{\mathcal{R}_e}(k)$ (or equivalently $\mathbf{R}_{\mathbf{z}}^{\mathcal{H}_e}(k)$) in $\mathbf{R}_{\mathcal{H}_e}^{\mathcal{R}_e}(k)$ is used to provide the force feedback correspondence with the interaction observed in the camera view.

This approach is particularly suited to the considered application, as it guarantees stability while providing the operator with a natural and intuitive tactile experience that closely resembles manual execution, especially in light of Remark 2. Within this framework, the parameters $\mathbf{K}_h$ and $\mathbf{D}_h$ of the virtual system in (3.69) are tuned to shape the perceived interaction, with the stiffness matrix $\mathbf{K}_h$ governing the transient response and the damping matrix $\mathbf{D}_h$ contributing to vibration attenuation. Moreover, the use of a second virtual impedance model to generate the force feedback moderates the influence of transient force spikes associated with sudden contacts, while preserving informative and natural haptic feedback. We envisage the possibility that the generated feedback may exceed the range of forces that the HD device can exert. Therefore, the HFC saturates the norm of the force feedback $\|\mathbf{f}_h^{\mathcal{H}_b}(k)\|$ to the maximum exertable force $f_{\max}^{\mathcal{H}_b} \in \mathbb{R}_+$:

$$\underline{\mathbf{f}}_h^{\mathcal{H}_b}(k) = \begin{cases} \mathbf{f}_h^{\mathcal{H}_b}(k), & \text{if } \|\mathbf{f}_h^{\mathcal{H}_b}(k)\| < f_{\max}^{\mathcal{H}_b}; \\ f_{\max}^{\mathcal{H}_b} \dfrac{\mathbf{f}_h^{\mathcal{H}_b}(k)}{\|\mathbf{f}_h^{\mathcal{H}_b}(k)\|}, & \text{otherwise.} \end{cases} \tag{3.71}$$

Finally, given the slow dynamics of $\tilde{\mathbf{p}}^{\mathcal{R}_e}$, the operator may perceive residual force even when the robot is no longer interacting. To address this, we introduce a force dead-band $f_{db} \in \mathbb{R}_+$ to prevent the HD from reacting to such residuals:

$$\bar{\mathbf{f}}_h^{\mathcal{H}_b}(k) = \begin{cases} \underline{\mathbf{f}}_h^{\mathcal{H}_b}(k), & \text{if } \left\|\mathbf{f}_e^{\mathcal{R}_e}(k)\right\| > f_{db}; \\ \mathbf{0}, & \text{otherwise.} \end{cases} \tag{3.72}$$

3.5.3.4 Integrated mechanical end-effector

In order to successfully perform any free-hand dental procedure, the operator relies on three basic factors: (a) the procedure-specific clinical tool; (b) the surgical field view, which may

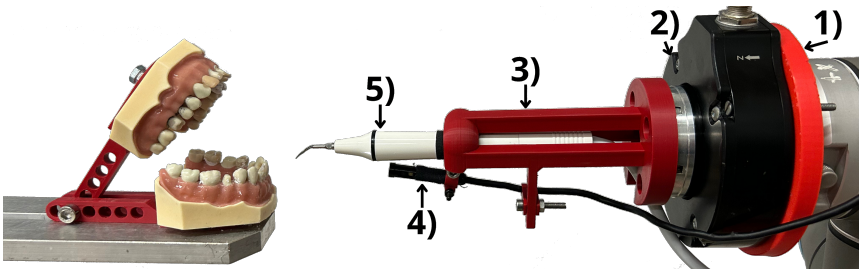


Figure 3.21: Integrated mechanical end-effector for free-hand procedures. Visible in the left side of the figure is also one of the dental models used in the experiments.

require external illumination and tools to show obstructed or poorly lit areas, e.g., a mirror; (c) the sense of touch to ensure the right pressure to be exerted on the area of interest, in order to achieve a safe and effective procedure. In this work, we design an integrated mechanical end-effector that can provide all the tools and sensory capabilities required to perform free-hand dental procedures.

With reference to Figure 3.21, the designed end-effector consists of five main components: (1) a *3D-printed mechanical interface* connecting the robot's flange with the force/torque sensor; (2) a *force/torque sensor* measuring contact forces; (3) a *3D-printed tool socket* supporting the clinical tool and the endoscopic camera: the interface consists of a rigid structure to enable proper transmission of forces from the tool to the sensor, a circular hole, adjustable via a bolt-and-nut mechanism, to accommodate tools of different sizes, and a movable camera-support ring, allowing for adjustments of the view and light beam angle; (4) an *high definition endoscopic camera*, equipped with LED illumination to ensure good visibility even in poorly lit areas; (5) a *clinical tool* for performing the procedure of interest: the tool is placed

in the supporting socket after being wrapped with friction tape to ensure good mechanical compliance, emulating the skin friction between the operator's hand and the tool; the tool used for the chosen use case is a scaler.

Although the current implementation does not fulfill yet all clinical requirements, such a design is compatible with future clinical adoption, as the end-effector is inherently compatible with standard sterilization and infection-control procedures commonly adopted in dentistry. Indeed, clinical instruments are intrinsically designed to withstand autoclave sterilization, and the literature reports the availability of sterilizable endoscopic cameras [198], as well as autoclavable or low-temperature–sterilizable materials, including medical-grade 3D-printed polymers, which would enable full sterilization of the entire assembly [199]. Moreover, the tool socket has been designed with smooth external surfaces and a reduced number of crevices, thereby facilitating cleaning and reprocessing. In addition, the socket enables rapid tool replacement by simple extraction and insertion of the clinical instrument, without requiring disassembly of the end-effector or disconnection of sensing and vision components. Components upstream of the end-effector, such as the force/torque sensor and the robot flange, which are not compatible with autoclave sterilization, can be isolated using sterile drapes or disposable sterile barriers, as commonly adopted in medical robotic systems [200]. With respect to aerosol management, a critical concern in dental procedures such as SRP, the proposed design does not interfere with conventional mitigation strategies. In a clinical deployment, aerosol generation could be managed through standard high-volume evacuation systems and saliva ejectors, without requiring any modification to the design.

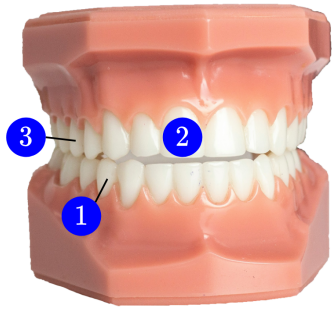


Figure 3.22: Target teeth for dental scaling experiments: 1) lower right first premolar; 2) upper right central incisor; 3) upper right second premolar.

3.5.4 Technical validation

To evaluate the performance of the proposed FH-HBTS, we conduct a set of experiments including static force application (Section 3.5.4.3), dynamic dental scaling motions (Section 3.5.4.5), and a free-space experiment (Section 3.5.4.4). During the experiments, the robot is out of the operator's view, who relies solely on the visual feedback from the camera and the force feedback from the HD. We select three target teeth: the lower right first premolar, the upper right central incisor, and the upper right second premolar, shown in Figure 3.22. The chosen targets are significant as each requires a different tool orientation, making the use of eye-hand coordination essential.

3.5.4.1 Experimental setup

The experimental setup involves the following equipment and materials: (I) a leader control station featuring a 6-degrees-of-freedom (DoF) force-feedback HD [72]and a workstation: the

latter is a general purpose computer executing the leader controller loop, and communicating with the FR over an Ethernet network, where delays and packet losses are negligible; (II) a FR consisting of the 6-DoF UR10 arm [142], equipped with the integrated mechanical end-effector of Section 3.5.3.4, where the force/torque sensor is the Robotiq FT150 [143]; (III) a high-strength resin dental model and a 3D-printed dental phantom, both life-sized models of a human mouth. The former is used for the experiments described in this section, while the latter only appears in [201].

3.5.4.2 Controller parameterization

3.5.4.2.1 Admittance controller parametrization Given the geometry of the task, the interaction experiments require modest compliance and high damping along all the Cartesian axes, as interaction is foreseen to happen across all directions of the workspace. Accordingly, Table 3.2 summarizes the selected admittance parameters; notably, a high damping ratio $\xi = \frac{\mathbf{K}_D}{2\sqrt{\mathbf{K}_P \mathbf{M}_d}} \approx 10.97$ is chosen over all linear axes, while a damping ratio of 0.8 is chosen on the angular axes to ensure smooth rotation coherence.

Regarding the force limitation strategy, a suitable trade-off between responsiveness and smoothness is identified by setting $K_s = 0.06\,\mathrm{N}^{-1}$ and by filtering the exerted force signals using a moving-average filter with a window size of $n = 500$. Force measurements are sampled at $f_s = 125\,\mathrm{Hz}$, therefore, the selected window corresponds to a group delay of approximately $\tau \approx 2\,\mathrm{s}$. This delay does not represent a dead time, as force information propagates continuously through the filter, and is consistent with the intended trade-off between smoothness and responsiveness of the force-limiting action.

Axis	$\mathbf{K}_P$ [N/m, Nm/rad]	$\mathbf{K}_D$ [Ns/m, Nms/rad]	$\mathbf{M}_d$ [kg, kgm^2/rad]
x	3000	8500	50
y	3000	8500	50
z	3000	8500	50
Roll	100	16	1
Pitch	100	16	1
Yaw	100	16	1

Table 3.2: Admittance control parameters.

Finally, limited by the non-ideal industrial equipment (mainly force-torque sensor and robot), we set $f_{th} = 20\,\text{N}$, and the translational and rotational safety thresholds used to prevent abrupt motions to 0.01 m and 0.01 rad, respectively.

3.5.4.2.2 Eye-hand coordination controller parametrization Given that the frequency of human hand tremors is around 6 Hz [202], we analyze the frequency response of a moving-average filter to identify the fixed window size n, such that the cutoff frequency f_c is lower than that of the tremors. Based on the analysis conducted, we set $n = 50$, which guarantees a cutoff frequency $f_c \approx 2\,\text{Hz}$.

In addition to frequency-domain considerations, we explicitly evaluate the temporal delay introduced by the moving average filtering of pose signals. Using the standard estimate of the group delay introduced by a moving-average filter, the delay τ can be approximated as:

$$\tau = \frac{n+1}{2f_s}, \tag{3.73}$$

where $f_s = 125\,\text{Hz}$ denotes the sampling frequency. For the selected window size, the resulting group delay on the pose signals is approximately $\tau \approx 0.204\,\text{s}$, which is well below the

Axis	Scaling factor
x	0.8
y	0.8
z	0.8

Table 3.3: Diagonal elements of the scaling matrix $\mathbf{\Lambda}$.

Axis	$\mathbf{K}_h$ [N/m]	$\mathbf{D}_h$ [N s/m]
x	250	100
y	250	100
z	250	100

Table 3.4: Virtual impedance parameters.

human perceptual threshold and therefore does not introduce any noticeable degradation in system responsiveness or operator perception.

With regard to the scaling factors, Table 3.3 presents the parameters of the diagonal scaling matrix $\mathbf{\Lambda}$ adopted for the translational degrees of freedom. The selected values provide high control accuracy while avoiding an excessive reduction of the available workspace.

3.5.4.2.3 Virtual feedback parametrization With regard to the virtualization of the force feedback, the virtual impedance matrices are tuned to provide the human operator with a natural sensation, ensuring both smooth transient response and reduced vibrations. Therefore, we set the parameters reported in Table 3.4.

Regarding the force dead-band, we set $f_{db} = 2\,\mathrm{N}$, which corresponds to the minimum force variation that can be reliably distinguished from sensor noise according to the manufacturer's

specifications. Similarly, $f_{\max}^{\mathcal{H}_b} = 3.3\,\mathrm{N}$ constitutes a strict HD hardware constraint.

3.5.4.3 Force limitation assessment

To assess the effectiveness of the proposed force limitation strategy, we perform 9 interaction experiments, with an average duration of $\sim 20\,\mathrm{s}$ each, 3 for each target tooth, without force limitation (Scenario A), 9 more with force limitation (Scenario B) and 9 with a passivity-based architecture (Scenario C), specifically TDPA-HD, where admittance control replaces Cartesian impedance control adopted in [40]. In the latter scenario, the force limitation is intentionally kept disabled in order to isolate the effects of TDPA-HD. For each scenario, we record the data sequence $\left\{a(k), b(k)\right\}_{k=1}^{N}$, sampling at a frequency of 125 Hz, where we set the force norm $\left\|\mathbf{f}_e^{\mathcal{R}_e}(k)\right\|$ as $a(k) \in \mathcal{A} \subseteq \mathbb{R}_+$, and the commanded virtual penetration $\left\|\mathbf{p}_{\mathcal{R}_{ed}}^{\mathcal{R}_e}(k)\right\|$ as $b(k) \in \mathcal{B} = \{b \in \mathbb{R} | b_{\min} = 0\,\mathrm{m} \leq b \leq b_{\max} = 0.007\,\mathrm{m}\}$. We discretize $\mathcal{B}$ with the step $b_{\text{step}} = 0.0001\,\mathrm{m}$, selected based on the repeatability of the FR, while $b_{\max}$ is the maximum virtual penetration observed across all experiments.

By binning data in $\mathcal{B}$, following [203], we estimate the conditional expectation of the exerted force $E\big(\|\mathbf{f}_e^{\mathcal{R}_e}\| \big| \|\mathbf{p}_{\mathcal{R}_{ed}}^{\mathcal{R}_e}\|\big)$ and the conditional standard deviation, obtained as the square root of the conditional variance $\mathrm{Var}\big(\|\mathbf{f}_e^{\mathcal{R}_e}\| \big| \|\mathbf{p}_{\mathcal{R}_{ed}}^{\mathcal{R}_e}\|\big)$, in all three scenarios. Visual inspection of Figure 3.23 showcases a significant reduction in the expected interaction force in Scenario B, given the same commanded virtual penetration. Notably, TDPA-HD [40] (Scenario C) cannot reduce the interaction force in quasi-static contacts due to the energy being approximately zero.

To evaluate the effectiveness of the force limitation strategy, we

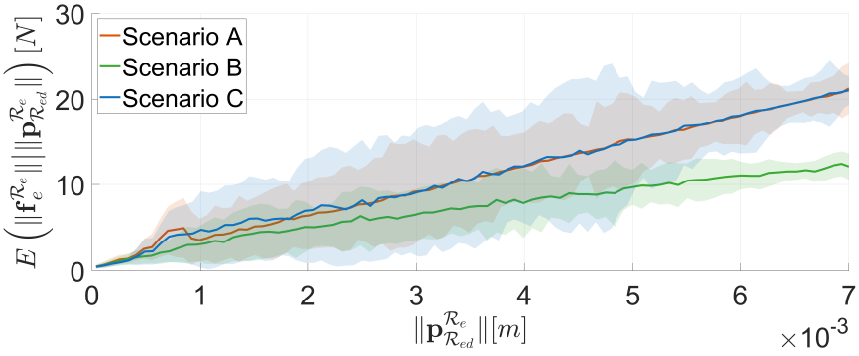


Figure 3.23: Comparison between the conditional expectation of the interaction force in all three scenarios.

compare $E\big(\|\mathbf{f}_e^{\mathcal{R}_e}\|\big|\|\mathbf{p}_{\mathcal{R}_{ed}}^{\mathcal{R}_e}\|\big)$ and $\mathrm{Var}\big(\|\mathbf{f}_e^{\mathcal{R}_e}\|\big|\|\mathbf{p}_{\mathcal{R}_{ed}}^{\mathcal{R}_e}\|\big)$ in all three scenarios. We assess differences in conditional variances through Levene's and Bartlett's tests in the comparisons involving Scenario B, i.e., B–A and B–C. Both tests indicate significantly different variances ($p \approx 0$), showing that the force limitation strategy affects the dispersion of the force norm $\big\|\mathbf{f}_e^{\mathcal{R}_e}(k)\big\|$ with respect to virtual penetration $\big\|\mathbf{p}_{\mathcal{R}ed}^{\mathcal{R}_e}(k)\big\|$. Since Levene's test suggests a significant variance difference, we apply Welch's t-test, which is more robust in the case of unequal variances. In the B–A comparison, the test yields a t-statistic $t = -4.52$ with $p \approx 0$, confirming a statistically significant force reduction in Scenario B. Beyond statistical significance, the magnitude of this effect is notable: the comparison yields a Cohen's $d = -0.63$, indicating a significant force reduction when the force limitation strategy is enabled. The corresponding confidence interval $[-0.91, -0.36]$ does not include zero, further supporting the robustness and consistency of the observed effect across the explored range of virtual penetration.

An analogous analysis is conducted for the B-C comparison. Also in this case, Welch's t-test confirms a statistically significant reduction of the normal force with respect to Scenario C ($p \approx 0$), indicating that the force limitation strategy yields lower contact forces than the passivity-based control architecture. The observed effect is comparable in magnitude to that of the B-A comparison (Cohen's $d = -0.68$ and confidence interval $[-0.97, -0.41]$), further supporting the robustness of the proposed approach across different control architectures.

3.5.4.4 Eye-hand coordination assessment

To perform a formal assessment of eye-hand coordination, we execute a teleoperated task in the free space. The operator performs a translatory motion with the HD, simultaneously rotating the viewing angle by rotating the HD's stylus by an angle φ about the $\mathbf{z}$ axis of $\mathcal{H}_e$. The validation is considered completed if the motion transferred to the robot varies as the viewing angle does. Figure 3.24 shows the φ angle, the position of HD's stylus and the position of the FR, respectively.

Results showcase that, as long as the angle $\varphi = 0\,\text{rad}$ (from $0\,\text{s}$ to $10\,\text{s}$), a motion along the x axis of $\mathcal{H}_b$ is mapped into a motion along the x axis of $\mathcal{R}_b$. When the angle turns into $\varphi = -\pi/2\,\text{rad}$, a motion along the x axis of $\mathcal{H}_b$ is mapped into a motion along the z axis of $\mathcal{R}_b$ (from $20\,\text{s}$ to $30\,\text{s}$).

These results confirm that the mapping of motion between HD space and FR space is affected by the rotation of the visual field. However, they do not provide any suggestion regarding the effectiveness of eye-hand coordination for the human operator. Therefore, in [201] we provide a comprehensive qualitative assessment of the latter.

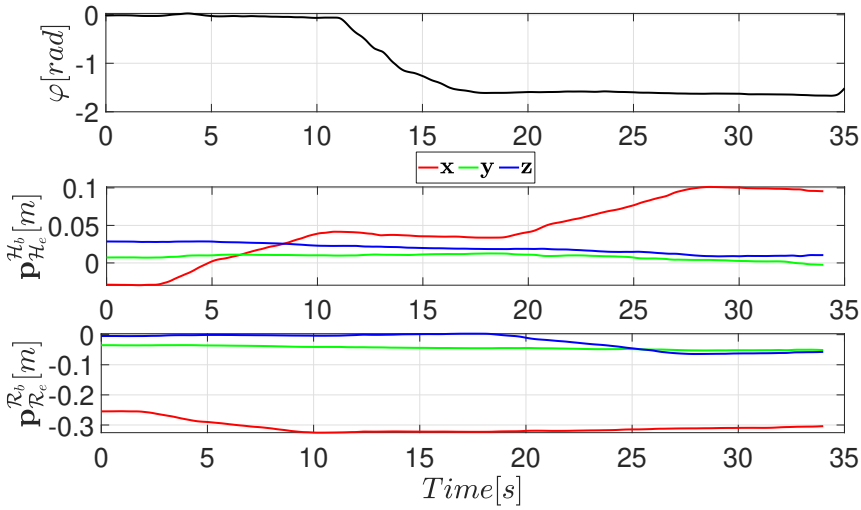
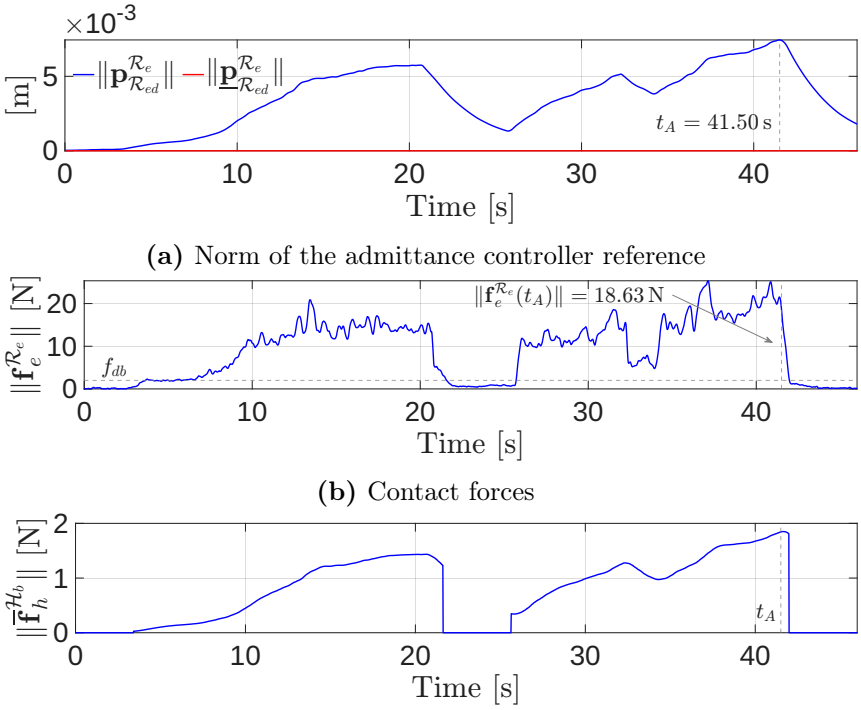


Figure 3.24: Eye-hand coordination assessment.

3.5.4.5 End-to-end experimental demonstration

We provide a demonstration of the end-to-end system's operation by executing a SRP procedure on the three target teeth. The procedure is performed using an inactive scaler and aims to emulate dynamic scaling motions representative of the real clinical practice. In this section, we report the outcomes of the execution of the procedure in Scenario B (Figure 3.26), i.e. with force limitation, highlighting two instants of the experiment (Figures 3.26a, 3.26b). We compare the results against those obtained in Scenario A (Figure 3.25), i.e. without force limitation, and Scenario C (Figure 3.27), i.e. with a passivity-based architecture. To avoid repetition, the analysis focuses on the outcomes of executing a dental scaling action on a single target tooth, the upper right second premolar, being them consistent across the other teeth.



(a) Norm of the admittance controller reference

(b) Contact forces

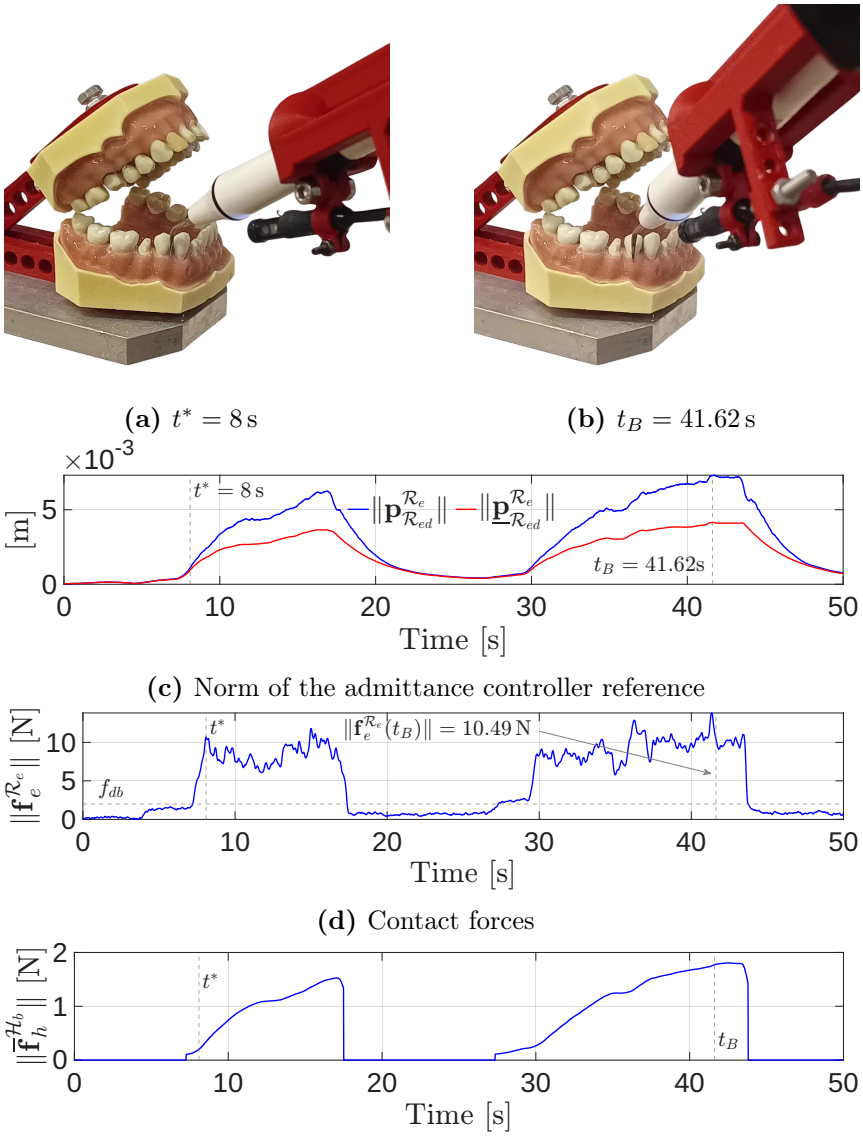
(c) Forces rendered on the HD

Figure 3.25: Outcomes of the dental scaling experiment in Scenario A (baseline configuration with no force limitation, no passivity).

In Figure 3.26d and Figure 3.25b, the normal forces exerted by the FR in both scenarios are shown. A visual inspection showcases a significant reduction in interaction forces when the free-hand force limitation strategy is active, with a decrease of approximately 44% in Scenario B, thereby confirming the technical assessment presented in the paper. The effectiveness of this strategy is made even more evident by comparing Figure 3.26c and Figure 3.25a. Notably, for equivalent virtual penetrations

(at $t_A = 41.5\,\text{s}$ and $t_B = 41.62\,\text{s}$ in Scenarios A and B respectively), the interaction forces in Scenario B are significantly lower than in Scenario A. Indeed, as shown in Figure 3.26d, the implementation of this strategy enables the scaling of the provided references, effectively reducing the contact forces and enhancing the system's safety. To confirm these conclusions by comparing Scenarios B and C, it is worth highlighting that, with a smaller penetration (at $t_C = 54.14\,\text{s}$), the measured forces are higher than those exerted in Scenario B (10.49 N vs. 12.09 N, respectively).

Finally, in Figure 3.26e and Figure 3.25c the forces rendered on the HD in Scenarios A and B are shown. As expected, the results are consistent between the two scenarios, while both showing high similarity to exerted force profiles as well as slow dynamics. Such aspects enhance naturalness for the human operator, as highlighted in the pre-clinical trials. On the other hand, the TDPA-HD [40] requires a direct force mapping, hence the forces rendered on the HD follow the same profile as the FR-side forces, as shown in Figure 3.27b and Figure 3.27c. In this case, the rendered forces $\overline{\mathbf{f}}_h^{\mathcal{H}_b}$ are computed with a nonlinear



(a) $t^* = 8\,\mathrm{s}$ **(b)** $t_B = 41.62\,\mathrm{s}$

(c) Norm of the admittance controller reference

(d) Contact forces

(e) Forces rendered on the HD

Figure 3.26: Snapshopts and outcomes of the dental scaling experiment in Scenario B (proposed system with force limitation).

mapping technique as follows:[1]

$$\overline{\mathbf{f}}_h^{\mathcal{H}_b} = \begin{cases} \underline{\mathbf{f}}_h^{\mathcal{H}_b}, & \text{if} \|\underline{\mathbf{f}}_h^{\mathcal{H}_b}\| < f_{\max}^{\mathcal{H}_b}, \\ f_{\max}^{\mathcal{H}_b} \frac{\underline{\mathbf{f}}_h^{\mathcal{H}_b}}{\|\underline{\mathbf{f}}_h^{\mathcal{H}_b}\|}, & \text{otherwise}, \end{cases} \tag{3.74a}$$

$$\underline{\mathbf{f}}_h^{\mathcal{H}_b} = \text{sign}(\mathbf{f}_h^{\mathcal{H}_b}) \cdot \big(\cosh(\mathbf{f}_h^{\mathcal{H}_b}) - 1\big), \tag{3.74b}$$

$$\mathbf{f}_h^{\mathcal{H}_b} = \frac{\mathbf{f}_e^{\mathcal{H}_b}}{\mathbf{f}_{e,\max}^{\mathcal{H}_b}} \log(4 + \sqrt{15}), \tag{3.74c}$$

$$\mathbf{f}_e^{\mathcal{H}_b} = \mathbf{R}_{\mathcal{R}_b}^{\mathcal{H}_b} \mathbf{R}_{\mathcal{R}_e}^{\mathcal{R}_b} \underline{\mathbf{f}}_e^{\mathcal{R}_e}, \tag{3.74d}$$

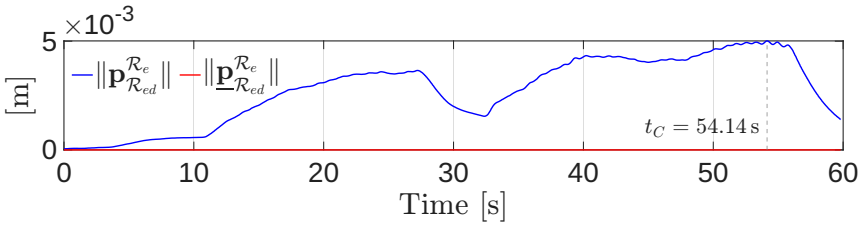
$$\mathbf{f}_{e,\max}^{\mathcal{H}_b} = \mathbf{R}_{\mathcal{R}_b}^{\mathcal{H}_b} \mathbf{f}_{e,\max}^{\mathcal{R}_b}, \tag{3.74e}$$

where $\underline{\mathbf{f}}_e^{\mathcal{R}_e}$ are the attenuated forces computed by the leader-side impedance passivity control module in [40], $f_{\max}^{\mathcal{H}_b} = 3.3\,\text{N}$ is the maximum force the HD hardware can render, and $\mathbf{f}_{e,\max}^{\mathcal{R}_b} = \begin{bmatrix} 20, & 20, & 20 \end{bmatrix}^\top$ are the task-specific maximum forces the robot can exert on the environment in FR frame $\mathcal{R}_b$, converted in LR frame $\mathcal{H}_b$ with (3.74e). As evidently inferred from Figure 3.26e and Figure 3.27c, it is immediate noticing that our virtual feedback rendering strategy delivers smoother HD-side forces, leading to a more comfortable human perception. Together with the experiments here discussed, 3 additional trials are carried out in Scenario B using a 3D-printed dental phantom: such experiments are presented in [201].

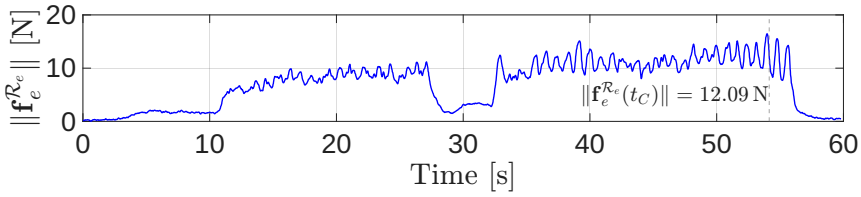
3.6 Clinical evaluation of the HBTS for free-hand dental procedures

We perform a clinical evaluation of the FH-HBTS presented in [76] to assess its feasibility in performing a SRP procedure on

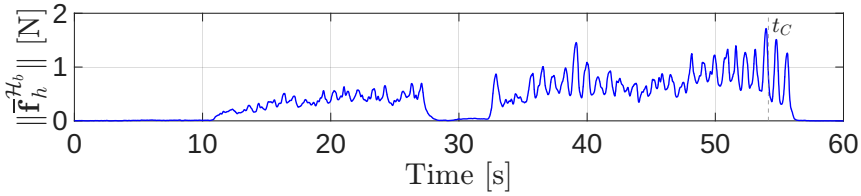
[1] In (3.74b)–(3.74c), we assume coefficient-wise operations.



(a) Norm of the admittance controller reference



(b) Contact forces



(c) Forces rendered on the HD

Figure 3.27: Outcomes of the dental scaling experiment in Scenario C (TDPA-HD [40]).

a realistic dental phantom with an active dental scaler. In Section 3.6.1 we present the study design, including the participant recruitment criteria (Section 3.6.2). The training and the clinical protocol are presented in Section 3.6.4.1 and Section 3.6.4.2, respectively, while the results of the study are presented in Section 3.6.7.

3.6.1 Study design

The study is conducted as an in-vitro experimental trial, based on the use of the FH-HBTS for supragingival instrumentation, within the context of Step I of periodontal therapy. Participants with varying levels of experience in the dental field are recruited.

Prior to the experimental phase, participants take part in a training session designed to facilitate the acquisition of competence in using the system.

Subsequently, during the experimental phase, they are asked to perform artificial calculus removal on specific surfaces of artificial teeth mounted on a resin model.

At the end of the experimental operations, each participant completes a questionnaire aimed at assessing their subjective experience with the system, while additional analyses focus on evaluating the effectiveness, efficiency, and safety of the procedures through objective measurements and expert assessments.

The study is carried out at the Robotics Laboratory of the University of Salerno.

3.6.2 Participants

A total of 19 participants are recruited to take part in the study. They differ based on their years of experience in the dental field:

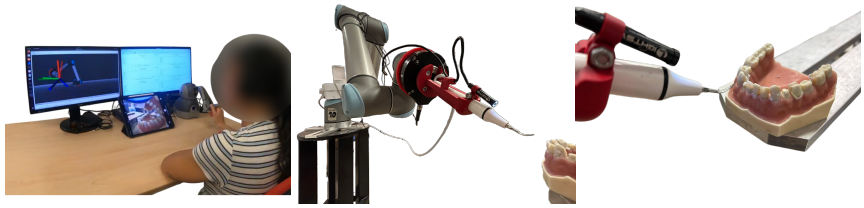
1. *Group 1*: 6 dental students who had performed at least 20 in vivo dental scaling procedures (31.6%);
2. *Group 2*: 7 dentists with less than 5 years of professional experience (36.8%);
3. *Group 3*: 6 dentists with more than 5 years of professional experience (31.6%).

3.6.3 Equipments and materials

3.6.3.1 Robotic teleoperation system

The FH-HBTS features a control station and a 6-DoF UR10 robotic arm by Universal Robots [142], equipped with a mechanical end-effector for free-hand dental procedures, as shown in Figure 3.28b. It includes a F/T sensor by Robotiq [143], measuring the interaction forces applied by the operator to the dental model, a semi-rigid endoscopic camera with eight LED lights, whose video feed is displayed on a screen located at the control station (Figure 3.28a), and a support interface for the dental scaler hand-piece. Through the latter, the dental scaler hand-piece is rigidly attached to the robotic arm and connected to its ultrasonic motor, which can generate different ultrasonic vibration frequencies. The motor is activated via a wireless foot pedal located at the control station. An ultrasonic scaling tip is mounted on the hand-piece to perform the supragingival instrumentation.

The control station, depicted in Figure 3.28a, features: (i) a 6-DoF HD, responsible for controlling the robotic arm and providing the operator with translational kinesthetic feedback that simulates resistance during interaction with the dental model; (ii) a screen displaying the visual feedback provided by the endoscopic camera; (iii) a pedal to activate the ultrasonic



(a) Control station. **(b)** Robotic system. **(c)** Resin dental model.

Figure 3.28: Teleoperation system and dental model used within the study.

scaler.

The FH-HBTS is configured according to the procedural requirements by experienced technicians, and the same configuration is used for all operators to ensure consistency across trials.

3.6.3.2 Dental model

For the experimentation, a high-strength resin dental model, depicted in Figure 3.28c, faithfully reproducing the anatomy of the dental arch, is used. The model is securely fixed to an immovable support to ensure stability during the operative maneuvers.

Certain dental surfaces are specifically prepared with the application of a special dental coating to simulate artificial calculus, accurately reproducing the clinical conditions required for experimental assessment.

3.6.4 Experimental procedures

3.6.4.1 Training protocol

A standardized training session is provided to instruct participants on how to operate the system before the experimental phase. The training aims to develop the operators' proficiency in using the FH-HBTS. It is structured to ensure that each participant could successfully complete three main tasks: reaching the dental surface, maintaining stable contact, and removing calculus from a selected tooth area.

Specifically, each participant is instructed to bring the scaler tip into contact with a dental surface three times and then maintain contact for five seconds with a stable force not exceeding 4 N. After this preliminary exercise, participants perform the removal of artificial calculus from the vestibular surface of tooth 3.1.

The training phase is considered complete once the operator demonstrates adequate confidence in handling the system, showing consistent motion control and effective interaction with the dental model under both static and dynamic conditions.

3.6.4.2 Clinical procedure

All experimental procedures are carried out on three selected dental surfaces: the vestibular surfaces of teeth 3.1 and 3.7, and the lingual surface of tooth 4.6. Each surface is uniformly coated with a thin layer of white paint simulating artificial calculus. For consistency, the same operator, not involved in the study, is responsible for applying the coating prior to each experimental trial.

The first experiment involves the teleoperated removal of artificial calculus from the vestibular surfaces of teeth 3.1 and

Experiment	Dental Surface	Auditory feedback
1	3.1	✓
1	3.7	✓
2	4.6	✓
3	4.6	✗

Table 3.5: Overview of the experiments with corresponding dental surface and auditory feedback condition.

3.7. The participants control the robotic arm, connected to the ultrasonic scaler, through the HD, relying on the visual feedback from the endoscopic camera, the haptic feedback provided by the interface, and the auditory feedback from the operative field. The experiment continues until the participant is satisfied with the outcome.

For the second experiment, the same procedure is repeated on the lingual surface of tooth 4.6.

For the third experiment, the procedure is repeated on the lingual surface of tooth 4.6 after reapplying the artificial calculus, with the participant wearing headphones (JBL 510BT) to suppress auditory feedback from the operative field. This setup allows for an assessment of the influence of auditory feedback on teleoperation performance.

The details of each experiment, including the dental surface and the auditory feedback condition, are reported in Table 3.5.

After the experiments, each participant completes the questionnaire to evaluate usability and effectiveness of the FH-HBTS.

3.6.5 Outcomes measures

3.6.5.1 Efficacy measurements

The efficacy of the system in removing calculus is evaluated through analysis of pre- and post-treatment images of each tooth, obtained using a high-resolution camera positioned at predetermined points to ensure consistent acquisition conditions in terms of angle, lighting, and distance. The assessment is carried out both quantitatively and qualitatively. The quantitative analysis is conducted using the image analysis program ImageJ [204], following the methodology described in [205]. For each tooth, the total treated surface area and the residual calculus area are calculated under blinded randomized conditions. The percentage of calculus removed was computed as:

$$\text{Calculus removal } (\%) = \left[\frac{\text{pre_treatment area} - \text{post_treatment area}}{\text{post_treatment area}}\right] \cdot 100 \tag{3.75}$$

The qualitative analysis is conducted by an independent expert dentist, not involved in the experiment, using a six-point ordinal scale:

- **0** = no removal
- **1** = minimal removal
- **2** = partial removal
- **3** = good removal
- **4** = nearly complete removal
- **5** = complete removal

3.6.5.2 System safety and efficiency measurements

For the training phase detailed in Section 3.6.4.1 and each of the experiments detailed in Section 3.6.4.2, the following data are collected:

- *total completion time*, from the first contact to task completion;
- *interaction forces* between the scaler tip and the dental model

System efficiency is assessed by measuring the average time (in seconds) required to complete the cleaning of each selected dental surface.

System safety is evaluated by monitoring macroscopic damage to the dental elements, recording operational errors, and analyzing the magnitude of the interaction forces $\|\mathbf{f}\| = \sqrt{\mathbf{f}_x^2 + \mathbf{f}_y^2 + \mathbf{f}_z^2}$ exerted during the procedure. These forces have already compensated for both the F/T sensor and the gravitational biases of the mounted clinical instrumentation.

3.6.5.3 System usability assessment

At the end of the experimental phase, participants complete a structured questionnaire designed to evaluate overall system usability and effectiveness. The 46-item questionnaire is divided into 7 sections [206]. The first section (Q1.1–Q1.7) collects demographic information and details on the participants' operational background, including prior experience with robotic systems, HDs, and ultrasonic dental scalers. The second section (Q2.1–Q2.15) focuses on the overall usability of the system, addressing aspects such as ease of use, intuitiveness, and ergonomics. The third section (Q3.1–Q3.3) explores the perceived mental and physical workload experienced during the proce-

dure. The fourth (Q4.1–Q4.8) and fifth (Q5.1–Q5.8) sections assess the perceived quality of the visual and haptic feedback, respectively, and their contribution in maintaining adequate situational awareness. The sixth section (Q6.1–Q6.3) investigates participants' perceived trust in and sense of safety with the system during task execution. Finally, the seventh section (Q7.1–Q7.9) evaluates the overall effectiveness of the different feedback modalities in completing the procedure. Sections 2 to 7 are rated on a five-point Likert scale. The semantic anchors of the scale vary depending on the section's content and are detailed in [206].

3.6.6 Statistical analysis

3.6.6.1 System efficacy

For the cleanness scores, results generated by ImageJ are expressed as percentages, while qualitative responses, collected on the six-point Likert scale, are treated as ordinal variables, acknowledging that Likert-scale responses reflect human perception. Regarding the quantitative analysis, for each dental surface, mean, standard deviation (STD), median and interquartile range (IQR) (Q1 - Q3) of the calculus removal percentage are calculated and reported in Table 3.6, while median, mode and IQR, related to qualitative analysis, are reported in Table 3.7. To assess the impact of the audio feedback on efficiency, a two-sided Wilcoxon signed-rank test is used to compare cleanness score in experiments 2 and 3. A Kruskal–Wallis test is chosen as a nonparametric alternative to one-way ANOVA to assess whether cleanness scores differ across operator experience levels for each of the experiments.

	Group 1			
Experiment	Mean	STD	Median	IQR
1	86.55	6.80	84.80	10.33
1	73.45	16.37	75.25	24.65
2	75.07	24.00	88.50	36.78
3	76.18	28.20	92.75	43.75
T statistic	7.0			
p-value	0.563			

	Group 1			
Experiment	Mean	STD	Median	IQR
1	90.44	3.93	91.90	3.65
1	79.40	11.79	84.50	13.30
2	77.51	7.65	79.90	10.70
3	86.44	8.76	90.60	12.00
T statistic	3.0			
p-value	0.078			

	Group 1			
Experiment	Mean	STD	Median	IQR
1	79.87	18.40	86.75	17.07
1	79.93	12.18	83.40	14.08
2	77.57	18.73	84.00	6.87
3	75.53	23.34	81.90	17.23
T statistic	2.5			
p-value	0.625			

	Kruskal–Wallis Test	
Experiment	H statistic	p-value
1	1.610	0.447
1	0.509	0.775
2	1.040	0.595
3	0.516	0.773

Table 3.6: Descriptive statistics of cleanness scores of each dental surface for each experience level, obtained using the quantitative analysis. Kruskal-Wallis test results for between-group differences and Wilcoxon signed-rank test results for evaluating the audio feedback impact in system efficacy.

	Group 1		
Experiment	Median	IQR	Mode
1	4	1	4
1	4	0	4
2	4	1	4
3	4	1	4
T statistic	2.5		
p-value	0.625		
	Group 2		
Experiment	Median	IQR	Mode
1	4	0	4
1	4	1	4
2	4	0	4
3	4	0	4
T statistic	1.5		
p-value	1.000		
	Group 3		
Experiment	Median	IQR	Mode
1	4	1	4
1	4	1	4
2	4	1	4
3	4	1	4
T statistic	2.5		
p-value	0.625		

	Kruskal–Wallis Test	
Experiment	H statistic	p-value
1	0.520	0.771
1	2.021	0.364
2	2.035	0.361
3	0.086	0.958

Table 3.7: Descriptive statistics of cleanness scores of each dental surface for each experience level, obtained using the qualitative analysis. Kruskal-Wallis test results for between-group differences and Wilcoxon signed-rank test results for evaluating the audio feedback impact in system efficacy.

3.6.6.2 Execution times

Some descriptive statistics including the mean, STD, median, and IQR are calculated for the execution times of the training and experimental phases, as reported in Table 3.8. A Kruskal–Wallis test is used to assess whether execution times differ across operator experience levels for each of the experiments.

3.6.6.3 Interaction forces

The interaction forces are first processed to extract the time intervals during which the ultrasonic scaler is in contact with the dental model. Subsequently, the mean, median, and maximum values are calculated for each participant. Finally, some descriptive statistics, including mean, STD, median, minimum, maximum, and IQR, are computed for each participant group, as listed in Table 3.9. A Kruskal–Wallis test is used to assess whether the magnitude of the interaction forces differ across operator experience levels.

3.6.6.4 Questionnaire

Questionnaire responses are on a five-point Likert scale and, as for the cleanness scores, are treated as ordinal data. For each question the median, mode, and IQR are calculated to summarize the central tendency and variability (see Table 3.10).

To assess whether the responses differ significantly from the neutral value of 3, a two-sided Wilcoxon signed-rank test is performed for each item with a significance threshold of $p = 0.05$. To clarify the direction of deviation, the sum of ranks of responses above the neutral value is compared with the sum of ranks of responses below the neutral value.

	Group 1			
Phase	Mean	STD	Median	IQR
Training	712.17	364.26	664.50	442.00
Experiment 1	512.17	200.09	536.00	386.25
Experiment 2	407.50	187.33	376.00	189.50
Experiment 3	184.50	83.94	177.50	90.25
T statistic	1.00			
p-value	0.063			
	Group 2			
Phase	Mean	STD	Median	IQR
Training	469.00	226.17	437.00	434.00
Experiment 1	505.71	205.90	361.00	402.50
Experiment 2	262.43	78.31	250.00	105.50
Experiment 3	183.00	63.60	162.00	68.00
T statistic	0.00			
p-value	0.016			
	Group 3			
Phase	Mean	STD	Median	IQR
Training	459.67	92.23	445.00	38.50
Experiment 1	429.67	137.32	411.00	139.00
Experiment 2	249.17	51.82	236.00	74.50
Experiment 3	212.33	54.30	204.50	66.00
T statistic	5.00			
p-value	0.313			

	Kruskal–Wallis Test	
Phase	H statistic	p-value
Training	1.53	0.465
Experiment 1	0.43	0.808
Experiment 2	3.11	0.211
Experiment 3	1.15	0.563

Table 3.8: Descriptive statistics of execution times for the training and experimental phases. Execution times are expressed in seconds. Kruskal-Wallis test results for between-group differences and Wilcoxon signed-rank test results for evaluating the audio feedback impact on execution times.

	Group 1					
	Mean	STD	Median	Min	Max	IQR
Mean $\|\mathbf{f}\|$	2.67	0.39	2.77	2.12	3.06	0.75
Median $\|\mathbf{f}\|$	1.95	0.34	2.02	1.38	2.28	0.54
Max $\|\mathbf{f}\|$	17.41	2.43	17.15	14.80	21.34	3.68
	Group 2					
	Mean	STD	Median	Min	Max	IQR
Mean $\|\mathbf{f}\|$	2.87	0.64	2.87	2.22	4.03	0.66
Median $\|\mathbf{f}\|$	2.17	0.58	2.01	1.53	3.20	0.61
Max $\|\mathbf{f}\|$	17.89	4.20	18.39	11.04	23.26	4.03
	Group 3					
	Mean	STD	Median	Min	Max	IQR
Mean $\|\mathbf{f}\|$	3.35	0.84	2.99	2.81	5.04	0.44
Median $\|\mathbf{f}\|$	2.55	0.72	2.36	1.79	3.93	0.31
Max $\|\mathbf{f}\|$	21.20	6.57	19.17	15.34	33.24	6.09

	Kruskal–Wallis test	
	H statistic	p-value
Mean $\|\mathbf{f}\|$	2.94	0.22
Median $\|\mathbf{f}\|$	3.66	0.16
Max $\|\mathbf{f}\|$	1.45	0.48

Table 3.9: Descriptive statistics of interaction forces for the whole clinical procedure across experience levels. The statistics are expressed in newtons. Kruskal–Wallis test results for between-group differences.

Additionally, Kruskal–Wallis tests are performed to assess between-group differences in responses across operator experience levels. When a statistically significant effect is found, a post-hoc pairwise comparison using Mann–Whitney U tests with Bonferroni correction is performed to investigate differences between experience levels.

3.6.7 Results

Table 3.6, Table 3.7 and Table 3.8 show descriptive statistics of the cleanness scores and execution times obtained by each group. No statistically significant differences between groups are found with Kruskal–Wallis tests at the $p = 0.05$ significance level neither in cleanness score obtained with quantitative analysis (Surface 3.1: $p = 0.447$; Surface 3.7: $p = 0.775$; Surface 4.6: $p = 0.595$; Surface 4.6 without audio: $p = 0.773$), nor in that obtained with qualitative analysis (Surface 3.1: $p = 0.771$; Surface 3.7: $p = 0.364$; Surface 4.6: $p = 0.361$; Surface 4.6 without audio: $p = 0.958$), nor in execution times (Experiment 1: $p = 0.81$; Experiment 2: $p = 0.21$; Experiment 3: $p = 0.56$). For both metrics, two-sided Wilcoxon signed-rank tests are used to compare Experiment 2 and 3 to assess the effects of auditory feedback, but only group 2 shows a statistically significant reduction in execution times on Experiment 3 ($p = 0.016$). Notably, mean and median execution times are all lower on Experiment 3 with respect to Experiment 2 while median cleanness scores stay constant, therefore the absence of auditory feedback do not affect system efficacy nor efficiency. Given that Experiment 3 is always performed after Experiment 2, this also shows that task repetition contributes to skill improvement, as participants become more efficient (shorter execution times) without compromising cleanness performance.

Regarding the magnitude of the interaction forces, Table 3.9 depicts the overall descriptive statistics obtained by each group. During the execution of the clinical procedures, the magnitude results in an overall mean of $2.67\,\mathrm{N} \pm 0.39\,\mathrm{N}$ for Group 1, $2.87\,\mathrm{N} \pm 0.64\,\mathrm{N}$ for Group 2, and $3.35\,\mathrm{N} \pm 0.84\,\mathrm{N}$ for Group 3. Comparing different groups, Kruskal–Wallis tests find no statistically significant differences between experience levels at

Question	Median	IQR	Mode	T statistic	p-value	Direction
Q2.1	3	2	3	33.00	1.000	-
Q2.2	4	2	4	37.50	0.188	-
Q2.3	4	2	5	6.00	0.004	>3
Q2.4	2	0	2	22.50	0.006	<3
Q2.5	4	1	4	13.00	0.021	>3
Q2.6	2	1	2	11.00	0.006	<3
Q2.7	4	0	4	0.00	< 0.001	>3
Q2.8	3	2	3	30.50	0.813	-
Q2.9	4	1	3	25.00	0.075	-
Q2.10	4	1	5	0.00	< 0.001	>3
Q2.11	4	1	4	38.00	0.033	>3
Q2.12	4	1	4	33.50	0.011	>3
Q2.13	3	1	3	13.50	0.248	-
Q2.14	4	2	4	77.00	0.686	-
Q2.15	3	2	4	46.00	0.408	-
Q3.1	3	2	3	45.00	0.628	-
Q3.2	2	2	2	4.50	0.002	<3
Q3.3	3	2	1	29.50	0.137	-
Q4.1	3	1	2	22.50	0.166	-
Q4.2	3	1	3	20.00	0.117	-
Q4.3	3	1	3	23.00	0.627	-
Q4.4	2	1	3	4.00	0.005	<3
Q4.5	4	0	4	26.50	0.014	>3
Q4.6	4	0	4	13.00	0.003	>3
Q4.7	4	2	2	45.50	0.125	-
Q4.8	3	2	2	45.00	0.593	-
Q5.1	4	1	3	9.00	0.008	>3
Q5.2	4	1	3	0.00	0.004	>3
Q5.3	4	1	4	11.00	0.011	>3
Q5.4	4	1	4	16.50	0.010	>3
Q5.5	4	1	5	4.00	0.001	>3
Q5.6	4	1	4	22.00	0.045	>3
Q5.7	4	1	4	5.50	0.002	>3
Q5.8	3	2	2	68.00	1.000	-
Q6.1	4	1	4	4.50	0.003	>3
Q6.2	5	1	5	6.00	< 0.001	>3
Q6.3	2	2	2	59.00	0.381	-
Q7.1	4	1	4	4.50	0.001	>3
Q7.2	1	0	1	11.50	< 0.001	<3
Q7.3	3	1	3	18.50	0.331	-
Q7.4	2	1	2	20.50	0.002	<3
Q7.5	4	3	5	30.00	0.012	>3
Q7.6	3	3	5	40.50	0.431	-
Q7.7	3	2	3	44.00	0.580	-
Q7.8	4	3	5	41.50	0.087	-
Q7.9	4	3	5	33.00	0.062	-

Table 3.10: Summary of questionnaire responses. Values reported for ordinal data: median, mode, IQR. Wilcoxon signed-rank test results for questionnaire items with significant deviation from the neutral value of 3 ($p < 0.05$). The direction indicates whether the median response was above (> 3) or below (< 3) the neutral value.

the $p = 0.05$ significance level neither in the max magnitude ($p = 0.48$), nor in the mean magnitude ($p = 0.22$). The distribution of the medians is similar to the distribution of the means.

The results of Wilcoxon signed-rank test on questionnaire responses are reported in Table 3.10. Participants deem the system to be coherent with their expectations ($p = 0.021$), easy to learn ($p < 0.001$) and intuitive to use ($p < 0.001$), reporting that they would be confident in using the system with minimal technical support ($p = 0.006$).

The physical workload of operating the system is lower than that of a manual operation ($p = 0.002$) although the participants perceive a lower efficacy than manual operation ($p = 0.006$).

Overall, the system is deemed reliable ($p = 0.003$) and safe to operate ($p < 0.001$).

Kruskal–Wallis tests show a statistically significant difference between experience groups only on question Q2.13 ($H = 7.43$, $p = 0.024$), suggesting that for most items, experience level did not substantially influence responses. Furthermore, none of the post-hoc pairwise comparisons are significant, suggesting that the observed overall difference is not attributable to any specific group comparison.

Although visual information are fluid enough ($p = 0.014$) and coherent with user inputs ($p = 0.003$), participants report lacking depth perception ($p = 0.005$).

Haptic feedback is deemed coherent with the visual information ($p = 0.011$) and useful to distinguish both first ($p = 0.008$) and prolonged ($p = 0.004$) contacts improving spatial understanding of the environment ($p = 0.01$). Overall, participants are satisfied with haptic feedback quality ($p = 0.002$).

Both visual ($p < 0.001$) and haptic ($p = 0.002$) perception are deemed essential to complete the task.

A Wilcoxon test shows no significant differences in the cleanness scores from experiments 2 and 3 ($T = 16.5$, $p = 0.21$), suggesting that the presence of auditory feedback did not improve system efficacy.

3.6.8 Discussion

The main objective of this study is to evaluate the potential of the FH-HBTS for free-hand dental procedures, using the SRP procedure as the experimental testbed.

The efficacy analysis of the system shows that the cleanness scores are consistently high, indicating a good overall execution quality. However, these values do not reach the condition of complete calculus removal typically achievable with the manual procedure, suggesting that the system enables satisfactory results but not yet fully comparable to those obtained through free-hand execution. This finding is consistent with the participants' subjective evaluations, who perceive the system as slightly less effective than manual operation.

From the standpoint of efficiency, the results reveal an interesting trend: execution times tend to decrease as the operator acquires experience with the system, suggesting that performance may progressively improve with practice. This evidence indicates the presence of a learning curve that is not fully stabilized within the scope of the present study and suggests that, with extended training, operators could achieve performance levels comparable to those of manual operation.

With regard to safety, the objective measurements and the participants' subjective perceptions provide complementary insights.

Although the questionnaire responses indicate that the system is perceived as safe for the operator, a different result emerges for patient safety, as highlighted by low scores on the related question (median = 2, IQR = 2). In fact, the quantitative analysis reveals that the magnitude of the interaction forces recorded during the procedures are higher than those observed during manual execution [207], [208], although no damage to the dental surfaces is detected. The higher magnitude of the interaction forces can be attributed to the mechanical characteristics of the industrial robotic system used in the experimental setup, which is designed to ensure robustness and structural stability rather than safe physical interaction. Furthermore, the employed F/T sensor features a resolution not optimized for precision tasks, making measurements below 1 N unreliable.

From the perspective of overall usability, the system's ease of use is positively evaluated: participants find it intuitive and easy to operate, and do not require technical assistance during its use. This suggests that the user interface and control system are effectively designed, allowing operators to focus on the clinical procedure rather than the control dynamics, thus promoting a progressive and natural acquisition of the skills required for completing the procedure remotely.

A crucial factor in achieving this level of usability and supporting procedure completion is the sensory feedback, which significantly contributes to perception and interaction control. The haptic feedback is generally rated as intuitive and effective in distinguishing the different contact phases, including the transition between approach and interaction. This form of sensory information plays an important role in improving procedure execution and situational awareness. The visual feedback, on the other hand, proves useful for completing the procedure, but do not

provide adequate depth perception due to its monoscopic nature. Conversely, auditory feedback shows no measurable influence on performance, suggesting that, in this specific context, its role is marginal compared to the visual and haptic modalities.

From an ergonomic standpoint, participants report a significant reduction in physical workload. This improvement can be attributed to the more comfortable posture allowed by the teleoperation setup, which enables performing the procedure in a seated position, unlike the usual posture required during manual operation. Such improved ergonomics could be particularly beneficial in reducing operator fatigue during long-duration procedures.

Chapter 4

Human supervisory control

Teleoperation can be implemented according to different control paradigms, which define how the human operator and the remote robot share the control of the task. Among the most common paradigms are *direct control*, which includes the haptic teleoperation discussed so far, and *shared autonomy*, where robot autonomy and human supervision coexist to reduce workload and improve efficiency. Within the shared autonomy paradigm lies *human supervisory control*, in which the human operator provides high-level commands while delegating the execution of low-level tasks to the remote robot. This approach mitigates the impact of communication constraints by minimizing the required data exchange and reduces the operator's cognitive load, since the robot operates more autonomously once a command is provided.

Over the years, numerous approaches have been proposed to balance autonomy and human intervention across these paradigms. Recent advancements often combine the strengths of human supervisory and direct control, resulting in more flexible and

robust teleoperation systems.

The remainder of this chapter is structured as follows:

- Section 4.1 introduces the main teleoperation paradigms, with some considerations on the appropriate level of autonomy for different procedures.
- Section 4.2 presents the human supervisory control paradigm, emphasizing aspects related to human–machine interface design;
- Section 4.3 introduces a novel control framework, and a robotic system implementing it [209], enabling dependable bolting operations by exploiting human supervision and state-of-the-art components, responding to specific requirement of flexibility, autonomy and fault tolerance.

4.1 Control paradigms

As mentioned in previous chapters, in a teleoperation system, the fulfillment of a task is carried out via a continuous exchange of information between the human operator and the FR via the communication channel. The nature of this information depend on the level of control given to the human operator, or analogously to the level of autonomy of the FR. Based on these aspects, three control paradigms can be distinguished, as shown also in Figure 4.1:

- *direct control*: the human operator acts as an online reference generator for the FR, whose movements are directly coupled to the human commands.
- *human supervisory control*: the human operator acts as a supervisor for the FR, which is capable of fully complet-

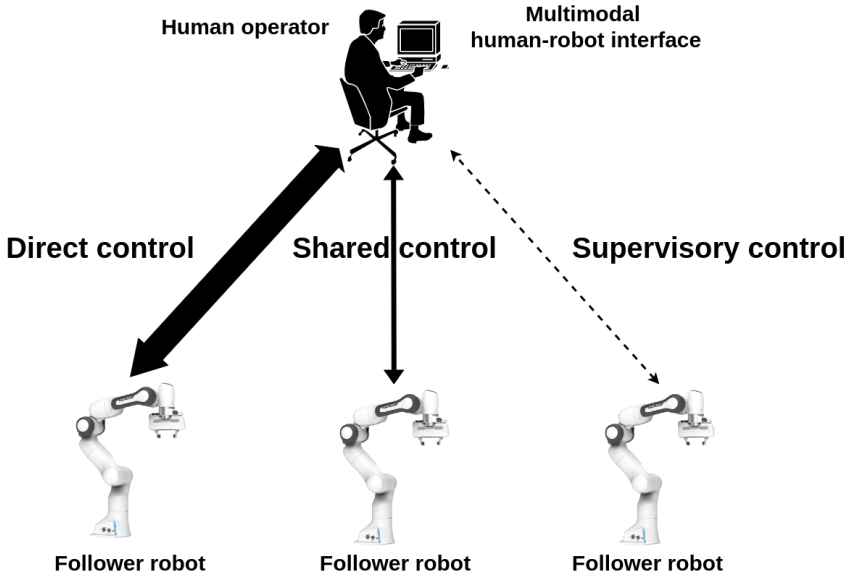


Figure 4.1: Control paradigms for teleoperation.

ing the task autonomously. In this case, only high level, intermittent commands are transmitted from the human operator while the FR engages in a closed-loop interaction with its environment;

- *shared control*: some degree of autonomy is given to the FR, but autonomous behaviors are continuously blended with human commands. For example, the control system could use local sensory information to take choices on behalf of the human operators, augment the human sensory experience or assist them in achieving a predicted goal. These architectures lie in the middle of direct and supervisory control.

In literature, human supervisory control and shared control are

subsumed under the term *shared autonomy*, which refers to a class of systems in which part of the workload is transferred from the human operator to the FR.

In this section, only shared control is presented, since direct control has already been extensively addressed in the previous chapters in the context of haptic teleoperation. Human supervisory control, on the other hand, is formally introduced in Section 4.2.

4.1.1 Shared control paradigm

Shared control seeks to merge the reliability and sense of presence offered by direct control with the intelligence of autonomous control [210].

This paradigm can take on different forms, depending on the process requiring it. For instance, the FR may correct motion commands, regulate subsets of joints or subtasks, or superimpose additional control signals. In scenarios with large communication delays, the human operator can only provide high-level commands, while the FR refines such commands using local sensory feedback [211]. Similarly, FR can autonomously manage subtasks, such as maintaining control over long periods of time [212]. In surgical robotics, shared control has been proposed to compensate for physiological movements, such as the beating of the heart [213]. Here, the sensed heart motion is overlaid on the surgeon's commands, enabling the procedure on a virtually stabilized target. A notable example of shared control is the concept of *virtual fixtures* [214], [215]. These are virtual elements, such as surfaces or velocity fields, superimposed into the visual or haptic workspace. Virtual fixtures assist the operator by constraining movements in restricted areas or guiding them

along desired paths. In this case, control is shared directly at the leader site, where prior knowledge of the task is exploited to adjust or complement the operator's inputs with autonomously generated signals. By leveraging robotic accuracy while preserving human oversight, teleoperation systems with virtual fixtures enable safer, faster, and more intuitive operation.

4.1.2 Discussion on level of autonomy

According to [216], a procedure is automated when it is automatically controlled by mechanical or electronic devices that take the place of the human in terms of observation, decision, and/or effort. As explained in [217], there are four stages of human information processing: information acquisition, information analysis, decision-making and actions. Each of these stages can potentially be automated. However, the desirability of automation depends on the specific context. Moreover, the level of autonomy applicable to each stage may vary according to the system's requirements. In [218], ten distinct level of autonomy are presented, ranging from the lowest level, where the human operator is responsible for all decisions and actions, to the highest level, in which the system operates fully autonomously, making decisions and executing actions independently of any human input, as shown in Figure 4.2.

Two principal approaches exist for determining whether a procedure should be automated and to what extent. [217] propose a *human-centered* perspective on automation, identifying several key factors to be considered. These include the implications for human performance, such as *mental workload*, *situation awareness*, and *skill degradation*, as well as the reliability of the automation and the cost associated with decision or action outcomes. According to this view, the goal of automation should be



Levels of automation of decision and action selection	
10	The computer decides everything, acts autonomously, ignoring the human
9	The computer informs the human only if it decides to
8	The computer informs the human only if asked
7	Executes automatically, then necessarily informs the human
6	Allows the human a restrictive time to veto before automatic execution
5	Executes if the human approves to
4	Suggests one alternative to the human
3	Narrows the selection down to a few
2	Offers to the human a complete set of decision/action alternatives
1	The computer offers no assistance: Human must take all decisions and actions

Figure 4.2: Level of automation [218].

to ensure that the human operator's mental workload remains appropriate for the task at hand, while preserving situation awareness and preventing complacency, which could result in failure detection deficits and a deterioration of operator skills.

In contrast, [219] introduce a *technology-centered approach*, which emphasizes the optimization of technological capabilities and the reduction of operational costs. In this context, achieving a high level of automation is particularly suitable for tasks that are straightforward and take place in highly structured environments.

A practical example is a screwing operation. This task is highly repetitive and routine, and its automation can alleviate the operator's cognitive load without compromising their situation awareness. Furthermore, existing technologies are capable of reliably performing this task. Nevertheless, specific tooling may need to be developed to accommodate environmental constraints such as limited space or restricted accessibility. It is also essential to determine the most appropriate level of autonomy for such tasks. Given its repetitive nature and its typical inclusion

as a subtask within broader procedures, automation may be designed to execute the screwing operation and subsequently notify the operator, corresponding to Level 7 in the established level of autonomy taxonomy. However, depending on the task's criticality, it may be preferable to implement a level of autonomy where the operator retains a limited opportunity to veto the automated action prior to its execution, corresponding to Level 6.

4.2 Human supervisory control paradigm

Human supervisory control is defined as a mode of control in which "one or more human operators are continually programming and receiving information from a computer that interconnects through artificial effectors and sensors to the controlled process or task environment." [216]. Although the terminology may appear similar, the notion of human supervisory control formulated by Sheridan differs fundamentally from the traditional meaning of supervisory control in industrial automation. Sheridan's paradigm describes a human–automation interaction in which the human operator defines goals, oversees autonomous behaviors, and intervenes when needed, emphasizing cognitive processes such as situational awareness, decision-making, and the management of unexpected events. In contrast, industrial supervisory control refers to a structural control architecture in which real-time regulation is handled by dedicated controllers, while higher-level supervisory layers focus primarily on monitoring and issuing limited setpoint or configuration commands. Thus, while industrial supervisory control characterizes how automation components are organized within a process, human supervisory control characterizes how the human remains in the loop and collaborates with automated functions.

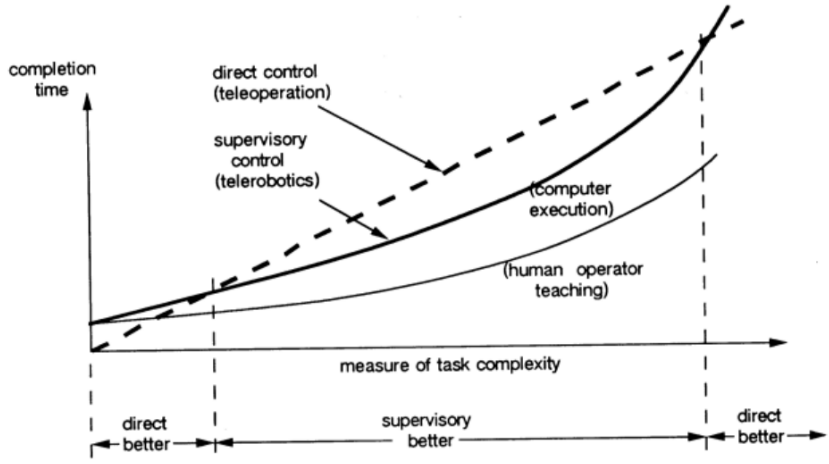


Figure 4.3: Recommended type of control based on the task complexity and the completion time [216].

Such paradigm may also be interpreted as an intermediate stage between direct control and full autonomy. Indeed, it typically corresponds to level of autonomy ranging from 5 to 7 in Figure 4.2. The human operator remains consistently in the loop and retains the ability to assume full manual control of the process at any moment.

This approach is particularly advantageous in contexts where the environment is sufficiently predictable and the task complexity and duration are moderate, as shown in Figure 4.3. A pertinent example is the maintenance of scientific facilities involving exposure to radiation, where automation has been employed to safeguard human operators from hazardous conditions [220], [221]. Traditionally, such procedures were carried out under direct control. However, recent developments have focused on increasing the level of autonomy for such tasks, thereby enabling

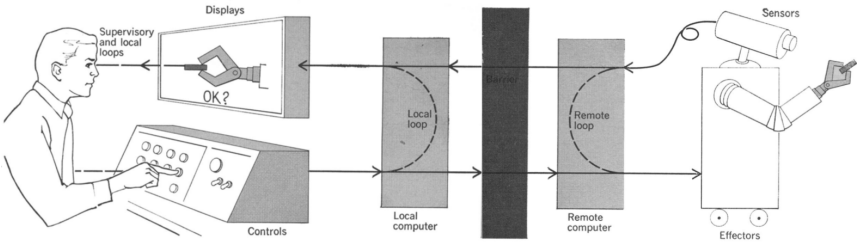


Figure 4.4: Schematic diagram of supervisory control of remote manipulation [223].

faster and safer maintenance operations [222]. Despite these advancements, human supervision remains indispensable due to the significant risks associated with automation failure. Indeed, the current operational paradigm, where certain tasks are highly automated while still requiring a human operator, is characterized by the use of human supervisory control.

4.2.1 Components of human supervisory control

The fundamental components of a human supervisory control system (SVCS) for manipulation are shown in Figure 4.4. These include the usual entities of a human-robot system, but three loops are closed, each representing a type of function [223]:

1. *remote loop*: closed through the low-level controller at the remote site, represents the remote robot with a short-range goal;
2. *local loop*: independent of the FR, represents the operator's use of their local computer to model the remote system, with the aim of predicting its behavior and thereby improving supervision;

3. *supervisory loop*: closed through the human operator, represents the operator's functions of setting goals for the FR, and, if needed, directly controlling it.

The local computer not only serves as an assistant for computation and simulation, but also translates input and output information between a form suitable for transmission and robot use, and a form adapted to the operator's displays and controls. Recent human supervisory control approaches extend this role by enabling the local computer to organize, filter, and prioritize sensory information, as well as to regulate how operator inputs are interpreted by the autonomous components. Through these higher-level support functions, the local computer helps prevent information overload and stabilizes supervision in the presence of human variability, workload fluctuations, or concurrent tasks.

4.2.2 Human supervisory roles and hierarchy

The *human supervisor's roles* in a SVCS can be summarized as follows:

1. *planning*: deciding what task to perform and how to perform it;
2. *teaching*: instructing the controlled system about the planned procedure;
3. *monitoring*: ensuring that operations proceed as expected and detecting potential failures;
4. *intervening*: resuming manual control after a fault is detected;
5. *learning*: drawing on past experience to improve future performance.

These roles typically unfold in sequence, but they can also be

represented as part of three nested supervisory loops [224]:

- *innermost loop*: corresponding to monitoring, which is self-contained. It involves identifying anomalies or completing a monitoring cycle triggers further checks or online tuning;
- *intermediate loop*: linking intervention to teaching, since human intervention often leads to the reprogramming of new goals;
- *outer loop*: connecting learning back to planning. Indeed, effective planning of subsequent tasks relies on lessons learned from prior ones.

These loops operate at different time scales: monitoring occurs over short intervals, programming new procedures takes place less frequently, and revisions to high-level planning occur only over much longer horizons.

4.2.3 Modeling human supervisory control operations

Human supervisory control operations can be effectively modeled as a sequence of discrete steps, each representing a low-level action required to accomplish the overall task. As shown in Figure 4.5, the SVCS transitions from one step to the next only after receiving validation from the human operator, who retains full authority to intervene at any point, either to repeat a step or to take manual control in the event of a fault. Each step concludes with a validation phase, during which feedback is provided to support the operator's decision-making.

While the system includes basic fault detection capabilities that enable it to recognize potential execution errors and return to the last known safe state when re-execution is required, the

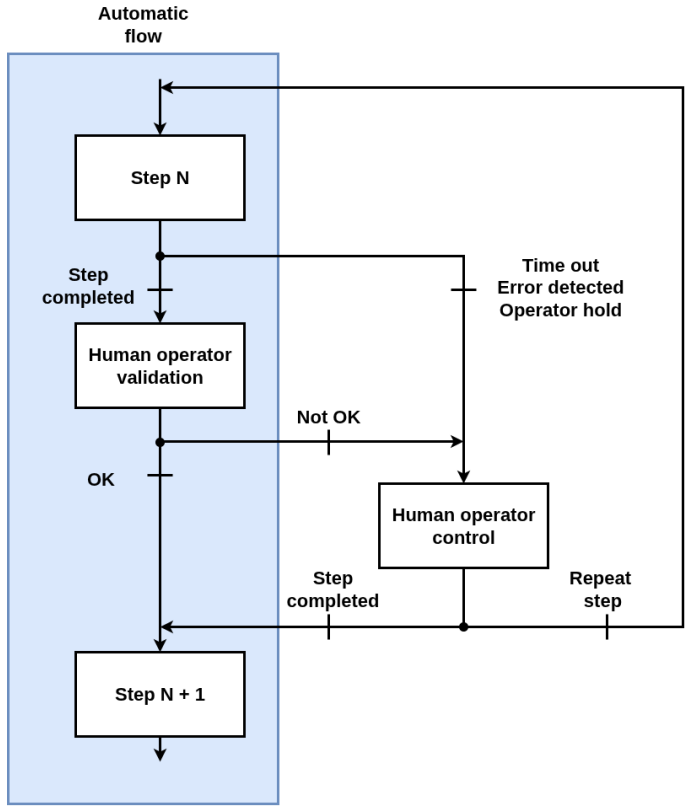


Figure 4.5: Diagram of a generic human supervisory control operation.

primary responsibility for monitoring and handling faults lies with the human operator, who supervises the operation and manages unforeseen situations.

4.2.4 Interface design for supervisory control

When working with *human supervisory control*, interface design plays a crucial role, as it must support effective interaction and usability, and improve the situational awareness of the human operator. Otherwise, the interface itself affects perceived workload and overall performance. For instance, [225] shows that intermittent messages from a chat communication tool interrupt primary task execution, highlighting how the design of alerts and alarms can unexpectedly degrade operator performance if they are implemented as independent features without integration into the overall interface.

Several methodologies are investigated to improve interface design in complex human supervisory control tasks. The *abstraction hierarchy* approach [226] allows decomposing a system into subcomponents to determine where autonomy can best support the human operator, while *cognitive task analysis* combines with situational awareness criteria to define requirements for next-generation interfaces [227]. Other efforts lead to practical guidelines, such as those proposed by [228], which emphasize four key principles: automation behavior remains highly visible to the operator, information access costs are minimized through integration and highlighting of relevant data, predicted changes and projected system responses are displayed clearly, and operators are provided with rapid means to reinstruct automated systems.

A complementary perspective is offered by user-centered design approaches. For example, [229] explore multi-agent system interfaces designed around principles such as compact presentation of relevant information, user-friendly layouts, minimal but essential information for decision-making, rapid interaction, support for dynamic role changes, and continuous feedback. Their re-

sults confirm that interfaces are most effective when they are compact and accentuate only the information most useful to decision-making.

Interface design also accounts for team processes, aiming at what is called a *team-centered interface design* [230]. The goal is to facilitate shared awareness and communication, thereby balancing task workload and interaction workload. This requires not only robust agent capabilities but also human trust and acceptance of the agent's actions, which depend on transparency of the agent's abilities and reliability [231].

Building on these foundations, several innovative directions emerge for interface design in human supervisory control. These include *multimodal displays and controls*, which counteract degraded perception in remote operation by integrating visual, auditory, and haptic cues, planning tools, schedule management aids, as well as visualization tools.

4.2.4.1 Multimodal display and control

In teleoperated environments, natural perceptual processing is decoupled from the physical environment, which can compromises human perception of the remote task and negatively impacts situation awareness and, consequently, overall task performance [232]. These degradations become more pronounced when video quality is suboptimal [233], [234]. To mitigate such issues, [235] proposes the use of spatial audio displays to augment operator situational awareness, discussing their benefits across the three levels of situational awareness. They recommend presenting visual and spatial audio information concurrently, and suggest that spatial audio may enhance telepresence. However, the relationship between presence and task performance remains unconfirmed, and spatial audio displays can be lim-

ited in noisy environments, where users may also experience front–back confusion. As a result, tactile displays emerge as a promising alternative. [236] compares a sensory display, which conveys warning information by altering physical stimuli, with a cognitive display, which requires symbolic manipulations to define critical signals. Their results indicate that the sensory display leads to more threat detections, fewer false alarms, faster response times, and lower perceived workload. In addition, [236] investigate different types of directional cueing interfaces, visual, spatial audio, and haptic, and find no significant differences in their effectiveness.

4.3 Control framework for dependable robotized bolting operations

As discussed in Section 4.1.2, highly repetitive tasks can benefit from granting the FR higher levels of autonomy while still preserving a human-in-the-loop approach, with the goal of reducing the operator's cognitive workload.

In Section 4.1, we introduced the main teleoperation paradigms, presenting alternatives to direct teleoperation that involve shared autonomy. In Section 4.2, we then described human supervisory control, highlighting both the central role of the human operator in monitoring task execution and the importance of designing appropriate visualization and control interfaces to enhance operator situation awareness.

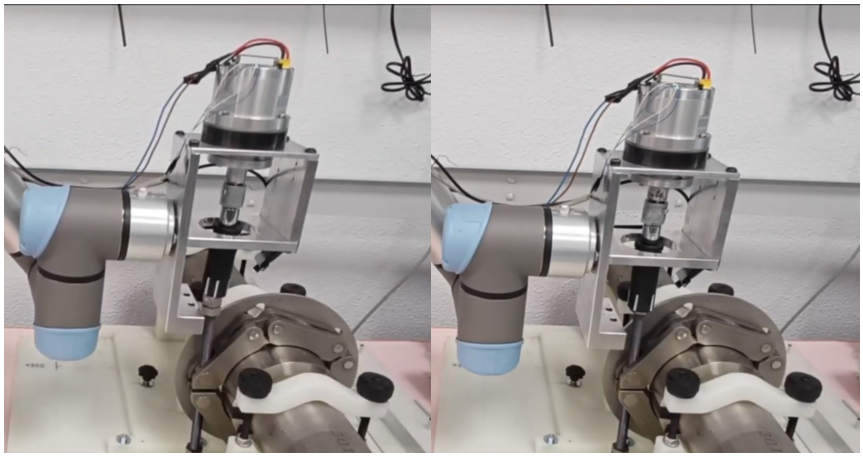
Therefore, in this section we present a novel a control framework for dependable robotized bolting tasks and instantiate it on a specific robotic system [209]. The framework integrates state-of-art components responding to specific requirements of

autonomy, flexibility and fault tolerance, and introduces a supervisor (SV) to orchestrate them, allowing for a seamless transition between autonomous and manual operations, while preserving the human operator's authority, consistently with the human supervisory control paradigm. Among these components, it enables direct teleoperation by integrating the HBTS proposed in [76], which allows the operator to manually handle contingencies and faults, thereby enhancing the dependability of the system. The framework also features a multimodal human–robot interface that provides real-time visualization of all relevant system information, thereby improving operator situation awareness.

4.3.1 Background

Bolting plays a vital role in both industrial assembly processes [237] and in the maintenance of large scientific facilities [238]. In scientific infrastructures, bolts and screws are widely employed across several systems requiring periodic maintenance. Threaded fasteners are commonly used to mount components to their supports [239], and precise alignment is often achieved by adjusting multiple bolts [240]. To avoid the need for cutting or welding, pipe flanges are typically joined using chain clamps, which allow for the replacement of pipe sections [241]. In industrial manufacturing, it is estimated that 37.9% of all mechanical assembly tasks involve bolt insertion and tightening [242].

Despite their prevalence, bolting operations remain among the most challenging tasks to fully automate [237], particularly in high-mix, low-volume production settings and in scientific maintenance, where tasks vary frequently and dedicated fixtures or precise part positioning are often unavailable. Indeed, many bolting operations are currently performed either manually by human operators, or through repetitive automated systems



(a) Coupling **(b)** Tightening

Figure 4.6: Example of coupling and tightening steps in a bolting operation.

that rely on complex fixtures and dedicated part feeders [243]. Manual bolting offers flexibility in handling different tools and adaptability to variations in geometry and positioning. However, it does so at the cost of consistency of the applied driving torque, besides being a time-consuming and labour-intensive process. Conversely, repetitive automation ensures higher efficiency and accuracy, but it offers limited flexibility and poor adaptability to environment variations. This highlights the demand for an automation approach that combines the flexibility and adaptability of manual execution with the skills of automatic systems. The literature proposes a variety of automation approaches [244], including 2D and 3D vision-guided methods. Early approaches [245] rely on 2D vision to monitor fastener alignment, but their accuracy is severely affected by environmental conditions and surface reflectivity. Hybrid sensing strategies, combining 2D

visual feedback with force/torque feedback [246], [247], improve insertion accuracy and enable fixtureless assembly, in some cases supported by learning-based correction mechanisms [248]. Despite these advances, 2D vision–based methods remain limited in degrees of freedom and prove effective only in structured environments. To address these limitations, 3D vision systems are increasingly adopted for fixtureless operations [249], enabling the direct detection of spatial features from component geometry [250]. Solutions based on rapid object registration techniques aim at maximizing robustness and computational efficiency, albeit at the expense of accuracy [251]. Geometric feature–based recognition methods [252] ensure high accuracy but require continuous visibility of reference features, while geometric primitive fitting techniques involve longer processing times and significant pose estimation errors [253]. Building on these principles, surface matching techniques are employed for fixtureless bolting operations [254]. An ongoing challenge concerns the detection of holes on multiple planes, especially in the presence of internal threads. Existing methods [255], [256] rely respectively on relationships between planes and edges, unsuitable for non-solid holes or on point set analysis, which requires several minutes to process medium-resolution point clouds. Therefore, although recent research continuously improves the integration of vision, force feedback, and learning-based strategies, current autonomous robotic systems for bolting operation still face limitations in terms of real-time performance, accuracy, reliability and adaptability to unstructured environments [257].

Furthermore, sporadic fault conditions may arise during bolting operations, which can lead to critical failures if undetected [258]. Typical fault conditions include part misalignment, overtightening, cross-threading, and jamming [237]. Cross-threading occurs when the external thread engages the internal one incor-

rectly, causing the threads on one side not to follow the same spiral as those on the opposite side, while jamming can occur when the tilt-angle control is too rigid and the initial inclination exceeds the locking angle [259]. In some cases, hardware failures can occur in the power tools used to perform bolting operations. For this reason, some studies investigate the use of robotic systems to operate hand tools originally designed for manual use [260]. Several works emphasize the use of wrench signals as the primary sensing modality for fault detection [261]–[263]. However, these methods typically cover only a narrow range of failure modes. Learning-based techniques have shown promise, particularly in structured low-variability environments, but often struggle to generalize under real-world uncertainty [264], [265]. Similar challenges arise in recent data-driven approaches to fault detection [266], [267].

Finally, compliance has long been acknowledged as a critical factor in autonomous bolting, to the extent that nearly all commercially available tools integrate compliant mechanisms in their design [237]. In addition, active compliance techniques, such as impedance and force control, are critical to improve safety and dependability during operations [268], especially when compared with rigid motion controllers [269].

In large scientific facilities, such as nuclear plants, unreliable autonomy or missed fault detection can have severe consequences. In such high-stakes contexts, telerobotics offers a powerful alternative. By extending human sensing and manipulation capabilities into remote, hazardous, and unstructured environments, it enables the safe execution of complex tasks and ensures immediate and effective detection and response to faults [270].

A pioneering example is the Joint European Torus (JET), where direct teleoperation was successfully employed in 1998 to replace

the facility's divertor [271]. Since then, telerobotics has become an essential component of maintenance strategies for major scientific infrastructures [222]. In some instances, it has been integrated only after the plant's construction, with maintenance procedures progressively adapted for robotic execution. Several examples of this approach can be found at CERN, where the MIRA robot is currently used to perform radiation surveys in the tunnel [272], alongside many other teleoperated interventions.

Nowadays, increasing efforts are being made toward achieving higher levels of automation in selected tasks, enabling faster and safer maintenance operations [222]. In such scenarios, the most commonly adopted paradigm is supervisory control [216], where specific phases of the procedure are automated, while the human operator retains control over transitions and can take control of the system at any time. Furthermore, new facilities under development are being designed with telerobotic compatibility in mind from the outset. In these cases, maintenance requirements are embedded directly into component design, and dedicated robotic interfaces are implemented to ensure seamless integration with telerobotic systems. Notable examples include IFMIF-DONES [273], ITER [274], and CFETR [275].

Motivated by the importance of bolting operations in both industrial assembly processes and the maintenance of scientific facilities, and considering the current technological limitations in terms of autonomy and fault detection reliability, in this work we propose a control framework enabling dependable robotized bolting operations, and a robotic system implementing it. The framework integrates state-of-art components responding to specific requirements of autonomy, flexibility and fault tolerance, and introduces a SV to orchestrate them, allowing for a seamless transition between autonomous and manual operations, and

viceversa. Given the practical impact of the proposed approach, a key contribution is a TRL-5 experimental validation of the system on a representative bolting operation, consisting of bolt tightening to join pipe flanges, under several fault conditions:

- control system failure in the absence of active compliance under part misalignment;
- vision system failure in bolt pose identification;
- hardware failure of the bolt driver used to complete the tightening process.

4.3.2 Methodology

Robotized bolting operations involve multiple steps, often including feeding, alignment, tightening, and postfastening, each relying on specific components and control strategies. The success of each step is essential to enable the correct execution of the following ones. In the most general case of an unstructured environment, the bolting task involves six DoF: five define the bolt alignment with the parts to be joined, or equivalently, the driver unit alignment with a fixed bolt, in terms of position in the three-dimensional space and axis orientation; the other one corresponds to the bolt's axial rotation and tightening. This latter DoF is typically provided by an independent actuator integrated into the bolt driver unit, which is designed for high-speed rotation and high-stiffness tightening.

The dependability of robotized bolting operations can be compromised by several potential failures in sensors, control and actuation systems, which may lead to undesired behaviors. Given the critical nature of bolting tasks, dependability must be ensured not only at the component level but also across the entire robotic system. Dependability is an integrated concept that

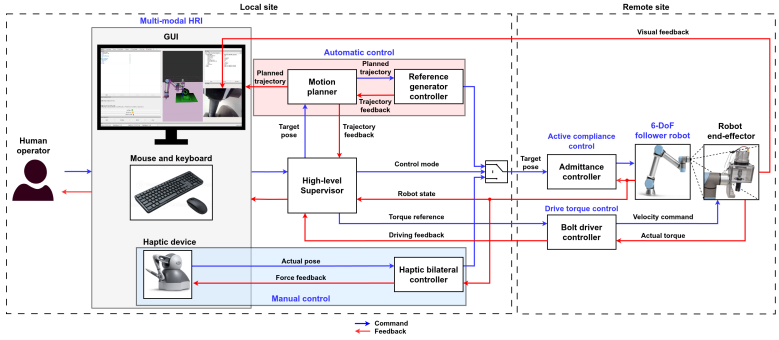


Figure 4.7: Control system for dependable bolting operations.

encompasses a set of essential system attributes, including robustness and safety. The former includes availability, reliability and maintainability [8], and refers to the system's capability to fulfill its intended functions in normal operation, but also to maintain acceptable performance under degraded or fault conditions, guaranteeing continuity and predictability of its behavior. The latter refers to the prevention of catastrophic consequences for the environment or the robot itself, even in the presence of failures, malfunctions or unexpected collisions.

One major challenge of robotized bolting operations in unstructured environments lies in relying on reliable sensing and actuation systems. As discussed in Section 4.3.1, unreliable sensing, perception, and actuation can significantly affect the robot's ability to complete the operation effectively, as inaccuracies in environment perception or torque application may compromise both the proper execution of the task and the overall system dependability. This becomes particularly critical considering that such unreliability constitutes the primary source of faults, but also leads to failures in detecting them. It is therefore useful to explicitly define the types of faults that can compromise the

operation: internal faults and interaction faults. The former include damage to mechanical components and actuators and/or sensor faults, such as driver unit failures. The latter include issues related to interaction with the environment, such as parts misalignment that cause the system to exceed its nominal limits.

Achieving dependability requires a set of strategies aimed at preventing, detecting, isolating, and actively handling such faults. This calls for modular human-in-the-loop control architecture and multimodal human-robot interface, which facilitate the monitoring, detection and handling of potential faults, and ensure the correct execution of each step of the operation. In addition, dependability can be achieved by exploiting the intrinsic redundancy of the robotic system with respect to the task, as most robots used in industrial and research environments are 6-DoF and therefore inherently redundant for bolting operations. Indeed, this extra DoF can be operatively employed to achieve bolting even in the case of a failure of the driver unit.

Regarding safety, Section 4.3.1 discussed how it is closely related to compliance and to the achievement of the desired driving torque, in order to prevent joint component failures. This requires active compliance techniques, as well as accurate control and monitoring of the driving torque and alignment angle, to also avoid common faults such as cross-threading and jamming.

Building upon this analysis, we propose a control framework for dependable bolting operation integrating monitoring and control components, each designed to fulfill specific requirements, and supporting autonomous and manual operations. Such framework integrates:

- *6-DoF FR*: intrinsically redundant with respect to the bolting task and equipped with all the tools, i.e. driver unit, force/torque sensor and cameras, required to perform

the operation;

- *active compliance control*: ensuring precise alignment angle control and guaranteeing operational safety;
- *driving torque control*: ensuring that the desired clamping force is achieved while providing operational safety and effectiveness
- *manual control*: including hardware interfaces and controllers to enable manual intervention and fault handling;
- *multimodal human-robot interface*: providing a unified environment for the supervision of operation execution, facilitating fault detection and handling on the part of a human operator;
- *high-level supervision*: orchestrating different components and allowing for a seamless transition between autonomous and manual control;
- *vision system*: providing pose targets to the system for the task execution.

With reference to Figure 4.7, which illustrates the system implementing the proposed control framework, the following sections describe its individual subcomponents. In Section 4.3.2.1 a detailed description of the multimodal human-robot interface is provided. Section 4.3.2.2 and Section 4.3.2.3 present, respectively, the admittance controller used to achieve active compliance and the Bolt driver controller (BDC) used to reach the desired driving torque. Finally, in Section 4.3.2.4 the description of the direct teleoperation system used for manual fault handling, is provided, while in Section 4.3.2.5 the objectives and the operation of the SV is presented. The design and integration of the vision system for bolt identification are not addressed in this work. Consequently, the bolt pose is assumed

to be known throughout the experimental validation. Nevertheless, the proposed framework is compatible with existing robust detection-based algorithms, such as the one described in [276], which could be integrated to achieve a higher level of autonomy in future implementations.

4.3.2.1 Multimodal human-robot interface

In robotized bolting operations, the operator's ability to maintain a high level of situational awareness is essential for a safe and effective operation. Situational awareness encompasses the perception of relevant elements in the environment, the understanding of their significance, and the prediction of how they may evolve over time. Therefore, a suitable design of the human-robot interface plays a fundamental role in supporting situational awareness, as it serves as the primary communication channel between the human and the robotic system.

In this work, we propose a multimodal human-robot interface providing a comfortable and uniform environment for the control of the FR. This includes standard input devices, such as a keyboard and mouse, along with a HD for direct teleoperation, and a GUI that communicates bidirectionally with the SV.

The GUI, shown in Figure 4.8, is designed to support the human operator in detecting fault conditions. To this end, it is designed around six main objectives:

1. Monitor the FR's state in real time, including its joint configuration, through continuous updates visualized in a 3D environment. This allows the operator to evaluate the results of the sent commands.
2. Visualize a 3D model of the interaction environment to support validation by the human operator.

3. Plan, rehearse, and validate collision-aware trajectories, as done in [14], during approach, coupling, and distancing steps. Eventually, the planned trajectories are transmitted to the robot.
4. Manage the transitions between automatic control and manual control, i.e. support the operator in engaging the FR with the HD when the orientation of the stylus and that of the bolt driver tip match.
5. Monitor the progress of the procedure in real time through the video stream from the camera mounted on the end-effector of the FR.
6. Enable the human operator to monitor the operation status through dedicated panels displaying state information and buttons for sending commands to the FR.

Alongside the GUI, real-time visualization of interaction forces and tightening torques is provided through the PlotJuggler tool. Such visualization enhances the operator's situational awareness and facilitates verification of the operation completion.

4.3.2.2 Active compliance control

In bolting operations ensuring active compliance during interaction is recognized as a fundamental requirement, especially to prevent failure conditions such as jamming.

Therefore, in our work, we adopt an admittance controller as the low-level controller for the FR. This controller has three key features. First, it guarantees the stability of the FR even in the event of communication loss, as it continues to follow the last received reference in the absence of new commands. Second, it prevents damage to both the FR and the manipulated environment by adapting the received references to enable compliant

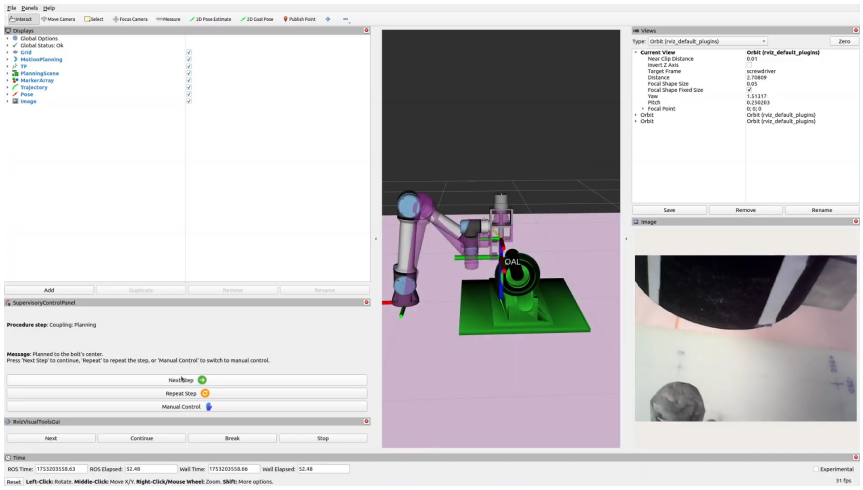


Figure 4.8: Screenshot of the system's GUI during operation.

interaction along both translational and rotational axes. This also facilitate the bolt alignment. Finally, it ensures command continuity by discarding reference poses that are too distant from the robot's current state, based on a configurable threshold. These features make the admittance controller particularly suitable for contact-rich tasks like bolting, where dependability and responsiveness to dynamic interactions are essential.

When the system operates under automatic control, the procedure is executed by following collision-aware trajectories. These are translated into references for the admittance controller by a Reference generator controller (RGC). At each control cycle, it provides a pose reference to the admittance controller according to the timing law of the input trajectory.

This modular structure ensures compatibility between trajectory execution and low-level interaction control. Moreover, it allows for flexible switching between control modes without modifying

the underlying control architecture.

4.3.2.3 Driving torque control

In both industrial assembly processes and the maintenance of large scientific facilities, ensuring secure tightening of bolts used to assemble different systems is essential to prevent catastrophic failures.

For this reason, in this work we integrate a bolt driver in the FR's end-effector and design a BDC that secures the bolt with the appropriate driving torque. This controller receives the target torque and commands a constant velocity to the bolt driver until the measured torque reaches the desired value. It also includes a safety mechanism that allows the tightening process to be interrupted upon reception of a stop signal.

The BDC can also receive position references, enabling it to rotate the bolt driver by a specified amount to safely complete the bolt releasing operation.

These functionalities make the BDC a reliable and flexible component for managing torque-controlled bolting operations, ensuring both operational safety and adaptability to task requirements.

4.3.2.4 Manual control

In bolting operations, effective fault detection and management are crucial to prevent catastrophic events. To enable manual handling without exposing the human operator to potentially hazardous environments, we enable direct teleoperation of the FR by integrating a Haptic bilateral controller (HBC). Since the contact-rich nature of such operations requires accurate control of the FR and natural haptic rendering, the HBC adopted in

this work is based on the architecture proposed in [76], which enables natural teleoperation and precise control of the FR.

Although in this work we refer to the HBC as a single entity, it actually consists of two controllers: a feedforward controller and a feedback controller.

The former is responsible for coupling the HD's stylus with the octagonal socket of the bolt driver. At each control cycle, it retrieves the current pose of the HD, filters it online using a moving average filter to remove human hand tremors, and maps it to a target pose for the FR. This mapping ensures motion correspondence between the movements performed by the human operator with the HD and those executed by the FR in the camera view.

The feedback controller is responsible for rendering force feedback on the HD, enabling the human operator to perceive the remote interaction. The force feedback is obtained by a second impedance model, which leverages the motion error generated by admittance control to provide a more comfortable and natural experience for the operator [75]. To this end, the feedback is also coordinated with the interaction observed through the camera.

4.3.2.5 High-level supervision

The presence of multiple heterogeneous subcomponents, each devoted to a specific function, demands a higher-level entity capable of overseeing their operation and ensuring coherent task execution. To address this need, we design a SV to monitor and orchestrate the operation and the interaction among the different subcomponents. By exploiting both the robot's autonomous capabilities and the human operator's supervisory ones, the SV embodies the human supervisory control paradigm, enabling

robust, adaptive, and safe operation execution.

To implement this concept, we define in Section 4.3.2.5.1 a task-specific pipeline that the SV follows during execution, ensuring consistency and dependability.

4.3.2.5.1 Bolt tightening pipeline Building upon the general framework presented in Section 4.2.3, in this section we present a task-specific modeling of a tightening operation. The procedure is broken down into the following steps:

1. *Approach*: the robot moves in the proximity of the bolt. It suffices that the bolt is framed in the camera, presumably mounted on the end-effector, which is responsible for identifying the bolt's center.
2. *Bolt identification*: a vision system identifies the bolt center and provides the estimated pose as a target for the control system.
3. *Coupling*: the robot precisely moves to the actual bolt location, coupling it with the bolt driver (Figure 4.6a).
4. *Tightening*: the bolt driver applies a controlled torque to tighten the bolt according to the specified parameters (Figure 4.6b).
5. *Releasing*: the bolt driver applies a small opposite torque to facilitate the decoupling with the bolt.
6. *Distancing*: the robot retracts from the bolt location to a safe position, thus completing the operation.

After each step, the operator validates the result based on feedback from the remote site and decides whether to proceed or repeat the step. This structured approach allows for safe, flexible, and operator-aware execution of bolting operations in

remote and unstructured environments.

4.3.2.5.2 Supervisor The proposed SV manages the execution of the procedure according to the step-based pipeline defined in Section 4.3.2.5.1. It supports two control modes, *automatic control* and *manual control*, and is designed to accomplish the following six goals:

1. Ensure that transitions between operation steps occur only after execution has been validated by the human operator. This guarantees that the execution flow remains consistent with the supervisory control paradigm, in which the human operator's authority is always preserved.
2. Reset the system to the last known safe state in the event of a fault, whether detected by the system through its basic fault detection capabilities or by the human operator, and allow either the re-execution of the step or the switch to manual control. This feature is critical to ensure the dependability of the execution, as it enables recovery from anomalous conditions without compromising the structural integrity of the system or the surrounding environment.
3. Interact with the human-robot interface to receive commands and/or validations from the human operator and provide state information of the operation to be displayed on the GUI, to support human decision-making and uphold situational awareness.
4. Interface with the planning system to provide reference trajectories to the RGC.
5. Manage the transition between automatic and manual control, i.e. enable relevant controllers and bring the system to a safe state before switching control.

6. Provide commands to the BDC to activate the tightening and releasing operations.

4.3.3 Experimental validation

This section presents an experimental validation of the proposed control framework performed by rehearsing the operation described in Section 4.3.2.5.1 under different fault conditions of the system implementing it. The aim of the experiments is to validate the dependability of the system in preventing and handling the most common failure causes. An end-to-end demonstration of the system, under nominal conditions, is provided in [277], where the full execution of the operation under automatic control is showcased.

With the aim of confirming the impact of active compliance on preserving the dependability and safety of the system under interaction faults, in Section 4.3.3.2 we compare the execution of the coupling operation under conditions of misalignment between the driver unit and the bolt, both with and without active admittance control.

In order to quantitatively assess the system's effectiveness in assisting the detection and management of faults in the unreliable autonomous system, we simulate a scenario in which the bolt is incorrectly identified by the vision system. The fault is detected by the human operator only during the execution of the coupling trajectory. In response, control is transferred to the operator, who completes the task via direct teleoperation. The results of this experiment are presented in Section 4.3.3.3.

Finally, in Section 4.3.3.4 we provide a formal assessment of the system's ability to handle hardware failures through the direct teleoperation system, by replicating a bolt unit malfunction

scenario, with the human operator performing the tightening step manually.

4.3.3.1 Experimental setup

The experimental setup involves the following equipment and materials:

- a workstation running Ubuntu 22.04 with robot operating system (ROS)2 Humble. The latter is a general purpose computer communicating with the FR over an Ethernet network. To guarantee deterministic and reliable control execution, the operating system was enhanced with the PREEMPT-RT real-time patch;
- a 6-DoF force-feedback HD [72];
- a 6-DoF UR5e robotics arm by Universal Robots [142]. It is equipped with a mechanical end-effector for bolting operations, featuring a camera for the visual feedback and the bolt driver. The bolt driver includes the ERob 70I rotary actuator [278] and an octagonal socket;
- two pipes joined using a bolted chain clamp.

The remote site of the experimental setup is shown in Figure 4.9.

4.3.3.2 Prevention of interaction faults

In order to evaluate the effectiveness of the system in preventing controller failures due to interaction, we perform 40 interaction experiments under conditions of misalignment between the octagonal socket and the bolt. Based on the pipeline described in Section 4.3.2.5.1, step 3 is executed 20 times with active admittance control (Scenario A) and 20 times with a rigid motion

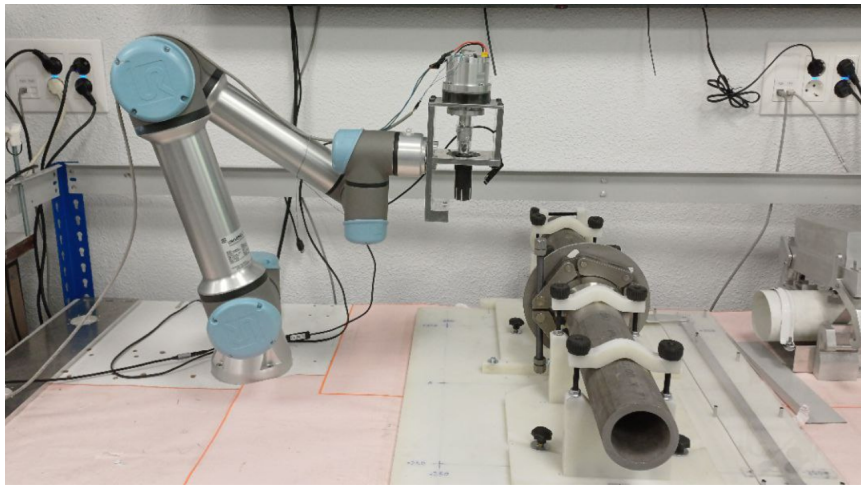


Figure 4.9: Remote site of the experimental setup, showing the UR5e robotic arm equipped with the mechanical end-effector and the pipes used for experimental validation.

controller (Scenario B). For each scenario, we record the interaction forces measured by the integrated force/torque sensor during the collision phase between the socket and the bolt.

To assess the effectiveness of active compliance, we compare the mean and the variance of the normal force applied to the bolt in both scenarios. Figure 4.10 reports the mean and standard deviation of the measured normal forces. Visual inspection showcases a significant reduction in the normal interaction force in Scenario A, given the same pose commanded. Furthermore, the FR is provided with a safety mechanism that stops the robot when high interaction forces are detected, requiring manual reset by a human operator. In 100% of the trials in Scenario B, this safety mechanism was triggered, compared to 0% in Scenario A.

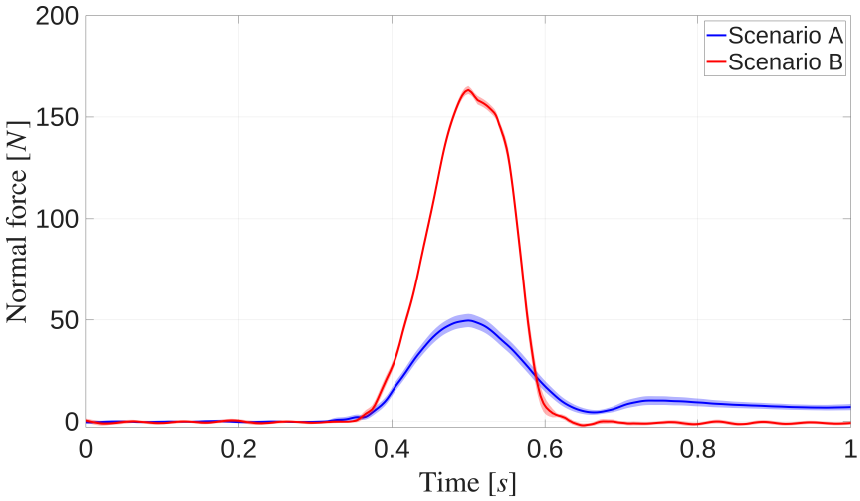


Figure 4.10: Comparison between the mean of the interaction force in Scenario A and Scenario B.

4.3.3.3 Handling of vision system failures

To perform a formal assessment of the system's capability to support the human operator in the detection and management of faults in the unreliable autonomous system, we execute steps 2 and 3 of the procedure described in Section 4.3.2.5.1, simulating an incorrect identification of the bolt's center. In such trials, we assume that the human operator fails to detect the identification fault during the validation phase of step 2 and proceeds with the execution of step 3. The fault is detected only during the execution of step 3, through the visual feedback provided by the camera, leading the operator to stop the automatic execution and take manual control. The validation is considered successful if the operator is able to complete the coupling with the bolt via direct teleoperation of the FR.

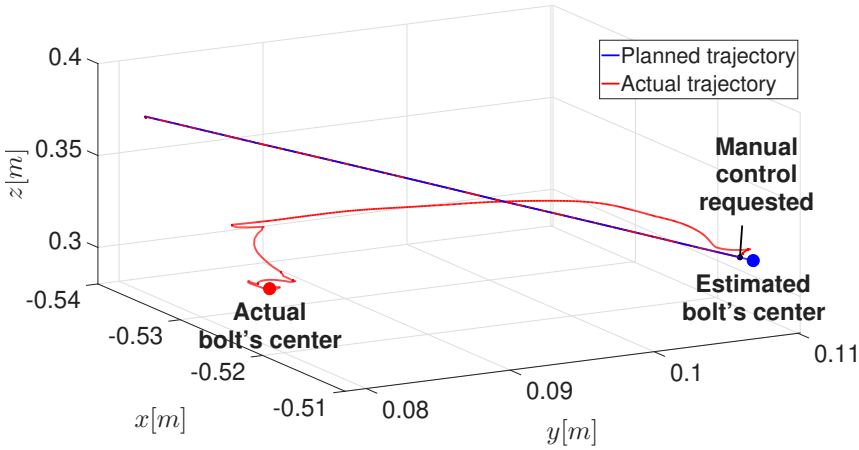


Figure 4.11: Comparison between the planned coupling trajectory and the one actually followed by the FR after human intervention.

Figure 4.11 illustrates both the planned trajectory generated by the motion planner and the actual trajectory followed by the robot. The results showcase that, once the fault is detected, the human operator is able to take manual control, and complete the coupling task. These observations confirm that the system provides all the necessary tools to enable the human operator to detect faults and effectively manage contingencies. However, they do not offer any insight into the effectiveness of the operator's intervention in completing the operation manually. Therefore, in [277] we provide a qualitative assessment of the latter.

4.3.3.4 Handling of bolt driver failures

Since the proposed system aims at ensuring manual contingency handling through direct teleoperation, we evaluate the direct

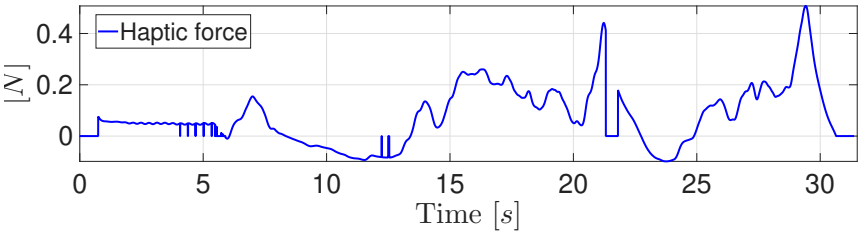


Figure 4.12: Forces rendered on the HD.

teleoperation system's capability to handle a bolt driver failure, by letting the human operator manually perform the tightening task.

The task consists of alternating between two steps, i.e. step 3 and step 4 of the operation described in Section 4.3.2.5.1, executed by the human operator via the HD. This alternation is necessary due to joint limits of the FR and the risk of self-collisions, which prevent the bolt from being fully tightened in a single step. The operation is considered successful if the bolt is correctly tightened. If at any step the force exerted exceeds a safety threshold, causing the robot to stop, or if the FR undergoes a self-collision, the operation is considered failed. Throughout the execution, the human operator can rely on both haptic and visual feedback to complete the coupling with the bolt, and on the real-time display of torque values to determine when the tightening has been successfully completed. We perform 20 trials with the same experienced operator on the same day. The results show a success rate of 95%, with a single failure due to self-collision of the FR, of which the operator remained unaware. These results highlight the system's effectiveness in completing a complex, contact-rich task, while also revealing the limitations of visual feedback in providing the operator with comprehensive situational awareness.

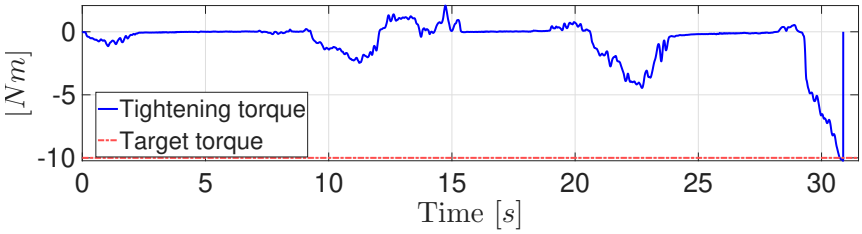


Figure 4.13: Tightening torque profile.

A demonstration of a manual tightening execution is provided in [277]. For the sake of completeness, in this section we also report the outcomes of one successful trial, in terms of both the haptic feedback perceived by the human operator and the measured tightening torque. The former is shown in Figure 4.12, while the latter is presented in Figure 4.13. Visual inspection of the haptic force profile reveals a slow dynamics, which enhances both operator comfort and situational awareness, facilitating the completion of the operation even in the presence of delays of the visual feedback.

Chapter 5

Conclusions

This chapter briefly reports the main achievements attained during this thesis, and discusses possible advancements left for future research, aiming at enhancing the obtained results. The following sections follow the same structure of the chapters of this dissertation: for each of the covered topics, the novelties introduced in this thesis are summarized and framed in the scope of thesis, defined in Section 1.2, discussing how the objectives defined in Section 1.3 have been pursued, and suggesting future improvements.

5.1 Haptic teleoperation under time delays

In Section 2.3 a new concept of operations and associated human-robot interface to assist human operators in the control of remote robotized systems for planetary ISRU missions [14]. We adopted a HBTS, based on a P-Fm architecture, to allow for accurate

remote manipulation, and a set of software tools and interfaces to plan and command trajectories from the control station. By alternating off-line planned trajectories and quasi-real-time teleoperation, the haptic control workspace is extended without sacrificing accuracy. At the same time, the proposed human-robot interface preserves the system's ease of use.

Through the rehearsal across multiple trials of an ISRU scenario including a peg-in-hole manipulation task, we confirmed that haptic control improves safety of the considered task, preventing damage to the collected sample, the robot, and its surroundings, increases human awareness, allowing to compensate for communication delays, and improves the usability of the system. In fact, our preliminary results suggest that inexperienced operators could be efficiently trained to complete the task with ease. This motivates further investigations involving a larger audience of operators with a heterogeneous background.

Through the employment of the proposed human-robot interface, we assess the impact of the haptic feedback on mission success: an interaction task requiring an elevated degree of accuracy can be performed 2.25 times more successfully when compared to unilateral teleoperation systems, providing only visual feedback, almost nullifying the probability of failure due to exceeding a safety threshold in the exerted forces. This highlights how the implicit compliance delivered by the human-in-the-loop is crucial for ensuring safe interaction. Moreover, haptic feedback supports the human operator in compensating for time delays, making the system robust to round-trip communication delays of up to 1.0 s.

5.1.1 Discussion

A limitation of the proposed system lies in the choice of the haptic feedback rendering methodology based on the measurement of interaction forces. As discussed in Section 2.1.2.2, although this feedback increases the transparency of the system, a fact confirmed by the reported results, it does not ensure overall stability. Indeed, during the trials, several oscillatory phenomena were observed which, although they did not prevent task completion, undoubtedly hindered the operator's ability to carry it out seamlessly.

These phenomena can be traced back to the step-dynamics of the interaction forces, generating the haptic feedback. In particular, unexpected contacts with the environment, for instance, caused by the lack of three-dimensional perception of relative object positions due to the limitations of visual feedback, produced sudden force changes that the human operator had to cope with. Such behavior conflicts with the operator's prior experience of interacting with the physical world. Indeed, as discussed in Section 3.1.2, humans are capable of perceiving both interaction events and interaction effects. However, the dynamics of the feedback described above prevent the perception of interaction events, thereby compromising system usability.

This limitation has motivated the design of novel systems capable of ensuring stability, safety, reliability, and usability, with the ultimate goal of enabling their deployment in real-world scenarios.

5.2 Improvements and limitations of novel haptic bilateral teleoperation systems

On the subject of the design of HBTSs, two novel control schemes, [75] and [76], are presented in Section 3.4 and Section 3.5, respectively, whereas a clinical evaluation of the latter is presented in Section 3.6. The related contributions are summarized separately in the next paragraphs, and a general discussion on them is conducted in Section 5.2.3.

5.2.1 Haptic bilateral teleoperation system for precision tasks

In Section 3.4 we introduced a novel HBTS to facilitate the execution of precision tasks [75]. By leveraging the intrinsic stability of the underlying P-P architecture, along with novel strategies for haptic feedback rendering and interaction control, it improves the base architectures in terms of both safety and usability.

We proposed a new virtualized force feedback that enables a natural perception of contact states, increasing human operator awareness and system stability. The latter is achieved through a secondary impedance model that exploits the motion error generated by an admittance-controlled robot. This approach allows decoupling the force rendering system from the control of the interaction: the rendered force is assigned with the desired dynamics, while the admittance control parameters are separately tuned to maximize interaction performance.

Recognizing the necessity to limit the forces exerted by the robot

on its surroundings, with the aim of meeting the more stringent requirements associated with the ongoing certification process for pHRI applications, we embed a saturation strategy of the motion references provided by the HD to admittance control.

The novel proposed system was validated in a teleoperated blackboard writing experiment, against two other architectures. Experiments illustrated that the proposed architecture improves both the accuracy and safety of the task, preventing damage to the instrumentation, or the manipulated environment.

The conducted trials also showed that the reference saturation strategy offers significant advantages in terms of limiting contact forces during the execution of a precision task, but gives no guarantees of a strict limitation below a desired bound, mainly because of the approximate knowledge of the environment. This is particularly evident in contact transition states, where saturation mechanisms are not active yet. Therefore, possible future works include employing methodologies for estimating online the environment properties, to limit the forces in all contact states [279].

Another limitation of our force limitation strategy is that it can be applied only to environments with uniform geometries, making it essentially unsuitable for most real-world teleoperation scenarios, where environments are highly unstructured and not known a priori. This drawback has motivated the development of a new strategy designed to overcome these challenges.

5.2.2 Haptic bilateral teleoperation system for free-hand dental procedures

In Section 3.5 we introduced a novel HBTS for free-hand dental procedures FH-HBTS [76]. The system features visual and

virtualized haptic feedback, that are appropriately combined and coordinated to allow for a natural teleoperation experience.

To improve the visibility of the intervention site, we designed a dedicated end-effector accommodating an eye-in-hand endoscopic camera, and ensuring compatibility with existing clinical tools. We also enhanced the accuracy of the procedure by introducing human tremor filtering and dynamic scaling of velocities.

We develop an eye-hand coordination mapping strategy that, combined with the TCP control, enables the human operator to perceive the motion correspondence between their movements and those of the end-effector observed in the camera view, preserving manual dexterity and expertise. Additionally, by appropriately transforming the virtualized force feedback, we also ensured the force correspondence, enabling the human operator to experience a highly natural sensory perception.

Finally, we enabled safe interactions, by scaling the motion references provided to the admittance controller. The proposed strategy allows for accurate force limitation in any contact state and for any orientation of the interaction tool, without requiring any prior modeling of the intervention site.

The novel FH-HBTS was validated in a dental scaling procedure using a 3D-printed dental phantom. The experiment proved that the system improves the naturalness and the safety of teleoperation, and represents a crucial step towards a broader adoption of robotics in dentistry, as it allows for accurate treatments, while preserving the operator's cognitive and technical abilities. Indeed, with respect to manual procedures, the system allows preserving operator's ergonomics, track operator's performance, and enable remote healthcare.

These findings were further confirmed by the clinical evalua-

tion in Section 3.6, where 19 participants with different levels of experience in the dental field performed four dental scaling procedures using the FH-HBTS with an active dental scaler on a resin model. The study confirmed the feasibility of the system for free-hand dental procedures and demonstrated consistent performance across different user groups. Participants were able to complete the procedures effectively, reporting high usability and comfort levels, which reinforces the potential of the FH-HBTS as a reliable and intuitive platform for clinical and educational applications.

We envisage several improvements to the FH-HBTS, starting from the collection of haptic and motion data. While this is crucial during the training phase of new operators for the evaluation of learning metrics, i.e. learning curves [280], it is also central towards the deployment of data-driven control architectures that leverage demonstrations to synthesize control policies [281]. Finally, these data can also be used to learn cost functions [282], and hence intentions, of experts fulfilling a given task. In the context of dental procedures, this means that data collected from experts executing the procedure can be used to train policies for autonomous robots.

Another limitation concerns the sensory and mechanical characteristics of the current setup. The 2D endoscopic view constrained depth perception, thereby reducing spatial awareness and limiting the precision of instrument positioning. Moreover, the limited resolution of the employed F/T sensor, combined with the mechanical stiffness of the industrial robotic platform, made it less suitable for delicate interaction tasks, potentially affecting the control of contact forces and, consequently, procedural safety. Therefore, possible future works include enhancing depth perception through stereoscopic or augmented visualiza-

tion, and increasing the mechanical compliance of the robotic system to enable safer, more adaptive, and more natural interactions. These developments will be essential to further improve the overall robustness and clinical applicability of the FH-HBTS.

One last improvement left for future developments regards validating the system under more demanding and dynamic conditions, such as in-vivo procedures, where automatic alignment and motion compensation mechanisms are required to account for anatomical variability and patient movement [283]. Addressing these aspects would help narrow the current performance gap between remote and manual operation, ultimately supporting the effective integration of haptic teleoperation into clinical practice.

5.2.3 Discussion

The novel HBTSs [75], [76] both decouple the force rendering system from the control of the interaction. This allows the enforcement of a desired feedback dynamics, either tailored to the human operator's preferences or to the task requirements. Such an approach offers a twofold benefit: on the one hand, it enhances system usability by enabling the operator to experience highly natural haptic sensations; on the other hand, it ensures that, in the perspective of training autonomous policies, expert demonstrations can be gathered in a way that closely replicates manual execution.

On the downside, this approach has the side effect of completely eliminating system transparency. In fact, the impedance perceived by the human operator, $Z_{to}(s)$, will depend solely on the impedance of the virtual spring–damper system. When this significantly diverges from the environment impedance, Z_e(s),

the operator may lack sufficient awareness of the actual magnitude of the interaction, potentially leading to safety issues. Consequently, the force limitation strategies introduced in [75] and [76] become essential to achieve an appropriate balance in the trade-off between usability and safety. This highlights the profound coupling among the different components of HBTSs, and, as a result, the importance of unified design approaches.

On the other hand, the stability and safety of the interaction may also be compromised by the capability of the interaction controller to properly regulate the contact. In both works, an admittance controller was employed, which is more accurate than impedance control in regulating position with smooth dynamics in soft environments, but can lead to instability in stiff environments [97]. Moreover, this controller exhibits high parameter sensitivity and requires environment-specific tuning [116].

In light of this discussion, it is worth noting that future research will be dedicated to exploring variable impedance approaches that exploit environment estimation to guarantee specific performance requirements [284], both on the leader and on the follower site. In the first case, such approaches could be integrated with the proposed force limitation strategies to ensure the fulfillment of performance requirements, such as contact stability, even in stiff environments. In the second case, applied to the virtual impedance model used to generate the force feedback, they could rebalance the trade-off between usability and safety, improving both the human operator's comfort and the transparency of the teleoperation.

5.3 Towards autonomy: human supervisory control

On the topic of human supervisory control, this thesis presented in Section 4.3 a novel control framework, and a relative system, for dependable robotized bolting operations.

The system features a middle/low-level control that guarantees accurate control of the bolt driver tip and active compliance throughout the whole operation, ensuring a safe interaction also in case of fault conditions. To enhance the human operator's situational awareness and ensure a smooth transition to manual control in case of contingencies, we designed a multimodal human-robot interface that includes real-time visualization of all remote site state information, including camera images, as well as several input interfaces to support different control modes. We also ensured the proper execution of the operation by designing a high-level SV that coordinates the operation flow and the control mode switching, ensuring consistency with the human supervisory control paradigm, in which the human operator's authority is always preserved.

The experimental validation of the system on a representative bolting task involving pipe flanges joining demonstrated the system's capability to effectively manage bolting operations, enabling reliable detection of the main system faults and operator intervention to handle them. However, this also revealed the limitations of the visual feedback provided by the single camera mounted on the end-effector, which does not allow full situational awareness of the remote environment.

The validation also demonstrated that human supervision, when combined with direct control capabilities, enables reliable fault detection and effective fault management, thereby enhancing the

system's dependability. This highlights the pivotal role of haptic teleoperation as an intermediate milestone toward autonomy: on the one hand, it counterbalances the current limitations of autonomous systems, enhancing dependability and safety; on the other, as discussed in 5.2.2, it enables the collection of haptic and motion data, which are essential for training autonomous control policies from expert demonstrations.

List of Figures

1.1 High-level scheme of a haptic bilateral teleoperation system. 9

2.1 Low-level scheme of a haptic bilateral teleoperation system. 19
2.2 Position-position architecture. 26
2.3 Position-force measured architecture. 28
2.4 Position-force computed architecture. 29
2.5 3-channel architecture. 30
2.6 4-channel architecture. 31
2.7 Network representation of a teleoperation system [33]. 34
2.8 Example of ISRU mission operations pipeline [55].40
2.9 High-level overview of the system architecture. .43
2.10 Haptic control system block scheme. 44
2.11 Onboard camera images during teleoperation. .46

2.12 Point-to-point trajectory planning in RVP. Together with ER and MR meshes, additional collision objects (in light green) are added to replicate (1) the ER's antennas, (2) the hole in which the sample is assembled, and (3) the front camera, modeled as a box to account for all possible orientations (being the front camera pair mounted on a passive pan-tilt unit, without encoders). . .49
2.13 Engagement procedure in RVP. The HD moving frame is shown with solid colors, while the fixed robot's end-effector frame is displayed as shaded.50

3.1 Kinaesthetic and tactile haptic interaction [80].59
3.2 Examples of graspable, wearable, and touchable haptic devices [84]. 62
3.3 Overview of control strategy synthesis in the interaction control framework based on natural and artificial constraints. 67
3.4 Impedance controller's block scheme. 72
3.5 Admittance controller's block scheme 74
3.6 Leader workspace-based partitioning for double zone with intention-based scaling factor technique [74]. 84
3.7 Haptic bilateral teleoperation system scheme. .88
3.8 Operation of the robot interaction control in the different contact states with the environment. .93
3.9 Human force profile representative of freehand writing for the sequence *A*-*C*-*G*. 95
3.10 Experimental setup to record human force profiles. 96
3.11 Outcomes of the blackboard writing task execution in the three scenarios. 97

3.12 Interaction forces along the axis perpendicular to the blackboard plane in Scenario A. 99
3.13 Interaction forces along the axis perpendicular to the blackboard plane in Scenario B. 99
3.14 Interaction forces along the axis perpendicular to the blackboard plane in Scenario C. 101
3.15 Forces rendered on the HD in Scenario C. . . .101
3.16 Manual (left) vs teleoperated (right) dental procedures (pictorial views). 103
3.17 Haptic device and robot reference frames. 110
3.18 Haptic bilateral teleoperation system scheme. .112
3.19 Engagement phase supported by the visualization tool. 115
3.20 Visualization of the rotational coupling between $\mathcal{H}_e$ and $\mathcal{R}_e$: (top) top view; (bottom) user view; (left) $\varphi = 0$; (right) $\varphi = \pi/2$. 118
3.21 Integrated mechanical end-effector for free-hand procedures. Visible in the left side of the figure is also one of the dental models used in the experiments. 125
3.22 Target teeth for dental scaling experiments: 1) lower right first premolar; 2) upper right central incisor; 3) upper right second premolar. 127
3.23 Comparison between the conditional expectation of the interaction force in all three scenarios. . .132
3.24 Eye-hand coordination assessment. 134
3.25 Outcomes of the dental scaling experiment in Scenario A (baseline configuration with no force limitation, no passivity). 135
3.26 Snapshopts and outcomes of the dental scaling experiment in Scenario B (proposed system with force limitation). 137

3.27 Outcomes of the dental scaling experiment in Scenario C (TDPA-HD [40]). 139
3.28 Teleoperation system and dental model used within the study. 142

4.1 Control paradigms for teleoperation. 161
4.2 Level of automation [218]. 164
4.3 Recommended type of control based on the task complexity and the completion time [216]. . . .166
4.4 Schematic diagram of supervisory control of remote manipulation [223]. 167
4.5 Diagram of a generic human supervisory control operation. 170
4.6 Example of coupling and tightening steps in a bolting operation. 175
4.7 Control system for dependable bolting operations.180
4.8 Screenshot of the system's GUI during operation.185
4.9 Remote site of the experimental setup, showing the UR5e robotic arm equipped with the mechanical end-effector and the pipes used for experimental validation. 192
4.10 Comparison between the mean of the interaction force in Scenario A and Scenario B. 193
4.11 Comparison between the planned coupling trajectory and the one actually followed by the FR after human intervention. 194
4.12 Forces rendered on the HD. 195
4.13 Tightening torque profile. 196

List of Tables

2.1 Success rate of the mission operations out of 20 trials in different scenarios. 51
2.2 Training time of 3 different operators. 53

3.1 Summary of robotic systems for free-hand dental procedures. 106
3.2 Admittance control parameters. 129
3.3 Diagonal elements of the scaling matrix $\mathbf{\Lambda}$. . . .130
3.4 Virtual impedance parameters. 130
3.5 Overview of the experiments with corresponding dental surface and auditory feedback condition.144
3.6 Descriptive statistics of cleanness scores of each dental surface for each experience level, obtained using the quantitative analysis. Kruskal-Wallis test results for between-group differences and Wilcoxon signed-rank test results for evaluating the audio feedback impact in system efficacy. . .148

3.7 Descriptive statistics of cleanness scores of each dental surface for each experience level, obtained using the qualitative analysis. Kruskal-Wallis test results for between-group differences and Wilcoxon signed-rank test results for evaluating the audio feedback impact in system efficacy. . .149
3.8 Descriptive statistics of execution times for the training and experimental phases. Execution times are expressed in seconds. Kruskal-Wallis test results for between-group differences and Wilcoxon signed-rank test results for evaluating the audio feedback impact on execution times. .151
3.9 Descriptive statistics of interaction forces for the whole clinical procedure across experience levels. The statistics are expressed in newtons. Kruskal–Wallis test results for between-group differences. 152
3.10 Summary of questionnaire responses. Values reported for ordinal data: median, mode, IQR. Wilcoxon signed-rank test results for questionnaire items with significant deviation from the neutral value of 3 ($p < 0.05$). The direction indicates whether the median response was above (> 3) or below (< 3) the neutral value. 154

List of Algorithms

1 Eye-hand coordination mapping and scaling . .119

Acronyms

4IR fourth industrial revolution. 1, 2, 4

I4.0 industry 4.0. 1

pHRI physical human-robot interaction. 4–8, 13, 17, 76, 86, 201

HD haptic device. 8, 12, 19, 37, 41, 42, 44, 46–48, 50, 52, 57, 59–63, 77, 85, 86, 88, 89, 94, 97, 98, 100, 101, 104, 108, 110–117, 119, 124, 127, 131, 133, 135–139, 141, 144, 146, 183, 184, 187, 191, 195, 201, 210–212

HBTS haptic bilateral teleoperation system. 8, 9, 11, 13, 17–21, 24, 27, 28, 32–34, 36–38, 57, 58, 63, 64, 77, 79, 86, 87, 94–96, 100, 104, 107–109, 112, 123, 174, 197, 200, 201, 204, 205

LR leader robot. 19–21, 26–30, 33, 35, 47, 63, 64, 77–84, 111, 138

FR follower robot. 19–21, 23, 26–30, 33, 35–37, 42, 47, 77–82, 87, 88, 94, 111–117, 119, 120, 122, 128, 131, 133, 135, 136, 138, 160–162, 167, 168, 173, 181, 183, 184, 186, 187, 191–195, 212

P-P position-position. 26–29, 35, 87, 200

F/T force/torque. 27–29, 64, 87, 141, 146, 157, 203

P-Fm position-force measured. 27–30, 32, 35, 64, 86, 96, 97, 197

P-Fc position-force computed. 28, 29, 32, 35

TDPA time domain passivity approach. 32–35, 111, 121, 131, 136, 139, 212

TDPC time domain passivity control. 33, 34, 41

PO passivity observer. 34, 35

PC passivity controller. 34, 35

TDPN time domain passivity networks. 35

TDPA-HD time domain passivity approach with high delay. 35, 37

MMT model-mediated teleoperation. 36, 37

MATM model-augmented haptic telemanipulation. 37

NASA National Aeronautics and Space Administration. 39, 40

ISRU in-situ resources utilization. 39, 40, 45, 47, 49, 197, 198, 209

ESA European Space Agency. 40

HET Human exploration telerobotics. 40

METERON Multi-purpose end-to-end robotic operation network. 40, 41

ISS International Space Station. 40, 41

DoF degree of freedom. 40, 41, 65, 78, 79, 88, 127, 128, 141, 179, 181, 191

GUI graphical user interface. 41, 48, 183–185, 189, 212

VR virtual reality. 42

ER exploration robot. 43, 44, 46, 47, 49, 50, 210

MR manipulation robot. 43–52, 210

UGV unmanned ground vehicle. 43

HC haptic controller. 44–47, 88, 97

RVP robot visualization & planning. 44–46, 48–50, 52, 210

SRP scaling and root planing. 102, 109, 126, 134, 138, 156

r-CAIS robotic computer-assisted implant surgery. 102

TRL technology readiness level. 107, 108, 179

FH-HBTS haptic bilateral teleoperation system for free-hand dental procedures. 108, 111, 127, 138, 140–144, 156, 201–204

TCP tool center point. 110, 114, 117, 119, 202

EHCC eye-hand coordination controller. 111, 112, 114–116, 122

HFC haptic feedback controller. 111, 112, 123, 124

STD standard deviation. 147, 148, 150–152

IQR interquartile range. 147–152, 154, 157, 214

SVCS human supervisory control system. 167–169

SV supervisor. 174, 178, 182, 183, 187–189, 206

JET Joint European Torus. 177

BDC bolt driver controller. 182, 186, 190

RGC reference generator controller. 185, 189

HBC haptic bilateral controller. 186, 187

ROS robot operating system. 191

List of Symbols

$Z_{to}(s)$ Impedance perceived by the human operator. 23, 27, 204

$Z_e(\mathbf{s})$ Environment impedance. 23, 27, 204

$\mathbf{h}$ Cartesian wrench. 23, 26–32, 34, 66, 69, 71, 72, 74, 109, 120

$\mathbf{f}$ Cartesian force. 23, 31, 66, 67, 85, 90–93, 98, 109, 120, 121, 123, 124, 131, 132, 136, 138, 146, 152

$\mathbf{m}$ Cartesian moment. 23, 109

$\mathbf{v}$ Cartesian twist. 23, 26, 27, 29–32, 34, 109, 116, 119, 120, 122

$\dot{\mathbf{p}}$ Cartesian linear velocity. 23, 67, 81, 82, 84, 85

$\boldsymbol{\omega}$ Cartesian angular velocity. 23, 82

$\mathbf{x}$ Cartesian pose. 26, 27, 29–31, 69–71, 73, 74, 89, 90, 109, 115, 119, 120, 122, 123

$\mathbf{p}$ Cartesian position. 26, 66, 67, 79–82, 84, 85, 89–92, 94, 109, 114–116, 118–124, 131, 132

$\hbar$ Unit quaternion. 26, 89, 90, 109, 115, 116, 119, 120, 122

$\mathbf{B}(\mathbf{q})$ Inertia matrix. 65, 66, 71

$\mathbf{q}$ Joint positions. 65, 66, 71, 79, 221, 222

$\ddot{\mathbf{q}}$ Joint accelerations. 65, 66, 71

$\mathbf{C}(\mathbf{q}, \dot{\mathbf{q}})$ Matrix accounting for Coriolis and centrifugal effects. 65, 66

$\dot{\mathbf{q}}$ Joint velocities. 65, 66, 71, 222

$\tau_f(\dot{\mathbf{q}})$ Joint friction vector. 65, 66

$\mathbf{g}(\mathbf{q})$ Gravitational torques. 65, 66

$\boldsymbol{\tau}$ Joint torque vector. 65, 66, 71

$\mathbf{n(q, \dot{q})}$ Bias. 66, 71

$\mathbf{K}_e$ Environment stiffness diagonal matrix. 66, 67, 75, 91, 92

$\mathbf{D}_e$ Environment damping diagonal matrix. 67

$\tilde{\mathbf{h}}$ Wrench error. 69, 70, 74

$\mathbf{M}_d$ Mass diagonal matrix. 71, 72, 74, 90, 96, 120, 128, 129

$\ddot{\mathbf{x}}$ Cartesian acceleration. 71, 72

$\mathbf{K}_D$ Damping diagonal matrix. 71, 72, 74, 90, 96, 120, 128, 129

$\dot{\tilde{\mathbf{x}}}$ Twist error. 71, 72, 74

$\mathbf{K}_P$ Stiffness diagonal matrix. 71–75, 90, 91, 96, 120, 128, 129

$\tilde{\mathbf{x}}$ Pose error. 71, 72, 74

$\ddot{\tilde{\mathbf{x}}}$ Acceleration error. 72, 74

$\mathbf{R}$ Rotation matrix. 80, 89, 91, 94, 98, 109, 114–120, 122, 123, 138

$\mathbf{r}$ Axis of the axis-angle representation. 82, 116, 118

ϑ Angle of the axis-angle representation. 82, 116, 118

$\mathbf{T}$ Homogeneous transformation matrix. 89, 109, 114, 115, 117, 119

$\tilde{\mathbf{p}}$ Position error. 90, 92–94

$\ddot{\tilde{\mathbf{p}}}$ Linear acceleration error. 90

$\tilde{\mathbf{p}}$ Linear velocity error. 90, 93, 94

$\tilde{\mathbf{f}}$ Force error. 90, 91

$\mathbf{K}_{eq}$ Equivalent stiffness. 91

Bibliography

[1] J. Effoduh, "The Fourth Industrial Revolution by Klaus Schwab," *The Transnational Human Rights Review*, vol. 3, no. 1, Dec. 2016. DOI: 10.60082/2563-4631.1023.

[2] Y. Lu, "Industry 4.0: A survey on technologies, applications and open research issues," *Journal of Industrial Information Integration*, vol. 6, pp. 1–10, Jun. 2017. DOI: 10.1016/j.jii.2017.04.005.

[3] V. Roblek, M. Meško, and A. Krapež, "A Complex View of Industry 4.0," *SAGE Open*, vol. 6, no. 2, p. 2 158 244 016 653 987, Apr. 2016. DOI: 10.1177/2158244016653987.

[4] S. Popović, "The Future of Jobs Employment, Skills and Workforce Strategy for the Fourth Industrial Revolution," 2016.

[5] Milton Guerry, Christopher Müller, Werner Kraus, and Susanne Bieller, *World Robotics 2021*, Oct. 2021. Available at: https://ifr.org/downloads/press2018/2021_10_28_WR_PK_Presentation_long_version.pdf.

[6] Marina Bill, Christopher Müller, Werner Kraus, and Susanne Bieller, *World Robotics 2024*, 2024. Available

at: https://ifr.org/img/worldrobotics/Press_Conference_2024.pdf.

[7] S. Haddadin and E. Croft, "Physical Human–Robot Interaction," in *Springer Handbook of Robotics*, Cham: Springer International Publishing, 2016, pp. 1835–1874. DOI: 10.1007/978-3-319-32552-1_69.

[8] A. De Santis, B. Siciliano, A. De Luca, and A. Bicchi, "An atlas of physical human–robot interaction," *Mechanism and Machine Theory*, vol. 43, no. 3, pp. 253–270, Mar. 2008. DOI: 10.1016/j.mechmachtheory.2007.03.003.

[9] M. Selvaggio, M. Cognetti, S. Nikolaidis, S. Ivaldi, and B. Siciliano, "Autonomy in Physical Human-Robot Interaction: A Brief Survey," *IEEE Robotics and Automation Letters*, vol. 6, no. 4, pp. 7989–7996, Oct. 2021. DOI: 10.1109/LRA.2021.3100603.

[10] A. Weiss, D. Wurhofer, M. Lankes, and M. Tscheligi, "Autonomous vs. tele-operated: How people perceive human-robot collaboration with hrp-2," in *Proceedings of the 4th ACM/IEEE international conference on Human robot interaction*, ser. HRI '09, New York, NY, USA: Association for Computing Machinery, Mar. 2009, pp. 257–258. DOI: 10.1145/1514095.1514164.

[11] R. Latikka, N. Savela, A. Koivula, and A. Oksanen, "Attitudes Toward Robots as Equipment and Coworkers and the Impact of Robot Autonomy Level," *International Journal of Social Robotics*, vol. 13, no. 7, pp. 1747–1759, Nov. 2021. DOI: 10.1007/s12369-020-00743-9.

[12] J. Złotowski, K. Yogeeswaran, and C. Bartneck, "Can we control it? Autonomous robots threaten human identity, uniqueness, safety, and resources," *International Journal of Human-Computer Studies*, vol. 100, pp. 48–54, Apr. 2017. DOI: 10.1016/j.ijhcs.2016.12.008.

[13] B. D. Argall, S. Chernova, M. Veloso, and B. Browning, "A survey of robot learning from demonstration," *Robotics and Autonomous Systems*, vol. 57, no. 5, pp. 469–483, May 2009. DOI: 10.1016/j.robot.2008.10.024.

[14] L. Pagliara, V. Petrone, E. Ferrentino, and P. Chiacchio, "Human-Robot Interface for Teleoperated Robotized Planetary Sample Collection and Assembly," in *2023 IEEE 10th International Workshop on Metrology for AeroSpace (MetroAeroSpace)*, Jun. 2023, pp. 171–176. DOI: 10.1109/MetroAeroSpace57412.2023.10189984.

[15] G. Raju, G. Verghese, and T. Sheridan, "Design issues in 2-port network models of bilateral remote manipulation," in *1989 International Conference on Robotics and Automation Proceedings*, May 1989, 1316–1321 vol.3. DOI: 10.1109/ROBOT.1989.100162.

[16] P. M. Kebria, H. Abdi, M. M. Dalvand, A. Khosravi, and S. Nahavandi, "Control Methods for Internet-Based Teleoperation Systems: A Review," *IEEE Transactions on Human-Machine Systems*, vol. 49, no. 1, pp. 32–46, Feb. 2019. DOI: 10.1109/THMS.2018.2878815.

[17] F. Ferraguti, M. Bonfè, C. Fantuzzi, and C. Secchi, "Optimized Power Modulation in Wave-Based Bilateral Teleoperation," *IEEE/ASME Transactions on Mechatronics*, vol. 26, no. 1, pp. 276–287, Feb. 2021. DOI: 10.1109/TMECH.2020.3013978.

[18] C. A. Desoer and M. Vidyasagar, *Feedback Systems* (Classics in Applied Mathematics). Society for Industrial and Applied Mathematics, Jan. 2009. DOI: 10.1137/1.9780898719055.

[19] Cristian Secchi, Cesare Fantuzzi, and Stefano Stramigioli, *Control of Interactive Robotic Interfaces* (Springer Tracts

in Advanced Robotics). Berlin, Heidelberg: Springer, 2007, vol. 29. DOI: 10.1007/978-3-540-49715-8.

[20] J. E. COLGATE and N. HOGAN, "Robust control of dynamically interacting systems," *International Journal of Control*, vol. 48, no. 1, pp. 65–88, Jul. 1988. DOI: 10.1080/00207178808906161.

[21] D. Lawrence, "Stability and transparency in bilateral teleoperation," *IEEE Transactions on Robotics and Automation*, vol. 9, no. 5, pp. 624–637, Oct. 1993. DOI: 10.1109/70.258054.

[22] *Springer Handbook of Robotics* (Springer Handbooks). Cham: Springer International Publishing, 2016. DOI: 10.1007/978-3-319-32552-1.

[23] I. O. for Standardization, *ISO 9241-210:2019 Ergonomics of human-system interaction - Human-centred design for interactive systems*, 2019. Available at: https://www.iso.org/standard/77520.html.

[24] K. Hastrudi-Zaad and S. Salcudean, "On the use of local force feedback for transparent teleoperation," in *Proceedings 1999 IEEE International Conference on Robotics and Automation (Cat. No.99CH36288C)*, vol. 3, May 1999, 1863–1869 vol.3. DOI: 10.1109/ROBOT.1999.770380.

[25] A. Sherman, M. C. Çavuşoğlu, and F. Tendick, "Comparison of Teleoperator Control Architectures for Palpation Task," American Society of Mechanical Engineers Digital Collection, Nov. 2021, pp. 1261–1268. DOI: 10.1115/IMECE2000-2441.

[26] M. Tavakoli, A. Aziminejad, R. Patel, and M. Moallem, "Enhanced Transparency in Haptics-Based Master-Slave Systems," in *2007 American Control Conference*, Jul. 2007, pp. 1455–1460. DOI: 10.1109/ACC.2007.4283078.

[27] R. Anderson and M. Spong, "Bilateral control of teleoperators with time delay," *IEEE Transactions on Automatic Control*, vol. 34, no. 5, pp. 494–501, May 1989. DOI: 10.1109/9.24201.

[28] G. Niemeyer and J.-J. Slotine, "Stable adaptive teleoperation," *IEEE Journal of Oceanic Engineering*, vol. 16, no. 1, pp. 152–162, Jan. 1991. DOI: 10.1109/48.64895.

[29] P. Pitakwatchara, "Control of time-varying delayed teleoperation system using corrective wave variables," in *2015 IEEE/RSJ International Conference on Intelligent Robots and Systems (IROS)*, Sep. 2015, pp. 4550–4555. DOI: 10.1109/IROS.2015.7354024.

[30] D. Sun, F. Naghdy, and H. Du, "Transparent four-channel bilateral control architecture using modified wave variable controllers under time delays," *Robotica*, vol. 34, no. 4, pp. 859–875, Apr. 2016. DOI: 10.1017/S026357471400191X.

[31] D. Sun, F. Naghdy, and H. Du, "A novel approach for stability and transparency control of nonlinear bilateral teleoperation system with time delays," *Control Engineering Practice*, vol. 47, pp. 15–27, Feb. 2016. DOI: 10.1016/j.conengprac.2015.11.003.

[32] B. Hannaford and J.-H. Ryu, "Time-domain passivity control of haptic interfaces," *IEEE Transactions on Robotics and Automation*, vol. 18, no. 1, pp. 1–10, Feb. 2002. DOI: 10.1109/70.988969.

[33] J. Artigas Esclusa, "Time domain passivity control for delayed teleoperation," phd, E.T.S.I. Industriales (UPM), 2014.

[34] J.-H. Ryu, D.-S. Kwon, and B. Hannaford, "Stable teleoperation with time-domain passivity control," *IEEE Transactions on Robotics and Automation*, vol. 20, no. 2,

pp. 365–373, Apr. 2004. DOI: 10.1109/TRA.2004.824689.

[35] J. Artigas, C. Preusche, and G. Hirzinger, "Time domain passivity for delayed haptic telepresence with energy reference," in *2007 IEEE/RSJ International Conference on Intelligent Robots and Systems*, Oct. 2007, pp. 1612–1617. DOI: 10.1109/IROS.2007.4399570.

[36] J.-H. Ryu, J. Artigas, and C. Preusche, "A passive bilateral control scheme for a teleoperator with time-varying communication delay," *Mechatronics*, Special Issue on Design and Control Methodologies in Telerobotics, vol. 20, no. 7, pp. 812–823, Oct. 2010. DOI: 10.1016/j.mechatronics.2010.07.006.

[37] J. Artigas, J.-H. Ryu, and C. Preusche, "Position drift compensation in time domain passivity based teleoperation," in *2010 IEEE/RSJ International Conference on Intelligent Robots and Systems*, Oct. 2010, pp. 4250–4256. DOI: 10.1109/IROS.2010.5652691.

[38] J. Artigas, J.-H. Ryu, and C. Preusche, "Time Domain Passivity Control for Position-Position Teleoperation Architectures," *Presence: Teleoperators and Virtual Environments*, vol. 19, no. 5, pp. 482–497, Oct. 2010. DOI: 10.1162/pres_a_00013.

[39] M. Panzirsch, J.-H. Ryu, and M. Ferre, "Reducing the conservatism of the time domain passivity approach through consideration of energy reflection in delayed coupled network systems," *Mechatronics*, vol. 58, pp. 58–69, Apr. 2019. DOI: 10.1016/j.mechatronics.2018.12.001.

[40] M. Panzirsch, A. Pereira, H. Singh, *et al.*, "Exploring planet geology through force-feedback telemanipulation

from orbit," *Science Robotics*, vol. 7, no. 65, eabl6307, Apr. 2022. DOI: 10.1126/scirobotics.abl6307.

[41] M. Panzirsch, H. Singh, T. Krüger, C. Ott, and A. Albu-Schäffer, "Safe Interactions and Kinesthetic Feedback in High Performance Earth-To-Moon Teleoperation," in *2020 IEEE Aerospace Conference*, Mar. 2020, pp. 1–10. DOI: 10.1109/AERO47225.2020.9172665.

[42] B. Hannaford, "A design framework for teleoperators with kinesthetic feedback," *IEEE Transactions on Robotics and Automation*, vol. 5, no. 4, pp. 426–434, Aug. 1989. DOI: 10.1109/70.88057.

[43] M. V. Noyes, "A Novel Predictor for Telemanipulation through a Time Delay," *Proc. of Annual Conf. on Manual Control, Moffet Field, CA, NASA ARC*, 1984.

[44] X. Xu, B. Cizmeci, C. Schuwerk, and E. Steinbach, "Model-Mediated Teleoperation: Toward Stable and Transparent Teleoperation Systems," *IEEE Access*, vol. 4, pp. 425–449, 2016. DOI: 10.1109/ACCESS.2016.2517926.

[45] K. Salisbury, F. Conti, and F. Barbagli, "Haptic rendering: Introductory concepts," *IEEE Computer Graphics and Applications*, vol. 24, no. 2, pp. 24–32, Mar. 2004. DOI: 10.1109/MCG.2004.1274058.

[46] Y. Wang, L. Feng, and K. Andersson, "Haptic force rendering of rigid-body interactions: A systematic review," *Advances in Mechanical Engineering*, vol. 13, no. 9, p. 16 878 140 211 041 538, Sep. 2021. DOI: 10.1177/16878140211041538.

[47] X. Xu, C. Schuwerk, and E. Steinbach, "Passivity-based model updating for Model-mediated Teleoperation," in *2015 IEEE International Conference on Multimedia &*

Expo Workshops (ICMEW), Jun. 2015, pp. 1–6. DOI: 10.1109/ICMEW.2015.7169831.

[48] T. Hulin, M. Panzirsch, H. Singh, *et al.*, "Model-Augmented Haptic Telemanipulation: Concept, Retrospective Overview, and Current Use Cases," *Frontiers in Robotics and AI*, vol. 8, Jun. 2021. DOI: 10.3389/frobt.2021.611251.

[49] M. Panzirsch, N. Bechtel, and T. Hulin, "Model-Augmented Energy-Flow Reference for High-Delay Telemanipulation," *IEEE Robotics and Automation Letters*, vol. 9, no. 4, pp. 3131–3138, Apr. 2024. DOI: 10.1109/LRA.2024.3362155.

[50] M. A. Viscio, E. Gargioli, J. A. Hoffman, P. Maggiore, A. Messidoro, and N. Viola, "A methodology to support strategic decisions in future human space exploration: From scenario definition to building blocks assessment," *Acta Astronautica*, vol. 91, pp. 198–217, Oct. 2013. DOI: 10.1016/j.actaastro.2013.06.015.

[51] NASA, *Artemis*, 2022. Available at: https://www.nasa.gov/specials/artemis/index.html.

[52] NASA, *Lunar Living: NASA's Artemis Base Camp Concept – Artemis*, 2022. Available at: https://blogs.nasa.gov/artemis/2020/10/28/lunar-living-nasas-artemis-base-camp-concept/.

[53] K. Mars, *Gateway*, Dec. 2019. Available at: https://www.nasa.gov/gateway.

[54] K. Coderre, C. Edwards, T. Cichan, *et al.*, "Concept of Operations for the Gateway," in *Space Operations: Inspiring Humankind's Future*, Cham: Springer International Publishing, 2019, pp. 63–82.

[55] Lorenzo Pagliara, Vincenzo Petrone, Enrico Ferrentino, and Pasquale Chiacchio, *Autonomous planning and hap-*

tic teleoperations in robotized planetary sample collection and assembly, 2022. Available at: https://www.youtube.com/watch?v=YNFft1pYCmE.

[56] M. Bualat, W. Carey, T. Fong, *et al.*, "Preparing for Crew-Control of Surface Robots from Orbit," Washington, DC, Jan. 2014.

[57] A. Schiele, M. Aiple, T. Krueger, *et al.*, "Haptics-1: Preliminary Results from the First Stiffness JND Identification Experiment in Space," in *Haptics: Perception, Devices, Control, and Applications*, ser. Lecture Notes in Computer Science, Cham: Springer International Publishing, 2016, pp. 13–22. DOI: 10.1007/978-3-319-42321-0_2.

[58] A. Schiele, T. Krüger, S. Kimmer, *et al.*, "Haptics-2 — A system for bilateral control experiments from space to ground via geosynchronous satellites," in *2016 IEEE International Conference on Systems, Man, and Cybernetics (SMC)*, Oct. 2016, pp. 000 892–000 897. DOI: 10.1109/SMC.2016.7844354.

[59] A. Schiele, J. Smisek, E. Den, *et al.*, *Towards the Interact Space Experiment: Controlling an Outdoor Robot on Earth's Surface from Space*. May 2015. DOI: 10.13140/RG.2.2.34553.52324.

[60] B. Weber, R. Balachandran, C. Riecke, F. Stulp, and M. Stelzer, "Teleoperating Robots from the International Space Station: Microgravity Effects on Performance with Force Feedback," in *2019 IEEE/RSJ International Conference on Intelligent Robots and Systems (IROS)*, Macau, China: IEEE, Nov. 2019, pp. 8144–8150. DOI: 10.1109/IROS40897.2019.8968030.

[61] J. Artigas, R. Balachandran, C. Riecke, *et al.*, "KONTUR-2: Force-feedback teleoperation from the international

space station," in *2016 IEEE International Conference on Robotics and Automation (ICRA)*, Stockholm, Sweden: IEEE, May 2016, pp. 1166–1173. DOI: 10.1109/ICRA.2016.7487246.

[62] M. Stelzer, B.-M. Steinmetz, P. Birkenkampf, J. Vogel, B. Brunner, and S. Kühne, "Software architecture and design of the Kontur-2 mission," in *2017 IEEE Aerospace Conference*, Mar. 2017, pp. 1–17. DOI: 10.1109/AERO.2017.7943816.

[63] P. Schmaus, D. Leidner, T. Krüger, *et al.*, "Preliminary Insights From the METERON SUPVIS Justin Space-Robotics Experiment," *IEEE Robotics and Automation Letters*, vol. 3, no. 4, pp. 3836–3843, Oct. 2018. DOI: 10.1109/LRA.2018.2856906.

[64] P. Schmaus, D. Leidner, R. Bayer, B. Pleintinger, T. Krüger, and N. Y. Lii, "Continued Advances in Supervised Autonomy User Interface Design for METERON SUPVIS Justin," in *2019 IEEE Aerospace Conference*, Mar. 2019, pp. 1–11. DOI: 10.1109/AERO.2019.8741885.

[65] P. Schmaus, D. Leidner, T. Krüger, *et al.*, "Knowledge Driven Orbit-to-Ground Teleoperation of a Robot Coworker," *IEEE Robotics and Automation Letters*, vol. 5, no. 1, pp. 143–150, Jan. 2020. DOI: 10.1109/LRA.2019.2948128.

[66] P. Schmaus, D. Leidner, T. Krueger, *et al.*, "On Realizing Multi-Robot Command through Extending the Knowledge Driven Teleoperation Approach," in *Proceedings of the International Astronautical Congress, IAC*, vol. IAC-22, Paris, France: International Astronautical Federation, IAF, Sep. 2022.

[67] H. Steimle and C. Norberg, "Astronaut selection and training," in *Human Spaceflight and Exploration*, ser. Springer

Praxis Books, Berlin, Heidelberg: Springer, 2013, pp. 255–294. DOI: 10.1007/978-3-642-23725-6_7.

[68] A. D. Garcia, J. Schlueter, and E. Paddock, "Training Astronauts using Hardware-in-the-Loop Simulations and Virtual Reality," in *AIAA Scitech 2020 Forum*, American Institute of Aeronautics and Astronautics. DOI: 10.2514/6.2020-0167.

[69] Franka Emika, *Franka Emika - Next Generation Robotics*, 2022. Available at: https://www.franka.de/.

[70] Clearpath Robotics, *Husky UGV - Outdoor Field Research Robot by Clearpath*, 2022. Available at: https://clearpathrobotics.com/husky-unmanned-ground-vehicle-robot/.

[71] M. T. Mason, "Compliance and Force Control for Computer Controlled Manipulators," *IEEE Transactions on Systems, Man, and Cybernetics*, vol. 11, no. 6, pp. 418–432, Jun. 1981. DOI: 10.1109/tsmc.1981.4308708.

[72] 3D Systems, *Touch - Haptic Device*, Jun. 2016. Available at: https://www.3dsystems.com/haptics-devices/touch.

[73] F. M. Fadrique, R. S.-B. Fernández, M. Barrera, P. Franceschetti, and L. Joudrier, "ExoMars 2020: Rover Operations Control System Design as part of the Rover Operations Control Center (ROCC)," in *2018 SpaceOps Conference*, American Institute of Aeronautics and Astronautics, May 2018. DOI: 10.2514/6.2018-2405.

[74] M. Radi, *Workspace scaling and haptic feedback for industrial telepresence and teleaction systems with heavy-duty teleoperators* (Forschungsberichte IWB 261). München: Herbert Utz Verlag, 2012.

[75] L. Pagliara, E. Ferrentino, A. Chiacchio, and G. Russo, "Safe haptic teleoperations of admittance controlled

robots with virtualization of the force feedback," in *2024 IEEE 20th International Conference on Automation Science and Engineering (CASE)*, Aug. 2024, pp. 1574–1579. DOI: 10.1109/CASE59546.2024.10711457.

[76] L. Pagliara, E. Ferrentino, A. Chiacchio, and G. Russo, *Haptic bilateral teleoperation system for free-hand dental procedures*, Jun. 2025. DOI: 10.48550/arXiv.2503.21288. Available at: http://arxiv.org/abs/2503.21288.

[77] D. Ravikanth, M. Mishra, and P. Hariharan, "Review on Haptics technology and its modeling, rendering and future applications on texture identification," in *2015 International Conference on Man and Machine Interfacing (MAMI)*, Dec. 2015, pp. 1–6. DOI: 10.1109/MAMI.2015.7456593.

[78] T. Brooks, "Telerobotic response requirements," in *1990 IEEE International Conference on Systems, Man, and Cybernetics Conference Proceedings*, Nov. 1990, pp. 113–120. DOI: 10.1109/ICSMC.1990.142071.

[79] K. Shimoga, "A survey of perceptual feedback issues in dexterous telemanipulation. I. Finger force feedback," in *Proceedings of IEEE Virtual Reality Annual International Symposium*, Sep. 1993, pp. 263–270. DOI: 10.1109/VRAIS.1993.380770.

[80] T. A. Kern, H. Haus, M. Matysek, and S. Sindlinger, "Actuator Design," in *Engineering Haptic Devices*, ser. Springer Series on Touch and Haptic Systems, Cham: Springer International Publishing, 2023, pp. 309–429. DOI: 10.1007/978-3-031-04536-3_9.

[81] M. Sreelakshmi and T. D. Subash, "Haptic Technology: A comprehensive review on its applications and future prospects," *Materials Today: Proceedings*, International

Conference on Computing, Communication, Nanophotonics, Nanoscience, Nanomaterials and Nanotechnology, vol. 4, no. 2, Part B, pp. 4182–4187, Jan. 2017. DOI: 10.1016/j.matpr.2017.02.120.

[82] K. Wen, D. Necsulescu, and J. Sasiadek, "Haptic force control based on impedance/admittance control aided by visual feedback," *Multimedia Tools and Applications*, vol. 37, no. 1, pp. 39–52, Mar. 2008. DOI: 10.1007/s11042-007-0172-1.

[83] A. Adilkhanov, M. Rubagotti, and Z. Kappassov, "Haptic Devices: Wearability-Based Taxonomy and Literature Review," *IEEE Access*, vol. 10, pp. 91 923–91 947, 2022. DOI: 10.1109/ACCESS.2022.3202986.

[84] H. Culbertson, S. B. Schorr, and A. M. Okamura, "Haptics: The Present and Future of Artificial Touch Sensation," *Annual Review of Control, Robotics, and Autonomous Systems*, vol. 1, no. 1, pp. 385–409, 2018. DOI: 10.1146/annurev-control-060117-105043.

[85] M. Kitagawa, D. Dokko, A. M. Okamura, B. T. Bethea, and D. D. Yuh, "Effect of sensory substitution on suture manipulation forces for surgical teleoperation," *Studies in Health Technology and Informatics*, vol. 98, pp. 157–163, 2004.

[86] V. Cesari, F. Melfi, A. Gemignani, and D. Menicucci, "Sensory substitution increases robotic surgical performance and sets the ground for a mediating role of the sense of embodiment: A systematic review," *Heliyon*, vol. 9, no. 11, e21665, Nov. 2023. DOI: 10.1016/j.heliyon.2023.e21665.

[87] C. E. Reiley, T. Akinbiyi, D. Burschka, D. C. Chang, A. M. Okamura, and D. D. Yuh, "Effects of Visual Force Feedback on Robot-Assisted Surgical Task Per-

formance," *The Journal of thoracic and cardiovascular surgery*, vol. 135, no. 1, pp. 196–202, Jan. 2008. DOI: 10.1016/j.jtcvs.2007.08.043.

[88] A. Abiri, J. Pensa, A. Tao, *et al.*, "Multi-Modal Haptic Feedback for Grip Force Reduction in Robotic Surgery," *Scientific Reports*, vol. 9, no. 1, p. 5016, Mar. 2019. DOI: 10.1038/s41598-019-40821-1.

[89] X. Gong, L. Wang, Y. Mou, *et al.*, "Improved Four-channel PBTDPA Control Strategy Using Force Feedback Bilateral Teleoperation System," *International Journal of Control, Automation and Systems*, vol. 20, no. 3, pp. 1002–1017, Mar. 2022. DOI: 10.1007/s12555-021-0096-y.

[90] I. Dekker, K. Kellens, and E. Demeester, "Design and Evaluation of an Intuitive Haptic Teleoperation Control System for 6-DoF Industrial Manipulators," *Robotics*, vol. 12, no. 2, p. 54, Apr. 2023. DOI: 10.3390/robotics12020054.

[91] H. Ji, S. Li, J. Wang, and Z. Ruan, "Improving Teleoperation Through Human-Aware Haptic Feedback: A Distinguishable and Interpretable Physical Interaction Based on the Contact State," *IEEE Transactions on Human-Machine Systems*, vol. 53, no. 1, pp. 24–34, Feb. 2023. DOI: 10.1109/THMS.2022.3227935.

[92] B. Siciliano, L. Sciavicco, L. Villani, and G. Oriolo, *Robotics* (Advanced Textbooks in Control and Signal Processing). London: Springer, 2009. DOI: 10.1007/978-1-84628-642-1.

[93] H. Seraji and R. Colbaugh, "Adaptive force-based impedance control," in *Proceedings of 1993 IEEE/RSJ International Conference on Intelligent Robots and Systems (IROS '93)*, vol. 3, Jul. 1993, 1537–1544 vol.3. DOI: 10.1109/IROS.1993.583844.

[94] H. Seraji and R. Colbaugh, "Force Tracking in Impedance Control," *The International Journal of Robotics Research*, vol. 16, no. 1, pp. 97–117, Feb. 1997. DOI: 10.1177/027836499701600107.

[95] S. Jung, T. Hsia, and R. Bonitz, "Force tracking impedance control of robot manipulators under unknown environment," *IEEE Transactions on Control Systems Technology*, vol. 12, no. 3, pp. 474–483, May 2004. DOI: 10.1109/TCST.2004.824320.

[96] K. Lee and M. Buss, "Force Tracking Impedance Control with Variable Target Stiffness," *IFAC Proceedings Volumes*, 17th IFAC World Congress, vol. 41, no. 2, pp. 6751–6756, Jan. 2008. DOI: 10.3182/20080706-5-KR-1001.01144.

[97] C. Ott, R. Mukherjee, and Y. Nakamura, "Unified Impedance and Admittance Control," in *2010 IEEE International Conference on Robotics and Automation*, May 2010, pp. 554–561. DOI: 10.1109/ROBOT.2010.5509861.

[98] J. Duan, Y. Gan, M. Chen, and X. Dai, "Adaptive variable impedance control for dynamic contact force tracking in uncertain environment," *Robotics and Autonomous Systems*, vol. 102, pp. 54–65, Apr. 2018. DOI: 10.1016/j.robot.2018.01.009.

[99] X. Liang, H. Zhao, X. Li, and H. Ding, "Force tracking impedance control with unknown environment via an iterative learning algorithm," in *2018 3rd International Conference on Advanced Robotics and Mechatronics (ICARM)*, Jul. 2018, pp. 158–164. DOI: 10.1109/ICARM.2018.8610769.

[100] X. Shu, F. Ni, K. Min, Y. Liu, and H. Liu, "An Adaptive Force Control Architecture with Fast-Response and Robustness in Uncertain Environment," in *2021 IEEE*

International Conference on Robotics and Biomimetics (ROBIO), Dec. 2021, pp. 1040–1045. DOI: 10.1109/ROBIO54168.2021.9739648.

[101] M. H. Raibert and J. J. Craig, "Hybrid Position/Force Control of Manipulators," *Journal of Dynamic Systems, Measurement, and Control*, vol. 103, no. 2, pp. 126–133, Jun. 1981. DOI: 10.1115/1.3139652.

[102] N. Hogan, "Impedance Control: An Approach to Manipulation," in *1984 American Control Conference*, Jun. 1984, pp. 304–313. DOI: 10.23919/ACC.1984.4788393.

[103] L. Roveda, F. Vicentini, and L. M. Tosatti, "Deformation-tracking impedance control in interaction with uncertain environments," in *2013 IEEE/RSJ International Conference on Intelligent Robots and Systems*, Nov. 2013, pp. 1992–1997. DOI: 10.1109/IROS.2013.6696621.

[104] L. Roveda, N. Iannacci, F. Vicentini, N. Pedrocchi, F. Braghin, and L. M. Tosatti, "Optimal Impedance Force-Tracking Control Design With Impact Formulation for Interaction Tasks," *IEEE Robotics and Automation Letters*, vol. 1, no. 1, pp. 130–136, Jan. 2016. DOI: 10.1109/LRA.2015.2508061.

[105] J. De Schutter, T. De Laet, J. Rutgeerts, *et al.*, "Constraint-based Task Specification and Estimation for Sensor-Based Robot Systems in the Presence of Geometric Uncertainty," *The International Journal of Robotics Research*, vol. 26, no. 5, pp. 433–455, May 2007. DOI: 10.1177/0278364907078091O7.

[106] H. Bruyninckx and J. De Schutter, "Specification of force-controlled actions in the "task frame formalism"-a synthesis," *IEEE Transactions on Robotics and Automation*, vol. 12, no. 4, pp. 581–589, Aug. 1996. DOI: 10.1109/70.508440.

[107] O. Khatib, "A unified approach for motion and force control of robot manipulators: The operational space formulation," *IEEE Journal on Robotics and Automation*, vol. 3, no. 1, pp. 43–53, Feb. 1987. DOI: 10.1109/JRA.1987.1087068.

[108] N. Hogan, "Impedance Control: An Approach to Manipulation: Part II—Implementation," *Journal of Dynamic Systems, Measurement, and Control*, vol. 107, no. 1, pp. 8–16, Mar. 1985. DOI: 10.1115/1.3140713.

[109] N. Hogan, "Impedance Control: An Approach to Manipulation: Part III—Applications," *Journal of Dynamic Systems, Measurement, and Control*, vol. 107, no. 1, pp. 17–24, Mar. 1985. DOI: 10.1115/1.3140701.

[110] N. Hogan, "Impedance Control: An Approach to Manipulation: Part I—Theory," *Journal of Dynamic Systems, Measurement, and Control*, vol. 107, no. 1, pp. 1–7, Mar. 1985. DOI: 10.1115/1.3140702.

[111] D. Lawrence and R. Stoughton, "Position-based impedance control - Achieving stability in practice," in *Guidance, Navigation and Control Conference*, ser. Guidance, Navigation, and Control and Co-located Conferences, American Institute of Aeronautics and Astronautics, Aug. 1987. DOI: 10.2514/6.1987-2265.

[112] D. Lawrence, "Impedance control stability properties in common implementations," in *1988 IEEE International Conference on Robotics and Automation Proceedings*, Apr. 1988, 1185–1190 vol.2. DOI: 10.1109/ROBOT.1988.12222.

[113] S. Eppinger and W. Seering, "Understanding bandwidth limitations in robot force control," in *1987 IEEE International Conference on Robotics and Automation Pro-*

ceedings, vol. 4, Mar. 1987, pp. 904–909. DOI: 10.1109/ROBOT.1987.1087932.

[114] S. Eppinger and W. Seering, "On dynamic models of robot force control," in *1986 IEEE International Conference on Robotics and Automation Proceedings*, vol. 3, Apr. 1986, pp. 29–34. DOI: 10.1109/ROBOT.1986.1087723.

[115] N. Hogan, "Stable execution of contact tasks using impedance control," in *1987 IEEE International Conference on Robotics and Automation Proceedings*, vol. 4, Mar. 1987, pp. 1047–1054. DOI: 10.1109/ROBOT.1987.1087854.

[116] A. Albu-Schaffer, C. Ott, and G. Hirzinger, "A passivity based Cartesian impedance controller for flexible joint robots - part II: Full state feedback, impedance design and experiments," in *IEEE International Conference on Robotics and Automation, 2004. Proceedings. ICRA '04. 2004*, vol. 3, Apr. 2004, 2666–2672 Vol.3. DOI: 10.1109/ROBOT.2004.1307463.

[117] L. Roveda, N. Castaman, P. Franceschi, S. Ghidoni, and N. Pedrocchi, "A Control Framework Definition to Overcome Position/Interaction Dynamics Uncertainties in Force-Controlled Tasks," in *2020 IEEE International Conference on Robotics and Automation (ICRA)*, May 2020, pp. 6819–6825. DOI: 10.1109/ICRA40945.2020.9197141.

[118] C. Vavra, "Tips for improving safety, ROI for collaborative robots: Collaborative robots are becoming more common on the plant floor. Deciding if they should be used requires considering safety and business goals and return on investment (ROI). See new safety guidance in a technical specification, ISO/TS 15066:2016 Robots and

robotic devices–collaborative robots," *Control Engineering*, vol. 63, no. 3, pp. 26–30, Mar. 2016.

[119] S. Stramigioli, "Energy-Aware Robotics," in *Mathematical Control Theory I*, Cham: Springer International Publishing, 2015, pp. 37–50. DOI: 10.1007/978-3-319-20988-3_3.

[120] J. Lachner, F. Allmendinger, E. Hobert, N. Hogan, and S. Stramigioli, "Energy budgets for coordinate invariant robot control in physical human–robot interaction," *The International Journal of Robotics Research*, vol. 40, no. 8-9, pp. 968–985, Aug. 2021. DOI: 10.1177/02783649211011639.

[121] H. Gao, X. Zhang, C. Ma, and C. Zhou, "Combined active and passive adaptive variable admittance compliant control for space robotic manipulators," in *2023 IEEE International Conference on Robotics and Biomimetics (ROBIO)*, Dec. 2023, pp. 1–8. DOI: 10.1109/ROBIO58561.2023.10355003.

[122] J. Cho, D. Choi, and J. H. Park, "Sensorless Variable Admittance Control for Human–Robot Interaction of a Dual-Arm Social Robot," *IEEE Access*, vol. 11, pp. 69 366–69 377, 2023. DOI: 10.1109/ACCESS.2023.3292933.

[123] C. Yang, G. Ganesh, S. Haddadin, S. Parusel, A. Albu-Schaeffer, and E. Burdet, "Human-Like Adaptation of Force and Impedance in Stable and Unstable Interactions," *IEEE Transactions on Robotics*, vol. 27, no. 5, pp. 918–930, Oct. 2011. DOI: 10.1109/TRO.2011.2158251.

[124] J. Kim, D. Lee, Y. Choi, and W. K. Chung, "Lie Group-Based User Motion Refinement Control for Teleoperation of a Constrained Robot Arm," *IEEE Robotics and Au-*

tomation Letters, vol. 9, no. 7, pp. 6154–6161, Jul. 2024. DOI: 10.1109/LRA.2024.3401135.

[125] J. Lachner, F. Allmendinger, S. Stramigioli, and N. Hogan, "Shaping Impedances to Comply With Constrained Task Dynamics," *IEEE Transactions on Robotics*, vol. 38, no. 5, pp. 2750–2767, Oct. 2022. DOI: 10.1109/TRO.2022.3153949.

[126] Y. Lin, H. Zhao, Y. Zhang, and H. Ding, "A Data-Driven Motion Mapping Method for Space Teleoperation of Kinematically Dissimilar Master/Slave Robots," in *2018 IEEE International Conference on Robotics and Biomimetics (ROBIO)*, Dec. 2018, pp. 862–867. DOI: 10.1109/ROBIO.2018.8665119.

[127] G. Salvietti, L. Meli, G. Gioioso, M. Malvezzi, and D. Prattichizzo, "Object-based bilateral telemanipulation between dissimilar kinematic structures," in *2013 IEEE/RSJ International Conference on Intelligent Robots and Systems*, Nov. 2013, pp. 5451–5456. DOI: 10.1109/IROS.2013.6697145.

[128] G. Gioioso, G. Salvietti, M. Malvezzi, and D. Prattichizzo, "Mapping Synergies From Human to Robotic Hands With Dissimilar Kinematics: An Approach in the Object Domain," *IEEE Transactions on Robotics*, vol. 29, no. 4, pp. 825–837, Aug. 2013. DOI: 10.1109/TRO.2013.2252251.

[129] G. Liu, X. Geng, L. Liu, and Y. Wang, "Haptic based teleoperation with master-slave motion mapping and haptic rendering for space exploration," *Chinese Journal of Aeronautics*, vol. 32, no. 3, pp. 723–736, Mar. 2019. DOI: 10.1016/j.cja.2018.07.009.

[130] F. Conti and O. Khatib, "Spanning large workspaces using small haptic devices," in *First Joint Eurohaptics Con-*

ference and Symposium on Haptic Interfaces for Virtual Environment and Teleoperator Systems. World Haptics Conference, Mar. 2005, pp. 183–188. DOI: 10.1109/WHC.2005.118.

[131] W. R. Ferrell, "Human Factors Applications in Teleoperator Design and Operation," *Nuclear Technology*, vol. 12, no. 3, pp. 335–335, Nov. 1971. DOI: 10.13182/NT71-A31019.

[132] A. Pérez and J. Rosell, "An assisted re-synchronization method for robotic teleoperated tasks," in *2011 IEEE International Conference on Robotics and Automation*, May 2011, pp. 886–891. DOI: 10.1109/ICRA.2011.5980069.

[133] S. Park, C. Seo, J.-P. Kim, and J. Ryu, "Robustly stable rate-mode bilateral teleoperation using an energy-bounding approach," *Mechatronics*, vol. 21, no. 1, pp. 176–184, Feb. 2011. DOI: 10.1016/j.mechatronics.2010.10.002.

[134] A. Pepe, D. Chiaravalli, and C. Melchiorri, "A hybrid teleoperation control scheme for a single-arm mobile manipulator with omnidirectional wheels," in *2016 IEEE/RSJ International Conference on Intelligent Robots and Systems (IROS)*, Oct. 2016, pp. 1450–1455. DOI: 10.1109/IROS.2016.7759236.

[135] N. Diolaiti and C. Melchiorri, "Teleoperation of a mobile robot through haptic feedback," in *IEEE International Workshop HAVE Haptic Virtual Environments and Their*, Nov. 2002, pp. 67–72. DOI: 10.1109/HAVE.2002.1106916.

[136] M. Mamdouh and A. A. Ramadan, "Development of a teleoperation system with a new workspace spanning technique," in *2012 IEEE International Conference on*

Robotics and Biomimetics (ROBIO), Dec. 2012, pp. 1570–1575. DOI: 10.1109/ROBIO.2012.6491191.

[137] J. Barrio, F. Suarez-Ruiz, M. Ferre, and R. Aracil, "A rate-position haptic controller for large telemanipulation workspaces," in *2012 IEEE/RSJ International Conference on Intelligent Robots and Systems*, Oct. 2012, pp. 58–63. DOI: 10.1109/IROS.2012.6385633.

[138] K. Komuta and T. Murakami, "An approach to expansion of workspace motion in master-slave control system," in *IECON 2012 - 38th Annual Conference on IEEE Industrial Electronics Society*, Oct. 2012, pp. 2650–2655. DOI: 10.1109/IECON.2012.6389158.

[139] V. H. Andaluz, L. Salinas, F. Roberti, J. M. Toibero, and R. Carelli, "Switching control signal for bilateral teleoperation of a mobile manipulator," in *2011 9th IEEE International Conference on Control and Automation (ICCA)*, Dec. 2011, pp. 778–783. DOI: 10.1109/ICCA.2011.6138029.

[140] I. Farkhatdinov and J.-H. Ryu, "Hybrid position-position and position-speed command strategy for the bilateral teleoperation of a mobile robot," in *2007 International Conference on Control, Automation and Systems*, Oct. 2007, pp. 2442–2447. DOI: 10.1109/ICCAS.2007.4406773.

[141] V. Duchaine and C. M. Gosselin, "General Model of Human-Robot Cooperation Using a Novel Velocity Based Variable Impedance Control," in *Second Joint EuroHaptics Conference and Symposium on Haptic Interfaces for Virtual Environment and Teleoperator Systems (WHC'07)*, Mar. 2007, pp. 446–451. DOI: 10.1109/WHC.2007.59.

[142] Universal Robots, *Collaborative robotic automation | Universal Robots Cobots*, 2024. Available at: https://www.universal-robots.com/.

[143] Robotiq, *Robotiq*, 2024. Available at: https://robotiq.com.

[144] F. L. Markley, Y. Cheng, J. L. Crassidis, and Y. Oshman, "Averaging Quaternions," *Journal of Guidance, Control, and Dynamics*, vol. 30, no. 4, pp. 1193–1197, Jul. 2007. DOI: 10.2514/1.28949.

[145] Z. Li, H. Huang, X. Song, W. Xu, and B. Li, "A fuzzy adaptive admittance controller for force tracking in an uncertain contact environment," *IET Control Theory & Applications*, vol. 15, no. 17, pp. 2158–2170, 2021. DOI: 10.1049/cth2.12175.

[146] L. Roveda, A. A. Shahid, N. Iannacci, and D. Piga, "Sensorless Optimal Interaction Control Exploiting Environment Stiffness Estimation," *IEEE Transactions on Control Systems Technology*, vol. 30, no. 1, pp. 218–233, Jan. 2022. DOI: 10.1109/TCST.2021.3061091.

[147] B. L. Somberg, "Character Aspect Ratio and Design Tradeoffs," *Proceedings of the Human Factors Society Annual Meeting*, vol. 34, no. 19, pp. 1461–1464, Oct. 1990. DOI: 10.1177/154193129003401909.

[148] J. Grischke, L. Johannsmeier, L. Eich, L. Griga, and S. Haddadin, "Dentronics: Towards robotics and artificial intelligence in dentistry," *Dental Materials*, vol. 36, no. 6, pp. 765–778, Jun. 2020. DOI: 10.1016/j.dental.2020.03.021.

[149] A. Podhorsky, P. Rehmann, and B. Wöstmann, "Tooth preparation for full-coverage restorations—a literature review," *Clinical Oral Investigations*, vol. 19, no. 5, pp. 959–968, Jun. 2015. DOI: 10.1007/s00784-015-1439-y.

[150] M. Sanz, D. Herrera, M. Kebschull, *et al.*, "Treatment of stage I–III periodontitis—The EFP S3 level clinical practice guideline," *Journal of Clinical Periodontology*, vol. 47, no. S22, pp. 4–60, 2020. DOI: 10.1111/jcpe.13290.

[151] A. Afshari, R. Shahmohammadi, S. A. Mosaddad, *et al.*, "Free-Hand versus Surgical Guide Implant Placement," *Advances in Materials Science and Engineering*, vol. 2022, no. 1, p. 6 491 134, 2022. DOI: 10.1155/2022/6491134.

[152] A. Kozlovsky, A. Rapaport, and Z. Artzi, "Influence of operator skill level on the clinical outcome of non-surgical periodontal treatment: A retrospective study," *Clinical Oral Investigations*, vol. 22, no. 8, pp. 2927–2932, Nov. 2018. DOI: 10.1007/s00784-018-2380-7.

[153] J. Y. N. Luo, P. P. Liu, and M. C. M. Wong, "Patients' satisfaction with dental care: A qualitative study to develop a satisfaction instrument," *BMC Oral Health*, vol. 18, no. 1, p. 15, Jan. 2018. DOI: 10.1186/s12903-018-0477-7.

[154] S. Schnutenhaus, M. Wagner, C. Edelmann, R. G. Luthardt, and H. Rudolph, "Factors Influencing the Accuracy of Freehand Implant Placement: A Prospective Clinical Study," *Dentistry Journal*, vol. 9, no. 5, p. 54, May 2021. DOI: 10.3390/dj9050054.

[155] S. Y. Soo, W. S. Ang, C. H. Chong, I. M. Tew, and N. A. Yahya, "Occupational ergonomics and related musculoskeletal disorders among dentists: A systematic review," *WORK*, vol. 74, no. 2, pp. 469–476, Feb. 2023. DOI: 10.3233/WOR-211094.

[156] A. Gupta, M. Bhat, T. Mohammed, N. Bansal, and G. Gupta, "Ergonomics in Dentistry," *International Journal*

of Clinical Pediatric Dentistry, vol. 7, no. 1, pp. 30–34, 2014. DOI: 10.5005/jp-journals-10005-1229.

[157] J. Field, J. Dixon, A. Towers, *et al.*, "Defining dental operative skills curricula: An ADEE consensus paper," *European Journal of Dental Education*, vol. 25, no. 2, pp. 405–414, 2021. DOI: 10.1111/eje.12595.

[158] E. L. McGleenon and S. Morison, "Preparing dental students for independent practice: A scoping review of methods and trends in undergraduate clinical skills teaching in the UK and Ireland," *British Dental Journal*, vol. 230, no. 1, pp. 39–45, Jan. 2021. DOI: 10.1038/s41415-020-2505-7.

[159] K. Uoshima, N. Akiba, and M. Nagasawa, "Technical skill training and assessment in dental education," *Japanese Dental Science Review*, vol. 57, pp. 160–163, Nov. 2021. DOI: 10.1016/j.jdsr.2021.08.004.

[160] H. L. Abouzeid, S. Chaturvedi, K. M. Abdelaziz, F. A. Alzahrani, A. A. S. AlQarni, and N. M. Alqahtani, "Role of Robotics and Artificial Intelligence in Oral Health and Preventive Dentistry - Knowledge, Perception and Attitude of Dentists," *Oral Health & Preventive Dentistry*, vol. 19, pp. 353–363, Jul. 2021. DOI: 10.3290/j.ohpd.b1693873.

[161] R. Yasin, P. Chalasani, N. Zevallos, *et al.*, "Evaluation of Hybrid Control and Palpation Assistance for Situational Awareness in Telemanipulated Task Execution," *IEEE Transactions on Medical Robotics and Bionics*, vol. 3, no. 1, pp. 31–43, Feb. 2021. DOI: 10.1109/TMRB.2020.3042992.

[162] D. Kundrat, A. Schoob, T. Piskon, *et al.*, "Toward Assistive Technologies for Focus Adjustment in Teleoperated Robotic Non-Contact Laser Surgery," *IEEE Transactions*

on Medical Robotics and Bionics, vol. 1, no. 3, pp. 145–157, Aug. 2019. DOI: 10.1109/TMRB.2019.2931438.

[163] Z. Deng, X. Wei, C. Pan, G. Li, and Y. Hu, "Shared Control of Tendon-Driven Continuum Robots Using Visibility-Guaranteed Optimization for Endoscopic Surgery," *IEEE Transactions on Medical Robotics and Bionics*, vol. 6, no. 2, pp. 487–497, May 2024. DOI: 10.1109/TMRB.2024.3381371.

[164] A. Y. Alqutaibi, H. H. Hamadallah, B. Abu zaid, A. M. Aloufi, and R. A. Tarawah, "Applications of robots in implant dentistry: A scoping review," *The Journal of Prosthetic Dentistry*, Dec. 2023. DOI: 10.1016/j.prosdent.2023.11.019.

[165] Y. Wu, S. Zou, P. Lv, and X. Wang, "Accuracy of an autonomous dental implant robotic system in dental implant surgery," *Journal of Prosthetic Dentistry*, vol. 0, no. 0, Aug. 2024. DOI: 10.1016/j.prosdent.2024.07.020.

[166] H. S. Talib, G. N. Wilkins, and I. Turkyilmaz, "Flapless dental implant placement using a recently developed haptic robotic system," *British Journal of Oral and Maxillofacial Surgery*, vol. 60, no. 9, pp. 1273–1275, Nov. 2022. DOI: 10.1016/j.bjoms.2022.05.008.

[167] Y. Kasahara, H. Kawana, S. Usuda, and K. Ohnishi, "Telerobotic-assisted bone-drilling system using bilateral control with feed operation scaling and cutting force scaling," *The International Journal of Medical Robotics and Computer Assisted Surgery*, vol. 8, no. 2, pp. 221–229, 2012. DOI: 10.1002/rcs.457.

[168] J. Jiang, Y. Guo, Z. Huang, Y. Zhang, D. Wu, and Y. Liu, "Adjacent surface trajectory planning of robot-assisted tooth preparation based on augmented reality,"

Engineering Science and Technology, an International Journal, vol. 27, p. 101 001, Mar. 2022. DOI: 10.1016/j.jestch.2021.05.005.

[169] L. Wang, D. Wang, L. Ma, *et al.*, "Preliminary experiments of a miniature robotic system for tooth ablation using ultra-short pulsed lasers," in *2013 IEEE/RSJ International Conference on Intelligent Robots and Systems*, Nov. 2013, pp. 2566–2571. DOI: 10.1109/IROS.2013.6696718.

[170] L. Wang, D. Wang, Y. Zhang, L. Ma, Y. Sun, and P. Lv, "An automatic robotic system for three-dimensional tooth crown preparation using a picosecond laser," *Lasers in Surgery and Medicine*, vol. 46, no. 7, pp. 573–581, 2014. DOI: 10.1002/lsm.22274.

[171] L. Ma, Y. Zhang, D. Wang, P. Lv, Y. Sun, and H. Wang, "Trajectory tracking control of a miniature laser manipulation robotic end-effector for dental preparation," in *2013 IEEE International Conference on Robotics and Biomimetics (ROBIO)*, Dec. 2013, pp. 468–473. DOI: 10.1109/ROBIO.2013.6739503.

[172] F. Yuan and P. Lyu, "A preliminary study on a tooth preparation robot," *Advances in Applied Ceramics*, vol. 119, no. 5-6, pp. 332–337, Jul. 2020. DOI: 10.1080/17436753.2019.1666555.

[173] Y. Zhang, Z. Zhao, R. Song, J. Lu, P. Lu, and Y. Wang, "Tooth arrangement for the manufacture of a complete denture using a robot," *Industrial Robot: the international journal of robotics research and application*, vol. 28, no. 5, pp. 420–425, Oct. 2001. DOI: 10.1108/01439910110401286.

[174] T. Otani, A. J. Raigrodski, L. Mancl, I. Kanuma, and J. Rosen, "In vitro evaluation of accuracy and precision of

automated robotic tooth preparation system for porcelain laminate veneers," *The Journal of Prosthetic Dentistry*, vol. 114, no. 2, pp. 229–235, Aug. 2015. DOI: 10.1016/j.prosdent.2015.02.021.

[175] F. Yuan, Y. Wang, Y. Zhang, Y. Sun, D. Wang, and P. Lyu, "An automatic tooth preparation technique: A preliminary study," *Scientific Reports*, vol. 6, p. 25 281, Apr. 2016. DOI: 10.1038/srep25281.

[176] J. Dong and H. Everett, "The Development of Endodontic Micro Robot," American Society of Mechanical Engineers Digital Collection, May 2009, pp. 201–204. DOI: 10.1115/IMECE2007-41562.

[177] J. Dong and S. Y. Hong, "Design of Z Axis Actuator and Quick Tool Change Assembly for an Endodontic Micro Robot," American Society of Mechanical Engineers Digital Collection, Apr. 2012, pp. 507–511. DOI: 10.1115/IMECE2010-40816.

[178] G. Hwang, A. J. Paula, E. E. Hunter, *et al.*, "Catalytic antimicrobial robots for biofilm eradication," *Science Robotics*, vol. 4, no. 29, eaaw2388, Apr. 2019. DOI: 10.1126/scirobotics.aaw2388.

[179] T. Gulrez, A. K. Shahid, U. Sana, and N. G. Chaudhary, "Visual guided robotic endodontic therapeutic system," in *2010 International Conference on Information and Emerging Technologies*, Jun. 2010, pp. 1–6. DOI: 10.1109/ICIET.2010.5625729.

[180] O. S. Ajani and S. F. M. Assal, "Hybrid Force Tracking Impedance Control-Based Autonomous Robotic System for Tooth Brushing Assistance of Disabled People," *IEEE Transactions on Medical Robotics and Bionics*, vol. 2, no. 4, pp. 649–660, Nov. 2020. DOI: 10.1109/TMRB.2020.3030317.

[181] P. Ahmad, M. K. Alam, A. Aldajani, *et al.*, "Dental Robotics: A Disruptive Technology," *Sensors*, vol. 21, no. 10, p. 3308, Jan. 2021. DOI: 10.3390/s21103308.

[182] L. Liu, M. Watanabe, and T. Ichikawa, "Robotics in Dentistry: A Narrative Review," *Dentistry Journal*, vol. 11, no. 3, p. 62, Feb. 2023. DOI: 10.3390/dj11030062.

[183] T. C. T. van Riet, K. T. H. Chin Jen Sem, J.-P. T. F. Ho, R. Spijker, J. Kober, and J. de Lange, "Robot technology in dentistry, part two of a systematic review: An overview of initiatives," *Dental Materials*, vol. 37, no. 8, pp. 1227–1236, Aug. 2021. DOI: 10.1016/j.dental.2021.06.002.

[184] Z. Xia, F. Ahmad, H. Deng, *et al.*, "Robotics Application in Dentistry: A Review," *IEEE Transactions on Medical Robotics and Bionics*, vol. 6, no. 3, pp. 851–867, Aug. 2024. DOI: 10.1109/TMRB.2024.3408321.

[185] Y. Li, Y. Inamochi, Z. Wang, and K. Fueki, "Clinical application of robots in dentistry: A scoping review," *Journal of Prosthodontic Research*, vol. 68, no. 2, pp. 193–205, 2023. DOI: 10.2186/jpr.JPR_D_23_00027.

[186] H. Ravichandar, A. S. Polydoros, S. Chernova, and A. Billard, "Recent Advances in Robot Learning from Demonstration," *Annual Review of Control, Robotics, and Autonomous Systems*, vol. 3, no. Volume 3, 2020, pp. 297–330, May 2020. DOI: 10.1146/annurev-control-100819-063206.

[187] M. Li, Y.-H. Liu, and Q. Huang, "An optimized haptic interaction model based on support vector regression for evaluation of endodontic shaping skill," in *2007 IEEE International Conference on Robotics and Biomimetics (ROBIO)*, Dec. 2007, pp. 617–622. DOI: 10.1109/ROBIO.2007.4522233.

[188] M. N. Milner, E. C. Anania, K. Candelaria-Oquendo, S. Rice, S. R. Winter, and N. K. Ragbir, "Patient Perceptions of New Robotic Technologies in Clinical Restorative Dentistry," *Journal of Medical Systems*, vol. 44, no. 2, p. 33, Dec. 2019. DOI: 10.1007/s10916-019-1488-x.

[189] G. Niemeyer, C. Preusche, S. Stramigioli, and D. Lee, "Telerobotics," in *Springer Handbook of Robotics*, Cham: Springer International Publishing, 2016, pp. 1085–1108. DOI: 10.1007/978-3-319-32552-1_43.

[190] I. Aliaga, A. Rubio, and E. Sanchez, "Experimental quantitative comparison of different control architectures for master-slave teleoperation," *IEEE Transactions on Control Systems Technology*, vol. 12, no. 1, pp. 2–11, Jan. 2004. DOI: 10.1109/TCST.2003.819586.

[191] K. Hashtrudi-Zaad and S. E. Salcudean, "Analysis of Control Architectures for Teleoperation Systems with Impedance/Admittance Master and Slave Manipulators," *The International Journal of Robotics Research*, vol. 20, no. 6, pp. 419–445, Jun. 2001. DOI: 10.1177/02783640122067471.

[192] K. Razi and K. Hashtrudi-Zaad, "Extension of Zeheb-Walach absolute stability criteria for robot-human interactions," in *2012 IEEE 51st IEEE Conference on Decision and Control (CDC)*, Dec. 2012, pp. 1186–1191. DOI: 10.1109/CDC.2012.6426356.

[193] M. Salehi and A.-A. Ahmadi, "Improvement in the conservatism of the time domain passivity approach in delayed position-position teleoperation system," *International Journal of Intelligent Robotics and Applications*, vol. 8, no. 3, pp. 619–628, Sep. 2024. DOI: 10.1007/s41315-024-00336-z.

[194] G. Flandin, F. Chaumette, and E. Marchand, "Eye-in-hand/eye-to-hand cooperation for visual servoing," in *Proceedings 2000 ICRA. Millennium Conference. IEEE International Conference on Robotics and Automation. Symposia Proceedings (Cat. No.00CH37065)*, vol. 3, Apr. 2000, 2741–2746 vol.3. DOI: 10.1109/ROBOT.2000.846442.

[195] S. E. Salcudean, M. Zhu, W.-H. Zhu, and K. Hashtrudi-Zaad, "Transparent Bilateral Teleoperation under Position and Rate Control," *The International Journal of Robotics Research*, vol. 19, no. 12, pp. 1185–1202, Dec. 2000. DOI: 10.1177/02783640022068020.

[196] C. Freschi, V. Ferrari, F. Melfi, M. Ferrari, F. Mosca, and A. Cuschieri, "Technical review of the da Vinci surgical telemanipulator," *The International Journal of Medical Robotics and Computer Assisted Surgery*, vol. 9, no. 4, pp. 396–406, 2013. DOI: 10.1002/rcs.1468.

[197] L. Wu, F. Yu, T. N. Do, and J. Wang, "Camera Frame Misalignment in a Teleoperated Eye-in-Hand Robot: Effects and a Simple Correction Method," *IEEE Transactions on Human-Machine Systems*, vol. 53, no. 1, pp. 2–12, Feb. 2023. DOI: 10.1109/THMS.2022.3217453.

[198] A. Boese, C. Wex, R. Croner, *et al.*, "Endoscopic Imaging Technology Today," *Diagnostics*, vol. 12, no. 5, May 2022. DOI: 10.3390/diagnostics12051262.

[199] P. Rynio, K. Galant, Ł. Wójcik, *et al.*, "Effects of Sterilization Methods on Different 3D Printable Materials for Templates of Physician-Modified Aortic Stent Grafts Used in Vascular Surgery—A Preliminary Study," *International Journal of Molecular Sciences*, vol. 23, no. 7, Mar. 2022. DOI: 10.3390/ijms23073539.

[200] E. M. van der Schans, M. A. J. Hiep, E. C. J. Consten, and I. A. M. J. Broeders, "From Da Vinci Si to Da Vinci Xi: Realistic times in draping and docking the robot," *Journal of Robotic Surgery*, vol. 14, no. 6, pp. 835–839, Dec. 2020. DOI: 10.1007/s11701-020-01057-8.

[201] L. Pagliara, E. Ferrentino, A. Chiacchio, and G. Russo, *Teleoperated dental scaling procedure*, 2025. Available at: https://drive.google.com/file/d/1tkW4I-cvnHpTwZMYVWSIIpvVRMs3MGMK/view?usp=drive_link.

[202] S. Calzetti, M. Baratti, M. Gresty, and L. Findley, "Frequency/amplitude characteristics of postural tremor of the hands in a population of patients with bilateral essential tremor: Implications for the classification and mechanism of essential tremor.," *Journal of Neurology, Neurosurgery & Psychiatry*, vol. 50, no. 5, pp. 561–567, May 1987. DOI: 10.1136/jnnp.50.5.561.

[203] R. Steyer and W. Nagel, *Probability and Conditional Expectation: Fundamentals for the Empirical Sciences*. John Wiley & Sons, May 2017.

[204] C. A. Schneider, W. S. Rasband, and K. W. Eliceiri, "NIH Image to ImageJ: 25 years of Image Analysis," *Nature methods*, vol. 9, no. 7, pp. 671–675, Jul. 2012. DOI: 10.1038/nmeth.2089.

[205] R. A. Yukna, S. Vastardis, and E. T. Mayer, "Calculus removal with diamond-coated ultrasonic inserts in vitro," *Journal of Periodontology*, vol. 78, no. 1, pp. 122–126, Jan. 2007. DOI: 10.1902/jop.2007.060207.

[206] A. Chiacchio, L. Pagliara, A. Langella, E. Ferrentino, and M. Caggiano, *Clinical-Experimental Evaluation of a Teleoperated Robotic Arm for Dental Procedures - Questionnaire*, 2025. Available at: https://drive.google.

com/file/d/1NPCi7pz4soY7jC6AnmqwDbb4vXcBraFZ/view?usp=sharing.

[207] M. Ruppert, J. Cadosch, J. Guindy, D. Case, and U. Zappa, "In vivo ultrasonic debridement forces in bicuspids: A pilot study," *Journal of Periodontology*, vol. 73, no. 4, pp. 418–422, Apr. 2002. DOI: 10.1902/jop.2002.73.4.418.

[208] D. Stutzer, M. Hofmann, S. Eick, N. Scharp, J. Burger, and T. Niederhauser, "In-Vitro Measurement of Forces During Debridement with a Piezoelectric Ultrasonic Periodontal Scaler," *Oral Health & Preventive Dentistry*, vol. 22, pp. 223–230, Jun. 2024. DOI: 10.3290/j.ohpd.b5458595.

[209] L. Pagliara, V. Redondo, E. Ferrentino, M. Ferre, and P. Chiacchio, *Improving dependability in robotized bolting operations*, Nov. 2025. DOI: 10.48550/arXiv.2511.10448. Available at: http://arxiv.org/abs/2511.10448.

[210] S. Hayati and S. Venkataraman, "Design and implementation of a robot control system with traded and shared control capability," in *1989 International Conference on Robotics and Automation Proceedings*, May 1989, 1310–1315 vol.3. DOI: 10.1109/ROBOT.1989.100161.

[211] G. Hirzinger, B. Brunner, J. Dietrich, and J. Heindl, "ROTEX-the first remotely controlled robot in space," in *Proceedings of the 1994 IEEE International Conference on Robotics and Automation*, May 1994, 2604–2611 vol.3. DOI: 10.1109/ROBOT.1994.351121.

[212] W. B. Griffin, W. R. Provancher, and M. R. Cutkosky, "Feedback Strategies for Telemanipulation with Shared Control of Object Handling Forces," *Presence*, vol. 14, no. 6, pp. 720–731, Dec. 2005. DOI: 10.1162/105474605775196634.

[213] T. Ortmaier, M. Groger, D. Boehm, V. Falk, and G. Hirzinger, "Motion estimation in beating heart surgery," *IEEE Transactions on Biomedical Engineering*, vol. 52, no. 10, pp. 1729–1740, Oct. 2005. DOI: 10.1109/TBME.2005.855716.

[214] L. Rosenberg, "Virtual fixtures: Perceptual tools for telerobotic manipulation," in *Proceedings of IEEE Virtual Reality Annual International Symposium*, Sep. 1993, pp. 76–82. DOI: 10.1109/VRAIS.1993.380795.

[215] J. J. Abbott, P. Marayong, and A. M. Okamura, "Haptic Virtual Fixtures for Robot-Assisted Manipulation," in *Robotics Research*, Berlin, Heidelberg: Springer, 2007, pp. 49–64. DOI: 10.1007/978-3-540-48113-3_5.

[216] T. B. Sheridan, *Telerobotics, automation, and human supervisory control*. Cambridge, Mass. : MIT Press, 1992.

[217] R. Parasuraman, T. Sheridan, and C. Wickens, "A model for types and levels of human interaction with automation," *IEEE Transactions on Systems, Man, and Cybernetics - Part A: Systems and Humans*, vol. 30, no. 3, pp. 286–297, May 2000. DOI: 10.1109/3468.844354.

[218] G. Calhoun, "Adaptable (Not Adaptive) Automation: Forefront of Human–Automation Teaming," *Human Factors*, vol. 64, no. 2, pp. 269–277, Mar. 2022. DOI: 10.1177/00187208211037457.

[219] M. R. ENDSLEY and D. B. KABER, "Level of automation effects on performance, situation awareness and workload in a dynamic control task," *Ergonomics*, vol. 42, no. 3, pp. 462–492, Mar. 1999. DOI: 10.1080/001401399185595.

[220] P. Allan, A. B. Loving, H. Omran, *et al.*, "Remote handling installation of diagnostics in the JET Tokamak," *Fusion Engineering and Design*, Proceedings of the 26th

Symposium of Fusion Technology (SOFT-26), vol. 86, no. 9, pp. 1821–1824, Oct. 2011. DOI: 10.1016/j.fusengdes.2010.11.038.

[221] G. D. Gironimo and S. Grazioso, "The DTT device: Preliminary remote maintenance strategy," *Fusion Engineering and Design*, vol. 172, p. 112 762, Nov. 2021. DOI: 10.1016/j.fusengdes.2021.112762.

[222] R. Buckingham and A. Loving, "Remote-handling challenges in fusion research and beyond," *Nature Physics*, vol. 12, no. 5, pp. 391–393, May 2016. DOI: 10.1038/nphys3755.

[223] W. R. Ferrell and T. B. Sheridan, "Supervisory control of remote manipulation," *IEEE Spectrum*, vol. 4, no. 10, pp. 81–88, Oct. 1967. DOI: 10.1109/MSPEC.1967.5217126.

[224] T. B. Sheridan, "Human Supervisory Control," in *Handbook of Human Factors and Ergonomics*, John Wiley & Sons, Ltd, 2012, pp. 990–1015. DOI: 10.1002/9781118131350.ch34.

[225] M. L. Cummings, "The need for command and control instant message adaptive interfaces: Lessons learned from Tactical Tomahawk human-in-the-loop simulations," *Cyberpsychology & Behavior: The Impact of the Internet, Multimedia and Virtual Reality on Behavior and Society*, vol. 7, no. 6, pp. 653–661, Dec. 2004. DOI: 10.1089/cpb.2004.7.653.

[226] M. P. Linegang, H. A. Stoner, M. J. Patterson, *et al.*, "Human-Automation Collaboration in Dynamic Mission Planning: A Challenge Requiring an Ecological Approach," *Proceedings of the Human Factors and Ergonomics Society Annual Meeting*, Oct. 2006. DOI: 10.1177/154193120605002304.

[227] C. E. Nehme, S. D. Scott, M. L. Cummings, and C. Y. Furusho, "Generating Requirements for Futuristic Heterogenous Unmanned Systems," *Proceedings of the Human Factors and Ergonomics Society Annual Meeting*, vol. 50, no. 3, pp. 235–239, Oct. 2006. DOI: 10.1177/154193120605000306.

[228] W. Olson and M. Wuennenberg, "Autonomy based human-vehicle interface standards for remotely operated aircraft," in *20th DASC. 20th Digital Avionics Systems Conference (Cat. No.01CH37219)*, vol. 2, Oct. 2001, 7D3/1–7D3/9 vol.2. DOI: 10.1109/DASC.2001.964199.

[229] C. S. Nam, S. Johnson, Y. Li, and Y. Seong, "Evaluation of human–agent user interfaces in multi-agent systems," *International Journal of Industrial Ergonomics*, vol. 39, no. 1, pp. 192–201, Jan. 2009. DOI: 10.1016/j.ergon.2008.08.008.

[230] S. Saget, F. Legras, and G. Coppin, *Collaborative model of interaction and Unmanned Vehicle Systems' interface*, Jun. 2008. DOI: 10.48550/arXiv.0806.0784. Available at: http://arxiv.org/abs/0806.0784.

[231] X. Fan, S. Oh, M. McNeese, *et al.*, "The influence of agent reliability on trust in human-agent collaboration," in *Proceedings of the 15th European conference on Cognitive ergonomics: the ergonomics of cool interaction*, ser. ECCE '08, New York, NY, USA: Association for Computing Machinery, Jan. 2008, pp. 1–8. DOI: 10.1145/1473018.1473028.

[232] D. Woods, J. Tittle, M. Feil, and A. Roesler, "Envisioning human-robot coordination in future operations," *IEEE Transactions on Systems, Man, and Cybernetics, Part C (Applications and Reviews)*, vol. 34, no. 2, pp. 210–218, May 2004. DOI: 10.1109/TSMCC.2004.826272.

[233] J. Y. C. Chen, E. C. Haas, and M. J. Barnes, "Human Performance Issues and User Interface Design for Teleoperated Robots," *IEEE Transactions on Systems, Man, and Cybernetics, Part C (Applications and Reviews)*, vol. 37, no. 6, pp. 1231–1245, Nov. 2007. DOI: 10.1109/TSMCC.2007.905819.

[234] J. Y. C. Chen and J. E. Thropp, "Review of Low Frame Rate Effects on Human Performance," *IEEE Transactions on Systems, Man, and Cybernetics - Part A: Systems and Humans*, vol. 37, no. 6, pp. 1063–1076, Nov. 2007. DOI: 10.1109/TSMCA.2007.904779.

[235] B. D. Simpson, R. S. Bolia, and M. H. Draper, "Spatial Audio Display Concepts Supporting Situation Awareness for Operators of Unmanned Aerial Vehicles," in *Human Performance, Situation Awareness, and Automation*, Psychology Press, 2005.

[236] D. V. Gunn, J. S. Warm, W. T. Nelson, R. S. Bolia, D. A. Schumsky, and K. J. Corcoran, "Target acquisition with UAVs: Vigilance displays and advanced cuing interfaces," *Human Factors*, vol. 47, no. 3, pp. 488–497, 2005. DOI: 10.1518/001872005774859971.

[237] Z. Jia, A. Bhatia, R. M. Aronson, D. Bourne, and M. T. Mason, "A Survey of Automated Threaded Fastening," *IEEE Transactions on Automation Science and Engineering*, vol. 16, no. 1, pp. 298–310, Jan. 2019. DOI: 10.1109/TASE.2018.2835382.

[238] V. Redondo, N. Barbosa, P. Espinosa, and M. Ferre, "Design and evaluation of an advanced robotic bolting tool applied to IFMIF-DONES," *Fusion Engineering and Design*, vol. 214, p. 114 877, May 2025. DOI: 10.1016/j.fusengdes.2025.114877.

[239] F. Arranz, G. Micciche, S. Coloma, *et al.*, "Remote Handling in the Accelerator Systems of DONES," *IEEE Transactions on Plasma Science*, vol. 48, no. 6, pp. 1743–1747, Jun. 2020. DOI: 10.1109/TPS.2020.2969262.

[240] F. Arranz, S. Becerril, D. Bernardi, *et al.*, "Alignment strategy for IFMIF-DONES facility," *Fusion Engineering and Design*, vol. 200, p. 114 181, Mar. 2024. DOI: 10.1016/j.fusengdes.2024.114181.

[241] Z. Chen, C. Gautier, and N. Bultman, "Spallation Neutron Source linac vacuum seal design and testing," in *PACS2001. Proceedings of the 2001 Particle Accelerator Conference (Cat. No.01CH37268)*, vol. 3, Jun. 2001, 2192–2194 vol.3. DOI: 10.1109/PAC.2001.987320.

[242] L. A. Martin-Vega, H. K. Brown, W. H. Shaw, and T. J. Sanders, "Industrial perspective on research needs and opportunities in manufacturing assembly," *Journal of Manufacturing Systems*, vol. 14, no. 1, pp. 45–58, Jan. 1995. DOI: 10.1016/0278-6125(95)98900-Q.

[243] K. Dharmara, R. P. Monfared, P. S. Ogun, and M. R. Jackson, "Robotic assembly of threaded fasteners in a non-structured environment," *The International Journal of Advanced Manufacturing Technology*, vol. 98, no. 5, pp. 2093–2107, Sep. 2018. DOI: 10.1007/s00170-018-2363-5.

[244] N. Dhayagude, Z. Gao, and F. Mrad, "Fuzzy logic control of automated screw fastening," *Robotics and Computer-Integrated Manufacturing*, vol. 12, no. 3, pp. 235–242, Sep. 1996. DOI: 10.1016/0736-5845(96)00009-9.

[245] S. Pitipong, P. Pornjit, and P. Watcharin, "An automated four-DOF robot screw fastening using visual servo," in *2010 IEEE/SICE International Symposium on System*

Integration, Dec. 2010, pp. 379–383. DOI: 10.1109/SII.2010.5708355.

[246] H. Chen, G. Zhang, H. Zhang, and T. A. Fuhlbrigge, "Integrated robotic system for high precision assembly in a semi-structured environment," *Assembly Automation*, vol. 27, no. 3, pp. 247–252, Aug. 2007. DOI: 10.1108/01445150710763277.

[247] H. Chen, J. Wang, G. Zhang, T. Fuhlbrigge, and S. Kock, "High-precision assembly automation based on robot compliance," *The International Journal of Advanced Manufacturing Technology*, vol. 45, no. 9, pp. 999–1006, Dec. 2009. DOI: 10.1007/s00170-009-2041-8.

[248] M. Peña-Cabrera, I. Lopez-Juarez, R. Rios-Cabrera, and J. Corona-Castuera, "Machine vision approach for robotic assembly," *Assembly Automation*, vol. 25, no. 3, pp. 204–216, Sep. 2005. DOI: 10.1108/01445150510610926.

[249] I. Díaz, D. Borro, O. Iparraguirre, *et al.*, "Robotic system for automated disassembly of electronic waste: Unscrewing," *Robotics and Computer-Integrated Manufacturing*, vol. 95, p. 103 032, Oct. 2025. DOI: 10.1016/j.rcim.2025.103032.

[250] G. M. Bone and D. Capson, "Vision-guided fixtureless assembly of automotive components," *Robotics and Computer-Integrated Manufacturing*, 12th International Conference on Flexible Automation and Intellig ent Manufacturing, vol. 19, no. 1, pp. 79–87, Feb. 2003. DOI: 10.1016/S0736-5845(02)00064-9.

[251] K. Böhnke and A. Gottscheber, "Fast Object Registration and Robotic Bin Picking," in *Research and Education in Robotics - EUROBOT 2009*, Berlin, Heidelberg: Springer, 2010, pp. 23–37. DOI: 10.1007/978-3-642-16370-8_3.

[252] S. Lee, J. Kim, M. Lee, K. Yoo, L. G. Barajas, and R. Menassa, "3D visual perception system for bin picking in automotive sub-assembly automation," in *2012 IEEE International Conference on Automation Science and Engineering (CASE)*, Aug. 2012, pp. 706–713. DOI: 10.1109/CoASE.2012.6386359.

[253] J.-K. Oh, S. Lee, and C.-H. Lee, "Stereo vision based automation for a bin-picking solution," *International Journal of Control, Automation and Systems*, vol. 10, no. 2, pp. 362–373, Apr. 2012. DOI: 10.1007/s12555-012-0216-9.

[254] P. S. Ogun, Z. Usman, K. Dharmaraj, and M. R. Jackson, "3D vision assisted flexible robotic assembly of machine components," Barcelona, Spain: The International Society for Optical Engineering, 2015, pp. 1–7. DOI: https://doi.org/10.1117/12.2229053.

[255] Y. Wang, R. Liu, F. Li, S. Endo, T. Baba, and Y. Uehara, "An effective hole detection method for 3D models," in *2012 Proceedings of the 20th European Signal Processing Conference (EUSIPCO)*, Aug. 2012, pp. 1940–1944.

[256] G. H. Bendels, *Detecting holes in point set surfaces*. Václav Skala - UNION Agency, 2006.

[257] W. H. Chen, G. Foo, S. Kara, and M. Pagnucco, "Automated generation and execution of disassembly actions," *Robotics and Computer-Integrated Manufacturing*, vol. 68, p. 102 056, Apr. 2021. DOI: 10.1016/j.rcim.2020.102056.

[258] P. Myer, "IXTOC I: Case Study of a Major Oil Spill," *Marine Affairs Theses and Major Papers*, Apr. 1984.

[259] E. Nicolson and R. Fearing, "Compliant control of threaded fastener insertion," in *[1993] Proceedings IEEE International Conference on Robotics and Automation*,

May 1993, 484–490 vol.1. DOI: 10.1109/ROBOT.1993.292026.

[260] L. Tang and Y.-B. Jia, "Robotic Fastening with a Manual Screwdriver," in *2023 IEEE International Conference on Robotics and Automation (ICRA)*, May 2023, pp. 5269–5275. DOI: 10.1109/ICRA48891.2023.10161139.

[261] M. Klingajay and N. Giannoccaro, "Comparison between least square & Newton Raphson for estimation parameters of an autonomous threaded fastenings," in *IEEE International Conference on Industrial Technology, 2003*, vol. 1, Dec. 2003, 163–168 Vol.1. DOI: 10.1109/ICIT.2003.1290261.

[262] W. C. Wilson, M. D. Rogge, B. H. Fisher, D. C. Malocha, and G. M. Atkinson, "Fastener Failure Detection Using a Surface Acoustic Wave Strain Sensor," *IEEE Sensors Journal*, vol. 12, no. 6, pp. 1993–2000, Jun. 2012. DOI: 10.1109/JSEN.2011.2181160.

[263] T. Matsuno, J. Huang, and T. Fukuda, "Fault detection algorithm for external thread fastening by robotic manipulator using linear support vector machine classifier," in *2013 IEEE International Conference on Robotics and Automation*, May 2013, pp. 3443–3450. DOI: 10.1109/ICRA.2013.6631058.

[264] K. Althoefer, B. Lara, Y. H. Zweiri, and L. D. Seneviratne, "Automated failure classification for assembly with self-tapping threaded fastenings using artificial neural networks," *Proceedings of the Institution of Mechanical Engineers, Part C: Journal of Mechanical Engineering Science*, vol. 222, no. 6, pp. 1081–1095, Jun. 2008. DOI: 10.1243/09544062JMES546.

[265] G. R. Moreira, G. J. G. Lahr, T. Boaventura, J. O. Savazzi, and G. A. P. Caurin, "Online prediction of

threading task failure using Convolutional Neural Networks," in *2018 IEEE/RSJ International Conference on Intelligent Robots and Systems (IROS)*, Oct. 2018, pp. 2056–2061. DOI: 10.1109/IROS.2018.8594501.

[266] M. Wende, M. Bender, M. Frye, D. Grunert, and R. H. Schmitt, "ML-Pipeline for the Quality Assessment of Screwdriving Processes," *Procedia CIRP*, 17th CIRP Conference on Intelligent Computation in Manufacturing Engineering (CIRP ICME '23), vol. 126, pp. 951–956, Jan. 2024. DOI: 10.1016/j.procir.2024.08.362.

[267] Z. Yang, P. G. Yazdi, and S. Thiede, "Machine-learning-enabled Decision Support for Screwdriving Process," in *2024 IEEE 22nd International Conference on Industrial Informatics (INDIN)*, Aug. 2024, pp. 1–6. DOI: 10.1109/INDIN58382.2024.10774335.

[268] O. M. Manyar, S. V. Narayan, R. Lengade, and S. K. Gupta, "Physics-Informed Learning to Enable Robotic Screw-Driving Under Hole Pose Uncertainties," in *2023 IEEE/RSJ International Conference on Intelligent Robots and Systems (IROS)*, Oct. 2023, pp. 2993–3000. DOI: 10.1109/IROS55552.2023.10342151.

[269] A. Claudia Carvalho, A. Isabel Carvalho, and R. Correia, "Robot With Vision Guidance System for Unscrewing Operation," in *2024 International Conference on Decision Aid Sciences and Applications (DASA)*, Dec. 2024, pp. 1–5. DOI: 10.1109/DASA63652.2024.10836165.

[270] R. Bicker, K. Burn, Z. Hu, W. Pongaen, and A. Bashir, "The Early Development of Remote Tele- manipulation Systems," in *International Symposium on History of Machines and Mechanisms*, Dordrecht: Springer Netherlands, 2004, pp. 391–404. DOI: 10.1007/1-4020-2204-2_30.

[271] A. C. Rolfe, "A perspective on fusion relevant remote handling techniques," *Fusion Engineering and Design*, Proceedings of the 24th Symposium on Fusion Technology, vol. 82, no. 15, pp. 1917–1923, Oct. 2007. DOI: 10.1016/j.fusengdes.2007.04.049.

[272] D. Forkel, *Towards Autonomous Robotic Radiation Surveys in the SPS*, Nov. 2024. Available at: https://indico.cern.ch/event/1459603/.

[273] G. Miccichè, M. Ascott, A. Bakic, *et al.*, "The remote handling system of IFMIF-DONES," *Fusion Engineering and Design*, SI:SOFT-30, vol. 146, pp. 2786–2790, Sep. 2019. DOI: 10.1016/j.fusengdes.2019.01.112.

[274] J. Lyytinen, P. Tikka, T. Määttä, T. Avikainen, and S. Rantala, "Development of the remote handling connector for ITER divertor diagnostic system," *Fusion Engineering and Design*, vol. 165, p. 112 243, Apr. 2021. DOI: 10.1016/j.fusengdes.2021.112243.

[275] W. L. Zhao, Y. Li, K. Lu, *et al.*, "Engineering Design and Analysis of the CFETR Divertor Remote Maintenance System," *IEEE Transactions on Plasma Science*, vol. 48, no. 6, pp. 1637–1640, Jun. 2020. DOI: 10.1109/TPS.2020.2980797.

[276] P. Espinosa Peralta, M. Ferre, and M. Á. Sánchez-Urán, "Robust Fastener Detection Based on Force and Vision Algorithms in Robotic (Un)Screwing Applications," *Sensors*, vol. 23, no. 9, p. 4527, Jan. 2023. DOI: 10.3390/s23094527.

[277] L. Pagliara, R. Violeta, E. Ferrentino, M. Ferre, and C. Pasquale, *Robotized bolting operation*, 2025. Available at: https://drive.google.com/file/d/1X8HnU1fIE0ODbYRTPzOtfOLtFsqeVmIW/view?usp=drive_link.

[278] Zero Err, *eRob 70I-ZeroErr eRob 70I Rotary Actuator*, 2025. Available at: https://en.zeroerr.cn/rotary_actuators/erob70i.

[279] C. Mei, J. Yuan, and R. Guan, "Adaptive unified Impedance and Admittance control using online environment estimation," in *2018 IEEE International Conference on Robotics and Biomimetics (ROBIO)*, Dec. 2018, pp. 1864–1869. DOI: 10.1109/ROBIO.2018.8665123.

[280] M. Zhuang, J. Chen, B. Tao, M. Gul, F. Wang, and Y. Wu, "Exploring the Learning Curve of Dental Implant Placement Using a Task-Autonomous Robotic System Among Young Dentists From Different Specialties—A Pilot Module Study," *Clinical Implant Dentistry and Related Research*, vol. 27, no. 1, e13402, Feb. 2025. DOI: 10.1111/cid.13402.

[281] D. Gagliardi and G. Russo, "On a probabilistic approach to synthesize control policies from example datasets," *Automatica*, vol. 137, p. 110 121, Mar. 2022. DOI: 10.1016/j.automatica.2021.110121.

[282] E. Garrabe, H. Jesawada, C. D. Vecchio, and G. Russo, "On convex data-driven inverse optimal control for nonlinear, non-stationary and stochastic systems," *Automatica*, vol. 173, p. 112 015, Mar. 2025. DOI: 10.1016/j.automatica.2024.112015.

[283] L. Cheng and M. Tavakoli, "COVID-19 Pandemic Spurs Medical Telerobotic Systems: A Survey of Applications Requiring Physiological Organ Motion Compensation," *Frontiers in Robotics and AI*, vol. 7, Nov. 2020. DOI: 10.3389/frobt.2020.594673.

[284] G. Peng, T. Li, C. Yang, and C. L. Philip Chen, "Approximation-Based Admittance Control of Robot-Environment Interaction With Guaranteed Perfor-

mance," *IEEE Transactions on Systems, Man, and Cybernetics: Systems*, vol. 54, no. 10, pp. 6482–6494, Oct. 2024. DOI: 10.1109/TSMC.2024.3430265.